Evolution of Barred Galaxies and Associated Structures

Sandor J. Kruk
Merton College
University of Oxford

A thesis submitted for the degree of
Doctor of Philosophy

Trinity 2018

Abstract

Bars are common in disc galaxies along with many associated structures such as disc-like bulges, boxy/peanut bulges, rings, etc. They are a sign of maturity of disc galaxies and can play an important role in their evolution. In this thesis, I investigate the specific role bars play in quenching the star formation in, and shaping of their host galaxies.

In order to test how bars affect their host galaxies, I study the discs, bars and bulges of what is currently the largest sample of barred galaxies ($\sim 3,500$), selected with visual morphologies from the Galaxy Zoo project. I perform multi-wavelength and multi-component photometric decomposition, with the novel GALFITM software. With the detailed structural analysis I obtain physical quantities such as the bar- and bulge-to-total luminosity ratios, effective radii, Sérsic indices and colours of the individual components. I find a clear difference in the colours of the components, the discs being bluer than the bars and bulges. An overwhelming fraction of bulge components have Sérsic indices consistent with being disc-like bulges. I compare the barred galaxies with a mass- and environment-matched volume-limited sample of unbarred galaxies, finding that the discs of unbarred galaxies are bluer compared to the discs of barred galaxies, while there is only a small difference in the colours of the bulges. I suggest that this is evidence for secular evolution via bars that leads to the build-up of disc-like bulges and to the quenching of star formation in the galaxy discs. I identify a subsample of unbarred galaxies that are better fitted with an additional component, identified as an inner lens/oval. I find that their structural properties are similar to barred galaxies, and speculate that lenses might be former bars.

Using the decompositions, I identify a sample of 271 late-type galaxies with curious bars that are off-centre from the disc. I measure offsets up to 2.5 kpc between the photometric centres of the stellar disc and stellar bar, which are in good agreement with predictions from simulations of dwarf-dwarf tidal interactions. The median mass of these galaxies is $10^{9.6} M_{\odot}$, and they are similar to the Large Magellanic Cloud, which also has an offset bar. Very few high mass galaxies with significant bulges show offsets, thus I suggest that the self-gravity of a significant bulge prevents the disc and bar from getting displaced with respect to each other. I conduct a search for companions to test the hypothesis of tidal interactions, but find that a similar fraction of galaxies

with offset bars have companions within 100 kpc as galaxies with centred bars. Since many of these galaxies appear isolated, interactions might not be the only way to produce an offset bar.

One suggested alternative is that the dark matter haloes surrounding the galaxies are lopsided, which distorts the potential, and imprints the lopsidedness and offsets onto the galaxy discs. I investigate the asymmetries in the kinematics of a subsample of such galaxies using data from the MaNGA survey, and find that the perturbations in the haloes are $\sim 6\%$, for both galaxies with off-centre and centred bars. I also measure the amplitude of non-circular motions in the outer discs due to an oval potential and find only minor departures from circularity, suggesting that the dark matter haloes are consistent with being spherical (axis ratio $q \gtrsim 0.96$). Therefore, the lopsidedness of the dark matter haloes cannot be the origin of the offsets. Either small companions are missed due to the incompleteness of the Sloan Digital Sky Survey spectroscopic survey, or interactions with dark matter satellites might explain the offsets. Modeling the kinematics of these galaxies, I find that the Hα gas rotation is centred closer to the centre of the bar than the centre of stellar rotation, suggesting that, in general, the bars are located closer to the dynamical centres of these galaxies than the discs. This implies that the discs are offset in these galaxies, not the bars.

If offsets are characteristic of low mass galaxies only, high mass galaxies show vertically extended bars, known as boxy/peanut bulges. I investigate, for the first time, the formation and evolution of these structures associated to bars, from $z \approx 0$ to $z = 1$. I compare two samples of moderately inclined galaxies with masses $M_* > 10^{10} M_\odot$, imaged by the Sloan Digital Sky Survey and the *Hubble Space Telescope*. Using a novel technique to classify bar isophotes, and based on the visual inspection of three expert astronomers, I find an evolving fraction of galaxies having boxy/peanut bulges from 30% at $z \approx 0$ to $\sim 0\%$ at $z = 1$, and a strong correlation with stellar mass. I find 26 galaxies (15 at higher redshifts) in the phase of bar buckling, the mechanism proposed to form boxy/peanut bulges. The peak redshift of buckling is $z \approx 0.75$, where the bar buckling fraction is 4 times higher than in the local Universe. My observations suggest that many, if not all, of the boxy/peanut bulges are formed via buckling, ~ 2 Gyr after bar formation, with the buckling phase lasting for approximately 0.8 Gyr.

I discuss my findings in the context of the evolution of barred galaxies and propose ideas for future work – applying similar decomposition techniques to higher redshift, and better resolution datasets, using integral field spectroscopic data to study the stellar populations of barred galaxies in greater detail, as well as a novel project to identify large nuclear discs in galaxies.

Statement of Originality

I carried out the work presented in this thesis at the Physics Department, Astrophysics Sub-department, University of Oxford, between October 2014 and July 2018 under the guidance and supervision of Prof. Chris Lintott. I was funded by the Science and Technology Facilities Council (STFC) Studentship Grant Code ST/MJ0371X/1. I hereby declare that no part of this thesis has been accepted or submitted in support of any other degree, diploma or qualification at the University of Oxford or elsewhere. Except where otherwise stated, or where reference is made to the work of others, the work in this thesis is entirely my own.

The work in Chapter 2 and Chapter 3 are based on work peer-reviewed and published in Kruk, Sandor J. et al., **Galaxy Zoo: secular evolution of barred galaxies from structural decomposition of multiband images**, Monthly Notices of the Royal Astronomical Society, Volume 473, Issue 4, p.4731-4753 (Kruk et al., 2018). As the lead author, I selected the barred and comparison samples, fitted the galaxies, analysed the results and wrote the manuscript. Dr Steven Bamford and Dr Boris Häussler contributed with their expertise in galaxy fitting, as the authors of GALFITM. The Galaxy Zoo team provided help in the interpretation of the results.

The work in Chapter 4 is based on work peer-reviewed and published in Kruk, Sandor J. et al., **Galaxy Zoo: finding offset discs and bars in SDSS galaxies**, Monthly Notices of the Royal Astronomical Society, Volume 469, Issue 3, p.3363-3373 (Kruk et al., 2017). As the lead author, I identified the sample of galaxies with off-centre bars, studied their properties and wrote the manuscript. The Galaxy Zoo team provided help in the interpretation of the results.

The work in Chapter 6 has been completed in collaboration with Dr. Peter Erwin (Max Planck Institute for Extraterrestrial Physics, Munich) and Dr. Victor Debattista (University of Central Lancashire) and is in preparation for submission to the Monthly Notices of the Royal Astronomical Society. I was responsible for identifying the samples, preparing the FITS images, setting up the project to classify the galaxies and analysing and interpreting the results. Erwin produced the contour plots used to classify the galaxy images and the galaxy evolution model used to predict the fraction of B/P bulges and buckling bars with redshift. Debattista produced the N-body simulations to compare to our results. All three of us classified the galaxy images in

this work and identified B/P bulges and buckling bar candidates. Erwin inspected the buckling bar candidates to identify the final sample.

The work in this thesis relies on observations from the Sloan Digital Sky Survey (SDSS). Funding for the SDSS III & IV has been provided by the Alfred P. Sloan Foundation, the U.S. Department of Energy Office of Science, and the Participating Institutions. SDSS-IV acknowledges. The SDSS web site is www.sdss.org. Part of Chapter 6 is based on observations made with the NASA/ESA Hubble Space Telescope, and obtained from the Hubble Legacy Archive, which is a collaboration between the Space Telescope Science Institute (STScI/NASA), the Space Telescope European Coordinating Facility (ST-ECF/ESA) and the Canadian Astronomy Data Centre (CADC/NRC/CSA). This investigation has been made possible by the participation of over 350,000 users in the Galaxy Zoo project. Their contributions are acknowledged at http://authors.galaxyzoo.org.

This thesis made extensive use of *Astropy* a community-developed core Python package for Astronomy (Astropy Collaboration, 2013), of the Tool for Operations on Catalogues And Tables (Taylor, 2005) and NASA's Astrophysics Data System Bibliographic Services.

Sandor Kruk, *July 2018*

"For us, there is only the trying. The rest is not our business."

– T. S. Eliot

Acknowledgements

It would have not been possible to write this thesis without all the support I have received over the past four years. First and foremost, an immense thank you to my supervisor Prof. Chris Lintott. Your guidance has been instrumental in me becoming a scientist. Thank you for always taking the time for me and my many questions and ideas, for your patience, for steering me in the right direction and for your continuous encouragement. I am extremely grateful for your support in all my endeavours, in academia and outside. You have been an inspiring mentor and an awesome supervisor. Thank you for taking the time and meeting me in London four years ago.

I would also like to thank the entire Galaxy Zoo Team for the inspirational science discussions, for the invaluable scientific inputs and feedback on my work, and in general, for making the collaboration so enjoyable. In particular, I would like to thank Karen Masters, Brooke Simmons and Steven Bamford for helping me along the way with their scientific expertise and their helpful career advice.

A special thanks to Victor Debattista for our collaboration, for your meticulous correspondence and readiness to answer my questions. I have really enjoyed our science chats and, as an observer, I gained a lot from your theoretical perspective. I would also like to thank Peter Erwin for our collaboration and for showing me how important it is to be attentive to details.

I would like to thank the British Physics Olympiad, and especially its chairman Robin Hughes, for allowing me to set up and coordinate the Astronomy and Astrophysics Olympiad here in the UK. Thank you for your trust. I have greatly enjoyed training and leading the UK team to three international olympiads, and I am not unhappy about the results either. All of this would not have been possible without the hard work of Lena, Sian, Alex and Charlie. Participating in the olympiad ten years ago, as a young student, inspired me to become an astronomer, so all your hard work in inspiring others will not go amiss. Thank you from all my heart and it has been a great pleasure working together.

My experience in Oxford has been made unforgettable by the friends I met along the way and by the amazing Romanian community I became part of. I loved our gatherings at the 'Poetry Shop' and discussing anything from art, music, science to

politics. And they were not all only discussions, since many of our plans became real. I enjoyed organising together the Oxford for Romania Summer School, an occasional art exhibition and music concert to a protest and inviting the ex-prime minister to Oxford. In particular, thanks to Mariela, Dani, Cip, Mihai, Cora, Dragos, Vlad, Cosmina, Marina, Alexandra for you readiness to help, for your friendship and kindness and for making me feel part of a family. Our country would be a whole new place if all these amazing people were to return. I would like to extend my gratitude to Mihai and Marina for also reading parts of this thesis.

To my office mates in 558, in particular John, Rupert and Alex, thanks for our daily chats, for the Thursday football, for help with coding and sharing LaTeX templates and for the occasional procrastination. I was lucky enough to write this thesis at the time of World Cup 2018, which has been phenomenal source of inspiration and procrastination. I thoroughly enjoyed watching all of the 66 games while writing this thesis. Luckily, I won the sweepstake: *Vive la France!*

My deepest thanks to my parents, brother and my extended family for their endless love, support and for believing in me. I missed you all!

Finally, my life in Oxford would have been incomplete without meeting Eliza. I was so lucky to meet you at that salsa class in 2014! You have been the joy of my life ever since. Thank you for always supporting me, understanding me and caring for me. My time in Oxford would have not been nearly the same without you.

pentru copilaş

Contents

List of Figures

Chapter 1

Introduction

Galaxies are gravitationally bound collections of stars, gas and dark matter. They are the building blocks of the Universe, which contains a trillion galaxies (Conselice et al., 2016). Understanding how galaxies form and change over time provides not only insight into the variety of galaxy shapes and sizes that we observe, but also reveals how the Milky Way, a barred spiral galaxy (Liszt & Burton, 1980; Blitz & Spergel, 1991; Binney et al., 1991; Freudenreich, 1998), came into existence. Unfortunately, we cannot directly observe the formation and evolution of galaxies, as these processes take millions or billions of years ('astronomical timescales'). However, what we see around us are still frames of galaxies in different phases of their evolution, as by observing them at different distances from us we are 'looking back' at the history of the Universe. By observing a large number of galaxies at various stages of their development, astronomers can infer important details about their formation and evolution.

The observation and classification of the visual appearance of galaxies makes a powerful tool to study their evolution. The appearance of a galaxy, referred to as its morphology, is a snapshot of the orbital distribution of stars, gas and dust, which give rise to structures such as discs, bars, rings, bulges or spiral arms. Almost a century ago, the famous American astronomer, Edwin Hubble, produced the most notable morphological classification scheme of galaxies, known as the 'Hubble Tuning Fork' (Hubble, 1926, 1936). In his seminal work, Hubble split galaxies into *ellipticals*, labelled based on their oblateness (from E0, being round, to E7, corresponding to an ellipticity of 0.7), and *spirals*. The class of *spiral galaxies* was further split into barred spirals (SB) and unbarred ('normal') spirals (S). These were ordered in a sequence Sa-Sb-Sc (and SBa-SBb-SBc) based on (1) the size of the bulge relative to the size of the disc and (2) the appearance of the spiral arms: specifically how tight the spiral arms are and how clearly resolved they are. Hubble (1926) referred to the three classes, a, b

and c, as 'early', 'intermediate' and 'late' types. Although having opposite temporal connotations, Hubble (1926) explicitly stated that this is not an evolutionary sequence (see Footnote I in Hubble 1926), but rather a sequence from simple to complex. A visual representation of the Hubble Tuning Fork (originally presented in Hubble 1926) created with images from the Sloan Digital Sky Survey (SDSS) can be seen in Figure 1.1. An intermediate class between spirals and ellipticals with a central bulge but without spiral arms, known as lenticular galaxies or S0s, predicted by Hubble (1936) to fill the gap between ellipticals and spirals, was later introduced in the *Hubble Atlas of Galaxies* (Sandage, 1961). Astronomers commonly refer to ellipticals and lenticular galaxies, sometimes including Sa spirals, as 'early-type galaxies' and to spiral galaxies as 'late-type' (terminology sometimes used interchangeably with ellipticals/spirals). In this thesis I refer to lenticulars and Sa spirals as early-type, and Sb-Sc etc. galaxies as late-type, and to all of them (excluding ellipticals), collectively, as 'disc' galaxies.

The focus of this thesis is on barred galaxies, in particular the properties and evolution of their structures. Bars in galaxies were first recognised by Curtis (1918) who referred to barred galaxies as ϕ-spirals. Hubble (1926) noticed that the bar never seemed to extend past the spiral arms, and the shape of these galaxies is more accurately represented by θ. He realised that they are abundant in the local Universe (20% of all spirals) which led him to dedicate a major part of his classification scheme to barred spiral galaxies (Hubble, 1926, 1936). Hubble (1926) also recognized that about 3% of galaxies do not show dominant nuclei and rotational symmetry, classifying them as 'irregular' galaxies.

de Vaucouleurs (1959) revised the Hubble sequence by recognizing the subtle continuity between different morphological types, introducing more detailed classifications for bars, rings and other features, in what is now known as the Comprehensive de Vaucouleurs Revised Hubble-Sandage (CVRHS) system (further described in the Third Reference Catalog of Bright Galaxies, de Vaucouleurs et al. 1991, and in Buta et al. 2007 and Buta 2013). de Vaucouleurs proposed two more classes of spiral (S) galaxies, following the 'a', 'b', 'c' sequence: types 'd' for dwarf spirals and 'm' for Magellanic spirals. The Sm galaxies, first classified as a distinct morphological class by de Vaucouleurs & Freeman (1972) and named after their prototype, the Large Magellanic Cloud, are an intermediate class between dwarf spirals (Sd) and irregular galaxies (Irr) and are characterised by one prominent spiral arm, no bulge, and sometimes a bar.

Additionally, for each type of spiral, de Vaucouleurs introduced three subclasses: SA (non-barred), SB ("strongly" barred) and an intermediate class, SAB (for "weakly" barred galaxies). These weakly barred galaxies have intermediate 'strengths' between

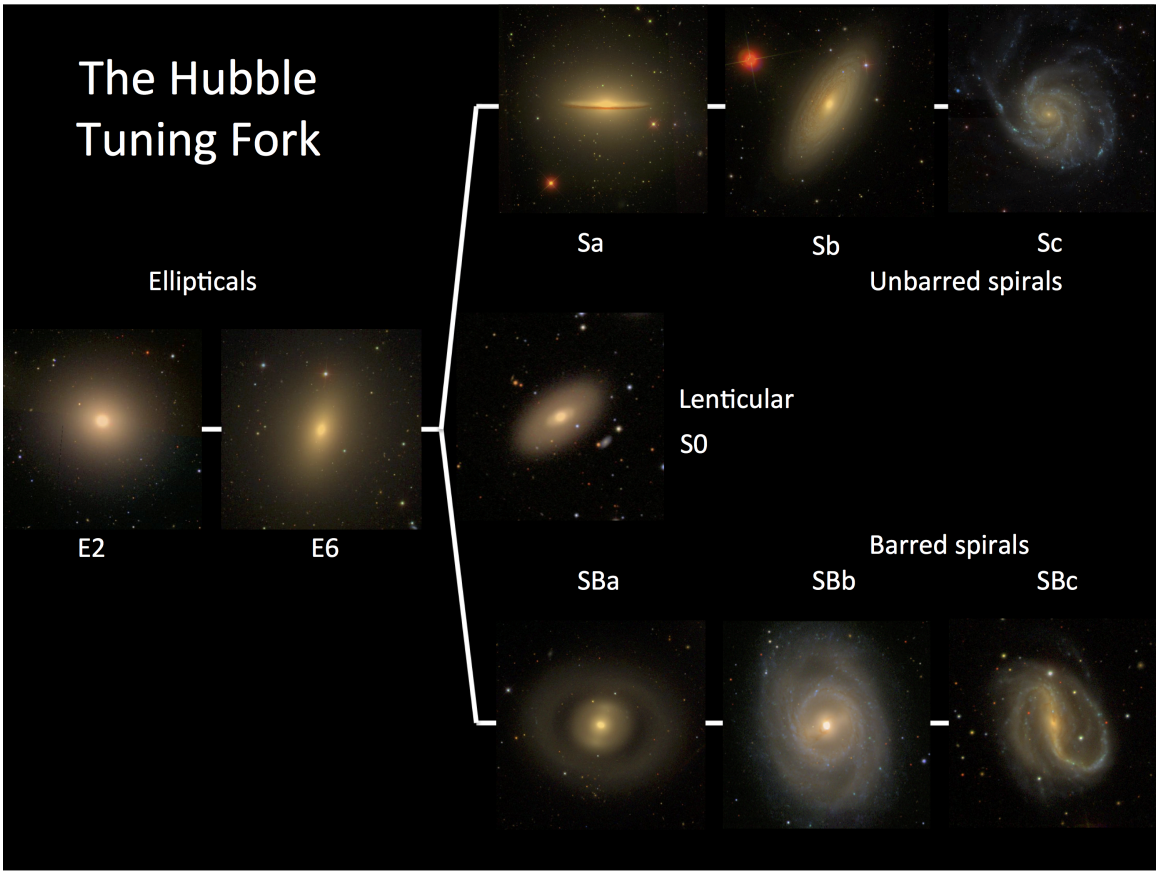

Figure 1.1: The Hubble Tuning Fork with *gri* colour composite images from the Sloan Digital Sky Survey of the original galaxies suggested by Hubble (1926). Galaxies: E2 - NGC 3379 (or M105); E6 - NGC 4621; Sa - NGC 4594 (or M104, Sombrero Galaxy); Sb - NGC 2841; Sc - NGC 5447 (or M101, Pinwheel Galaxy); SBa - NGC 2859; SBb - NGC 3351 (or M95); SBc - NCG 7479. A lenticular, S0 galaxy (NGC 6278) is included, although not part of Hubble (1926) as no examples were known at that time. Credit: Masters et al. (in prep., 2018) and SDSS.

SA and SB, where by strength de Vaucouleurs meant the relative length and contrast compared to the disc. A small and faint bar is labeled as a weak bar, and a long and prominent bar is labeled as a strong bar. Figure 1.2 illustrates the different types of spiral subclasses and bars in galaxies in a Hubble sequence from E to Sm, as classified by Buta (2011) using the CVRHS system.

The bar in the vast majority of galaxies is situated at the centre of the disc. Nonetheless, some galaxies are observed to host a bar which is offset from the centre of the stellar disc, in particular galaxies of types SBm and SABm, as shown in Figure 1.3. One famous example of such a galaxy is the Large Magellanic Cloud. The formation of the bar and the origin of the observed offsets in these galaxies are still uncertain. Various scenarios have been proposed, such as an interaction with a companion galaxy

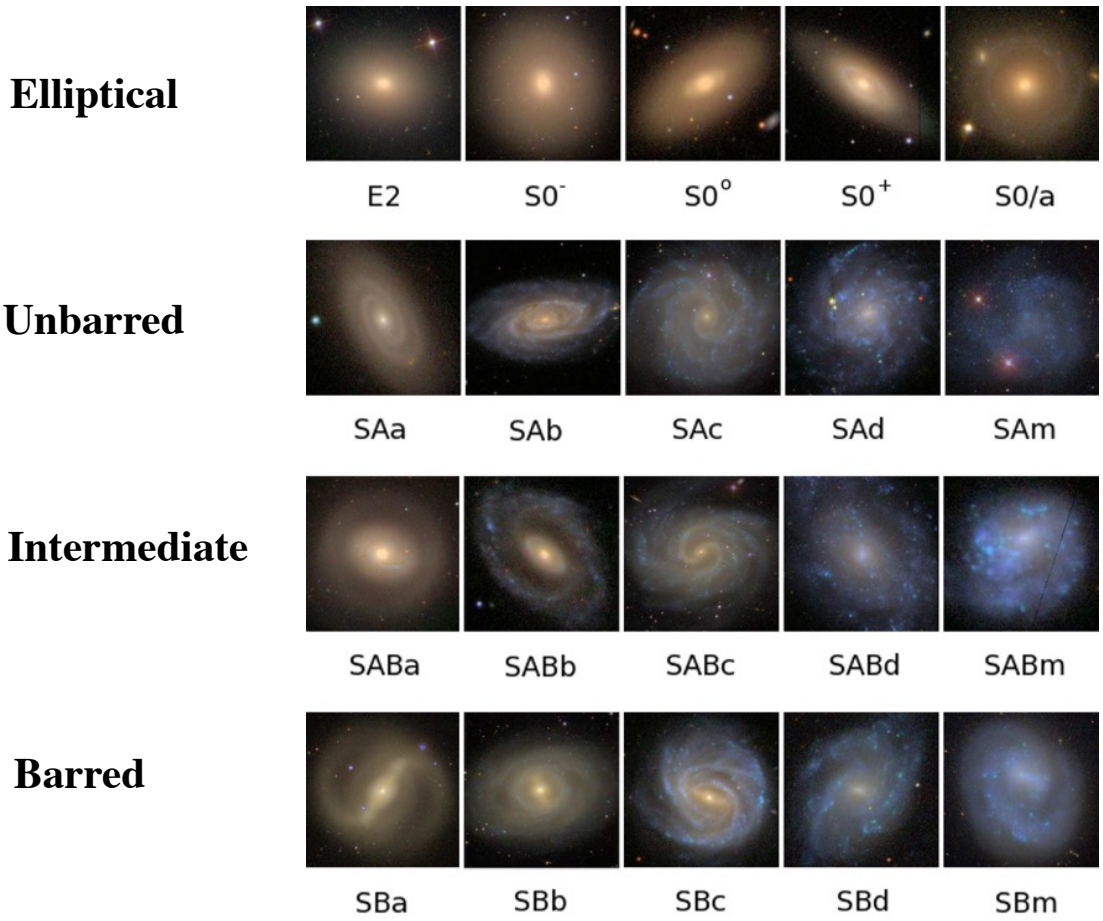

Figure 1.2: The Hubble Tuning Fork according to the CVRHS system, with de Vaucouleurs (1959) classification of spiral galaxies into SA (unbarred), SAB (weakly barred) and SB (strongly barred) galaxies, and in types $a - d$ based on bulge size and spiral arm tightness. The m class of irregular galaxies was added by de Vaucouleurs & Freeman (1972). *gri* colour-composite images from SDSS. Modified image and classifications from Buta (2011).

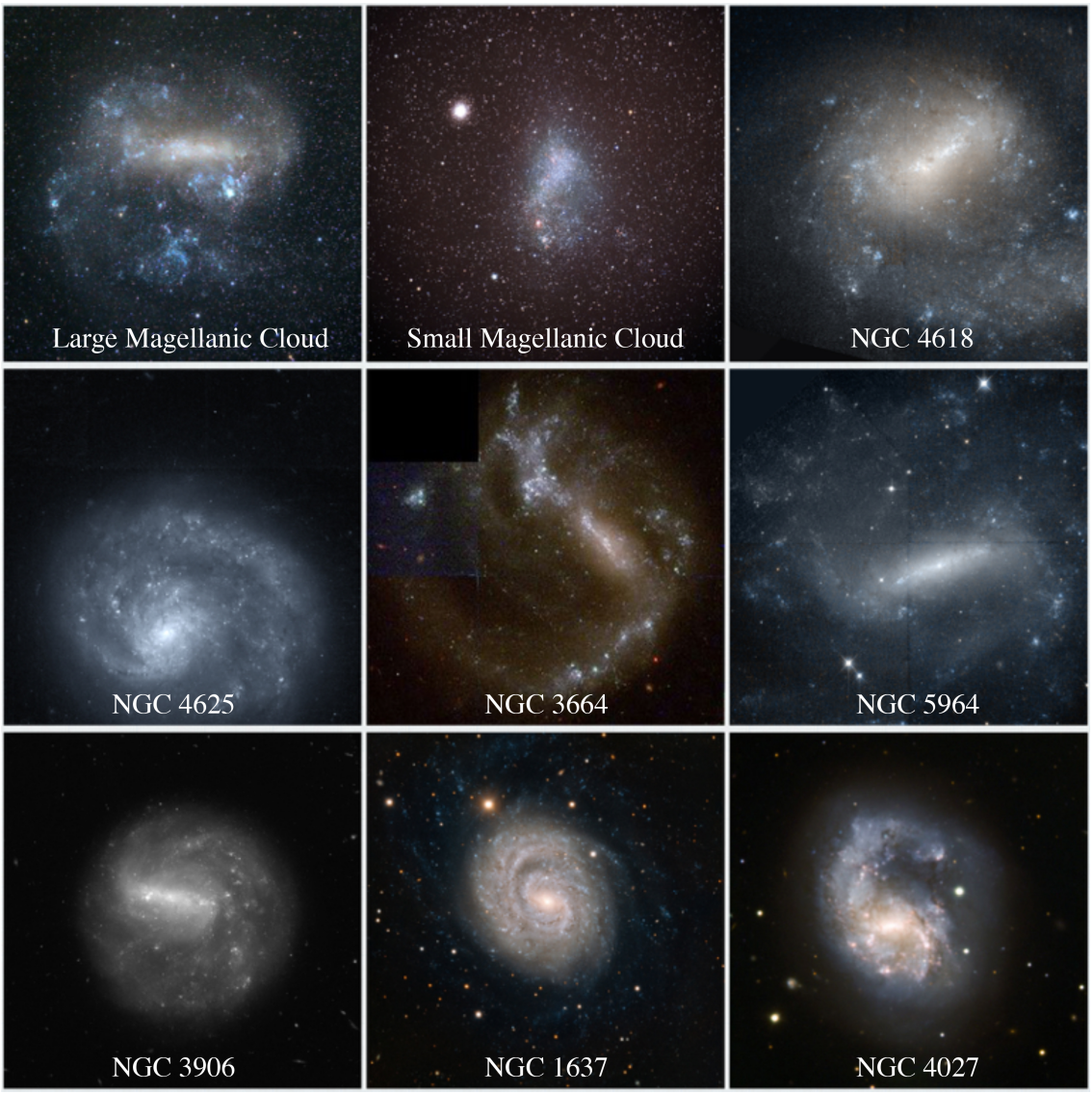

Figure 1.3: Nearest Magellanic barred spirals and barred Sc and Sd-type galaxies (NGC 1637 and NGC 3906) showing a bar that is offset from the centre of the disc and no bulge. Image credits: Large Magellanic Cloud (Primoz Cigler, http://astro.primozcigler.net/gallery/image/295/large-magellanic-cloud), Small Magellanic Cloud (ESA/Hubble, Akira Fujii), NGC 4618, NGC 4625, NGC 3664, NGC 5964, NGC 3906 (all NASA/ESA *Hubble Space Telescope*), NGC 1637, NGC 4027 (both ESO/VLT).

(Besla et al., 2012; Pardy et al., 2016), a collision with a dark matter halo (Bekki, 2009), the off-centering between the galaxy and the dark matter halo (Levine & Sparke, 1998; Noordermeer et al., 2001) and the asymmetry of the dark matter halo surrounding the galaxy (Jog, 1997, 2000). Although these galaxies were historically referred to as 'offset bars', it is still unknown which of the two components (the disc or the bar) is actually off-centre from the centre of the dark matter potential.

More recently, a new paradigm in the classification of early-type galaxies was introduced by the ATLAS^{3D} team (Cappellari et al., 2011b), based on galaxy kinematics inferred through spectroscopy. Studying the kinematics helps distinguish between face-on disc galaxies and spheroids. In a detailed study of the resolved kinematics of 260 early-type galaxies (Emsellem et al., 2007; Cappellari et al., 2011a), Cappellari et al. (2011b) split the galaxies into fast rotators (having ordered disc-like rotation) and slow rotators (showing no ordered rotation), based on their stellar angular momentum and ellipticity. ATLAS^{3D} has shown that many ($\sim 65\%$) elliptical galaxies are in fact rotating like discs (fast rotators) and should be placed in a parallel sequence to spiral galaxies. The kinematic classification of galaxies, known as the ATLAS^{3D} comb, is shown in Figure 1.4 (from Cappellari et al. 2011b). Both normal spirals and barred galaxies show ordered rotation and are considered fast rotators in this classification scheme, placed at the three teeth of the comb. The ATLAS^{3D} kinematic classification of galaxies provides a different, physically motivated classification of galaxies, complementary to the visual classifications in the traditional Hubble Tuning Fork. For example, the kinematic classification of galaxies can help distinguish between ellipticals and S0s, whose visual classification might be biased by the viewing angle, while the visual classification can identify structures such as bars, bulges, rings or spiral arms which might not be apparent in the kinematic maps of the galaxies.

1.1 Galaxy scaling relations

Galaxy size scales with stellar velocity and luminosity (or stellar mass), in what are known as dynamical scaling relations. For late-type spiral galaxies, the luminosity scales with the circular velocity of galaxies, referred to as the Tully-Fisher relation, $L \propto V_c^4$ (Tully & Fisher, 1977). For elliptical galaxies, the luminosity scales with the stellar velocity dispersion measured within an aperture (for example within the half-light radius r_e), $L \propto \sigma_e^4$ (Faber-Jackson relation, Faber & Jackson 1976), while the galaxy surface brightness, and thus the luminosity, scales with galaxy size (Kormendy relation, Kormendy 1977). The last two relations are projections of the Fundamental Plane that describes the (L, σ_e, r_e) of galaxies (Dressler et al., 1987; Djorgovski &

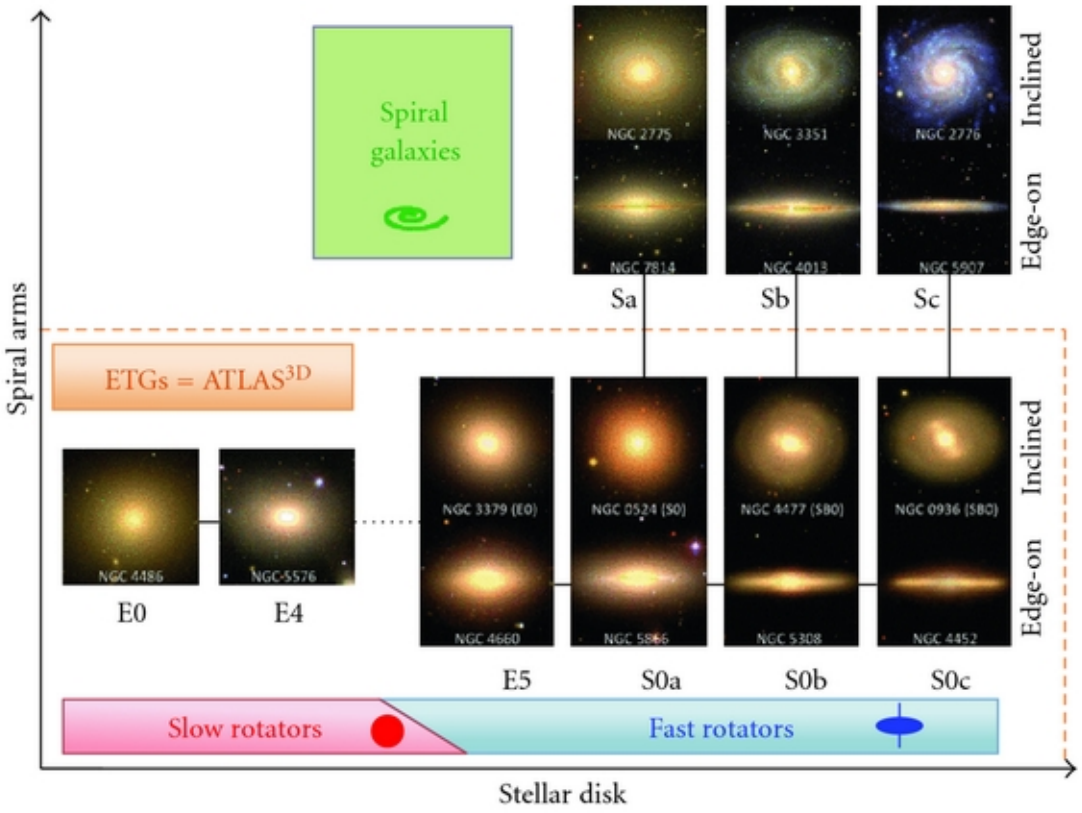

Figure 1.4: The ATLAS^{3D} comb diagram showing the kinematic classification of galaxies. Galaxies are split into slow rotators, showing no ordered rotation, and a parallel sequence of fast rotators, showing disc-like rotation. E-type galaxies can have different kinematics, although they show similar visual morphologies. Original diagram from Cappellari et al. (2011b).

Davis, 1987). The luminosity of galaxies in the Fundamental Plane can be replaced by stellar mass, derived dynamically (Cappellari et al., 2013), leading to a Mass Plane (M_*, σ_e, r_e), which has as one projection the mass-size $(M_* - r_e)$ relation, shown in Figure 1.5, with parallel lines of constant σ_e, for galaxies of all Hubble types.

The Mass Plane scaling relations show breaks in both the $M_* - \sigma_e$ and $M_* - r_e$ relations at characteristic masses of $2\times10^9\,M_\odot$, $3\times10^{10}\,M_\odot$ and $2\times10^{11}\,M_\odot$, as shown in Figure 1.5. The first break represents a transition from bulgeless dwarf irregulars and spheroidal galaxies to late-type galaxies. Above this mass, galaxies follow parallel lines of constant velocity dispersion, which trace equal mass concentration or bulge mass fraction (shown with an arrow in Figure 1.5, Cappellari 2016). Late-type spirals are located near the top of the diagram, at any given mass, while early-type spiral galaxies, with lower r_e, have larger σ_e and are located lower in the diagram. The

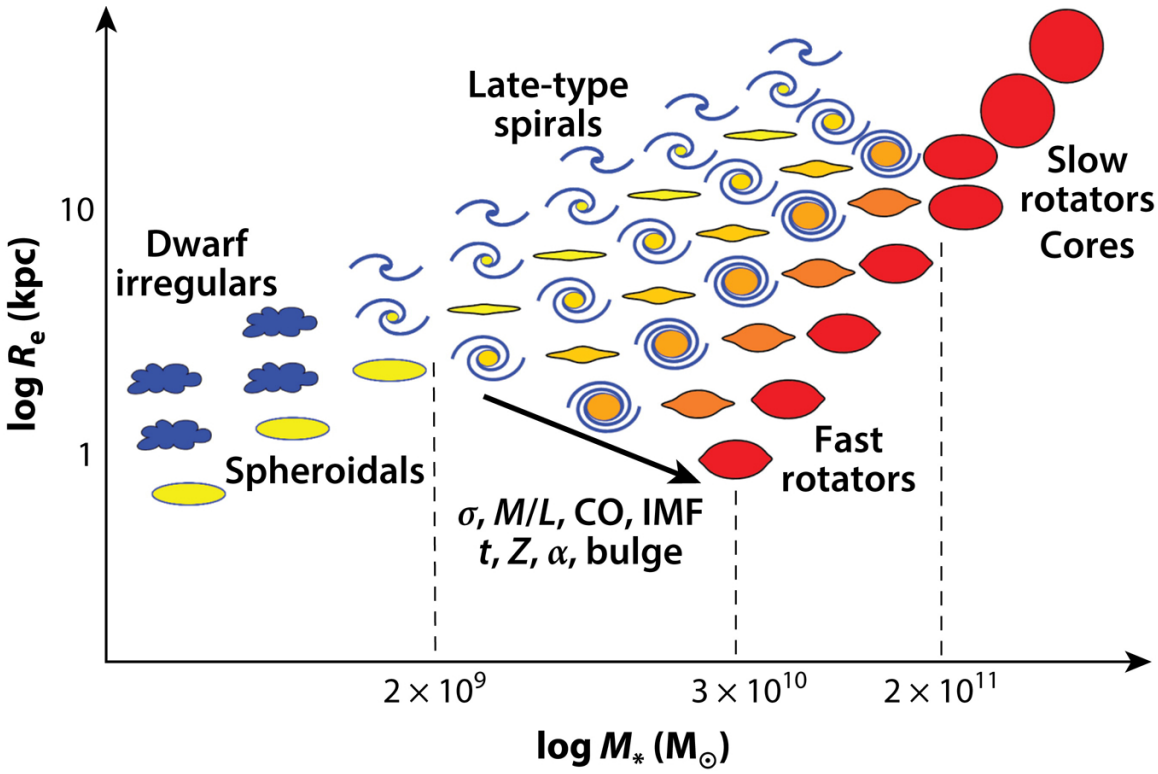

Figure 1.5: Galaxy properties and morphologies on the mass-size ($M_* - r_e$) diagram. Galaxies properties (mass-to-light ratio, gas content, initial mass function, metallicity, bulge fraction etc.) vary across parallel lines of constant velocity dispersion σ, increasing in the direction of the arrow. Late-type spiral galaxies are situated at the top of the diagram, while the more centrally concentrated early-type spirals and fast rotators (discs) are situated towards the bottom of the diagram, at lower r_e and higher σ_e, for a given mass. The stellar masses on the x-axis indicate three characteristic masses, corresponding to transitions between dwarf irregulars and spirals (at $M_* \approx 2 \times 10^9\, M_\odot$), a break in the scaling relations setting a minimum size and maximum density for fast rotators and spirals (at $M_* \approx 3 \times 10^{10}\, M_\odot$), and a transition from fast rotators and slow rotators (at $M_* \approx 2 \times 10^{11}\, M_\odot$). Original diagram from Cappellari (2016).

second break is at $M_* \approx 3 \times 10^{10}\, M_\odot$, where the slope changes and early-type galaxies reach their minimum size (Cappellari, 2016). This mass was identified by Kauffmann et al. (2003b) as the mass at which the properties of galaxies in the low redshift Universe change radically. Lower mass galaxies have younger stellar populations and are disc-dominated, while higher mass galaxies tend to be passive, more concentrated and with higher stellar mass surface densities typical of bulges. Figure 1.5 illustrates this transition, revealing that the velocity dispersion, σ_e, is a better indicator of galaxy properties (size, colour, metallicity, stellar population age, bulge fraction, molecular gas content, mass-to-light ratio etc.) than stellar mass (Graves et al., 2009; Cappellari, 2016). At $M_* \approx 2 \times 10^{11}\, M_\odot$ there is a transition from fast rotators, showing evidence

for discs, to slow rotators with a core surface brightness profile (Cappellari, 2013). Above this mass, spiral galaxies and fast rotators are essentially absent.

Individual galaxy components (for example discs and bulges) have their own scaling relations, which can be obtained using photometric decompositions (Kormendy & Bender, 2012). Understanding how barred galaxies and their structural components fit in this picture is important in our developing view of galaxy formation and evolution, and it is a goal of this thesis.

1.2 Theoretical considerations

In the ΛCDM cosmological model (Perlmutter et al. 1999; Sahni & Starobinsky 2000, etc.), galaxies form out of primordial fluctuations in the early Universe, which grow exponentially with time (Peebles, 1982; Blumenthal et al., 1982; Peebles, 1993). This standard model is characterised by a cosmological constant (denoted by Λ), associated with dark energy, and cold dark matter (CDM). Observations suggest that the Universe is flat and is made up of $\sim 5\%$ baryonic (visible) matter, $\sim 26\%$ dark matter and $\sim 69\%$ dark energy (Planck Collaboration, 2016). In hierarchical clustering models, matter (dominated largely by dark matter) in the overdense regions of the Universe collapses under its own gravity and forms dark matter haloes which grow through accretion and mergers with other haloes, producing an inhomogeneous large-scale structure (referred to as the 'cosmic web') made up of clusters, filaments and voids. The baryonic matter, primordially made up of hydrogen, helium and traces of lithium, follows the dark matter haloes, and when it cools, it collapses forming stars and protogalaxies. If the collapsing gas in a region has sufficient angular momentum, a disc galaxy will form (Fall & Efstathiou, 1980). Subsequent mergers with other galaxies and dark matter haloes can significantly disturb the appearance of the galaxy, especially early in the Universe when mergers were more common (Conselice et al., 2003; Lotz et al., 2011). At later times, the evolution of galaxies was dominated by external processes such as harassment (high-speed fly-by, Moore et al. 1999), tidal stripping, ram pressure striping (Gunn & Gott, 1972; Abadi et al., 1998) or strangulation (Peng et al., 2015), which are all related to the environment of the galaxies, and internal processes related to the re-arrangement of mass and energy in galaxies due to structures such as bars and spiral arms. Bars are common in disc galaxies, thus it is important to understand their formation, evolution, dynamics and how they affect their host galaxies, which is the topic of this thesis.

1.2.1 Bar formation

Following the gravitational collapse that forms stars in a disc, the rotationally supported disc galaxy can become gravitationally unstable if the Toomre parameter (Q) (Toomre, 1964) is

$$Q = \frac{\sigma_r \kappa}{3.36 G \Sigma} < 1, \tag{1.1}$$

where σ_r is the radial velocity dispersion, κ is the epicyclic frequency, G is the Gravitational constant and Σ is the surface density of the disc. If $Q < 1$, the disc has a tendency to form 'massive condensations' within its plane (Toomre, 1964). The first N-body simulations of collisionless disc galaxies showed that, in a response to the gravitational instability in the stellar disc, a bar shaped structure forms (Miller & Prendergast, 1968; Hockney & Hohl, 1969; Hohl, 1971; Kalnajs, 1972, 1977) on dynamical timescales (which corresponds to the disc crossing time). The bar can be considered a standing wave, a superposition of a leading and a trailing wave, reflected and amplified (through swing amplification, Toomre 1981) at the corotation radius and at the centre of the disc. The standing wave grows by transferring angular momentum outwards, with angular momentum being absorbed and emitted at the resonances (Lynden-Bell & Kalnajs, 1972). Thus, first a small, weak bar forms, which then elongates and becomes stronger with time, slowing down as it loses angular momentum. The disc instability provides a natural explanation for bar formation, thus it is perhaps puzzling why the majority of galaxies do not possess a strong bar (Sellwood, 2013).

1.2.2 Dynamics of barred galaxies

The orbits of individual stars are governed by the large scale gravitational potential. In the absence of a non-axisymmetric feature such as a bar, disc stars follow nearly circular orbits. Seen from an inertial frame, the orbits appear to have the shape of an open rosette due to the combination of small radial oscillations around a guiding centre (epicyclic approximation, Binney & Tremaine 1987) and revolution around the centre (Sellwood & Wilkinson, 1993). In the epicyclic approximation, the frequency of the radial oscillations (epicyclic frequency) is (Binney & Tremaine, 1987)

$$\kappa^2 = \frac{2v}{r}\left(\frac{v}{r} + \frac{dv}{dr}\right), \tag{1.2}$$

where v is the circular rotation velocity as a function of radius r and the angular frequency of the stars around the centre of the galaxy is $\Omega = v/r$.

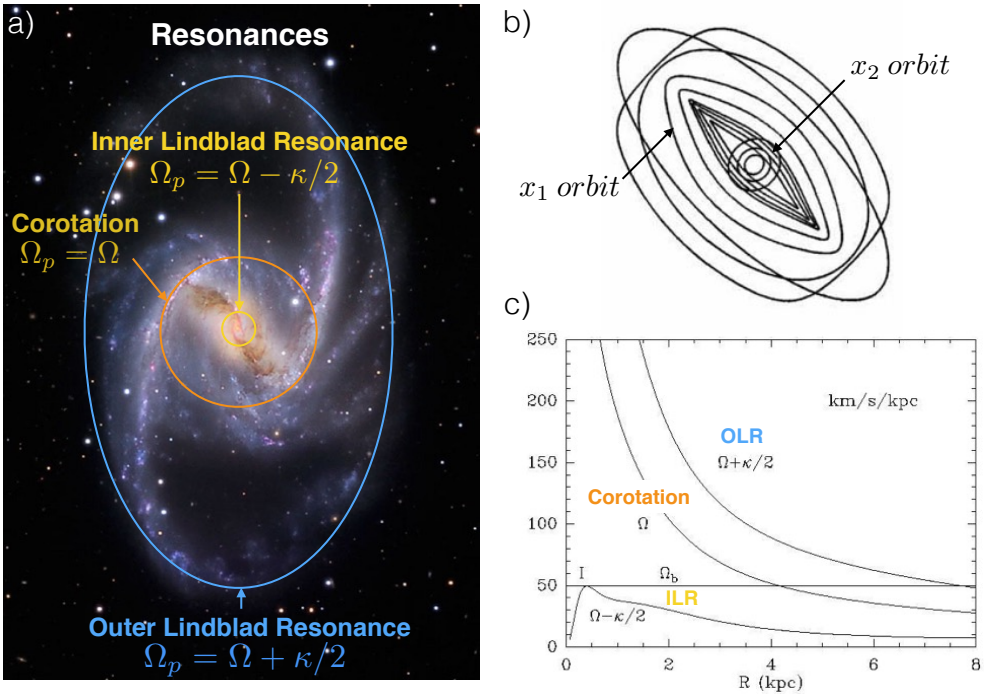

Figure 1.6: (a) Inner, Outer Landbland resonances and Corotation radius illustrated superimposed on NGC 1365 (Credit: NASA Astronomy Picture of the Day, Martin Pugh https://www.martinpughastrophotography.space/work/#/ngc-253-1/); (b) Schematics of orbits in a bar: x_1 orbits, elongated parallel to the bar and x_2 orbits perpendicular to the bar; (c) Frequency $\Omega = v/r$ as a function of radius in a barred galaxy, with the $\Omega \pm \kappa/2$ frequencies corresponding to ILR and OLR, and the frequency of corotation illustrated (b and c taken from Kormendy 2013).

In barred galaxies, however, the stellar orbits in the gravitational potential are not nearly circular and the frequencies of radial oscillations are not small. The standing wave, represented by the bar, can perturb the stellar orbits in the central region of the galaxy, forcing them to align with the bar (Lynden-Bell, 1979). The motion in these orbits is coupled with the rotation of the bar, in what are known as resonant orbits. These are closed orbits in the reference frame that rotates with the bar, which has a pattern speed Ω_p (Contopoulos & Grosbol, 1989). The bar pattern speed is an important physical parameter since it sets the location of the resonances and determines the dynamics of the galaxy. The resonant orbits satisfy the condition

$$l\kappa + m(\Omega - \Omega_p) = 0, \tag{1.3}$$

where $(l : m)$ are a pair of integers describing the resonance in the plane of the disc (Ceverino & Klypin, 2007). The most important resonances in barred galaxies are

corotation $(0:1)$ and the inner $(-1:2)$ and outer $(1:2)$ Lindblad resonances, as illustrated in Figure 1.6 (a).

The strongest resonance in a barred galaxy, corotation, is the resonance at which stars and the bar pattern rotate at the same angular frequency, $\Omega = \Omega_p$. At this radius, the mean position of the stars does not change with respect to the rotating frame of the bar. At radii smaller than the corotation radius, stars are trapped in the bar pattern and rotate in closed orbits ('bar orbits') around the centre of the galaxy. Another important resonance at smaller radii is one at which a star oscillates radially twice for each revolution around the centre, known as the inner Lindblad resonance (ILR). At the ILR, the bar pattern speed is $\Omega_p = \Omega - \kappa/2$. At this radius, there is a strong interaction between stars, gas and the bar pattern (Kormendy, 2013). Similarly, there exists an outer Lindblad resonance, where the pattern speed is $\Omega_p = \Omega + \kappa/2$, and the stars oscillate radially twice for each revolution around the centre. Figure 1.6 (c) shows the angular frequency curves (in km s^{-1} kpc^{-1}) of the stars in the disc corresponding to the different resonances in galaxies. If the bar pattern speed Ω_p is known, it is possible to determine the location of the resonances in the galaxy by intersecting the line corresponding to the Ω_p value with the angular frequency curves at the resonances. In the particular example in Figure 1.6 (c), the ILR is located at 0.5 kpc from the centre, corotation at 4 kpc and OLR at 8 kpc, respectively. The location of the resonances is important since these are the places where angular momentum is exchanged in a galaxy.

The bar pattern speed, Ω_p has a physical upper limit set by the periodic orbits of stars in the bar. A bar cannot extend past the corotation radius ($r_{\rm CR}$) since the main stellar orbit family supporting the bar pattern, the x_1 orbit family (see e.g. Contopoulos & Papayannopoulos 1980), becomes unstable at $r > r_{\rm CR}$. In fact, the bar pattern speed can be parametrised by the ratio between the corotation radius ($r_{\rm CR}$) and the bar semi-major axis ($a_{\rm bar}$), $\mathcal{R} = r_{\rm CR}/a_{\rm bar}$. Simulations show that the bars are actually slightly shorter than the corotation radius, with a ratio of $\mathcal{R} = 1.2 \pm 0.2$ (Athanassoula, 1992). Bars can be categorized into 'fast' bars, with $1 \leq \mathcal{R} \leq 1.4$ and 'slow' bars, with $\mathcal{R} > 1.4$. Thus, the location of corotation is just beyond the end of the bar.

In contrast to the x_1 orbits supporting the bar, inside ILR lies another family of orbits, perpendicular to the bar, known as x_2 orbits. As shown in Figure 1.6 (b), the eccentricities and orientation of these orbits change between the resonances, making the intersection of orbits unavoidable (Sellwood & Wilkinson, 1993). Orbit crossing is feasible for stars, since they are non-collisional, but gas clouds collide and shock when the orbits intersect. This causes gas to build up and compress, enhancing star

formation (see e.g. Binney et al. 1991) and forming structures that we identify as disc-like pseudobulges and inner rings (Kormendy & Kennicutt, 2004).

1.3 Simulations

Although theoretical work has provided great insight into our understanding of galaxy dynamics (Binney & Tremaine, 2008), many problems in the evolution of galaxies cannot be solved analytically. Computer simulations allow us to solve the equations of motions of systems of many particles (N-body problem) under the influence of their mutual gravity, being particularly useful when studying the formation of bars, their properties, interactions, the influence of dark matter and the time evolution of these systems (Fortin et al., 2011).

1.3.1 Bar instability and buckling

Collisionless N-body simulations of isolated galaxies show that galactic bars arise because of instabilities in the disc (Sparke & Sellwood, 1987; Sellwood & Wilkinson, 1993). They can develop over a large range of disc masses, growing by transferring angular momentum and trapping stars in bar orbits (Lynden-Bell, 1979). As a result, the bar elongates and becomes stronger in time, while its pattern speed decreases. Although some simulations suggested that bars can be recurrent, being formed and destroyed multiple times in a Hubble time (Bournaud & Combes, 2002; Bournaud et al., 2005a), most N-body simulations show that bars are robust and persist for a long time ($\sim$ 5-10 Gyr, e.g. Shen & Sellwood 2004; Debattista et al. 2006). After the bar forms and grows, it can develop vertical instabilities, buckle and thicken out of the plane of the disc. It forms 'boxy', 'peanut' or 'X-shaped' structures when viewed edge-on, depending on the orientation of the bar in the galaxy (Combes et al., 1990; Pfenniger & Friedli, 1991; Raha et al., 1991; Laurikainen & Salo, 2017). These are idealised simulations of isolated galaxies, starting with an already existing disc. However, the scenario of galaxies evolving in isolation is unrealistic for the real Universe, especially at high redshifts where interactions are common. Thus, the effect of galaxy interactions on the evolution of barred systems deserves further attention.

1.3.2 Bar formation in galaxy interactions

Simulations of two interacting galaxies suggest that bars can also be induced in tidal interactions (Noguchi, 1987; Gerin et al., 1990; Berentzen et al., 2004; Athanassoula et al., 2016; Martinez-Valpuesta et al., 2017; Łokas, 2018). These bars are referred

to as 'tidally induced' bars. In a recent simulation of galaxy interactions between systems of a comparable mass (Milky Way-like galaxies), Łokas (2018) showed that the formation and the strength of a tidally induced bar depends strongly on the orbital configuration of the encounter, as well as on the relative spins. Prograde interactions form strong bars, while retrograde interactions have little effect on the morphology of the galaxies. Furthermore, bars can be tidally induced in dwarf galaxies following an interaction with a Milky Way-like galaxy (Gajda et al., 2017). In all these scenarios, the formation of the bar does not depend solely on the properties of the disc, but also on the parameters of the interaction (mass of the companion, impact parameter, velocity, orbit and spin).

1.3.3 The role of gas in bar formation and evolution

Most of the N-body simulations of bar formation presented above neglect the gas component and star formation, yet gas plays an important role in the formation and evolution of bars, since it can respond to the perturbations in the potential introduced by the bar. The gas in a barred galaxy follows x_1 orbits, but compared to stars, gas is collisional and shocks at orbit crossing, for example between the x_1 and x_2 orbits or at the end of the x_1 orbits (Athanassoula, 1992).

Berentzen et al. (2004), Debattista et al. (2006), Villa-Vargas et al. (2010) and Athanassoula et al. (2013) produced simulations of bar formation in gaseous discs with different gas physics, for example including star formation, cooling and feedback (sub-grid physics). Athanassoula et al. (2013) found that in gas-poor (gas fraction $< 20\%$) and gas-less simulations the bar forms earlier and evolves to be longer and stronger than in gas-rich simulations (gas fraction $> 75\%$). The bars in these simulations were never destroyed, an argument for long-lived bars.

Large scale bars redistribute the angular momentum in galaxies (Sellwood & Wilkinson, 1993; Regan et al., 1999; Athanassoula & Misiriotis, 2002) and can efficiently drive the gas towards the centre (Simkin et al., 1980; Shlosman et al., 1990; Athanassoula et al., 2005), building central mass concentrations (Athanassoula, 1992; Athanassoula et al., 2013). Athanassoula (1992) showed that the gas in the bar region shocks, which causes the gas to lose energy and inevitably fall to the centre with a speed of ~ 1 km s^{-1} (~ 1 kpc Gyr^{-1}). The result is that the inner region of barred galaxies can be depleted of gas during the evolution of a galaxy if bars are indeed long lived ($\gtrsim 1$ Gyr). Recent simulations of isolated disc galaxy evolution, including gas (Fanali et al., 2015; Khoperskov et al., 2018), as well as zoomed-in cosmological simulations (such as ErisBH, Spinoso et al. 2017), confirm that strong bars are capable of driving gas to the nuclear centre of galaxies, removing the gas in the bar regions and

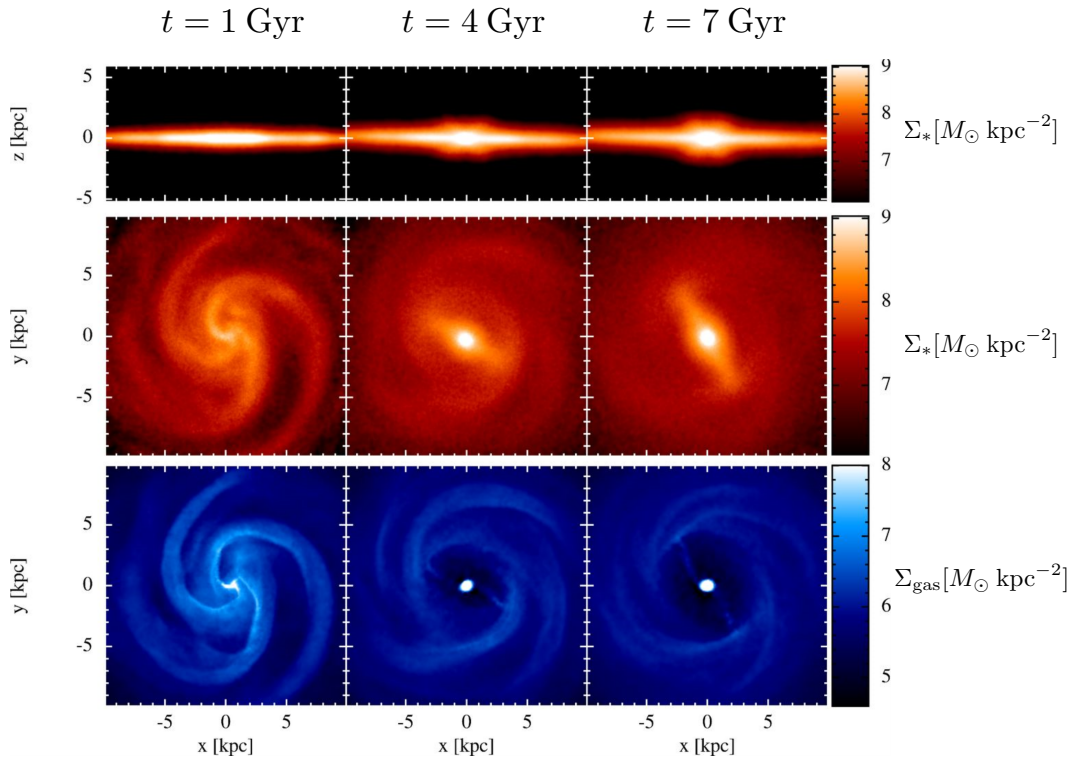

Figure 1.7: Simulations by Fanali et al. (2015) of the evolution of an isolated disc galaxy developing a strong bar. The different columns show three time steps from the simulation ($t = 1, 4, 7$ Gyr), while the rows show an edge-on view (*first row*), a face-on view of the stellar surface density (*second row*) and of the gas surface density (*third row*). By $t = 7$ Gyr, the gas in the central region, within the bar corotation radius, is swept out by bar and is channeled to the centre of the galaxy, where a pseudobulge forms.

quenching the star formation on $\sim$ kiloparsec (kpc) scales in $\sim$ Gyr timescales. For example, the high-resolution numerical simulations of Fanali et al. (2015), with 10^6 gas and star particles, show the dynamical effects a forming bar exerts on the gas in an isolated disc galaxy. Figure 1.7 shows the stellar and gas surface densities during the development of a bar in the simulations of Fanali et al. (2015), at three time steps (1, 4 and 7 Gyrs after the start of the simulations). The disc being unstable, it forms a kpc-scale bar after $\sim$ 2 Gyr, followed by strong episodes of bar inflow, forming a bright core and carving out a lower density region between the inner Lindblad resonance and the corotation radius. After the 'dead zone' is formed, further massive gas inflows are halted. After 7 Gyrs, gas is present only at the centre of the galaxy and outside the bar radius. This particular simulation also finds that the strong inflows during the bar development phase, rather than during the strong bar phase, can

trigger an Active Galactic Nucleus (AGN).

The lack of gas might be a reason why bars appeared so robust in collisionless N-body simulations. Pfenniger & Norman (1990), Kormendy & Kennicutt (2004) and Shen & Sellwood (2004) suggest that the bar's contribution to building up a central concentration actually weakens the bar; thus there is a competition between bars getting stronger due to the outward transport of angular momentum and getting weaker due to the inner transport of material. Kormendy (1979) proposed that bars can be destroyed by possibly evolving into lens components (discussed in Section 3.5), however this is not fully supported by theory or simulations.

1.3.4 The effects of the halo on the formation and evolution of bars

It is believed that galaxies are surrounded by large haloes of dark matter, which dominates their total mass. The formation and evolution of a bar depends on the shape and spin of the dark matter halo, and the type of halo considered – a static halo potential or a halo made up of particles (a 'live' halo). Athanassoula (2003) has shown that the strength, length and slowdown rate of bars is strongly determined by the angular momentum exchanged in a galaxy. A live dark matter halo can absorb the angular momentum emitted by the bar near-resonance and the bar can evolve and become stronger in time (Debattista & Sellwood, 1998; Athanassoula & Misiriotis, 2002; Saha et al., 2012). In contrast, a rigid halo, characterised by a static potential cannot exchange angular momentum and, in this case, the bar develops slower. The ratio of the halo to disc mass is also important in the development of the bar (Athanassoula, 2003). If the halo mass dominates in the central region of the galaxy, bar formation is delayed, while if the disc mass dominates, the bars form earlier and faster. The shape of the halo is also important in bar formation (Athanassoula et al., 2013). Galaxies in triaxial haloes form bars faster, but which grow slower and are weaker than in galaxies hosted by spherical haloes.

The rotation of the halo can also have an important impact on bar formation. Hohl & Feix (1967) have shown that massive, hot, non-rotating spheroidal dark matter haloes can stabilize stellar discs against bar formation. A dark matter halo spinning in the same direction as the disc promotes bar formation, while a counter-rotating halo suppresses bar formation (Saha et al., 2013). The different properties of the dark matter haloes might explain why some spiral galaxies do not develop a bar.

1.3.5 Bars in cosmological simulations

The works discussed above are idealised models of bars forming in pre-existing discs. However, mergers and cosmological accretion of gas are frequent in the Universe and bars and discs form and grow simultaneously. Cosmological simulations, where the formation of structures is simulated in volumes of ∼100 Mpc a side, can shed a light on the formation and evolution of bars. In cosmological simulations, galaxies form out of perturbations and grow via mergers and accretion, while also acquiring angular momentum.

Several cosmological simulations have so far achieved sufficient numerical resolution with sufficiently realistic physical models to produce barred galaxies (e.g. Kraljic et al. 2012; Scannapieco & Athanassoula 2012, Illustris, Vogelsberger et al. 2014, EAGLE, Schaye et al. 2015). In a 'zoomed-in' cosmological simulation (originally presented in Martig et al. 2012) with a spatial resolution of 150 pc and mass resolution of $10^4 - 10^5\ M_\odot$, Kraljic et al. (2012) studied the evolving fraction of disc galaxies hosting bars, finding that bars are absent at $z \gtrsim 1.5$ and, in general, are weak up to $z \sim 1$. This is followed by a steep increase in the fraction of strong bars to $\sim 70\%$ at $z \approx 0$. The epoch of bar formation is $z \sim 1$ when the stellar discs emerge, and mergers become less frequent. In hydrodynamic cosmological simulations, Scannapieco & Athanassoula (2012) show that bars form naturally in a ΛCDM Universe. The strongest bars formed in this cosmological simulation are similar in strength to bars in dynamical simulations with significant angular momentum exchanged between the bars and the dark matter haloes.

More recently, Algorry et al. (2017) found that 20% of the massive disc galaxies in the EAGLE cosmological simulations (Schaye et al., 2015) contain strong bars, 20% contain weak bars and 60% are unbarred. Bars develop at $z \approx 1.3$, with strong bars forming quickly in gas-poor, disc dominated galaxies, in agreement with dynamical simulations, while weak bars take longer to form and are still growing at $z = 0$. In EAGLE, bars slow down surprisingly quickly reaching $\mathcal{R} \sim 10$ at $z = 0$, in disagreement with both dynamical simulations and observations.

Similarly, in the Illustris simulation (Vogelsberger et al., 2014), Peschken & Łokas (2018) found a bar fraction of 26% at $z = 0$ amongst high-mass disc galaxies ($M_* \gtrsim 10^{11}\ M_\odot$), which were shown by Dickinson et al. (2018) to have comparable morphologies to real galaxies. The bar fraction increases with stellar mass and decreases with the amount of gas in a galaxy, in agreement with the findings of Athanassoula et al. (2013). Tracing back the interaction history of galaxies, Peschken & Łokas (2018) conclude that the vast majority of the strong bars are induced by interactions rather

than disc instabilities. The strength of the induced bars depends on the strength of the interaction and the relative orientations of the orbits.

Although cosmological simulations provide insight into how interactions and gas accretion influence the development of a bar, very few galaxies with $M_* \lesssim 10^{11}\ M_\odot$ form bars (Peschken & Łokas, 2018), probably due to insufficient resolution (Dickinson et al., 2018), which is contrary to what we observe in the real Universe. Furthermore, another disadvantage of cosmological simulations is that currently attainable spatial resolution is insufficient to resolve the nuclear region of galaxies.

1.3.6 Summary

Simulations show that bars arise naturally out of disc instabilities, but the epoch when the bars form and their strength depend on the amount of gas present in a galaxy and the shape, profile and rotation of the dark matter halo. Bars might also be triggered in galaxy interactions, or on the contrary, bar formation can be suppressed, depending on the masses of the interacting galaxies, their velocities and the orientations of the orbits. Once formed, bars are efficient in driving gas inwards to the central regions, forming dense central concentrations, and depleting the gas in the inner region of the galaxies and suppressing star formation.

In this thesis I explore observationally the properties of bars in galaxies and investigate whether they are efficient in suppressing star formation, by comparing the structural parameters (light profile, axis ratios, etc.) and colours of galaxy components (discs, bars and bulges) in barred and unbarred galaxies.

1.4 Observations of barred galaxies

In order to assess the importance of bars in reshaping galaxies, one needs to know how frequent they are and in what types of galaxies they occur.

1.4.1 The fraction of bars in local disc galaxies

For the past three decades, astronomers have measured the fraction of disc galaxies that are barred ($f_{\rm bar}$) in the local Universe and found values between 30% at optical wavelengths (Sellwood & Wilkinson, 1993) and 70% in the infrared (Menéndez-Delmestre et al., 2007; Buta et al., 2015). With the advent of large surveys, in particular the Sloan Digital Sky Survey (SDSS; York et al. 2000), astronomers have investigated the fraction of galaxies that are barred using different methods: ellipse

fitting in a sample of 3,600 galaxies (Barazza et al. 2008, $f_{\rm bar} \sim 50\%$), ellipse fitting and Fourier analysis in a sample of 2,000 disc galaxies (Aguerri et al. 2009, $f_{\rm bar} \sim 45\%$), expert visual classification in a sample of $\sim 8,000$ disc galaxies (Nair & Abraham 2010b, $f_{\rm bar} \sim 30\%$), similarly in a sample of $10,000$ disc galaxies (Lee et al. 2012, $f_{\rm bar} \sim 30\%$), and visual classifications completed by non-expert volunteers in the Galaxy Zoo project in a sample of $\sim 15,000$ disc galaxies (Masters et al. 2011; Skibba et al. 2012; Cheung et al. 2013, $f_{\rm bar} \sim 30\%$). The discrepancies between the SDSS studies arise because of the different sample selection used in the magnitude-limited SDSS survey. Barazza et al. (2008) and Aguerri et al. (2009) selected more nearby galaxies ($z < 0.03$), thus being dominated by dwarf galaxies, while Nair & Abraham (2010b) and the Galaxy Zoo studies selected volume-limited samples of galaxies up to $z < 0.06$ and thus are dominated by more massive systems, and missing dwarf systems.

Observing galaxies in the infrared shows a higher fraction of local disc galaxies that are barred, $f_{\rm bar} \sim 60 - 70\%$ (Sheth et al., 2008; Buta et al., 2015; Erwin, 2018), suggesting that smaller bars can be missed in optical studies (Block et al., 2001; Laurikainen & Salo, 2002). In infrared it is possible to penetrate through dust absorption, star formation, and through the population of young stars, thus observing the older stellar population which constitutes most of the stellar mass of a galaxy. Various studies (e.g. Gadotti 2011, including Galaxy Zoo 2, Willett et al. 2013) comment on a possible bias against identifying smaller bars in SDSS. In particular, in a more recent study comparing infrared observations of a closer (D <25 Mpc) sample of 570 galaxies from the Spitzer Survey of Stellar Structure in Galaxies (S^4G, Sheth et al. 2010) with the above-mentioned SDSS studies, Erwin (2018) suggests that the resolution of the observations is important for being able to identify bars in galaxies and that bars with sizes less than twice the Full Width at Half Maximum (FWHM) might be missed in SDSS. The observed bar fraction of $\sim 30\%$ in SDSS resembles the fraction of SB galaxies more closely, as identified in infrared (see e.g. Figure 1.9), suggesting that the bars detected in SDSS studies, thus in the Galaxy Zoo project are indeed strong bar cases.

1.4.2 Evolution of bar fraction

Bars have been observed in the higher redshift Universe as well. Studies using the *Hubble Space Telescope (HST)* have measured the fraction of galaxies hosting strong bars at redshifts $z = 0.2 - 1$ (Abraham et al., 1999; Elmegreen et al., 2004; Sheth et al., 2008; Cameron et al., 2010) and found the bar fraction to be evolving. The bar fraction decreases by a factor of 2 from $f_{\rm bar} \sim 30\%$ at $z = 0.2$ to $f_{\rm bar} \sim 15\%$ at

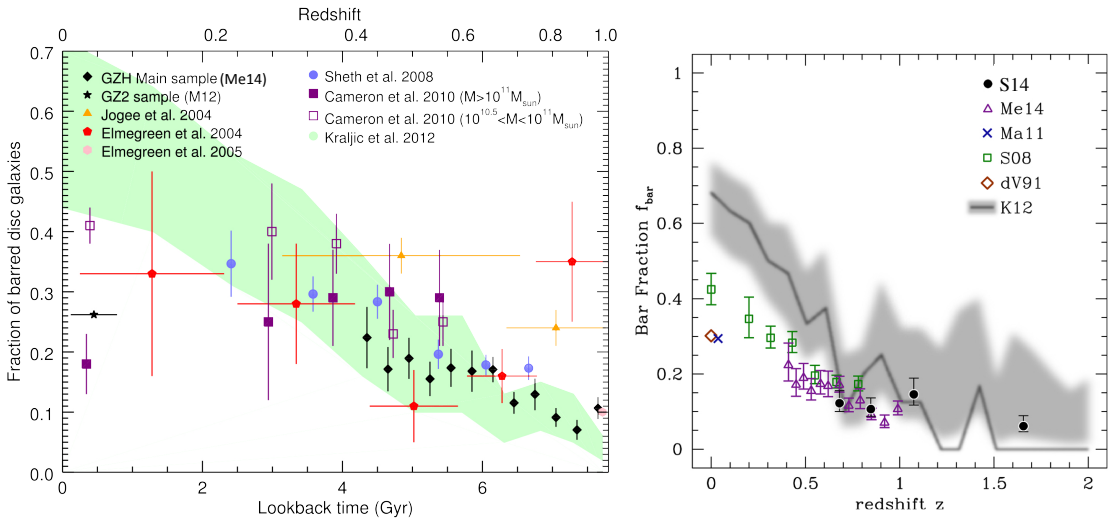

Figure 1.8: The evolution of the bar fraction to $z = 1$ (*left*) and $z = 2$ (*right*) from the Galaxy Zoo: Hubble project (Melvin et al. 2014, Me14) and Galaxy Zoo: CANDELS projects (Simmons et al. 2014, S14). The decrease in bar fraction is compared to the evolution found in other observational studies (Elmegreen et al., 2004; Jogee et al., 2004; Sheth et al., 2008; Cameron et al., 2010) and to the local bar fractions (de Vaucouleurs et al., 1991; Masters et al., 2011). The evolution of the bar fraction in cosmological simulations (Kraljic et al., 2012) is shown with the shaded area in both plots. Adapted from Melvin et al. (2014) and Simmons et al. (2014).

$z = 1$, as shown in Figure 1.8, including measurements from the Galaxy Zoo: Hubble project (Melvin et al., 2014) (Figure 1.8 *left*) and the Galaxy Zoo: CANDELS project (Simmons et al., 2014) (Figure 1.8 *right*). The latter study found no evolution in the bar fraction from $z \sim 1$ to $z \sim 2$ (although with low number statistics), where the highest redshift barred galaxy was found (at $z = 1.97$). Additionally, integral field spectroscopic observations of the stellar populations of an inner ring (believed to be formed from gas brought in by a bar) in NGC 4371 places its formation at a redshift $z \approx 1.8$ (Gadotti et al., 2015), in agreement with the highest redshift barred galaxy ever found.

This shows that some bars have been in place as long as ~ 10 Gyr ago, implying that some discs have been mature enough to develop a bar even $3 - 4$ Gyr after the Big Bang. The observed evolution of the bar fraction agrees well with the predictions from zoomed-in cosmological simulations by Kraljic et al. (2012): a local bar fraction of $f_{\rm bar} \sim 70\%$, matching the local fraction observed in the infrared, followed by a decrease to $f_{\rm bar} \sim 10\%$ at $z \sim 1$.

1.4.3 Bar formation in tidal interactions

Observations regarding the origin of bars in galaxy interactions have been inconclusive. Some studies find no correlation (van den Bergh, 2002; Li et al., 2009; Marinova et al., 2012), some a very weak correlation (Lin et al., 2014), and some a correlation (Giuricin et al., 1993; Eskridge et al., 2000) between the presence of a bar and the environment, using different measures for the environment (projected two-point correlation function, nearest neighbors, overdensity in the local environment, and separating between field and cluster galaxies). Méndez-Abreu et al. (2012) suggest that environment can have a dual effect on the galaxies, triggering bar formation in bright disc galaxies and inhibiting bar formation in dim disc galaxies, because of tidal heating. With a sample of barred galaxies selected from the Galaxy Zoo project, Skibba et al. (2012) found a weak correlation of the likelihood for a galaxy to be barred with the denser environments, on scales $> 150\,h^{-1}$ kpc. With a similar sample, also with Galaxy Zoo morphologies, Casteels et al. (2013) found a decrease in the bar likelihood in pairs separated by $\leq 30\,h^{-1}$ kpc, suggesting that bars can be destroyed in interactions. Therefore, observational evidence on whether galaxy interactions can trigger or inhibit bar formation has been contradictory, in many cases because the samples considered are not sufficiently large, after controlling for other correlations (mass, colour, etc.). In this thesis I do not attempt to study the correlations with environment nor the formation of bars in galaxy interactions. However, I investigate the large scale environment barred and unbarred galaxies are situated in when studying their component colours and the offsetting of an already existing bar in galaxy interactions.

1.4.4 Bar strength (strong versus weak bars)

The Comprehensive de Vaucouleurs Revised Hubble-Sandage (CVRHS) system (de Vaucouleurs, 1963) classifies disc galaxies into barred (SB) and intermediate (SAB) classes, however there is no strong consensus on the definition of strong and weak in the literature. In the CVRHS system an SB galaxy is a galaxy with a conspicuous, strong and obvious bar. In contrast, an SAB is a galaxy with a weaker bar strength, often identifiable only as a hint of a bar (de Vaucouleurs et al., 1991). Nair & Abraham (2010a,b) define a strong bar as one that is dominating the light distribution of a galaxy, and weaker bar is one that is smaller in size and contains only a small fraction of the light of the galaxy. Nair & Abraham (2010a) note that there is not necessarily an equivalence between their classification of bar strength and the CVRHS system - all of their weak bars are definite bars rather than galaxies which possibly contain

bars. Thus, the weakly barred galaxies in the classification of Nair & Abraham (2010a) can be viewed rather as a subdivision of the SB types. Nevertheless, the visual classification of bar strength can be subjective.

Some quantitative studies have been proposed to measure bar strength in galaxies. For example, a commonly used parameter to represent bar strength is the normalized maximum amplitude of the $m = 2$ Fourier mode (A_2^{max}). Other measures are the maximum ellipticity of the bar isophotes (Laurikainen & Salo, 2002; Erwin, 2004), the boxiness of the isophotes (Gadotti, 2011), the relative bar length (Nair & Abraham, 2010a), the maximum torque produced by the bar, measured as the ratio of the tangential to radial forces (Sanders & Tubbs, 1980; Combes & Sanders, 1981; Laurikainen & Salo, 2002; Laurikainen et al., 2004a; Buta et al., 2007; Cameron et al., 2010), or the light deficit within the bar radius (Kim et al., 2017). Most studies show a consistency between the different measurements of bar strength, as the different proxies correlate with each other and with the SAB-SB classification (Laurikainen et al., 2004a; Díaz-García et al., 2016). However, there are also some conflicting trends. For example, the largest A_2^{max} is measured for the most massive galaxies, while the maximum gravitational torque decreases with stellar mass (Díaz-García et al., 2016; Erwin, 2018).

In this thesis I use bars identified in the Galaxy Zoo project. The strength of these bars can be described by the definition of strong and weak bars of Nair & Abraham (2010a), since the visual classifications used the same imaging (SDSS). A comparison between the different bar types identified in Galaxy Zoo is discussed in Section 2.3.1. Furthermore, in this thesis I did not consider a third type of bars, nuclear bars, situated inside the bulge (discussed further in Section 1.4.7.1), since their small sizes ($\lesssim 0.5$ kpc, Erwin 2004) makes it almost impossible to identify them at the resolution of the SDSS imaging.

1.4.5 Dependence of the bar fraction on galaxy properties

Another important aspect of understanding how bars affect their host galaxies is establishing what types of galaxies are more likely to be barred. One parameter to explore is galaxy colour. The distribution of $f_{\rm bar}$ against $g-r$ colour for various optical (SDSS) and infrared (S^4G) studies can be seen in Figure 1.9. Many SDSS studies suggest that the fraction of disc galaxies hosting bars increases with redder colours (Lee et al., 2012; Consolandi, 2016), including previous Galaxy Zoo studies (Masters et al., 2011, 2012; Skibba et al., 2012; Cheung et al., 2013). Barazza et al. (2008) found an opposite trend in SDSS. However, they selected a more local sample of blue discs (with a cut in the $U-V$ versus M_v colour-magnitude diagram), thus inadvertently

removing many massive red discs. The work of Nair & Abraham (2010b) which includes a larger range of stellar masses than both Barazza et al. (2008) and Masters et al. (2011) attempts to reconcile the two trends, finding a bimodal distribution in which $f_{\rm bar}$ increases for both the bluest disc galaxies ($g-r \sim 0.2$) and for the reddest ones ($g-r \sim 0.7$). They suggest that the presence of two types of bars is responsible for this trend: weak bars at blue colours and strong bars at red colours. Erwin (2018) found a relatively flat trend of bar fraction with $g-r$ colours for galaxies observed in the infrared, classified as SB and SAB by Buta et al. (2015). They do not notice an increase in the bar fraction at the redder colours, however, their study is incomplete for S0 galaxies and they mention (in their Appendix B) that by including S0s in their sample the bar fraction would increase at the highest masses, and, hence at the reddest colours as well.

Observations of atomic HI gas in disc galaxies suggests that there is an anti-correlation between the presence of a bar and the amount of gas in a galaxy. This is expected given the trend with galaxy colour and the fact that colour is strongly related to gas content (Saintonge et al., 2011). The bar fraction increases in HI gas-poor galaxies, as observed by Masters et al. (2012) and Cervantes Sodi (2017) in SDSS-based studies.

The SDSS-based observations that the fraction of galaxies with strong bars is higher in red, gas-poor disc galaxies suggests that (1) either bars can have an important role in the formation of red spirals by turning off star formation in galaxies (Masters et al., 2011; Lee et al., 2012; Cheung et al., 2013) or (2) large-scale bars are harder to form in gas-rich discs than in gas-poor ones (Athanassoula et al., 2013). The former is a rather slow, non-violent process, so (1) is a type of *secular evolution*, a term first used by Kormendy (1979).

1.4.6 Effects of bars on the evolution of galaxies

Evidence that secular evolution is important in disc galaxies lies in the observations of dense concentrations of stars and gas at the centre of barred galaxies, called pseudobulges, which have properties (such as ordered stellar orbits) similar to discs (Kormendy & Kennicutt, 2004; Athanassoula et al., 2005), thus they are also referred to as nuclear discs. Barred galaxies have higher concentrations of molecular gas in the central kpc (Sakamoto et al., 1999; Sheth et al., 2005; Jogee et al., 2005), evidence for molecular gas being funneled by the bars to the centre of galaxies. The higher fraction of molecular gas can be related to the enhanced star formation rate at the centre of barred galaxies (Martinet & Friedli, 1997; Martin & Friedli, 1997; Oh et al., 2012), observed through the presence of low-ionization nuclear emission-line regions

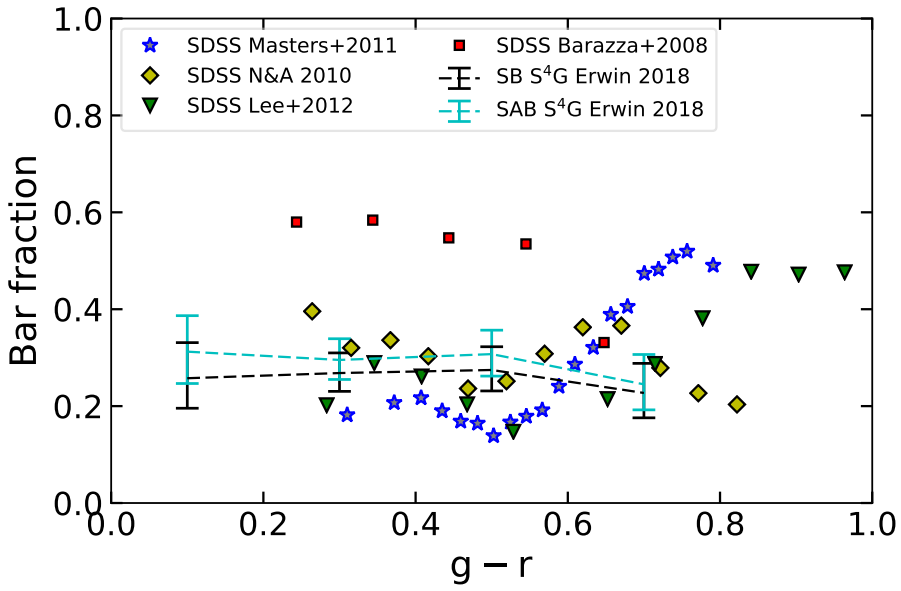

Figure 1.9: The fraction of disc galaxies hosting bars against $g-r$ colour in four SDSS studies (in optical) with different bar identifications: ellipse fitting (Barazza et al., 2008), expert visual classifications (Nair & Abraham, 2010b; Lee et al., 2012) and Galaxy Zoo volunteers' classification (Masters et al., 2011). Superimposed are the trends for strong (SB) and weak (SAB) classification of bars from the more local S^{4}G infrared study from Erwin (2018).

(LINERs; Heckman 1980; Ho et al. 1997), starbursts (Jogee et al., 2005), a peak in the Hα emission profile (James et al., 2009) and SDSS spectroscopy (Ellison et al., 2011; Lin et al., 2017). The increased star formation leads to the formation of nuclear rings (Knapen, 2005; Knapen et al., 2006) and the integrated star formation in the ring over a longer time leads to the formation of a nuclear disc. There are also hints of bimodal (both young and old) stellar populations at the centres of barred galaxies (Peletier et al., 2007; Pérez & Sánchez-Blázquez, 2011; Coelho & Gadotti, 2011) suggesting that bars can rejuvenate the bulges of disc galaxies, replenishing the gas reservoir with accreted gas, and triggering new star formation in the bulge. In addition, bars can flatten the metallicity gradients in galaxies (Friedli & Benz, 1995; Martel et al., 2013).

The gas driven in by the bar can reach the inner kpc and could in theory trigger AGN activity (Shlosman et al., 2000; Wada, 2004). However, whether bars induce or facilitate AGN is not yet settled. Some authors find a statistically significant increase in bar fraction in galaxies that host AGN compared to those that do not (Galloway et al., 2015). Other authors find that strong bars do not influence the accretion rate of supermassive black holes (Goulding et al., 2017) and there is no significant difference in the AGN fraction in barred and non-barred galaxies across $z = 0.2 - 1$ (Cheung

et al., 2015a; Cisternas et al., 2015), once the effects of stellar mass have been removed. These conflicting results are not surprising given that timescales vary considerably for bar driven motions ($\sim$ Gyr, suggested by the simulations of Athanassoula 2000) and AGN activity ($\sim$ Myr, Hickox et al. 2014). The different results might thus be due to the stochasticity of the AGN phenomena; finding a definitive link between bars and AGN is difficult.

There is an emerging picture that bars can regulate the star formation in a galaxy, first suggested by Tubbs (1982). By facilitating gas inflows and enhancing star formation, bars can deplete a considerable region of the host discs of gas, especially if they are long-lived structures. Alternatively, it is possible that the gas is not entirely depleted in the inner disc region, but the star formation efficiency is low. Strong bars can induce strong shocks that prevents the gas from collapsing and forming new stars (Reynaud & Downes, 1998), thus changing the overall star formation. In the absence of an external gas supply, the bar inflows or the low star formation efficiency can turn the barred galaxies into red spirals (Masters et al., 2011, 2012), and hence moving a galaxy from the 'blue cloud' to the 'red sequence'. Many authors have studied whether the bars can decrease the global star formation in a galaxy, with contradictory findings (e.g. Aguerri 1999; Cheung et al. 2013; Gavazzi et al. 2015; Consolandi et al. 2017). Cheung et al. (2013), for example, found that the likelihood of a galaxy hosting a bar is anti-correlated with the specific star formation rate, regardless of stellar mass or bulge prominence.

The observations mentioned above as well as the simulations presented in Section 1.3.3 have prompted the idea of *bar-driven quenching*, whereby bars in massive galaxies can reduce the star formation rate in a galaxy (Cheung et al., 2013). In a few dynamical timescales ($\sim$ Gyr) the bar can remove most of the gas from the central region (within the corotation radius) (Gavazzi et al., 2015), halt star formation and leave the central region 'red and dead' (Cheung et al., 2013; Fanali et al., 2015; Spinoso et al., 2017). Spectroscopic observations of the region swept out by the bar have shown that the star formation is heavily suppressed, sparking astronomers to name the central region (within the bar radius, $\sim$ few kpc) as the 'star formation desert' (James & Percival, 2015, 2016, 2018). Haywood et al. (2016) suggests that bar quenching might have acted in the Milky Way, since the last significant drop in star formation ($\sim$ 9 Gyr ago) corresponds roughly to the epoch of bar formation.

An issue though that remains is whether the bar inflows can cause the entire disc to become 'red and dead' or just the central 'star formation desert' zone. The cosmic accretion of gas is expected to replenish the gas reservoir in the outer disc and trigger new star formation.

I conclude this section by remarking that secular evolution and secular quenching might not be confined to currently barred systems alone. Bars might have been present in a galaxy in the past, but could have been destroyed after the galaxy has been quenched by the bar and turned into a red spiral. Furthermore, observational evidence by Hart et al. (2017) that two armed unbarred spirals are observed with redder colours than many armed unbarred spirals suggests that spiral arms in two-armed galaxies can also transport gas to the centre, where it is consumed to form new stars, while the star formation in the rest of the galaxy is quenched. Therefore, unbarred spirals can also evolve secularly.

1.4.7 Structures associated with bars

In the previous sections I discussed how bars can rearrange the disc material at resonances and in instabilities, forming structures such as pseudobulges, boxy/peanut bulges and rings. Examples of all these structures associated with bars and secular evolution can be seen in Figure 1.10. In the following subsections I discuss their properties.

1.4.7.1 Bulges

Perhaps the name 'bulge' is a confusing term in astronomy since different authors refer to different components with this term. In two-dimensional bulge+disc image decompositions it has been customary to refer to the inner component of galaxies as the 'bulge' (Simard et al., 2011). However, bars have been shown to be abundant in the local Universe, therefore the 'bulges' in two component decompositions often include the light from bars. In this thesis by the term 'bulge' I refer to the *centrally concentrated component of galaxies*, often located at the *centre* of stellar bars.

Kormendy (1979) clearly differentiates between spheroidal (elliptical-like) bulges, believed to be formed by mergers (Hopkins et al., 2012; Martig et al., 2012), and known as classical bulges, and pseudobulges, built by secular processes. The two types of bulges have different observational characteristics. Classical bulges have smooth isophotes, with the light intensity I declining as $\ln I \propto r^{1/n}$ from the centre, where $n = 4$ (known as de Vaucolouers profile, de Vaucouleurs 1948), although Fisher & Drory (2008) suggest a range of indices $n = 2 - 4$. Similarly to elliptical galaxies, classical bulges satisfy the fundamental plane relation (Djorgovski & Davis, 1987; Faber et al., 1987; Bender et al., 1992), between the effective radius r_e, the velocity dispersion σ and the mean surface brightness I_e at the effective radius. The brightness profile of pseudobulges, on the other hand, falls off less sharply than for the classical

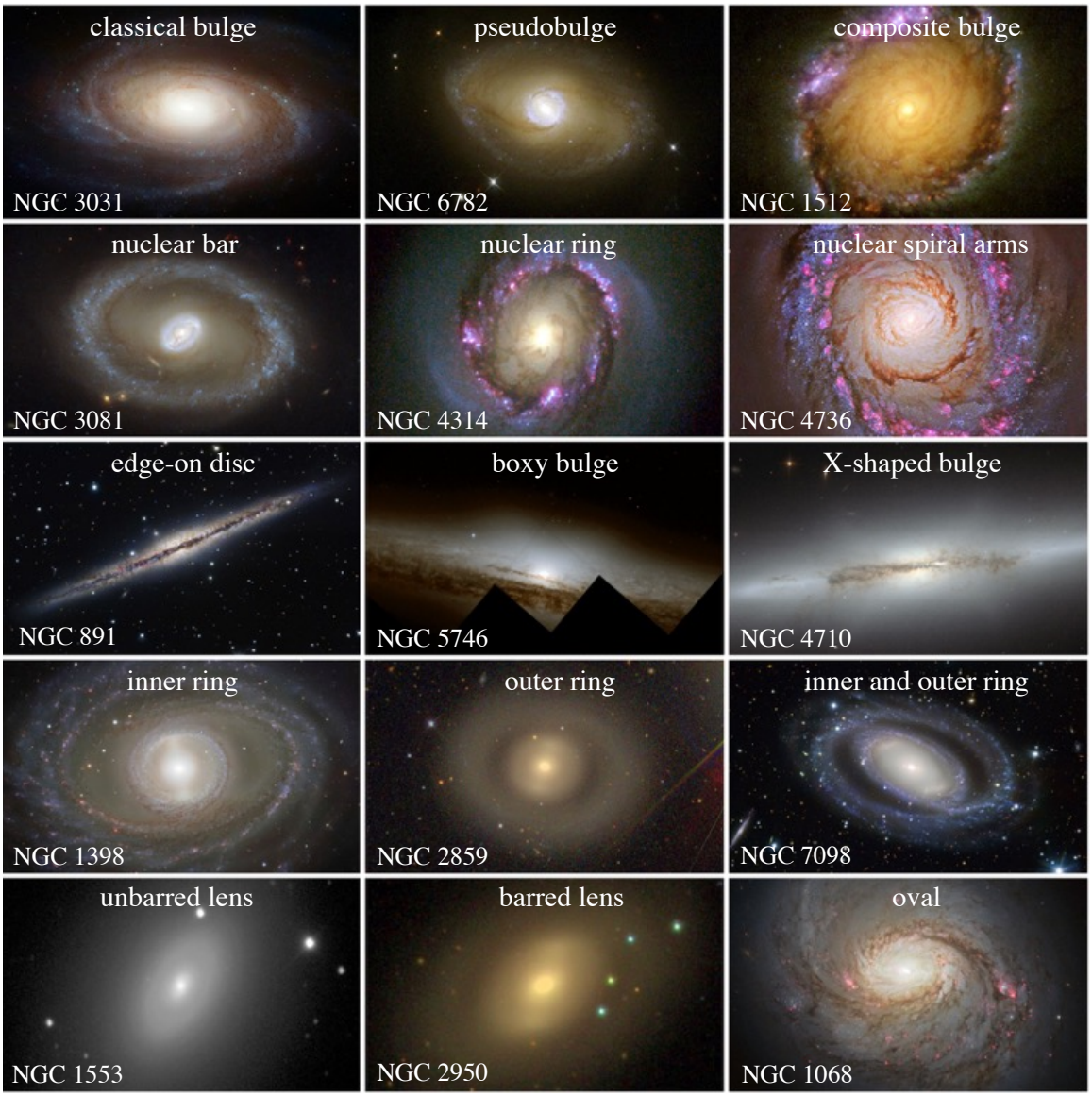

Figure 1.10: Structures associated with bar-driven secular evolution: (1^{st} row) pseudobulges, in comparison with classical bulges being built by mergers and composite bulges thought to have more complex formation scenarios; (2^{nd} row) a zoom-in on pseudobulges reveals further disc-like features: nuclear bars, nuclear rings and spiral patterns; (3^{rd} row): edge-on galaxies can reveal out of plane structure such as a boxy bulge, or an X- or peanut-shaped bulge; (4^{th} row): bars build up inner and outer rings at resonances; (5^{th} row): lenses in unbarred and barred galaxies, and ovals, also associated with secular evolution. Images of some of the most nearby NGC galaxies, classified by Buta (2011). Image credits: NASA, ESA and the Hubble Heritage Team (STScI/AURA) (Additional acknowledgements) – NGC 3031 (A. Zezas and J. Huchra, Harvard-Smithsonian Center for Astrophysics), NGC 6782 (R. Windhorst, ASU), NGC 1512 (D. Maoz, Tel-Aviv University), NGC 3081 (Buta et al., 2004), NGC 4314 (G. Fritz Benedict, Andrew Howell, University of Texas), NGC 4736, NGC 891 (Michael Joner, David Laney, West Mountain Observatory, BYU), NGC 5746, NGC 4710 (P. Goudfrooij, STScI); NGC 1398 (ESO/VLT), NGC 2859 (SDSS), NGC 7098 (ESO/VLT), NGC 1553 (NOAO), NGC 2950 (SDSS) and NGC 1068 (NASA, ESA & A. van der Hoeven).

bulges (typically, $n = 0.5 - 2$; Fisher & Drory 2008). There is increasing evidence of exponential ($n = 1$) discs at the centre of barred galaxies (Courteau et al., 1996; Carollo, 1999), in both optical and infrared images (Seigar et al., 2002). In contrast to classical bulges, pseudobulges show ongoing star formation and dust. Fisher et al. (2009) explains that the observed specific star formation rate (sSFR) at the centre of barred galaxies is consistent with the formation of pseudobulges in several Gyrs; thus, it is plausible that many bulges in the Universe were formed in galaxies via secular processes. Finally, pseudobulges are rotation-dominated, like discs. If plotted on an anisotropy ($V_{\rm max}/\sigma - \epsilon$) diagram (Binney, 2005), pseudobulges occupy the same place as fast rotating disc galaxies rather than slow rotators (Kormendy & Fisher, 2008). The SAURON IFU survey has shown that many central discs of galaxies are rotationally supported (Falcón-Barroso et al., 2006), with lower velocity dispersion than classical bulges, and often with younger stellar populations than the rest of the galaxy (Peletier et al., 2007).

The picture becomes more complicated, as higher-resolution observations with the *HST* have shown the existence of bars within pseudobulges (see e.g. nuclear bars, Shaw et al. 1995; Erwin & Sparke 2002; Erwin 2004), spiral arms within bulges (see e.g. Courteau et al. 1996), nuclear rings (found to be occurring in 20% of disc galaxies, Cameron et al. 2010, sites for intense starburst; Benedict et al. 2002). Furthermore, observations show that some barred galaxies have composite bulges, with classical and pseudobulges coexisting (Méndez-Abreu et al., 2014; Erwin et al., 2015). This latter result points to a more complex formation scenario for bulges, one which is both secular and merger driven.

1.4.7.2 Boxy/peanut bulges

Some bars extend vertically higher than the discs that host them, appearing as a 'boxy', 'peanut' or 'X' shaped feature when the galaxies are observed edge-on (as seen in Figure 1.10, *3rd row*). These features are collectively referred to as boxy/peanut bulges and their morphology differs by the orientation of the bar in the galaxies. Perhaps misleadingly named, boxy/peanut bulges are actually part of the bar (Bureau & Freeman, 1999), not the bulge, so the name 'boxy/peanut bulge' is a misnomer. Although, initially believed to be formed via the accretion of external material (Binney & Petrou, 1985), they are now believed to form due to dynamical instabilities, in a process referred to as *buckling*, first observed in simulations by Combes & Sanders (1981), and subsequently by Raha et al. (1991). Another possible mechanism for the thickening of bars is a resonance between the rotation of the bar and the vertical motion of the stars (Combes et al., 1990; Pfenniger & Friedli, 1991). The boxy/peanut

shape in the edge-on view of a galaxy is now seen in many simulations of disc galaxies (Athanassoula & Misiriotis, 2002; Martinez-Valpuesta & Shlosman, 2004; Debattista et al., 2004), including those mentioned earlier (Fanali et al., 2015; Spinoso et al., 2017), as shown in Figure 1.7 (*top row*). Understanding the formation and occurrence of boxy/peanut bulges in galaxies has received increased interest since there is now growing evidence that the Milky Way hosts an X-shaped feature, as first reported in observations by the COBE satellite (Dwek et al., 1995), and since then in many other studies (e.g. McWilliam & Zoccali 2010; Wegg & Gerhard 2013; Wegg et al. 2015; Ness & Lang 2016).

1.4.7.3 Rings

The original Hubble Tuning Fork failed to recognise an important feature related to bars - rings. de Vaucouleurs (1959) added a further classification, dividing rings into *inner* and *outer rings*, based on their position within a galaxy (some examples are shown in Figure 1.10, 4^{th} *row*). The formation of these rings is linked to the angular momentum exchanged in a barred galaxy by moving the gas outwards at near-resonance. The inner ring is formed at the corotation radius of the galaxy and the outer ring, at the outer Lindblad resonance (Kormendy, 2013). Gas at radii smaller than corotation loses angular momentum and is driven to the centre to form new stars at the inner Lindblad resonance, often forming a another ring, referred to as a nuclear ring.

Observations suggest that the formation of an inner ring rather than the formation of spiral arms depends on the pattern speed of the bar - slow bars tend to form rings at the bar ends, while fast bars (having smaller corotation radii) tend to form spiral arms (Kormendy, 2013). Even if there is an inner ring surrounding the bar it is often continued with spiral arms extending further out. This inner ring is often young and star forming, in contrast to the associated bar. The outer rings are typically situated at twice the radius of the bar, or twice the radius of the inner ring (Buta, 2017). Properties of inner and outer rings are summarized in Kormendy (1979) and Buta & Crocker (1993), including for rings identified in Galaxy Zoo and SDSS (Buta, 2017). Rings can also arise following galaxy collisions, but they often have different morphologies and orientations, revealing their merger history. These are known as collisional ring galaxies (e.g. the famous Cartwheel ring galaxy, Zwicky 1941, see Appleton & Struck Marcell 1996 for a review) or polar ring galaxies (Bournaud & Combes, 2003; Moiseev et al., 2011).

1.4.7.4 Lenses/Ovals

A lens[1] component is a fairly round feature (axis ratio $\sim 0.85 - 0.9$) with a shallow light profile ('plateau'), surrounding either the bulge or the bar of a galaxy, where the bar extends across the major axis of the lens (Buta et al., 2007). They are common in barred, but also occur in unbarred galaxies, in particular in galaxies of earlier-types (Laurikainen et al., 2007, 2009). An example of a barred and an unbarred (S0) galaxy with a lens can be seen in Figure 1.10 (5^{th} *row*). Kormendy (1979) suggested that bars can weaken over time and dissolve into lenses. Furthermore, Laurikainen et al. (2009) also suggest that lenses and ovals in S0s are formed by bar weakening in the presence of a large central mass concentration, given the large observed fraction of these features compared to bars in S0s, if lenticular galaxies are indeed descendants of spiral galaxies. However, simulations have not yet provided evidence for this.

Another structure in disc galaxies possibly related to bars is a deviation from axisymmetry known as an oval component, surrounding the bulge, which is observed in late-type unbarred galaxies. Similar to lenses, they have an axis ratio of $\sim 0.85-0.9$ (Bosma, 1981). They are believed to be driving the secular evolution of unbarred galaxies, in a similar way to bars in barred galaxies (Kormendy & Kennicutt, 2004), however it is not yet know how efficient they are in channeling gas towards the centre of galaxies. Some authors (e.g. Bosma 1981; Kormendy 2013) argue that the ovals are just the equivalent of lenses, but in late-type spirals.

Even though both features (lenses and ovals) are recognisable in galaxies, and have been known to exist for decades, it is surprising that they have not entered more in the astronomical discussion. There has been considerably more research and interest in stellar bars than in either of these components.

1.5 Aims and outline of the thesis

Even though substantial progress has been achieved over the last few decades in understanding how bars form and affect the evolution of their host galaxies, both observationally and in simulations, several puzzles remain to be solved before we can form a complete picture of secular evolution driven by bars and of the plethora of structure associated with bars. I address some of these puzzles in this thesis:

1. How do bars relate to the quenching of star formation in the galaxy?

2. How frequent are pseudobulges in barred galaxies?

[1] not related to gravitational lenses; it is an unfortunate naming convention

3. What are the properties of galaxies hosting lenses? What is the origin of lenses?

4. What are the frequency and the properties of galaxies with offset bars? What is the origin of the offsets? Which of the two components is offset?

5. How does the fraction of boxy/peanut bulges change with time?

6. Can the buckling instability explain the observed fraction of galaxies with boxy/peanut bulges?

7. What causes buckling and when does it occur?

In order to address the first point, one needs to measure the ages of the stellar populations within the individual components of galaxies (discs, bars, bulges). This has only been achieved for very small samples so far, and it is only now becoming possible with large samples, with the advent of the integral field spectroscopic surveys, such as CALIFA (Sánchez et al., 2012), SAMI (Croom et al., 2012) or MaNGA (Bundy et al., 2015). Nevertheless, before large samples are available, one possibility is to use the optical colour of the different components as a proxy for stellar ages and star formation histories, so that a redder component implies an older stellar population, while a bluer colour implies a younger stellar population and recent star formation. If bars indeed act to quench the star formation in the disc of a galaxy, one would expect a redder disc in barred galaxies compared to non-barred galaxies (if all the other parameters also known to affect star formation are matched).

Bars have been shown to be able to grow central bulges, but there might be other possible scenarios for bulge formation in barred galaxies. Therefore, it is important to study the frequency of pseudobulges compared to bulges formed via a different mechanism. The idea of bars evolving into lenses needs to be tested by comparing the properties of the galaxies hosting lenses with barred and unbarred galaxies, as well as the structural properties (luminosity ratios, concentration) of lenses/ovals, bars and pseudobulges.

In order to investigate the points presented above, I structure the thesis as follows: **Chapter 2**. In this chapter I present the data used in this thesis, from the SDSS imaging survey (SDSS-III) and MaNGA integral field spectroscopic survey (SDSS-IV), as well as the morphological classification of galaxies provided by the Galaxy Zoo project. Furthermore, in order to address the first three points, I use multi-wavelength and multi-component decomposition on the largest sample of barred galaxies to date ($\sim 3,500$), a sample 10 times larger than previous decompositions including a bar component, with the GalfitM software.

Chapter 3. In this chapter I present the measured structural parameters of the discs and bulges, as well as the colours of the components of the $\sim 3,500$ barred galaxies, together with a comparison with a mass-matched sample of unbarred galaxies. Unbarred galaxies with lenses are also identified in the sample and compared to barred galaxies.

Chapter 4. Galaxies with offset discs and bars, as well as bars in lower mass galaxies, in general, have been insufficiently well explored in the literature, although they constitute a significant fraction of the population of galaxies. I explore the frequency and properties of a sample of 271 galaxies with offset discs and bars, identified in the large sample of barred galaxies using the decompositions, in a first systematic search for such galaxies in SDSS. I study the masses and lopsidedness of these galaxies as well as the possible correlations with neighbouring galaxies.

Chapter 5. In this chapter I explore the kinematics of galaxies with offset discs and bars in the SDSS-IV MaNGA survey, and compare the centres of gas and stellar rotations with the centres of the photometric components. Furthermore, I investigate the kinematic lopsidedness and non-circular motions in barred galaxies induced by bar flows and due to lopsided or oval dark matter haloes.

Chapter 6. In order to address points 5-7 I investigate how the fraction of galaxies hosting boxy/peanut bulges changes with redshift, by comparing a local sample of galaxies from SDSS with a sample of galaxies observed by *HST* at $z = 0.2 - 1$. I explore whether the fraction of boxy/peanut bulges observed locally and at higher redshifts is consistent with them being formed by the buckling instability, and the possible causes of buckling.

Chapter 7. Finally, I present a review of the findings of this thesis as well as their implications in the evolution of galaxies. In addition, I present further research avenues which have been revealed by the work on this thesis and which can be explored in the future.

When necessary, in this thesis, I adopt the WMAP Seven-Year Cosmological parameters (Jarosik et al., 2011) with $(\Omega_M, \Omega_\Lambda, h) = (0.27, 0.73, 0.71)$.

Chapter 2

Data and methods

This chapter describes the data used in this thesis – imaging and spectroscopic data from the Sloan Digital Sky Survey as well as morphological classification of galaxies from the Galaxy Zoo citizen science project. The chapter also describes in detail the multi-component and multi-wavelength decomposition of galaxy images with the GALFITM software, used to measure the structural parameters of galaxy components (colours, sizes, shapes and light profiles). Finally, it summarises the datasets used in subsequent chapters.

2.1 Sloan Digital Sky Survey

The Sloan Digital Sky Survey (SDSS; Gunn et al. 1998; York et al. 2000) is an optical imaging and spectroscopic redshift survey completed using a 2.5-m telescope at Apache Point Observatory (APO) in New Mexico, USA. Its aim is to study the large-scale distribution of galaxies and quasars. SDSS data release 10 (DR10, Ahn et al. 2014), used in this study, covers 14,000 deg^2 of the sky and comprises millions of resolved sources, imaged to depths $r \sim 22.5$ magnitudes, in five broad-band filters, *ugriz* (Fukugita et al., 1996; Smith et al., 2002), centred on 3551Å, 4686Å, 6166Å, 7480Åand 8932Å, respectively. The five SDSS bands and the SDSS camera filter throughput curves are shown in Figure 2.1. Covering $\sim 26\%$ of the sky, mostly in the northern part, SDSS is one of the largest publicly available sky surveys. SDSS also imaged an equatorial region of $\sim$300 deg^2 70-90 times, resulting in ~ 2 magnitudes deeper images than single epoch data (to a depth of $r \sim 24.6$ magnitudes; Jiang et al. 2014), referred to as SDSS Stripe 82.

SDSS took spectra of all extended objects with Petrosian r-band magnitude $r \leq 17.77$ within its footprint, with a multi-object spectrograph with 1,000 fibers (in

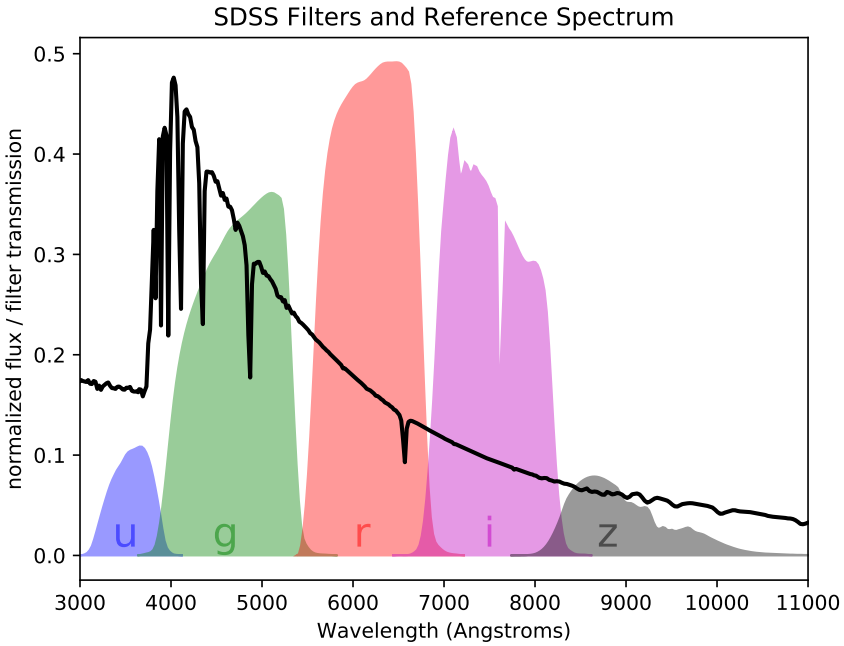

Figure 2.1: The transmission curves for the five SDSS *ugriz* bands used for the imaging and the reference spectrum of Vega. SDSS filters and spectrum reproduced from http://www.astroml.org/examples/datasets/plot_sdss_filters.html.

SDSS-I/II and the SDSS-III Baryon Oscillation Spectroscopic Survey, BOSS; Dawson et al. 2013). The spectra cover the redshift range 3800-9200Å, with a resolution $R \sim 2,000$ and each fiber has a diameter of $3''$, which corresponds to the central 1-3 kpc of galaxies, for objects at redshifts $0.01 < z < 0.06$. The resulting spectroscopic sample of $\sim 800,000$ galaxies with accurately measured spectroscopic redshifts (errors within $\Delta z = 10^{-4}$) is known as the Main Galaxy Sample (MGS; Strauss et al. 2002), and contains objects with a median redshift of $z \sim 0.1$. The physical size of the fiber cladding, does not allow two fibers to be placed closer than $55''$ from each other. This produces an incompleteness for spectroscopic measurements of galaxies which match the brightness criteria ($r \leq 17.77$) of 6%, in particular for galaxy pairs. Furthermore, the SDSS deblending algorithm can erroneously identify fragments of spiral galaxies (for example bright knots of star formation in the spiral arms) as individual spectroscopic targets (problem known as shredding), which can bias the spectroscopy of the brightest and most extended (thus nearest) galaxies (Strauss et al., 2002; Blanton et al., 2005). However, deblending was improved in later data releases.

2.1.1 SDSS data

In this thesis, I make use of multiple physical quantities derived from SDSS data. The derived galaxy properties (stellar masses and star formation rates) are taken from the MPA-JHU[1] catalogue.

The stellar masses in the catalogue are based on the *ugriz* photometry and are fits made to a grid of star formation histories based on Bruzual & Charlot (2003) models. The broad-band photometry was corrected for the small contribution (<0.1 mag) from nebular emission. The catalogue contains mean, median and modes of the masses, based on the likelihood distribution from the star formation history models. Masses were also derived from spectroscopy using the methodology of Kauffmann et al. (2003a), based on the D4000Å break strength and the Balmer absorption-line index $H\delta_A$. In this thesis, I decided to use the stellar masses obtained from photometry rather than spectroscopy, because for the particular galaxies studied here (disc galaxies) the SDSS fiber targets only the inner galaxy regions, which are likely to have different stellar populations compared to the outer galaxy. The mass estimates obtained from photometry for the general population of SDSS galaxies agree well[2] with masses derived from spectroscopy using the methodology of Kauffmann et al. (2003a) and scaled for the size of the galaxy. Therefore, I use the mean of the mass likelihood distribution (`MASS AVG`), based on fits to the galaxy photometry. The median uncertainty for the photometric mass estimates is $\Delta \log M_* \approx \pm 0.1$.

In addition to stellar masses, in Chapter 5 I use star formation rates (SFR) from the MPA-JHU catalogue. These star formation rate (SFR) measurements, made by Brinchmann et al. (2004), are based on emission line luminosities for star forming galaxies modeled using Charlot & Longhetti (2001) models. For non-star forming, AGN, composite and LINER galaxies the SFR are measured indirectly based on the D4000Å or a conversion factor between the Hβ Balmer emission line and SFR (Brinchmann et al., 2004). In the MPA-JHU catalogue, the SFR were also corrected for the aperture, by fitting the photometry in the outer regions of galaxies in order to correct for the overestimates in the SFR identified by Salim et al. (2007). The catalogue also contains three quantities based on the likelihood distribution of the SFR: mean, median and mode. The SFR used in this thesis are the mean values, `SFR AVG`.

Other quantities such as magnitudes, galaxy sizes and image resolution are available through the online SDSS Skyserver `CasJobs`[3] query system. For the galaxy

[1] The catalogue is available online at http://wwwmpa.mpa-garching.mpg.de/SDSS/DR7/
[2] see https://wwwmpa.mpa-garching.mpg.de/SDSS/DR7/mass_comp.html for a comparison
[3] http://skyserver.sdss.org/casjobs/

apparent magnitudes, I use the Petrosian magnitudes (`petroMag`) (Petrosian, 1976) in the five SDSS bands, calculated as the (Petrosian) flux within twice the Petrosian radius in the r-band, defined as the radius at which the local surface brightness is 20% of the mean surface brightness (Blanton et al., 2001; Yasuda et al., 2001). The Petrosian magnitudes were K-corrected (Blanton & Roweis, 2007) to $z = 0.0$ and corrected for Galactic reddening and extinction using[4] the dust maps from Schlegel et al. (1998). The K-corrections are small because the selected galaxies are nearby ($z < 0.1$). Absolute magnitudes are calculated based on the apparent Petrosian magnitudes and the distance modulus derived from measured spectroscopic redshifts. For galaxy sizes, I use the Petrosian radius containing 90% of the Petrosian Flux, `petroRad90`. This radius is sufficiently large to contain the flux of galaxies, but small enough to avoid significant background noise. Finally, as estimates of galaxy axis ratios and position angles I use the values from the automatic exponential fits to the SDSS galaxies in the r-band (`expAB_r` and `expPhi_r`). The exponential fits provide better estimates than the de Vaucouleurs (`deV`) fits because the galaxies considered in this thesis are disc galaxies.

2.2 SDSS-IV MaNGA

The SDSS spectroscopic survey (Strauss et al., 2002) has been instrumental in determining how the star formation rates, stellar populations, and metallicities vary with mass and environment. However, the SDSS spectroscopic survey has been limited to observing the integrated spectra within the fiber (3″ diameter), which is constrained, in many cases, to the inner region of galaxies only, and possible gradients in galaxies are washed out. One-dimensional gradients in galaxies can be obtained with long-slit spectroscopy, however observations are limited to a single position angle and observing multiple objects with long-slit spectroscopy is time expensive. An innovative method in taking spectra across the entire projected spatial distribution of a galaxy is using an integral field unit (IFU), which is an optical instrument with both spatial and wavelength resolution. IFUs use different techniques[5] to obtain the spectra, for example slicing the optical images and placing slits on the different slices, placing a lenslet array at the spectrograph entrance, effectively acting like spatial pixels, or using fibre bundles. One of the first IFUs used in astronomy was the SAURON instrument (Bacon et al., 2001) (using a lenslet array), which demonstrated the power of IFUs in obtaining gas and stellar kinematics and line-strength distributions of nearby

[4] using https://github.com/rjsmethurst/ebvpy

[5] see https://www.eso.org/public/unitedkingdom/teles-instr/technology/ifu/ for illustrations

galaxies. The SAURON instrument has been used to study resolved spectral maps for samples of hundreds of galaxies, for example the ATLAS^{3D} survey (Cappellari et al., 2011b).

The potential of IFUs has rapidly been recognized, and IFUs with better spectral and spatial resolution have been built, for example the MUSE instrument (Multi Unit Spectroscopic Explorer, Bacon et al. 2010) and the KMOS instrument (K-band Multi-Object Spectrograph, Sharples et al. 2006) on the ESO Very Large Telescope (VLT). However, the size of the VLT constrains the observations to a small portion of the sky, therefore these instruments allow only small samples of galaxies to be studied in detail. There is a need for resolved spectroscopy of large statistical samples of galaxies to address questions in galaxy formation and evolution (Bundy et al., 2015). One such survey is the now finished CALIFA (Calar Alto Large Integral Field Area, Sánchez et al. 2012) survey, targeting 600 nearby galaxies (preferentially selected). More recently, two IFU surveys targeting samples of $> 1,000$ galaxies in the northern hemisphere (MaNGA survey, Bundy et al. 2015) and southern hemisphere (SAMI, Croom et al. 2012) are in progress. MaNGA (Mapping Nearby Galaxies at APO) includes spectral measurements across the face of ∼10,000 nearby galaxies using 17 integral field units (IFUs), each containing a different number of optical fibers. The aim of MaNGA is to produce maps of the emission lines and stellar and gas kinematics from the spectrum, which together with the two spatial dimensions produces a 3-D data cube for each galaxy. The IFUs each contain a total of 37, 61, 91 or 127 fibers with diameter of 0.5″ (so with sizes 17.5″, 22.5″, 27.5″ and 32.5″, respectively), arranged in a hexagonal shape.

MaNGA provides detailed two dimensional maps of stellar and emission line velocities and velocity dispersions, stellar and gas metallicities, gas emission line fluxes, equivalent widths, etc. (Bundy et al., 2015). The galaxies were selected based on redshift ($z < 0.1$) and i-band luminosity in order to achieve a flat stellar mass distribution across the range $10^9 M_\odot < M_* < 10^{11} M_\odot$ and uniform radial coverage (Wake et al., 2017). No cuts were made on size, inclination, colour, morphology or environment, thus providing a representative sample of the local galaxy population. The IFU is matched to the observed target such that each galaxy is imaged to $1.5r_e$ (Primary sample) or $2.5r_e$ (Secondary sample). The targets are selected from the enhanced NASA-Sloan Atlas (NSA), based on the SDSS DR7 galaxy sample.

Because of the round shape of the IFU fibers fitted tightly into a hexagon shape, the sampling of the galaxies is irregular (i.e. there are spaces between the fibers which are not observed). To overcome this, MaNGA uses observations in a 3-point dithered observation pattern – the position of the telescope is offset slightly between three

different exposures of 15 minutes, providing a uniform coverage of the source for the IFU (explained in detail in Law et al. 2015). The required dithering offset (motion between exposures) was at most 0.4″, with the majority of observations being done with $< 0.2''$. All the MaNGA data was reduced by the science team with the custom built 2-D Data Reduction Pipeline (DRP) (Law et al., 2016).

In this thesis (in Chapter 5) I use data products from the Data Analysis Pipeline (DAP; Westfall et al. in prep.) which provides maps of measured quantities from the MaNGA IFU observations including stellar and gas kinematics. The DAP uses the penalized Pixel-Fitting (pPXF) method (Cappellari & Emsellem, 2004; Cappellari, 2017) to derive the line-of-sight velocity distribution using simulated stellar spectra from the MILES stellar library (Falcón-Barroso et al., 2011). To ensure that the MaNGA data is well sampled across the whole IFU I used the Voronoi binned stellar and Hα velocity maps provided by the MaNGA DAP. These data are binned in spatial and spectral bins with signal-to-noise ≥ 10 (Cappellari & Copin, 2003). The reason for using Voronoi binning is to achieve the best possible spatial resolution with the signal-to-noise threshold, by adapting the size of the (hexagonal) bins.

2.3 Galaxy Zoo

Galaxy Zoo (GZ) is a crowdsourced astronomy project (referred to as citizen science) which invites hundreds of thousand of members of the public to classify galaxy images online[6]. The original project, Galaxy Zoo 1 (GZ1), asked volunteers to classify $\sim 900,000$ SDSS galaxies, including the entire Main Galaxy Sample (Strauss et al., 2002), into smooth, spiral, star or mergers (Lintott et al., 2008, 2011) and the rotation direction of spiral galaxies. In a follow-up project, Galaxy Zoo 2 (GZ2; Willett et al. 2013)[7], volunteers were asked to make more detailed classifications of a subset of $300,000$ galaxies classified in GZ1. The galaxies are selected from SDSS Data Release 7 with an apparent magnitude $r < 17$, radius `petroRad90`$> 3''$ and redshifts $z < 0.25$, with measured spectroscopic redshifts (245,500 galaxies, main *specz* sample) and photometric redshifts (42,462 galaxies, *photoz* sample), in addition to deeper ($r < 17.77$) images from SDSS Stripe 82 (17,787 galaxies). In contrast to GZ1, GZ2 measures finer morphological features of well-resolved galaxies such as the presence of bars, bulges, spiral arms, edge-on versus face-on discs as well as quantifying the prominence of bulges and spiral arms.

[6] www.galaxyzoo.org

[7] The data including raw and debiased vote fractions for each task of the classification tree can be found at http://data.galaxyzoo.org

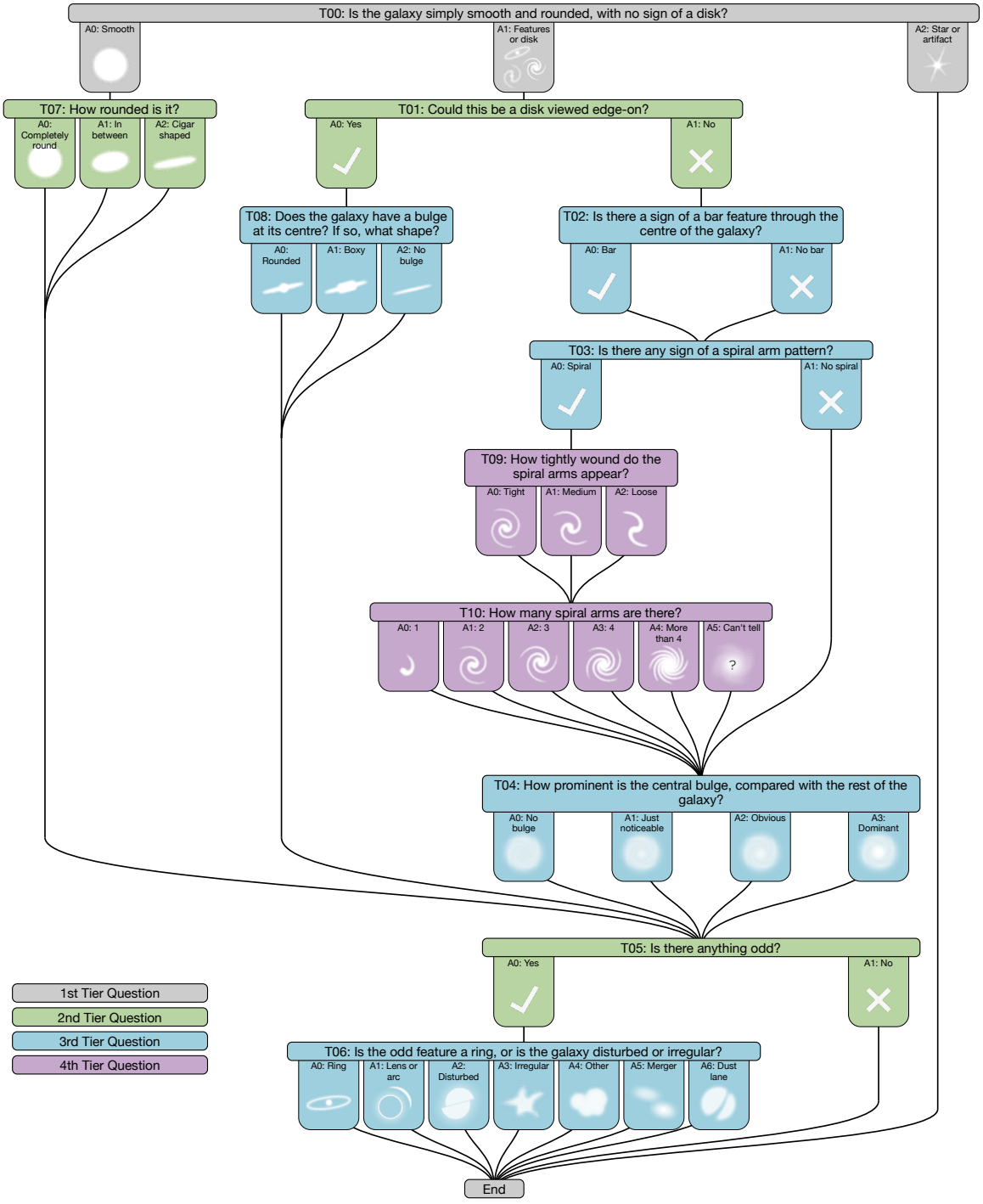

Figure 2.2: Diagram of the GZ2 decision tree from https://data.galaxyzoo.org/gz_trees. Volunteers begin at the top of the tree (Task T00) and work their way down by answering the questions. The colour coding suggests the relative depth of each task, in tiers, based on the answers to the previous question. Tasks T00 and T05 are the only questions that are always answered for each classification.

In GZ2, users are shown SDSS *gri* colour composite images and asked for the presence of the above-mentioned features using a multi-step decision tree, as shown in Figure 2.2. A *classification* is the total information collected about a galaxy, completing each step or *task*, of the decision tree, consisting of a *question* with a finite set of *responses*. The selection of an answer by each volunteer is referred to as a *vote*. The appearance of subsequent tasks in the decision tree depends on the user's previous responses.

Each GZ2 image is classified by at least 17 independent users and the mean number of classifications per galaxy is 42. Using the classifications from all the volunteers GZ calculates a *raw vote fraction* for each answer by dividing the number of users giving a particular response by the total number of answers. For example, if 6 out of 10 people answered that a galaxy has a bar, and 4 out of 10 answered that it does not, the galaxy would have a raw vote fraction for the bar question 0.6. The vote fractions are then weighted for the consistency of users, down weighting unreliable classifiers (typically a few percent of the volunteers), whose classifications are consistent with random selections. The *weighted vote fractions* are adjusted for redshift biases, due to the fact that galaxies further away appear dimmer and smaller in the images, with the effect that finer morphological features are more difficult to identify (Bamford et al., 2009). For example, the classification for 'smooth' increases with redshift from $z = 0$ to $z = 0.15$, while the classification for 'featured' decreases. The answers to the bar question show a similar effect, with the average number of 'yes' answers decreasing with redshift. These are unlikely to reflect a real evolution in the morphological properties of galaxies over such a small redshift range. Willett et al. (2013) corrected for these effects by adjusting the mean vote fractions and assuming that the SDSS survey is shallow enough that there is no evolution with redshift, using a similar method as in Bamford et al. (2009), referred to as debiasing. The correction is made by binning the galaxies as a function of absolute magnitude, Petrosian half-light radius (R_{50}) and redshift, in bins of 0.25 mag, 0.5 kpc and $\Delta z = 0.01$, respectively, and computing the ratio of the binary answers (smooth vs featured, barred vs not barred, etc.) in each bin, for the galaxies with a sufficient number of classifications ($N_{\rm task} \geq 10$). Assuming that the lowest redshift bin can be used as a baseline, reflecting the real (unbiased) physical properties of galaxies, the higher redshift bins are corrected using an analytic function fitted to the higher redshift bins. Accounting for the redshift biases gives the *debiased vote fraction* for each answer. A comparison between the raw and debiased vote fractions is shown in Figure 4 of Willett et al. (2013); the result of debiasing is a flattening of the galaxy finer morphology classification (featured, bar, bulge, etc.) with redshift. Nevertheless, the debiasing has a small effect on the vote

Desciption	Criterion	No.
GZ2	all GZ2[a]	243,500
MPA-JHU Catalogue	match	240,419
Nearby	$0.005 < z < 0.06$	81,736
Moderately inclined	$i < 60°$	52,851
Discs	$N_{\rm bar} \geq 10$	24,478
Non-interacting	$p_{\rm merger} < 0.4$	23,868
Strong bars	$p_{\rm bar} \geq 0.5$	5,282
Weak bars	$0.2 < p_{\rm bar} < 0.5$	6,013
No bars	$p_{\rm bar} \leq 0.2$	12,573
Volume-limited Strong Bars	$M_{\rm r} < -20.15$	3,547
Volume-limited Weak Bars	$M_{\rm r} < -20.15$	3,717
Volume-limited Unbarred	$M_{\rm r} < -20.15$	8,689

[a]With spectroscopic redshifts.

Table 2.1: Criteria to select Galaxy Zoo barred and unbarred samples and sizes.

fractions in this thesis ($\lesssim 10\%$), since the samples used are nearby. In this thesis, all the vote fractions used are the debiased vote fractions, unless otherwise stated, and are considered to be *likelihoods* of a galaxy having a certain morphological feature (for example the *debiased bar likelihood*, denoted $p_{\rm bar}$).

The subsequent reincarnations of the Galaxy Zoo project, classifying higher redshift galaxy images from the Hubble Space Telescope (HST) Legacy Surveys in GZ: CANDELS (Simmons et al., 2017) and GZ: Hubble (Willett et al., 2017) follow similar classification trees.

In what follows I describe the selection of barred galaxies using Galaxy Zoo morphologies, which is relevant for the next chapters.

2.3.1 Selecting samples of barred and unbarred galaxies

Cross-correlating the main GZ2 spectroscopic sample with the MPA-JHU catalogue (Kauffmann et al., 2003a), yields a total of 240,419 galaxies with stellar mass measurements. To ensure that the galaxies are sufficiently well resolved and that the bar detection by visual inspection is reliable, I restricted the sample to galaxies in a redshift range $0.005 < z < 0.06$. The lower redshift limit is adopted due to the previously discussed problem of shredding and deblending. Additionally, identifying bars in highly inclined galaxies is challenging, thus I selected only galaxies with an axis ratio of $b/a > 0.5$ given by the r-band automatic exponential model fits in SDSS (Stoughton et al., 2002) (`exp_AB`), corresponding to inclinations $i \lesssim 60°$.

Following Masters et al. (2011) and the recommendation of Willett et al. (2013), I only selected galaxies for which there were at least 10 answers to the question *Is*

there a sign of a bar feature through the centre of the galaxy?. This selection is to ensure that sufficient volunteers have inspected each galaxy, in order to have reliable bar classifications, and that the bar question is well-sampled, free from contamination by misclassified smooth galaxies. In order to reach the bar question a user must first classify a galaxy as a non edge-on galaxy with a disc or features. Thus, selecting galaxies for which at least a quarter of the classifiers answered the bar question is equivalent to selecting a non-edge on disc sample. Table 2.1 shows the number of galaxies resulting from making the above-mentioned selections in the main GZ2 spectroscopic sample.

To avoid potential problems with the deblending of galaxy images, merging or overlapping galaxies can be excluded with a cut of the GZ1 (Lintott et al., 2011) merging parameter $p_{\rm merger} < 0.4$, calculated from the merger question in Galaxy Zoo (Darg et al., 2010). Although the galaxies in this thesis are selected from GZ2 which used a more complex decision tree than GZ1, a similar selection is made to exclude merging and overlapping galaxies. Casteels et al. (2013) shows that the $p_{\rm merger}$ parameter has a strong correlation with the projected galaxy separation, therefore, a cut in $p_{\rm merger}$ reliably removes merging galaxies. This gives a total of 23,868 non-interacting disc galaxies.

By imposing various cuts on $p_{\rm bar}$ it is possible to select samples of barred galaxies with varying purity and completeness. A high $p_{\rm bar}$ selection means that a pure, but incomplete sample of barred galaxies is selected, while a low value of $p_{\rm bar}$ results in a more complete sample, but contaminated with non-barred galaxies. Therefore, by assessing the competition between purity and completeness, one needs to place a suitable limit on $p_{\rm bar}$ to select a barred sample. This threshold can be estimated by comparing the volunteers' classification with expert classifications.

2.3.2 Comparison to expert classifications

The largest sample (14,034 galaxies) with expert morphological classifications of SDSS galaxies is the work of Nair & Abraham (2010a) (hereafter N&A10). N&A10 selected galaxies in the redshift range $0.01 < z < 0.1$ and brighter than $g < 16$ mag, and recorded their fine morphological classification (the presence of bars, rings, lenses and spiral arms) inspecting the SDSS g band images. With a large overlap with the GZ2 main spectroscopic sample (12,400 galaxies), N&A10 classified bars in galaxies according to their strength as strong (200 galaxies), intermediate (1,131 galaxies) or weak (838 galaxies), depending on the bar sizes relative to the discs and on their prominence.

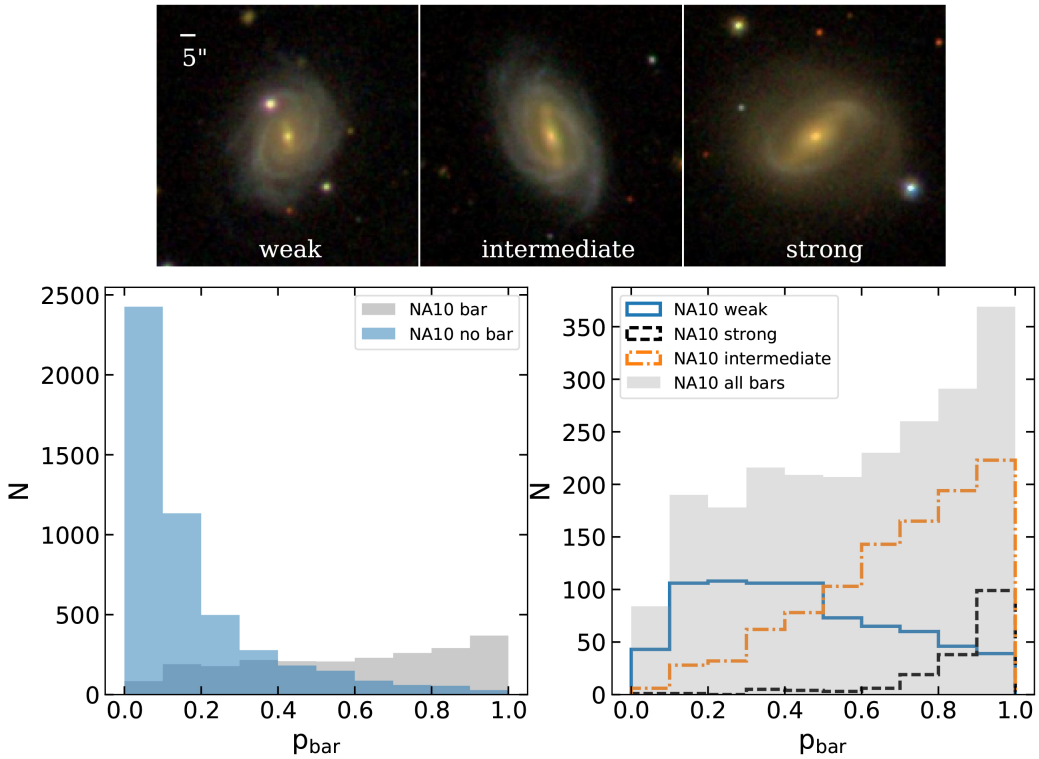

Figure 2.3: Comparison between the bar classifications in N&A10 Nair & Abraham (2010a) and Galaxy Zoo 2 (Willett et al., 2013), for 7,000 disc galaxies in common between the two studies. The top panels show examples from the three bar classifications in N&A10: weak, intermediate and strong. The *bottom left panel* shows the bar likelihood distribution for galaxies classified as barred (of any type) and not barred by N&A10. The *bottom right panel* shows the same distribution, but only for the N&A10 barred galaxies, and split into the different types.

A comparison between the bar classifications in N&A10 and Galaxy Zoo 2 bar likelihoods for a common sample of $\sim 7,000$ disc galaxies (selected as in Table 2.1) can be seen in Figure 2.3. A similar comparison was done by Willett et al. (2013) and Masters et al. (2012) (their Appendix A). The Galaxy Zoo volunteers detect almost all (>85%) the strong and intermediate bars in N&A10 and the contamination of unbarred galaxies is small (10%), if selecting a sample with a threshold $p_{\rm bar} \geq 0.5$. The majority of weak bars have intermediate $p_{\rm bar}$ likelihoods, $0.2 < p_{\rm bar} < 0.5$. A sample selected with $0.2 < p_{\rm bar} < 0.5$ would contain mostly weak bars, and the contamination with unbarred galaxies is $\sim 30\%$. Finally, a threshold of $p_{\rm bar} \leq 0.2$ can be used to select unbarred galaxies with a completeness of $\sim 90\%$. In this comparison, I used the classifications of N&A10 as 'gold standard', however their expert classifications are not perfect. When classifying 10,000 galaxies it is impossible to avoid misclassifications, even for experts. Comparing galaxies with high $p_{\rm bar}$ which

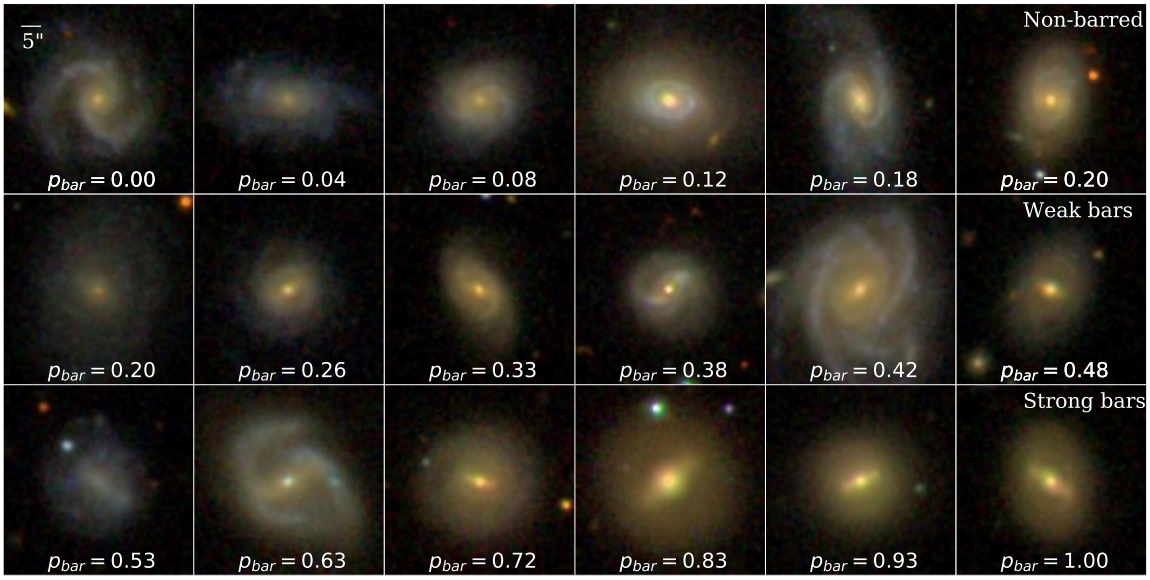

Figure 2.4: Examples of galaxies with strong and weak bars and unbarred galaxies in the volume-limited samples. The $p_{\rm bar}$ shows the Galaxy Zoo debiased likelihood of a disc galaxy being barred, based on the volunteers' inspection and classifications. The galaxies were randomly selected, approximately equally spaced in $p_{\rm bar}$ values.

were classified as 'not barred' by N&A10 I find that the majority of them are indeed barred. Therefore, the volunteers classifications are reliable to identify bars in SDSS images.

A threshold of $p_{\rm bar} \geq 0.5$ adopted by previous Galaxy Zoo studies (Masters et al., 2011, 2012; Melvin et al., 2014; Cheung et al., 2015a,b) is adequate for selecting a clean sample (containing $> 85\%$) of strong and intermediate bars. From now on, in this thesis I refer to both the strong and intermediate bar classifications as strong bars. A sample of weak bars can be selected with $0.2 < p_{\rm bar} < 0.5$ as previously done by Galloway et al. (2015) and also discussed in Skibba et al. (2012) and Masters et al. (2012). The selections described above result in a GZ2 sample of 5,282 strongly barred galaxies, 6,013 galaxies with weak bars and 12,573 unbarred galaxies, respectively, as shown in Table 2.1.

2.3.3 Classification of galaxy bulges

In Galaxy Zoo, after answering the bar question, citizen scientists were asked to visually classify the prominence of bulges of galaxies into four categories: *no bulge*, *just noticeable*, *obvious*, *dominant* (e.g. see Figure 2.2). The classifications for this question can be used to divide the samples of galaxies into disc dominated systems and systems with significant bulges. Since the question has four possible answers it

is possible to sort galaxies into two categories by combining the debiased likelihoods for two of the answers:

1. *disc-dominated*: having $p_{\text{no bulge}} + p_{\text{just noticeable}} > p_{\text{obvious}} + p_{\text{dominant}}$
2. *obvious bulge*: having $p_{\text{no bulge}} + p_{\text{just noticeable}} < p_{\text{obvious}} + p_{\text{dominant}}$

Therefore, each sample of galaxies (with strong bars, weak bars or unbarred) can be divided into these two categories, based on the prominence of their bulges. Simmons et al. (2013) has shown that, by combining the volunteers' visual classifications of bulges as above, it is possible to select a reliable sample of bulgeless galaxies. Additionally, the criterion for selecting galaxies with *obvious bulges* is in good agreement with measurements of bulge prominence, as is shown in Section 2.4.7.

2.3.4 Volume-limited samples

To accurately compare galaxies from different samples one needs to correct for the fact that galaxies of a given intrinsic luminosity will appear brighter if they are closer than galaxies of the same luminosity which are further away. Therefore, to study the statistical distribution and properties of barred and unbarred galaxies, I selected a volume-limited sample of each category, brighter than $M_{\text{r}} < -20.15$, which is the r-band Petrosian absolute magnitude corresponding to the GZ2 completeness magnitude of 17, at the redshift limit of $z = 0.06$. There are 3,547, 3,717 and 8,689 galaxies in the volume-limited samples of strong, weak and unbarred galaxies, respectively, as shown in Table 2.1. Examples of strongly, weakly barred and unbarred galaxies in the volume-limited samples can be seen in Figure 2.4.

To account for effects due to stellar mass and study the effects due to the presence of bars alone, I mass-match, in distributions with a tolerance of $\log M_* = 0.1$, the volume-limited samples with strong and weak bars, independently, with volume-limited samples of unbarred galaxies. This is possible because the sample of unbarred galaxies is larger than the two other samples.

2.4 Galaxy image decomposition

In this thesis I aim to go beyond the visual morphological classification of galaxies to a more quantitative measurement of morphologies. The advantages of quantitative measurements over visual classification are that they are less subjective (do not depend on a classifier) and are reproducible. The main disadvantage is that quantitative morphology relies on a model, which may or may not be physically meaningful.

Quantitative measures of galaxy morphology (parametric or non-parametric) rely on a key observable, which is the spatial distribution of light in a galaxy. Non-parametric tools for characterizing galaxy morphology include the Gini index G, the moment of light statistic M_{20} (Abraham et al., 2003), concentration (C), asymmetry (A) and clumpiness (S) (known as the CAS system, Conselice 2003). They are useful tools when the visual morphologies of galaxies are not known. Parametric tools, on the other hand, rely on fitting a model to the surface brightness profiles of galaxies, either one- or two-dimensional. This is a useful way of quantifying the morphology of galaxies, when the presence of various features in galaxies is known through visual classification. It allows galaxy components (for example discs, bars and bulges) to be separated and characterised by their individual light profiles in a technique known as decomposition. One such profile, widely used in parametric fitting, is the generalised Sérsic profile (Sersic, 1968)

$$I(r) = I_e \exp\left\{-b_n\left[\left(\frac{r}{r_e}\right)^{\frac{1}{n}} - 1\right]\right\}, \tag{2.1}$$

where I_e is the intensity at the effective radius r_e that encloses half of the total light from the model (Ciotti, 1991). b_n is a constant dependent on the chosen model ($b_n \approx 2n - 0.327$ for $0.5 < n < 10$, Capaccioli 1989) and the Sérsic index n describes the shape (concentration) of the light profile.

Caon et al. (1993) has shown that the generalised Sérsic profile is a good description of the light distribution of galaxies and that there is a correlation between n and the size of the galaxy. A special case is the de Vaucouleurs profile, with $n = 4$, empirically found to be a good representation of the light profile of elliptical galaxies (de Vaucouleurs, 1948, 1959). Another special case is the exponential profile, with $n = 1$, which was found to be a remarkably good representation of the light profile of galaxy discs (Patterson, 1940; de Vaucouleurs, 1959; Freeman, 1970).

The first decompositions were one-dimensional, where the central surface brightness and radial scale length[8] are determined by a linear fit to the light profile of the disc region and a de Vaucouleurs profile fit in the bulge region, separately (Freeman, 1970). One-dimensional decompositions, assume an azimuthally averaged profile of the components, without taking into account the different shapes of components. Two-dimensional fitting methods have been developed to solve this issue and to be able to determine the ellipticity and position angle of galaxy components. Such two-dimensional fitting tools include GIM2D (Simard, 1998), GALFIT (Peng et al.,

[8] h_r, the radius at which the intensity drops by a factor e, equivalent to 0.596 r_e for an exponential disc

2002), MGE (Cappellari, 2002), BUDDA (de Souza et al., 2004), GASP2D (Méndez-Abreu et al., 2008), IMFIT (Erwin, 2015), PROFILER (Ciambur, 2016) and PROFIT (Robotham et al., 2017). The differences between these numerous fitting tools are (1) the methods used to compute the best-fit (Levenberg-Marquardt, Multi-Gaussian Expansion, Bayesian analysis, etc.) given a multi-component input model, and (2) different functions to describe the light profile of the components which are implemented in the code (generalized Sérsic, de Vaucouleurs, Moffat, Ferrers, Gaussian, Edge-on disc profiles, etc.). In general, these differences result in faster (or slower) computation, sensitivity to local minima, better exploration of the parameter space and the desire of the user to utilize different model light profiles. Nevertheless, the goal of all these codes is the same – to obtain the best fit parameters given an input single- or multi-component model for the light profile of a galaxy.

2.4.1 GALFITM

Perhaps the most popular and widely used two-dimensional galaxy fitting code is GALFIT[9] (Peng et al., 2002, 2010). GALFIT is a well-tested software, proven to be reliable in fitting and measuring galaxy structural parameters, but despite being a very versatile code, it can only fit a single image at a time.

Since the aim of this work is to obtain multi-wavelength structural parameters and colours of components, I use a modified version of GALFIT3.0, called GALFITM[10], developed by the MegaMorph project (Bamford et al., 2011; Häußler et al., 2013; Vika et al., 2013), to perform automatic two-dimensional disc+bar+bulge, disc+bar and disc+bulge decompositions. The advantage of GALFITM is that it is able to fit simultaneously multiple images of the same galaxy taken in different wavebands, making use of the full wavelength coverage of surveys (Häußler et al., 2013). Thus, GALFITM provides increased accuracy of measured parameters, by using as much physical information as possible across the optical spectrum, as well as improving the magnitude and effective radii estimation in low S/N bands.

GALFITM performs simultaneous fitting by constraining the galaxy model parameters to be Chebyshev polynomials of the first kind (Abramowitz & Stegun, 1965) as a function of wavelength (Häußler et al., 2013)

$$p_i(\lambda_i; \{q_{i,j}\}) = \sum_{j=0}^{m_i} q_{i,j} T_j[z(\lambda)], \tag{2.2}$$

[9]GALFIT is publicly available at https://users.obs.carnegiescience.edu/peng/work/galfit/galfit.html
[10]GALFITM is publicly available at http://www.nottingham.ac.uk/astronomy/megamorph/

where p_i is the function with m_i parameters $q_{i,j}$ which describes the variation of the model parameter i with wavelength λ, chosen to be a series of Chebyshev polynomials $T_j(z)$, restricted to $z \in [-1, +1]$, and defined by the recurrence relation

$$\begin{aligned} T_0(z) &= 1 \\ T_1(z) &= z \\ T_{n+1}(z) &= 2zT_n(z) - T_{n-1}(z). \end{aligned} \tag{2.3}$$

For parameter i, $q_{i,j}$ are the fitted Chebyshev coefficients. In GALFITM the user has the possibility to select the maximum order of the Chebyshev polynomials. Setting m one less than the number of bands fitted allows complete independence of the parameters with wavelength (being the equivalent of fitting the bands separately with GALFIT). The reason for using Chebyshev polynomials is to relate the parameters in different bands with a user-specified smoothness (see Häußler et al. 2013 for more details).

GALFITM uses the Levenberg-Marquardt algorithm to minimise a single χ^2_ν residual between the multi-band images ($data(x, y)$) and the PSF-convolved model, by changing the parameters of the wavelength dependent model ($model(x, y, \lambda)$). The χ^2_ν is defined as

$$\chi^2_\nu = \frac{1}{N_{\rm dof}} \sum_{x=1}^{n_x} \sum_{y=1}^{n_y} \frac{[data(x, y) - model(x, y, \lambda)]^2}{\sigma(x, y)^2}, \tag{2.4}$$

where $N_{\rm dof}$ is the number of degrees of freedom in the fit (roughly $n_x \times n_y$, numbers of pixels in the x and y dimensions). σ is the error map defined as the standard deviation of the flux in each pixel and it is internally created by GALFITM. Apart from a data image, GALFITM requires a PSF image to convolve the model with, a mask image with the pixels to disregard in the fitting and a robust estimate of the sky background. I discuss all of these aspects in more detail in the next subsection.

2.4.2 FITS images

I use publicly available frames in the five *ugriz* bands from the SDSS DR10 website. To make cutouts[11] of galaxy images I use the corrected and background-subtracted SDSS fields[12] in which the galaxies appear. The SDSS fields[13] cover $10' \times 13'$ of the sky (corresponding to 1489 by 2048 pixels), and overlap by $0.84'$ (128 pixels)

[11] Using the routine available at https://github.com/eddedmondson/sdss_fits_cutout
[12] From http://data.sdss3.org/fields
[13] Identified by the sequence `run-camcol-field`

with adjacent fields. The routine first acquires all the fields with coverage within 8 Petrosian radii of a particular galaxy and combines the frames into a single mosaic using the MONTAGE software[14] (Jacob et al., 2010a). This method is useful when dealing with galaxies that are at the edges of fields, as well as to increase the S/N of the final FITS galaxy postage stamps. MONTAGE combines different fields into a single mosaic by reprojecting the input images to a common coordinate system and spatial scale, and by modeling the background to a common flux scale and background level (Jacob et al., 2010b). I discuss how the coadding of images might affect the galaxy fitting in Section 2.4.8.2. Square cutouts with a side length of 8 times the r-band Petrosian radius, centred on the galaxies are then created. This chosen size ensures that there is sufficient background around the galaxies to be measured and properly accounted for in the fitting process.

The necessary inputs for GALFITM (and GALFIT) to correctly generate an error image, therefore to compute χ^2_ν are the GAIN (since the unit of the σ image needs to be electrons, i.e. ADU $\times$ GAIN), the exposure time and the zero-point magnitude for each band. For the GAIN I used the average for each *ugriz* band across the whole survey: 1.65, 3.82, 4.73, 5.16 and 4.73.

To create a model of a galaxy with a similar resolution to the observations, it is important to convolve the model with a **point-spread function (PSF)**. The PSF varies with the atmospheric conditions (seeing), with the waveband and even within an image due to the optical aberrations of the telescope. I constructed a PSF at the position of the galaxy[15] in the corresponding SDSS `psFields`[16] frames. The PSF is constructed based on bright, isolated stars in the frame, in each wave band. Further details about the method used by SDSS to construct the PSF can be found in Lupton et al. (2001). These PSFs were used throughout the fitting procedures.

There are other methods for constructing PSFs. For example, an alternative is to construct the PSF using an analytic function, the prevalent functions being Gaussian models, double Gaussian or a Moffat profile (Moffat, 1969) (which is better suited to space based observations). I discuss the effects of using an analytical PSF in Section 2.5, when comparing my work with that of Gadotti (2009) who used PSFs created using a Gaussian model, in the decomposition of barred galaxies using the BUDDA software.

The estimation of the **background level** is also important for a successful fit (Häussler et al., 2007), as a wrong sky value is a common cause of systematic error in

[14]See http://montage.ipac.caltech.edu/ for more details
[15]Using the `read_psf` algorithm in https://www.sdss.org/dr12/algorithms/read_psf/
[16]As explained in http://www.sdss3.org/dr10/imaging/images.php

fitting (Peng et al., 2010). Although the SDSS images are background subtracted, the SDSS pipeline sky subtraction is inevitably imperfect. Therefore I used concentric elliptical annuli around the galaxy to measure the background value at the point where the surface brightness gradient is flat (further details about this measurement method in Barden et al. 2012). Nevertheless, the measured background values are small (and in few cases negative due to oversubtraction). These sky values were kept as a fixed parameter throughout the fitting process with GALFITM.

Finally, to achieve a good fit it is important to eliminate all possible sources of interference such as bright galaxies or stars in the proximity of the fitted galaxy, in what is referred to as a **pixel mask image**. To create the mask images, I first used Source Extractor (SEXTRACTOR, Bertin & Arnouts 1996) to identify all the bright sources in the image. With a set of input parameters such as the threshold on the pixel values above the background level for a source to be identified and the FWHM of the observations, SEXTRACTOR creates a segmentation map (mask array) with the pixels in the FITS image masked out. From the mask, I removed only the pixels corresponding to the galaxy to be fitted, leaving the target unmasked. For simplicity, I used the same mask (from the r-band) in all the five bands.

2.4.3 Galaxy models

GALFITM can fit multiple components to galaxy images. As discussed earlier, the number of fitted components is taken from the morphological information from Galaxy Zoo, provided by the different bar likelihoods. Thus, I fitted the unbarred, weakly and strongly barred galaxies with disc+bulge, disc+bar and disc+bar+bulge components, depending on the presence of a bar, as identified by the Galaxy Zoo volunteers and on the prominence of the bulges, based on my visual inspection of the residuals at the galaxy centres.

When fitting SDSS images, GALFITM fits all the five bands simultaneously and the user has the choice of varying all the parameters between the bands or fixing some of them. The reasons for fitting the bands simultaneously are to increase the overall signal-to-noise (S/N), and to measure consistent colours for each component. The main parameters of GALFITM for each component and for each band are: the centre (x_c, y_c), the effective radius (r_e), the Sérsic index (n), the axis ratio (b/a), the position angle (θ) and magnitude m. In the fitting procedure I constrained all the parameters except the magnitude to be the same in all five bands. The shapes of the galaxy components are not expected to vary significantly between bands. This approximation ensures that the colours for each component are measured consistently, i.e. at the same r_e in each band. However, it assumes no colour gradients within the

component models, which is a simplified picture of galaxy structure. I present test runs where the variation of structural parameters is allowed in Section 2.4.8.1.

To fit the galaxies I use an iterative process, in which I add one component at a time. The process I use for fitting is as follows:

I. **One component**. Firstly, I fit a single Sérsic profile for each galaxy, with the purpose of providing initial values for the parameters of the subsequent fits, as well as to measure the luminosity of the galaxy. As initial estimates for this fit, I used $n = 1$, and magnitudes, r-band Petrosian radii, ellipticities and position angles obtained from SDSS, as discussed in Section 2.1.

II. **Two components**. I then use the values from the single Sérsic fit as input into a two component model: an exponential disc and a second component. The user can specify the initial parameters for a second component to be the typical parameters of a bar or a bulge, however GALFITM will produce a fit best describing the component present in the galaxy. To start with, for the barred galaxies, I added a bar as the second component, with a slightly dimmer initial magnitude than the single Sérsic fit, with an initial effective radius 60% that of the disc in the one component fit, an initial Sérsic index of $n = 0.7$ and the axis ratio $b/a = 0.2$ (since the bar is an elongated feature, which according to Kormendy & Kennicutt 2004 has an axis ratio between 0.2-0.4). The position angle was set to be perpendicular to the major axis of the first component.

Bars are often modeled using a Ferrers function (Binney & Tremaine, 1987), which is a function with a nearly flat core and outer truncation. Without knowing the length of the bars a priori, it is difficult to establish where the radius of truncation for the bar profile should be, in an automated manner. Furthermore, since the order of the components in GALFITM can interchange during the fitting, to avoid the Ferrers function converging to a different component than the bar, I chose to use a general Sérsic profile to model the bar. Nevertheless, a Sérsic profile with a low index, $n \lesssim 0.5$ has a similar shape to a Ferrers profile (Peng et al., 2010). Kim et al. (2015) also show that there is a good agreement between the Sérsic model and Ferrers model for bars.

The 2D shape of some bars is closer to a box rather than to an ellipse (Athanassoula & Misiriotis, 2002), however GALFITM diverged very quickly from a boxy profile in the fitting procedure for most bars when I tried to constrain their shape. This is caused by a degeneracy between ellipticity and boxiness in the minimisation, GALFITM cannot constrain a highly elliptic boxy shape. Thus I modeled the bars using a more general ellipse shape, which is a reasonable approximation for bars.

After fitting a disc+bar model in step II, for many galaxies with a significant bulge present the second fitted component did not appear to be a real bar. The light from the bulge and from the bar were modeled together in one component by GALFITM, resulting in an elongated component with a high Sérsic index (68% with $n \geq 1$) and an r_e larger than the typical r_e of a bulge, but smaller than the typical r_e of a bar. These galaxies require a third component to separate the contribution of a bar from that of a bulge.

In the case of unbarred galaxies, in the second step of the fitting process I fitted a disc and a bulge. For the bulge, I used 10% of the disc component's effective radius (from step I) as an initial guess, an initial Sérsic index of $n = 2$ and an initial axis ratio of $b/a = 0.8$. The absolute values of the initial bulge r_e were, on average, similar to the initial guesses in the case of barred galaxies, so the models for barred and unbarred galaxies are consistent. This was the last step in fitting the unbarred galaxies.

III. **Three components**. Only the galaxies for which the two components successfully converged were fitted with three components. Based on the parameters from the two component fit as initial guesses, I added a third component, modeled as a bulge, with a free Sérsic profile. I started with an initial disc having slightly larger (125%) $r_{e,\mathrm{disc}}$ than the r_e of the disc in the two component fit and a bar with an $r_{e,\mathrm{bar}}$ of 50% the r_e of the disc in the two component fit. As an initial estimate for the bulge effective radius I used 25% of the r_e of the second component in step II, while for the initial axis ratio of the bulge, I used a value of $b/a = 0.8$ since the bulge should be a nearly round feature. The initial position angle was arbitrarily set to that of the disc. The initial Sérsic index of the bulge was set to $n = 2$, so that it is sufficiently different from the other components. This is also the boundary noted by Fisher & Drory (2008) to distinguish pseudobulges from classical bulges.

It is worth noting that adding the initial guesses for the components in a different order (for example disc+bulge+bar instead of disc+bar+bulge) did not make a difference in the final fit. GALFITM finds the best fit for the galaxies in the images with the number of components specified by the user. As in GALFITM the three components can interchange, I identified the disc as being the component with the largest effective radius, the bar being the elongated component and the bulge the component with the smallest effective radius at the end of step III.

2.4.4 Parameter constraints

Because the galaxy images and masks were not visually inspected before the fitting, a few issues might arise which can affect the fitting. Neighbouring galaxies or bright

stars that were not masked out might be treated as a component, or a component might be too dim for GALFITM to extract meaningful parameters. Therefore, to reduce the chances of GALFITM converging to an unphysical fit, it is useful to set constraints on the range of values various parameters can take during the fitting: the brightness was required to be within 6 magnitudes of the input value, the effective radii between 0.5 and 500 pixels and the Sérsic indices smaller than 8 for all components. I also required the bar and bulge components to have the same centre, in order to avoid one of the components converging to a clump, or overlapping star. However, the discs and the bar or bar+bulge components were not constrained to have the same centre, they were allowed to vary within $12''$ (which is the median $r_{\rm Petro90}$) in the sample. This led to finding that a significant fraction of galaxies have bars that are offset from the photometric centres of the discs, as discussed in more detail in Chapter 4.

The constraints mentioned above are reasonable and useful to guide the fitting process, but occasionally one or more of the fitted parameters converges to a limit imposed by a constraint. In other cases, the fits for the parameters without constraints might fail[17] to converge. In such cases, the resulting fits are probably wrong so they were discarded from further analysis, as discussed in Section 2.4.6.

It is worth emphasizing that the models used in this work are simple representations of galaxy structures, in which the galaxies can be represented by a bulge, bar and an exponential disc. In reality, galaxies are more complex, showing complex structures such as spiral arms and rings. Although fitting all these different features in GALFITM is possible, it would require much more detailed attention for each galaxy. The aim of this work was to keep the models relatively simple and uniform over a large range of angular sizes and surface brightness, while also quantifying bar structural parameters for a large sample of barred galaxies.

2.4.5 Measuring asymmetry

In GALFITM it is also possible to fit Fourier modes which can be interpreted as higher order deviations from a basic galaxy shape. According to Peng et al. (2010), this asymmetry can be quantified by expressing the shape of a galaxy as a Fourier perturbation on a perfect ellipse

$$r(x,y) = r_0(x,y)\Big(1 + \sum_{m=1}^{N} a_m \cos(m(\phi + \phi_m))\Big), \tag{2.5}$$

[17]Parameter marked between *...* in the GALFITM output

where $r_0(x, y)$ is the radial coordinate of a traditional ellipse, ϕ_m denotes the phase of the m component and the amplitude of the Fourier component is defined as $A_m = |a_m|$. The amplitude of the first Fourier mode ($m = 1$), A_1, normalised to the surface brightness of the galaxies (A_0), quantifies the lopsidedness of the galaxy disc, the variation in the size of the effective radius on opposing sides of the galaxy. The amplitude of the second Fourier mode ($m = 2$) A_2 quantifies the strength of the distortions by structures which have symmetry on rotation by 180°, such as bars or spiral arms.

To study the lopsidedness of galaxies with strong bars, I fitted an $m = 1$ Fourier mode on an exponential profile using GALFITM and measured the A_1 amplitude. The measured A_1 amplitudes are used to study the lopsidedness of galaxies with offset discs and bars in Chapter 4.

2.4.6 Inspecting the models

Figure 2.5 shows an example of the GALFITM outputs. For the strongly barred galaxies, the model in the third step of the fitting process converged for 4,492 of 5,282 galaxies, or 85% of the initial galaxies. In most of the cases where it failed, GALFITM either failed to converge for one of the parameters (for example the bar or bulge axis ratio being too small) or the low S/N made it impossible to extract a magnitude in one of the five bands. To clean up the fitted sample of galaxies, I only selected the fits with the following physical constraints: discs, bars and bulges have $r_e < 200$ pixels, all the components of disc galaxies should have effective radii smaller than 1.20′(corresponding to ∼10 kpc at the lowest redshift of the sample). I also selected only bulges with $n_{\rm bulge} < 8$ and axis ratio $b/a > 0.3$ and bars with $n_{\rm bar} < 8$ to avoid components converging to a constraint, as discussed in the Section 2.4.4. There were 1,031 galaxies for which GALFITM converged, but were discarded because the models were unphysical and did not represent a suitable disc+bar+bulge nor disc+bar model: in some cases a spiral arm, brighter star formation knot (clump) or overlapping star was fitted instead of one of the components. In other cases, one of the components converged to a nearby star or galaxy which had had not been masked out.

Finally, I inspected all the fits and compared the two component (disc+bar) to the three component fit (disc+bar+bulge), by looking at the image, model and residuals. GALFITM returns a goodness-of-fit reduced χ^2 value, χ^2_ν, which is an indicator if one model is favoured over another. However, the lowest χ^2 value does not ensure that a model is physically meaningful. Thus, it is not possible to decide over disc+bar or disc+bar+bulge models solely based on χ^2. Because of the complex morphology of

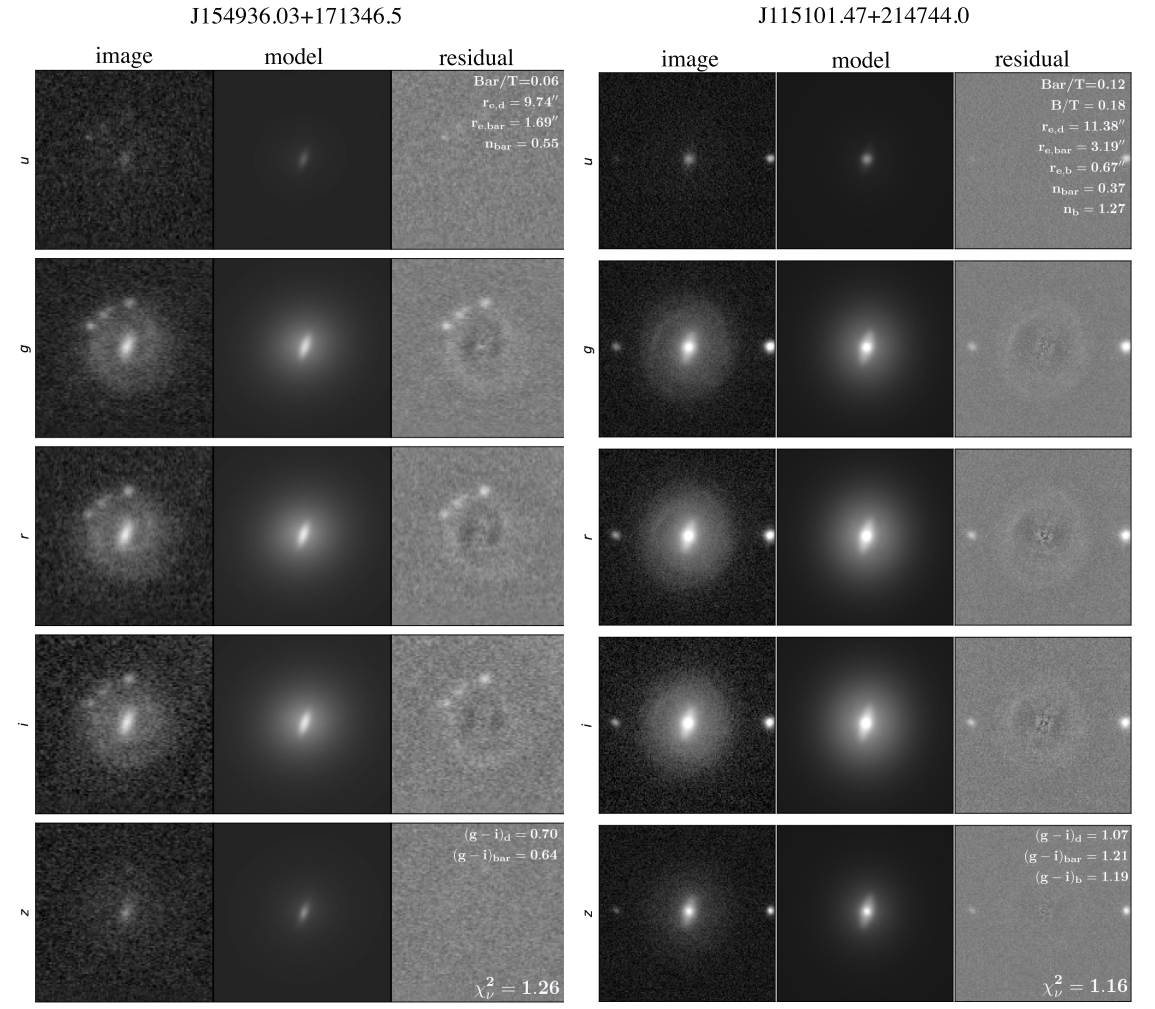

Figure 2.5: Example outputs from GALFITM of a two component (disc+bar) fit (*left*) and a three component (disc+bar+bulge) fit (*right*). The first column shows the image in 5 bands, *ugriz*, with the u and z bands having lower S/N compared to the rest. The second column shows the model fit from GALFITM with two and three components, respectively. The third column shows the residual (the model subtracted from the image). All panels have the same scale and their sizes are $40'' \times 40''$, a zoom-in of the actual fitting regions to show greater detail. The disc, bar and bulge r_e (in arcsec) and n, the Bar/T and B/T luminosity ratios are shown at the top of the u band residual. The $(g-i)$ colours for each component, corrected for Galactic extinction are shown at the top of the z-band residual. The reduced χ^2_ν is also shown.

galaxies, adding a further component always decreases the χ^2_ν of the model, as the number of degrees of freedom is increased. In the fits, 98% of the χ^2_ν values were between 1 and 2, with a median $\chi^2_\nu \sim 1.2$.

For 1,246 galaxies, the two component (disc+bar) fit proved to be a better fit (when judged by eye), given the lack of a significant third component (a bulge) in the galaxy images and in the residuals. There were 1,692 galaxies with good three

component (disc+bar+bulge) fits. For 523 barred galaxies, the second stage of the fitting process converged to a fit resembling a disc+bulge model – the axis ratio of the second component was $b/a > 0.6$, which is larger than the typical axis ratio of a bar. Since a bar was present in the galaxy images, I refitted these galaxies with three components, adding a bar, with the same initial parameters as in the second step of the fitting procedure. **3,461 strongly barred galaxies** have meaningful fits out of the initial 5,282 (66%). This is a significantly large sample to study the properties of barred galaxies.

Using a similar selection criteria for the weakly barred galaxies, only **2,617 weakly barred galaxies** out of 6,013 were successfully fitted, giving a final success rate of ∼44%. This might be because weakly barred systems are harder to fit with a model including a bar and the weakly barred sample is contaminated by unbarred galaxies. To assess the degree of this contamination, inspecting the residuals of single Sérsic fits (first step in the fitting) to 1,000 galaxies with $0.2 < p_{\rm bar} < 0.5$, I find that $\sim 75\%$ of these galaxies show signatures of a bar feature and $\sim 25\%$ do not.

For comparison reasons, only the volume-limited sample of unbarred galaxies was fitted with disc+bulge components (8,689 galaxies). **5,080 unbarred galaxies** were fitted successfully (58% success rate). The fits for the weakly barred and unbarred galaxies were not individually inspected, but their selection was based on similar physical constraints as for the barred galaxies.

This work mainly focuses on strongly barred galaxies (selected in Galaxy Zoo with bar likelihoods $p_{\rm bar} \geq 0.5$), while unbarred and weakly barred samples are used for comparison. Therefore, additional care has been taken, by inspecting the fits and performing the additional tests described in the following sections to ensure the reliability of the decompositions.

2.4.7 Two-component versus three-component model

As discussed in the previous section, the best fit disc+bar or disc+bar+bulge model for a galaxy was chosen based on my visual inspection of the residual images. If a significant residual was present at the centre of galaxies after removing the disc and the bar, I deemed the disc+bar+bulge model to be a better physical representation of the galaxy. This split the sample of galaxies with strong bars into DISC DOMINATED (fitted with disc+bar) and OBVIOUS BULGES (fitted with disc+bar+bulge). Only the most suitable model for each galaxy was taken, therefore the two samples of DISC DOMINATED and OBVIOUS BULGES do not overlap.

I compare my structural classification of DISC DOMINATED and OBVIOUS BULGE systems with the GZ classification of bulges in two categories, as discussed in Section

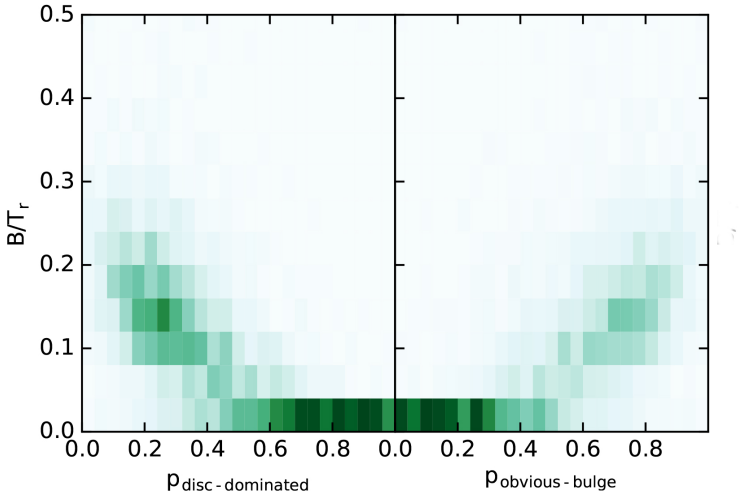

Figure 2.6: I fitted disc dominated barred galaxies with 2 components (disc+bar) and barred galaxies with obvious bulges with 3 components (disc+bar+bulge) using visual inspection of the fits and residuals. This correlates well with the GZ volunteers' classification of the bulges into: *no bulge*, *just noticeable*, *obvious*, *dominant*. In this plot I compare the measured B/T with the volunteers' classification with: $p_{\rm disc\ dominated} = p_{\rm no\ bulge} + p_{\rm just\ noticeable}$ and $p_{\rm obvious\ bulge} = p_{\rm obvious} + p_{\rm dominant}$.

2.3.3. The fraction of galaxies where my visual classification of bulges, based on the structural decomposition of the fits and residuals, differed from the GZ volunteers' classification of the bulge prominence was only 15%. This is mostly due to galaxies fitted with disc+bar+bulge components being classified as disc dominated (10%) and 5% of galaxies fitted with two components being identified as having obvious bulges. In Figure 2.6 I plot the r band B/T luminosity ratio versus the GZ vote fractions for the bulge prominence. There is a clear correlation between the volunteers' classification, my inspection and the B/T measured in the decompositions.

2.4.8 Tests

I first compare the parameters in multi-band fitting with the parameters obtained in fitting each band individually (thus using GALFITM in the same way as GALFIT), then the fits performed on coadded frames with fits on single frames. In the next subsection I discuss the uncertainties in the fits, and, finally, I compare the measured structural parameters with parameters from other published studies.

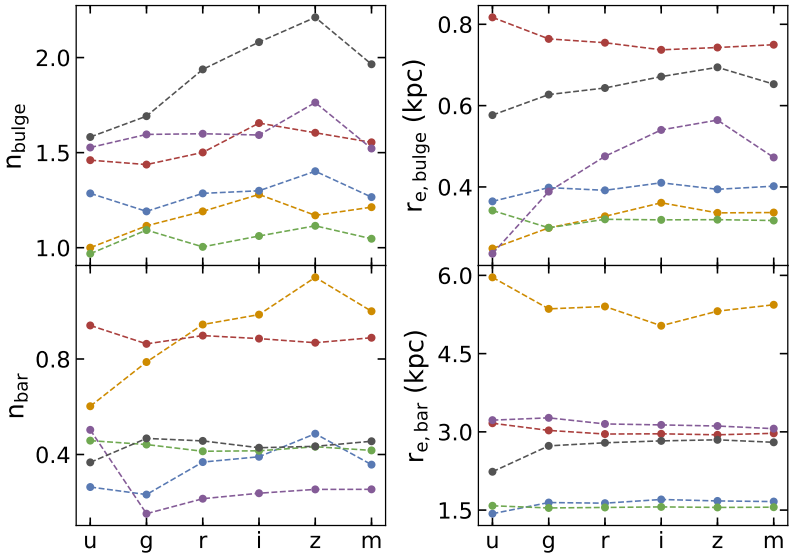

Figure 2.7: The dependence of the bulge and bar parameters with wave band for 6 randomly selected galaxies, fitted independently in the *ugriz* bands. For comparison, I also plot the parameters in the multi-band fitting, denoted by m, where the r_e's and n's were kept constant with wavelength. Thus, there is a single value for r_e and n for all the bands.

2.4.8.1 Fitting the *ugriz* bands independently

For the strongly barred galaxies, I first tested the reliability of constraining the parameters to be wavelength dependent compared to fitting individual bands separately (therefore comparing GALFITM with GALFIT). Thus, I fitted the strongly barred galaxies with two (disc+bar) and three components (disc+bar+bulge) in the five (*ugriz*) SDSS bands, allowing r_e and n to vary freely with band. I used the parameters from the multi-band fitting as initial estimates for all bands. I constrained the axis ratio and position angle to be the same in all the fits in order to prevent the components from interchanging and making the parameter extraction more complicated. When fitting each band independently, 3,102 strongly barred galaxies converged, a 58% success rate compared to 66% in multi-band fitting, suggesting that constraining parameters in multi-band fitting increases the number of reliable fits.

The structural parameters for the bars and for the bulges of the fitted galaxies vary slightly with wavelength, but do not change significantly with wavelength, nor between multi-band and individual band fitting (typically much less than a factor of two), while the parameters of the discs are very similar. In Figure 2.7 the parameters (r_e and n) for the bar and the bulge, respectively are shown for 6 randomly selected galaxies out of the 3,102 fitted galaxies, in all five bands and the multi-band fittings are denoted with m. The multi-band parameters agree well with the parameters fitted

in individual bands, especially with those in the g, r, i bands compared to u or z. In particular, the converged values are more similar to the values in the i-band, which is the least noisy band, and, hence the band in which the decompositions are most reliable.

Ideally, in multi-band fitting a higher weight should be given to images with the best signal-to-noise. The χ^2 minimisation uses the measured pixel-by-pixel noise as a weight. So although one cannot specify weights for individual bands, those which are noisier (u, z) will have lower weights, while g, r and i bands will have, on average, higher weights. A similar multi-band fitting procedure was applied to bulge-disc decompositions of 163 artificially redshifted nearby galaxies and shown to improve the measurements of structural parameters (Vika et al., 2014). Figure 1 in Vika et al. (2014) shows a similar trend for the measured parameters of a two component fit with wavelength.

To check whether the estimated colours are similar between the single and multi-band fitting, I plot the $(g - i)$ colours in Figure 2.8 for all 3,102 galaxies. There is a clear one-to-one correlation for all the three components, the discs showing the smallest spread and the bars showing the largest spread in colours. Even though the magnitudes for the components of individual galaxies do not match exactly, the advantage of using multi-band fits is that they effectively use the same aperture in each band (same r_e), while the colours of the single-band fits vary due to inconsistent decompositions in different bands. Therefore, the parameters and colours in the multi-band fitting are more reliable compared to the parameters in each band independently. Thus the multi-band parameters will be used in this work.

2.4.8.2 Coadded versus single frames

Secondly, I tested the effect of fitting coadded images compared to single fields. Some galaxies extend over more than one SDSS field, or they are very close to the field edges. To make cutouts of galaxies situated too close to the edges of SDSS fields I used the MONTAGE software to combine the SDSS fields in which a galaxy appears into a larger mosaic. Thus, using MONTAGE and multiple fields has some obvious advantages: being able to create images of galaxies close to the edges of the fields, with sufficient background around them, while also increasing the S/N ratio. It also has some disadvantages, such as combining PSFs from different observations when coadding the frames. To test the effect of using MONTAGE to create the images, I fit three components, using the same method as before, to ∼1,500 strongly barred galaxies which are situated at field edges, but this time with performing smaller cutouts in single frames. There is a higher failure rate for the galaxies in the single

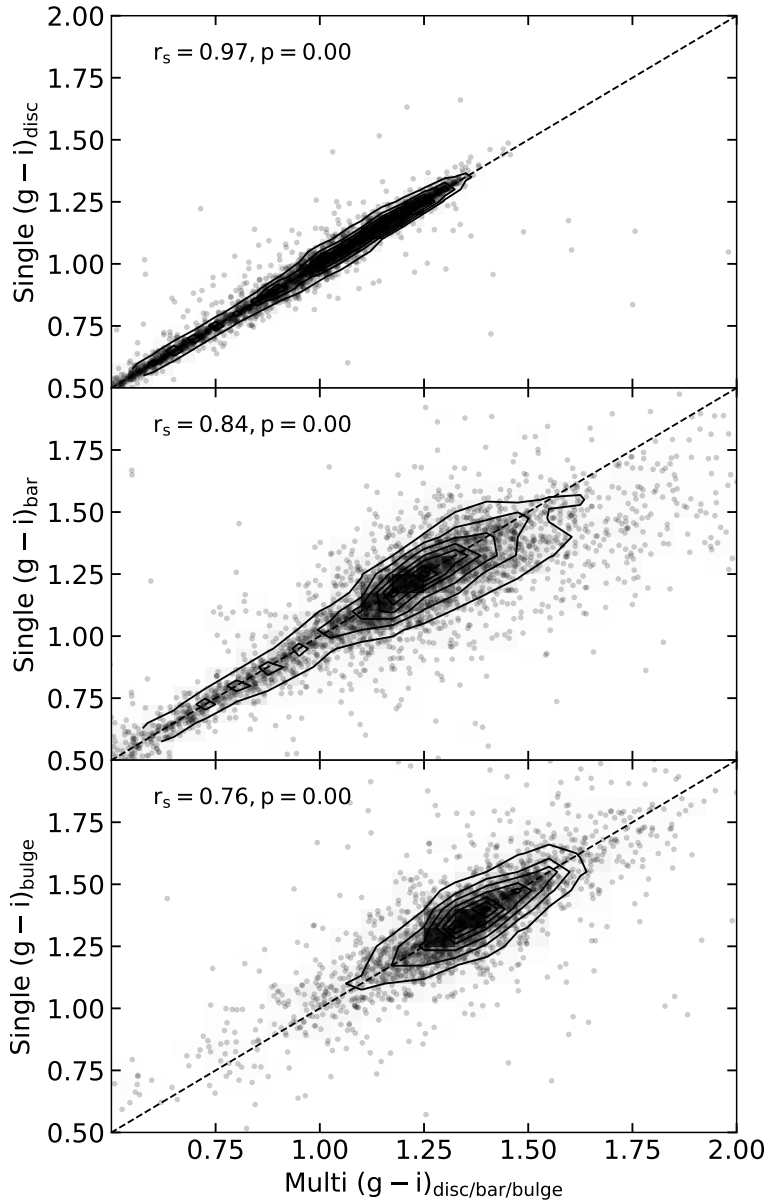

Figure 2.8: The correlation of $(g-i)$ colours for the disc, bar and bulge components with the bands fitted independently (y-axis) against the same colours in multi-band fitting (x-axis). The Spearman r_s-coefficient is shown at the top and the one-to-one line is drawn. The two values are clearly correlated and lie on the 1-1 line, with the bar component showing the largest spread.

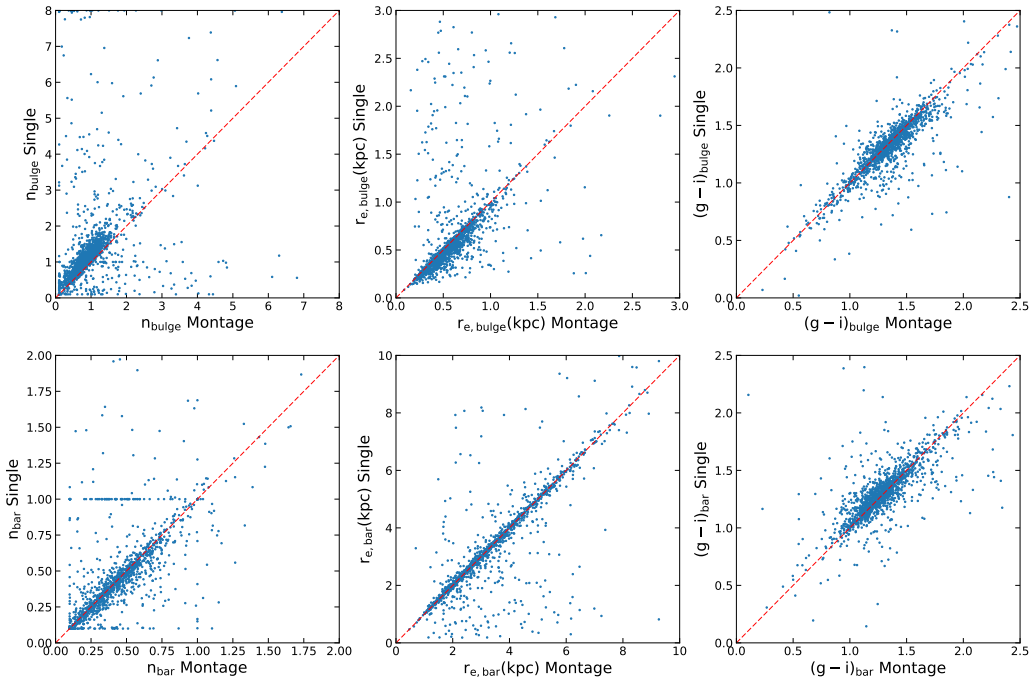

Figure 2.9: The parameters (n, r_e and colours) of the bulges and of the bars in the single versus coadded images with MONTAGE. The 1-1 line is plotted with a red dotted line. In general, the parameters are consistent, except for $n_{\rm bulge}$ and $r_{\rm e,bulge}$, which are systematically larger by a factor of 1.3 (above the 1-1 line) and 0.9 (under the 1-1 line), respectively.

frames compared to the stacked images, because of the lower S/N ratio of the images, and also because the fitting region did not include sufficient sky area around the galaxies.

I compared all the measured parameters for galaxies fitted in both the single frames and coadded frames and found a clear correlation and no systematics in most parameters, as shown in Figure 2.9. The only parameters for which I noticed a systematic change between the single frame and coadded ones are for the bulges, which might be due to the modified PSF. The bulge Sérsic indices, $n_{\rm bulge}$, in the single frames were 1.3 times larger than those in the MONTAGE frames and the bulge effective radii, $r_{\rm e,bulge}$ were 0.9 as large. However, this is the same effect observed for the two parameters. The n and r_e are related for a component with fixed flux, therefore one expects that a change in one parameter to result in a change for the other. The median colours of the three components change insignificantly (of the order 1-2%): $\Delta(u-r) = 0.04$, $\Delta(g-i) = 0.02$, $\Delta(r-z) = 0.01$. The same small effects occur for both the fits of barred and unbarred galaxies.

Therefore, it is beneficial to use MONTAGE to recover the parameters of a higher fraction of galaxies which are at the field edges, with the expense of smoothing the

data to a small extent, having the main effect of producing estimates of bulge Sérsic indices which are 0.77 times as large.

2.4.8.3 Uncertainties

GALFITM computes statistical errors (typically of order a few percent) internally based on the covariance matrix produced during the least-squares minimisation by the Levenberg-Marquardt algorithm. This method is known to underestimate the true error because it assumes that the only source of error is the Poisson noise after removing the model (Häussler et al., 2007). This is true only in simulated images. In reality, uncertainties are underestimated because the algorithm does not take into account the errors due to sky measurements, improper masking, correctness of the PSF, the assumed models for the galaxy and parameter degeneracy. Uncertainties in the background level are one of the main sources of errors, especially for components with high Sérsic indices, as these have extended wings, as discussed in Peng et al. (2010). Thus, more realistic uncertainties can be obtained by other processes, such as comparing results based on different models.

Vika et al. (2013) showed that the uncertainties in a single Sérsic fit with GALFITM of images similarly created with MONTAGE in the *ugriz* bands are typically: for *magnitude* ($\pm 0.09-0.13$ mags), r_e ($\pm 11-15\%$) and n ($\pm 9-17\%$). These were based on the uncertainties in estimating the sky flux, which dominates the error budget. The uncertainties on fitting multiple components are more complex, Vika et al. (2014) shows that the bulge n and r_e can vary by up to 25%, while the uncertainties in the disc components in the disc+bulge decompositions are similar to the uncertainties in the single Sérsic fits. Since I used the same software and images of the same quality, the uncertainties in the disc, bar and bulge parameters are similar to those found by Vika et al. (2014) in disc+bulge decompositions.

2.4.8.4 Unsuccessful fits

One possible bias is preferentially excluding a large number of galaxies because their fits were unsuccessful. Out of the 5,282 fitted galaxies, the fits for 1,821 galaxies were excluded either because the two or three component fits failed in GALFITM, or the models were unphysical, as discussed in Section 2.4.6. Here I check the properties of barred galaxies excluded due to failed fits, and those fitted successfully.

In Figure 2.10 I plot the distribution of $p_{\rm bar}$, stellar masses and $(u-r)$ colours. The galaxies for which the fits failed have preferentially lower $p_{\rm bar}$, lower masses and are bluer. The least bias is for $p_{\rm bar}$ (K-S test $k = 0.09$, $p_{\rm KS} = 2 \times 10^{-9}$) – there are $\sim$10% more galaxies that failed and were excluded near the cutoff of $p_{\rm bar} \sim 0.5$

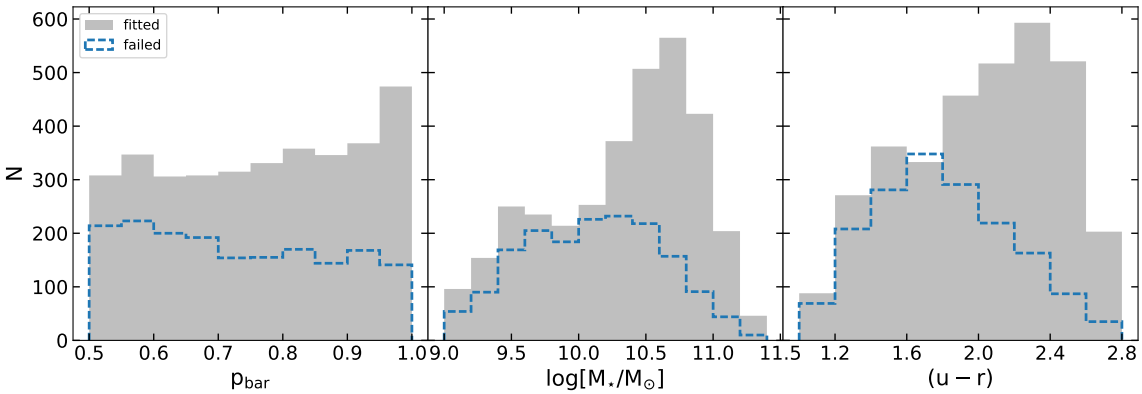

Figure 2.10: Distribution of $p_{\rm bar}$ (*left*), stellar masses (*middle*) and $(u-r)$ colours (*right*) for the fitted galaxies and those that were excluded due to failed fits.

compared fits that failed for galaxies with $p_{\rm bar} = 1$. This small difference is probably due to the higher fraction of weak bars near the cutoff that failed or the small possible contamination with unbarred galaxies, as discussed earlier, which should have vote fractions closer to $p_{\rm bar} = 0.5$.

This difference in the stellar mass distribution and colour can be explained by the fact that it is more difficult to fit lower mass, bluer galaxies which have lower surface brightness. The successfully fitted sample of barred galaxies is biased towards galaxies with higher surface brightness. When comparing their properties to unbarred galaxies it is important therefore to mass-match the two samples. Nevertheless, fitting the unbarred and weakly barred samples suffers from similar bias.

2.5 Comparison with previous fits

To ensure that the fitted parameters are robust, I first compare the parameters from GALFITM with other published studies, using similar (SDSS) imaging. Simard et al. (2011) (hereafter S11) used the GIM2D software to automatically decompose over one million g and r band SDSS images of galaxies into bulge and disc components. Almost the entire sample of strongly barred galaxies in this study overlaps with S11 (3,108 galaxies, or 90% of the the successfully fitted strongly barred sample). I compare the results from my decomposition with their exponential disc + free $n_{\rm b}$ decompositions (they also provide decompositions with fixed $n_{\rm b} = 4$, but the free bulge Sérsic index best resembles the technique used in my work). To consistently compare the parameters, I split my sample into galaxies fitted with two (disc+bar) and three (disc+bar+bulge) components, and I compare them with the two components fit in S11 separately.

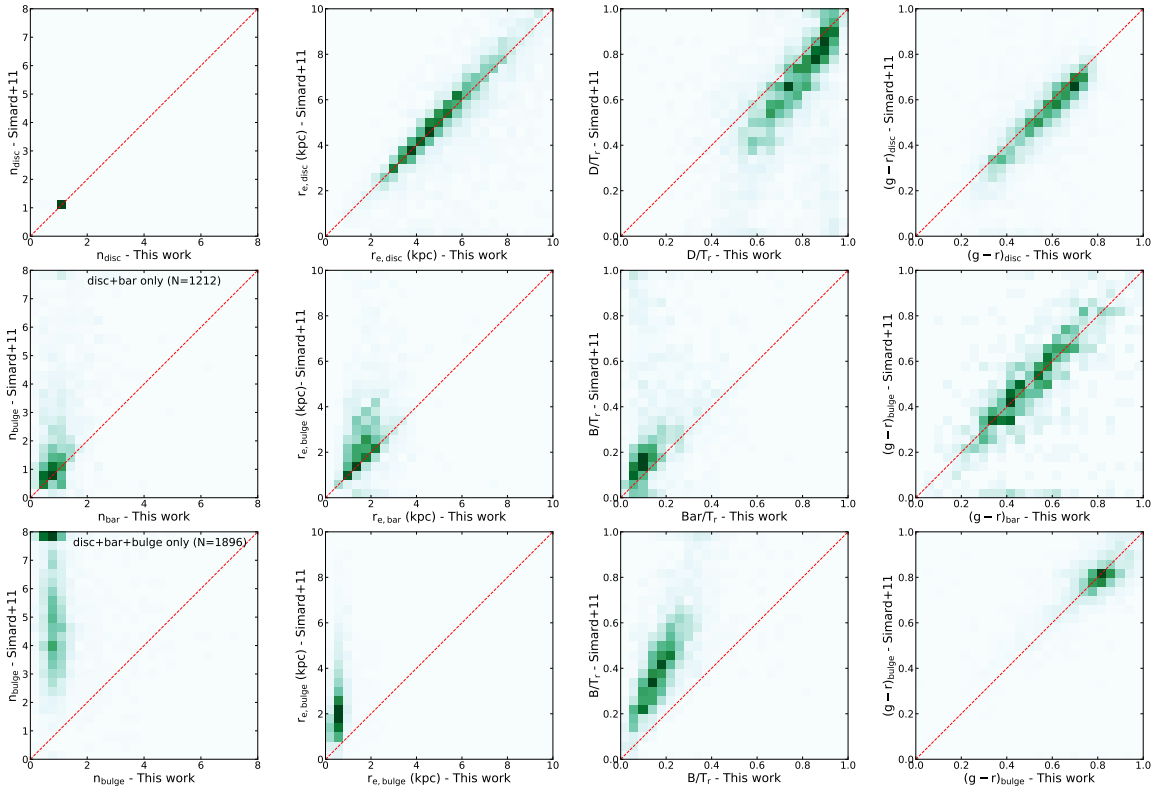

Figure 2.11: 2D histograms showing the correlation between the disc parameters in the decomposition of strongly barred galaxies in this thesis (*top panels*) and S11, between the bar parameters in the disc+bar decompositions and disc+bulge decompositions in S11 (*middle panels*) and between the bulge parameters in the disc+bar+bulge decompositions and disc+bulge decompositions in S11 (*bottom panels*). The red dotted lines illustrate a perfect match. The *bottom panels* show that the traditional disc+bulge decompositions are inadequate when modeling galaxies with strong bars.

Figure 2.11 shows the comparison for the disc parameters (*top panel*) for all my fits (3,108 galaxies); the middle panel shows the bar parameters versus the 'bulge' parameters in S11 in the two component fits and the *bottom panel* shows the comparison between my bulge parameters in the three component fit versus the 'bulge' parameters in S11. I find a good agreement for all the parameters of the disc between my decompositions and those of S11. For the galaxies fitted with two components, again, I find a good agreement between our two studies, with perhaps a tail towards larger $n_{\rm bulge}$ and $r_{\rm e,bulge}$ in S11. I find, however, significant discrepancies when comparing the bulges in my three component fits with the bulges in S11. All the 'bulges' in the disc+bulge fits of S11 have large $r_{\rm e,bulge}$, B/T and $n_{\rm bulge}$ (many of them converging to the limit of $n_{\rm bulge} = 8$ in S11). All of these galaxies have strong bars, as identified by visual inspection. The traditional bulge+disc decompositions overestimate, sometimes by more than 100%, the $r_{\rm e,bulge}$, $n_{\rm bulge}$ and B/T when bars are omitted,

thus they are inadequate for fitting barred galaxies (as also shown by Laurikainen et al. 2005 and Gadotti 2008). This can lead to erronous interpretations, such as a prevalence of classical bulges (with $n \sim 4$) in the Universe.

A better comparison is between decompositions with the same number of components. Gadotti (2009) (hereafter G09) fitted 291 face-on (with axis ratios $b/a \geq 0.9$) barred galaxies (based on the authors' visual inspection) with masses $M_\star > 10^{10} M_\odot$ in g, r, and i band images from SDSS. The overlap between our studies is 74 strongly barred galaxies. More recently, Méndez-Abreu et al. (2017) (hereafter MA17) decomposed 162 local ($z < 0.03$) galaxies from the CALIFA survey, (Sánchez et al., 2012) with a bar component, in individual g, r and i SDSS DR7 bands, with the GASP2D (Méndez-Abreu et al., 2008) software. The overlap between my sample and MA17 is of only 27 galaxies, due to the lower redshift limit of their survey. Even though all three studies use similar decomposition technique (three components and relying on human supervision to inspect the fits), there are some important differences, for example: the codes used, the different models of PSFs used for convolution, the slightly different data (I used DR10, MA17 used DR7 images, both of which are background subtracted while G09 used the earlier SDSS DR2 images which were not background subtracted) and different modeling of the galaxy components.

A comparison between the disc, bar and bulge parameters for the common galaxies in this study, MA17 and G09 can be seen in Figure 2.12. The parameters in the i-band are plotted for all three studies. There is, in general, a good agreement for the disc parameters ($n_{\rm d}$[18], $r_{\rm e,d}$[19], D/T, $(g-i)_{\rm d}$). MA17 used a double exponential function for the discs of 14/27 barred galaxies, with an inner scale length and outer scale length, as illustrated by the vertical dotted lines in Figure 2.12. The parameters for the bar component are more difficult to compare because of the different models used for the bar in the three studies. MA17 fixes all the galaxies to have the same (Ferrers) light profile, corresponding roughly to a profile with a Sérsic index of 0.4-0.5, and models the semi-major axis of the bar (having an ellipse shape), not the effective radius. Nevertheless, there is a good correlation between their measured bar size and $r_{e,\rm bar}$ and between our estimated Bar/T. G09, on the other hand, uses a boxy model for the bar and, similarly, a Sérsic profile for the bar as in this study, but constrained it, preventing it from attaining low values. This is not necessarily a physically motivated choice, as many bars have flatter profiles (see e.g. Elmegreen & Elmegreen 1985; Kim et al. 2015 and Section 3.3.3 of this work). There is a discrepancy in $r_{\rm e,bar}$ as well, G09 measuring smaller values; however this reflects the discrepancy in $n_{\rm bar}$ as the

[18] All three studies used an exponential model ($n_{\rm d} = 1$) for the disc
[19] Both MA17 and G09 measure the disc scale-length, $h = r_e/1.67835$

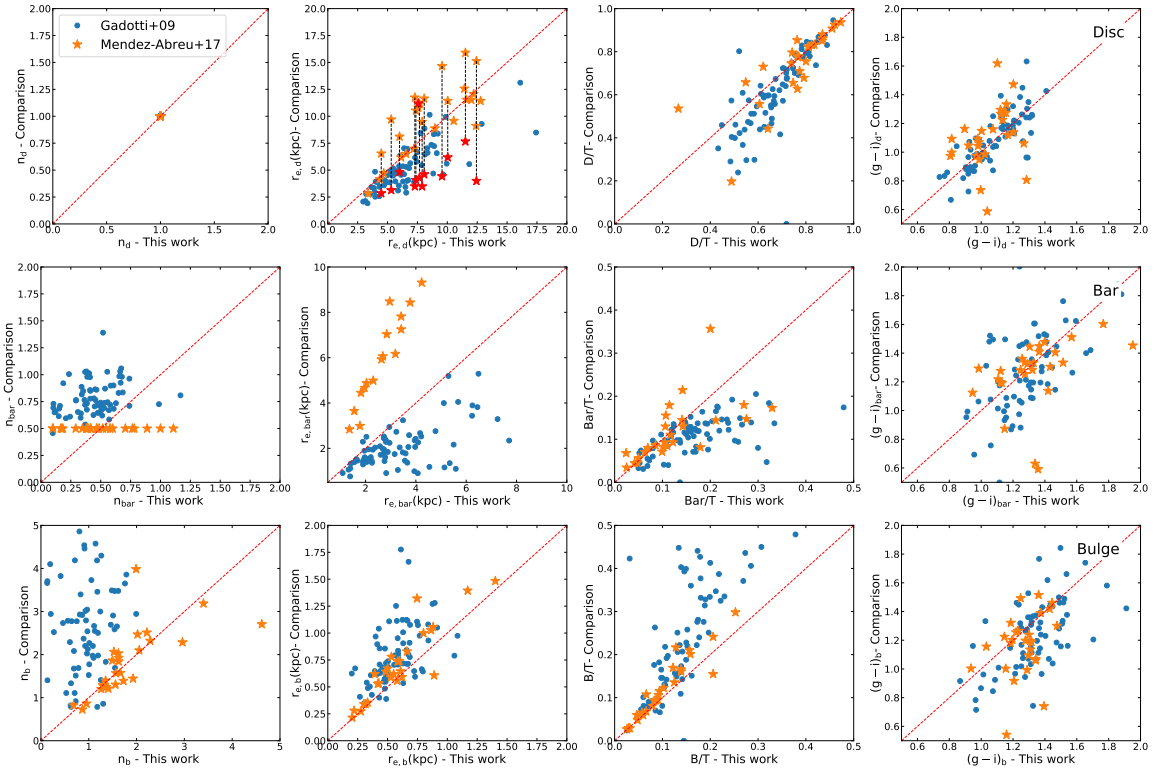

Figure 2.12: Comparison between the disc (*top panels*), bar (*middle panels*) and bulge (*bottom panels*) parameters measured in this work and in Gadotti (2009) and Méndez-Abreu et al. (2017). The red dotted lines show what would be a perfect match. The dotted line in the 2$^{\rm nd}$ *top panel* show the measured inner and outer disc radii for 14 galaxies fitted with a disc break in MA17. MA17 models the bar with a fixed Ferrers profile (corresponding to $n_{\rm bar} \sim 0.4$) and measures the bar semi-major axis, instead of $r_{\rm e,bar}$, quantities which are plotted in the *middle-left panels*.

two parameters are not independent (see discussion in Section 2.4.8.2). Additionally, because of the boxy bar shapes fitted in G09, and the ellipse shapes used in this work, my measured Bar/T are slightly larger.

The largest discrepancies between the studies are for the bulge parameters ($n_{\rm bulge}$, $r_{\rm e,bulge}$, B/T). My measurements for the bulge parameters agree very well with MA17, but both studies disagree with G09. G09 consistently measure larger $n_{\rm bulge}$, although their models constrain $n_{\rm bulge} \geq 0.8$ and they mention that this parameter is the least robust, and the hardest to constrain when varying the input parameters (see G09 Appendix A, Figure A1). I investigated the source of this discrepancy and found that the model used for the PSF has a moderate effect on the bulge Sérsic index. For the convolution, in my decompositions the PSF was reconstructed empirically based on stars in the SDSS fields (as discussed in Section 2.4.2), while G09 used a circular PSF based on a theoretical Gaussian profile, with the FWHM given by SDSS (private

conversation with the author). A simple, Gaussian function is a less accurate model for a PSF than one constructed based on the stars in the image, since it does not take into account the time- and position-varying distortions in the shape and profile of the PSF. Using a similar, theoretical Gaussian PSF model, I recover slightly larger values for $n_{\rm bulge}$ (median $n_{\rm bulge} = 1.6$ compared to $n_{\rm bulge} = 1.3$) and a better correlation with G09 ($r_s = 0.5$, where r_s is the Spearman rank correlation coefficient), but the majority of the values are still $n \sim 1$ lower than the ones measured by G09 (median $n_{\rm bulge} = 2.5$). Therefore, there might be other reasons for the observed discrepancies. Another difference between the two studies is in the different codes used for fitting (BUDDA versus GALFITM), which is discussed further in Section 3.4.4.

The $(g-i)$ colours of the three components agree across studies, within scatter, and the medians are consistent. The scatter is larger for the bar and bulge components compared to disc. The scatter arises because of using different measures for the magnitudes (this work and G09 measure the integrated colours, while MA17 measures the central surface brightness of the components) or the magnitudes are extracted within different apertures (at the same $r_{\rm e}$ in the g and i bands in this work, while in G09, $r_{\rm e}$ in the g and i bands was allowed to vary).

The fact that the parameters measured in this study agree well with MA17 (and to some extent with G09), without systematic biases, suggests that they are reliable and can be used to compare the different components (bars, discs and bulges), as well as different types of galaxies (barred and unbarred). Even though the individual fits can have substantial scatter, the median values for the entire population are robust.

2.6 Summary

In this chapter I discussed the data used in this thesis – imaging data from the Sloan Digital Sky Survey (SDSS), integral field spectroscopic data from the SDSS-IV MaNGA survey and Galaxy Zoo morphological classifications. Based on volunteers' visual inspection of galaxies I selected a large sample of 5,282 galaxies with strong bars (based on the bar prominence and relative size to the disc, in good match with expert classification of bars), and comparison samples of galaxies with weak bars (6,013 galaxies) and without bars (12,573 galaxies). Using the novel GALFITM software I fitted multi-band *ugriz* SDSS images of strongly and weakly barred galaxies with disc+bar and disc+bar+bulge models, chosen based on my visual inspection inspection of the presence of bulges in the fits and residuals. I have also fitted unbarred galaxies with disc+bulge models. I summarize the samples of fitted galaxies that will be used in the next chapters in Table 2.2.

Description	Original	Successfully fitted	Volume-limited
Strongly barred	5,282	3,461	2,435
DISC DOMINATED (disc+bar)	2,575[a]	1,246[b]	395
OBVIOUS BULGES (disc+bar+bulge)	2,707	2,215	2,040
Weakly barred	6,013	2,617	1,580
DISC DOMINATED (disc+bar)	3,929	1,726	772
OBVIOUS BULGES (disc+bar+bulge)	2,084	891	808
Unbarred	12,573	5,080[c]	5,080
disc+bulge	12,573	5,080[d]	5,080

[a]DISC DOMINATED vs OBVIOUS BULGES based on volunteers' classification
[b]DISC DOMINATED vs OBVIOUS BULGES on my inspection of the residuals
[c]Only the galaxies in the volume-limited unbarred sample were fitted (8,689 galaxies).
[d]All unbarred galaxies were fitted with disc+bulge components and then mass-matched to barred samples.

Table 2.2: Summary of the samples of fitted galaxies used in the following chapters.

I have found that traditional disc+bulge decompositions are inadequate when fitting barred galaxies, as the light from the bar is erroneously assigned to the bulge, overestimating its contribution to the luminosity of the galaxies and its concentration. It is important to model the bars in disc galaxies, since they are observed in a significant fraction of the disc galaxy population.

The decomposition with GALFITM provides measurements for the disc, bar and bulges in the five *ugriz* bands: component centre (x_c, y_c), effective radius (r_e), Sérsic index (n), axis ratio (b/a), position angle (θ) and magnitude m. The parameters, except the magnitude, were constrained to be the same in all bands thus there is one best fit measurement for the parameters. The colours (difference in magnitude between different bands) are measured within the same aperture (same r_e).

Chapter 3

Bars in SDSS

I present the results of two-component (disc+bar) and three-component (disc+bar+bulge) multi-wavelength photometric decomposition of what is currently the largest sample of barred galaxies (∼3,500) fitted with models that include a bar. I compare the colours of the disc, bar and bulge components and investigate for evidence of secular evolution leading to the quenching of star formation and the build-up of pseudobulges in barred galaxies. I examine the properties of bars (light profiles, sizes, luminosity ratios) and their dependence on the stellar mass of galaxies. By comparing the barred galaxies with a mass- and environment-matched volume-limited sample of unbarred galaxies, I examine the connection between the presence of a large-scale galactic bar and the properties of discs and bulges. I identify a subsample of unbarred galaxies with an inner lens/oval and investigate their properties in comparison with barred and unbarred galaxies.

3.1 Motivation and background

I have been motivated by previous Galaxy Zoo results which showed that the bar fraction increases with redder colours and in galaxies with more prominent bulges (Masters et al., 2011). In Masters et al. (2012) the authors relate the increase in bar fraction with colour to the decrease in the atomic gas content of galaxies: gas-poor galaxies are significantly more likely to host bars than gas-rich galaxies, this correlation being observed even at fixed stellar masses. This observed trend could be caused by: (a) bars depleting the gas in the host galaxies; (b) the higher atomic gas content suppresses bar formation; (c) possible correlations with the environment (bars might be triggered in denser environments, while the gas removal is caused by environmental effects such as strangulation).

In a subsequent paper using a similar sample of galaxies from Galaxy Zoo and SDSS, Cheung et al. (2013) found that the likelihood of a galaxy hosting a bar is anticorrelated with the specific Star Formation Rate (sSFR), independent of stellar mass or bulge prominence. Thus, they find tentative evidence of bar-driven quenching, the process in which bars lead to the cessation of star formation in the galaxies and the build-up of high central densities in systems which become quiescent in such a way. However, they identify galaxies with pseudobulges and with classical bulges based on the global Sérsic index, using $n = 2.5$ as a discriminator between the two (classical bulges with $n \geq 2.5$, peseudobulge otherwise). They suggest that a more accurate identification of pseudobulges is needed, and that finding a population of quiescent disc galaxies hosting only pseudobulges would be a strong evidence of bar-driven quenching having acted in these galaxies.

The role of bars in quenching the star formation and the details of this process are still unclear. To investigate these, one has to study the stellar populations of the individual components (bars, discs and bulges) separately, in detail. Many authors have applied 2D decomposition methods to separate discs and bulges. The largest two-band image bulge+disc decomposition, of over a million galaxies in SDSS, was carried out by Simard et al. (2011). However, simple bulge+disc decompositions can give inaccurate fits when applied to strongly barred galaxies, with the bar flux being erroneously assigned primarily to the bulge, as shown in Section 2.5.

A few works have decomposed galaxies including a bar component. For example, Laurikainen et al. (2007) decomposed 216 nearby disc galaxies in detail, some including bar components, and found strong evidence for pseudobulges across all Hubble types. Reese et al. (2007) also attempted to decompose the light of 68 disc galaxies into discs, bulges and bar components. Weinzirl et al. (2009) decomposed 143 bright H-band galaxies, ∼80 including a bar component, and studied the correlations between bulges of barred and unbarred galaxies concluding that bulges are likely to have been built by a combination of secular processes and minor mergers in the recent Universe. Using the BUDDA software (de Souza et al., 2004), Gadotti (2009) (G09) performed disc+bulge+bar decomposition in three bands (g, r and i) on a sample of 291 barred galaxies from SDSS and studied their properties in Gadotti (2011). More recently, Salo et al. (2015) decomposed 2,352 nearby (< 40 Mpc) galaxies in 3.6 μm images from the S^{4}G survey (Sheth et al., 2010), out of which ∼800 included a bar component, but without investigating their properties in detail. Kim et al. (2015) fitted 144 face-on barred galaxies from the same S^{4}G survey with a bar component. Additionally, Méndez-Abreu et al. (2017) (MA17) decomposed 162 local ($z < 0.03$) barred galaxies from the CALIFA survey (Sánchez et al., 2012).

The aim of this chapter is to present meaningful physical parameters for the bulges, discs and bars of the largest sample of strongly barred galaxies to date (∼3,500), selected using Galaxy Zoo morphologies, and compare them with unbarred galaxies using the most complete multi-wavelength data for nearby galaxies from SDSS. The bulge-to-total (B/T), bar-to-total (Bar/T) luminosity ratios, effective radii, component colours and Sérsic indices are analysed with the aim of understanding the effect of bars on the evolution of barred galaxies. The multi-wavelength and multi-component decomposition of these galaxies in five SDSS bands ($ugriz$) with the GALFITM software is presented in detail in Chapter 2.

In this chapter I used the successfully fitted sample of 3,461 galaxies with strong bars and, for comparison, the successfully fitted samples of galaxies with weak bars (2,617 galaxies) and unbarred galaxies (5,080 galaxies), as well as the volume-limited subsamples, as presented in Chapter 2, Table 2.2. The structural parameters, luminosity ratios and colours of the discs, bars and bulges for ten of the successfully fitted 3,461 galaxies with strong bars are given in Table 3.1 and 3.2. The colours of the different components of barred galaxies (discs, bars and bulges) are compared and discussed in Section 3.2 and the properties of bars in Section 3.3. Section 3.4 shows a comparison between the barred and unbarred galaxy components, including colours (Section 3.4.1) and structural parameters of bulges (Section 3.4.3). Section 3.5 discusses the properties of a subsample of unbarred galaxies with inner lenses/ovals. In each section I compare the measurements from the decompositions with other published studies on barred galaxies and discuss the importance of the findings in the context of secular evolution of disc galaxies.

3.2 Component colours of barred galaxies

In this section I investigate the colour distribution of discs, bars and bulges of barred galaxies, the differences in component colours within individual galaxies, and the trends with stellar mass. The colours of the individual components are important because they reflect the distribution of stellar populations within galaxies.

One important result of this multi-wavelength study is the distribution of colours of the three components. In Figure 3.1 I plot three different colour distributions, $(u-r)$, $(g-i)$, $(r-z)$ for the discs, bars and bulges. In $(g-i)$ colours, the median difference between bulges and discs is $\Delta(g-i)_{\rm b,d} = 0.33$ and between the bars and discs $\Delta(g-i)_{\rm bar,d} = 0.20$. The median colour difference between the different components of galaxies with strong bars narrows from the $(u-r)$ to $(r-z)$ colours (for example $\Delta(u-r)_{\rm bulge,d} = 0.68$, $\Delta(g-i)_{\rm bulge,d} = 0.33$, $\Delta(r-z)_{\rm bulge,d} = 0.19$), suggesting that

(1)	(2)	(3)	(4)	(5)	(6)	(7)	(8)	(9)	(10)	(11)	(12)	(13)	(14)
SDSS Name	Fit components	Disc				Bar				Bulge			
		mag	n	r_e	b/a	mag	n	r_e	b/a	mag	n	r_e	b/a
J161802.49+113044.5	disc+bar	15.57	1.0	26.96	0.84	18.68	0.33	3.84	0.38	-	-	-	-
J161102.82+130715.5	disc+bar	16.78	1.0	11.28	0.86	16.76	1.01	2.86	0.60	-	-	-	-
J160916.62+131538.8	disc+bar+bulge	14.75	1.0	19.48	0.98	17.17	0.39	5.29	0.33	17.15	0.63	1.48	0.83
J160718.22+131340.9	disc+bar	15.81	1.0	24.59	0.87	17.24	1.05	9.47	0.33	-	-	-	-
J160217.54+122742.6	disc+bar+bulge	14.69	1.0	28.37	0.79	15.78	0.43	13.58	0.43	16.05	1.13	3.35	0.68
J161735.43+185254.6	disc+bar	15.59	1.0	21.92	0.72	17.95	1.90	4.81	0.19	-	-	-	-
J161729.64+192159.2	disc+bar	16.58	1.0	13.09	0.75	18.44	0.38	7.28	0.31	-	-	-	-
J155613.84+141600.0	disc+bar+bulge	15.44	1.0	20.92	0.86	16.03	0.38	11.76	0.29	17.02	1.25	3.35	0.49
J155354.13+140218.8	disc+bar+bulge	15.65	1.0	21.04	0.68	18.27	0.10	14.42	0.17	19.63	0.30	1.22	0.34
J153110.17+002410.1	disc+bar+bulge	16.29	1.0	16.25	0.94	16.57	0.74	7.53	0.47	16.96	0.66	1.43	0.69

Table 3.1: Structural parameters of discs, bars and bulges for 10 randomly selected barred galaxies out of the 3,461 galaxies fitted with disc+bar or disc+bar+bulge components. Columns (3), (7), (11) show the integrated i-band magnitudes (from fits, not corrected for Galactic extinction), columns (4), (8), (12) show the Sérsic indices, columns (5), (9), (13) the effective radii in pixels and columns (6), (10), (14) the axis ratios from the multi-band fits of the three components. The measured bulge Sérsic indices in the coadded frames are 0.77 times as large as those in single frames, as discussed in Section 2.4.8.2. The magnitudes in the u, g, r, z bands are also available. Full table is available in the electronic version of Kruk et al. (2018).

(1)	(2)	(3)	(4)	(5)	(6)	(7)	(8)	(9)	(10)	(11)	(12)
SDSS Name	Redshift	$M_{\rm r}$	$\log(M_\star)$	$p_{\rm bar}$	Disc		Bar		Bulge		
			$[M_\odot]$		D/T	$(g-i)_{\rm d}$	Bar/T	$(g-i)_{\rm bar}$	B/T	$(g-i)_{\rm b}$	χ^2_ν
J161802.49+113044.5	0.036	-20.11	9.92	0.56	0.95	0.67	0.05	0.88	-	-	1.19
J161102.82+130715.5	0.035	-19.64	9.80	0.61	0.49	0.45	0.51	0.88	-	-	1.19
J160916.62+131538.8	0.047	-21.72	10.90	0.72	0.82	0.98	0.09	1.27	0.09	1.50	1.20
J160718.22+131340.9	0.035	-19.85	9.24	0.69	0.79	0.48	0.21	0.33	-	-	1.22
J160217.54+122742.6	0.035	-21.38	10.85	0.81	0.60	1.19	0.22	1.18	0.17	1.18	1.15
J161735.43+185254.6	0.058	-21.29	10.31	0.59	0.90	0.52	0.10	0.92	-	-	1.25
J161729.64+192159.2	0.031	-19.11	9.42	0.82	0.85	0.79	0.15	0.54	-	-	1.14
J155613.84+141600.0	0.037	-20.98	10.53	0.96	0.55	0.88	0.32	0.90	0.13	1.19	1.22
J155354.13+140218.8	0.035	-20.14	10.00	0.65	0.90	0.82	0.08	0.96	0.02	1.60	1.20
J153110.17+002410.1	0.039	-20.53	10.37	0.56	0.43	1.00	0.33	1.07	0.23	1.15	1.13

Table 3.2: Properties of the same 10 galaxies as in Table 3.1, fitted with disc+bar or disc+bar+bulge components. Redshifts and r-band Petrosian absolute magnitudes ($M_{\rm r}$) are drawn from SDSS DR7 and the stellar masses are drawn from average values in the MPA-JHU catalogue (Kauffmann et al., 2003a). Column (5) shows the debiased bar likelihood of the galaxies from the GZ2 catalogue (Willett et al., 2013), based on the volunteers' visual inspection. Disc-, bar- and bulge-to-total luminosity ratios in the i-band are given in columns (6), (8), (10). Columns (7), (9), (11) show the $(g-i)$ colours of the three components, corrected for Galactic reddening and extinction using the maps from Schlegel et al. (1998) and K-corrected (Blanton & Roweis, 2007). Finally, column (12) shows the reduced-χ^2 value of the fits. Full table is available in the electronic version of Kruk et al. (2018).

the bluer colour of discs is due to additional star formation. In what follows I focus on the $(g-i)$ colours because the two bands are sufficiently separated in wavelength to probe both the star forming and the quiescent stellar populations (while u and z bands are noisy), and they are less prone to dust extinction.

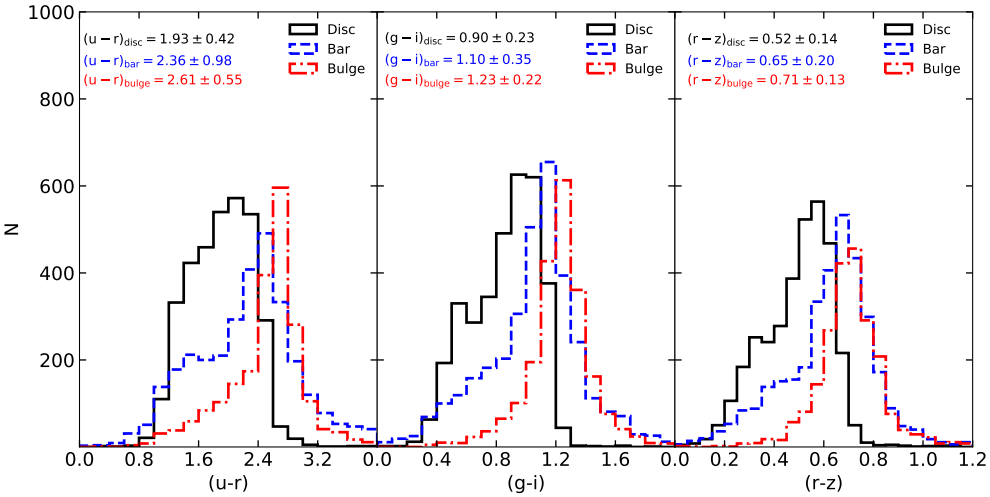

Figure 3.1: The $(u-r)$, $(g-i)$ and $(r-z)$ colours of the different galaxy components for all the fitted galaxies with strong bars (3,461 galaxies). The discs are bluer than the bars, which in turn are slightly bluer than the bulges. The median colours and their corresponding 1σ spreads are shown for each component, since the median is less sensitive than the mean to outliers.

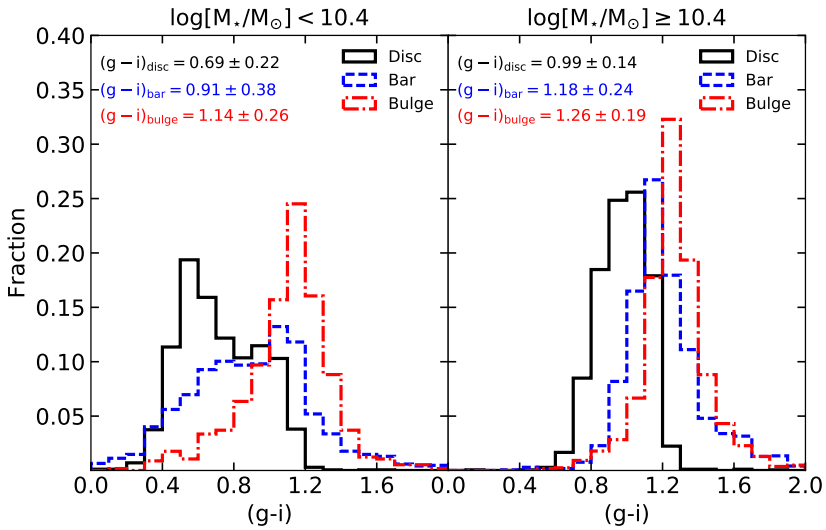

Figure 3.2: Normalised histograms of the $(g-i)$ colours of the different galaxy components, split by galaxy stellar mass. There were 1,135 low mass galaxies fitted with disc+bar and 575 with disc+bar+bulge. Similarly, there were 1,640 high mass galaxies fitted with disc+bar+bulge and 111 with disc+bar. The discs and bars of lower mass galaxies are bluer than those of high mass galaxies, while the bulges are moderately bluer compared to their high mass counterparts. The median colours and their corresponding 1σ spreads are shown for each component.

The sample of galaxies with strong bars contains galaxies with stellar masses between $10^9 M_\odot$ and $10^{11.5} M_\odot$, while the colours depend strongly on stellar mass of galaxies. I split the large sample of barred galaxies by stellar mass into low-mass, $M_\star < 10^{10.4} M_\odot$ (1,710 galaxies), and high-mass $M_\star \geq 10^{10.4} M_\odot$ (1,751 galaxies) and plotted the distribution of component $(g-i)$ colours, in Figure 3.2. This stellar mass threshold was chosen to divide the sample of galaxies with strong bars into approximately equal subsamples. As expected, there is an important dependence of component colours on stellar mass, reflecting the dependence of the global colour on stellar mass (the median difference in global colour between the high mass and low mass sample is $\Delta(g-i)_{\rm global,\,highM-lowM} = 0.3$). The component colours of lower mass galaxies, particularly the discs and bars are bluer compared to their counterparts in high-mass galaxies (by differences in the median colours of $\Delta(g-i)_{\rm disc,\,highM-lowM} = 0.30$, $\Delta(g-i)_{\rm bars,\,highM-lowM} = 0.27$). The change in $(g-i)$ colours between low and high mass galaxies is smaller for the bulges ($\Delta(g-i)_{\rm bulge,\,highM-lowM} = 0.12$), although there are only 575 low mass galaxies fitted with a bulge; bulges still appear red in colour compared to other components, but the spread of the bulge colours at lower masses increases.

Figure 3.2 shows that the colours of different components (especially for discs and bars) depend on the mass of the galaxy. Therefore, instead of looking at the distributions of colours for the entire population of galaxies with strong bars, in Figure 3.3 I plot the colour difference between each two of the three components against the galaxy stellar mass. The *top panel* shows that bars are consistently redder than the accompanying discs by $\Delta(g-i)_{\rm bar,d} \sim 0.2$ and that there is a slight trend with stellar mass - highest mass galaxies have the reddest bars when compared to the corresponding discs. The *middle panel* shows that bulges are almost always redder than their associated discs by, $\Delta(g-i)_{\rm bulge,d} \sim 0.25$, on average. Finally, the *bottom panel* shows that within the same galaxy, the bulges and bar have similar colours $\Delta(g-i)_{\rm bulge,d} \lesssim 0.05$. Initially, this similarity of the bulge and bar colours seems to be in contrast with the distribution of colours shown in Figure 3.1. However this is because the disc dominated galaxies (fitted without a bulge component) have bluer bars compared to bars in galaxies with obvious bulges. Galaxies with obvious bulges have bars and bulges of comparable colours. Furthermore, the relatively flat trend with stellar mass shown in Figure 3.3 (*bottom panel*) suggests a possible link between the stellar populations of bars and bulges. In addition, although most bulges are in higher mass galaxies, they tend to become bluer than their corresponding bar at lower masses. The fact that some bulges are bluer (younger) than bars suggests

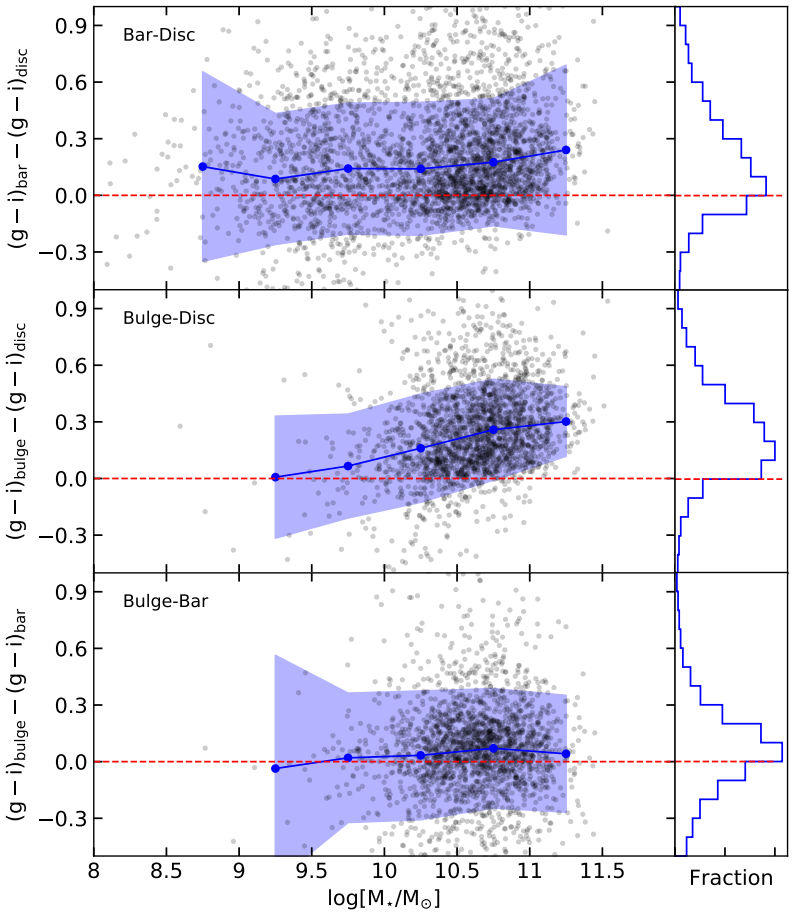

Figure 3.3: The differences in $(g-i)$ colours of the three galaxy components for galaxies with strong bars, showing the change in colour for each individual galaxy. This plot contains all the successfully fitted barred galaxies (3,461) with disc+bar (1,246 galaxies) and disc+bar+bulge (2,215 galaxies) components. The median $(g-i)$ colour is plotted with blue in stellar mass bins of $\log(\frac{M_\star}{M_\odot}) = 0.5$ (excluding $> 10\sigma$ outliers) and the shaded band shows the 1σ scatter.

that if bars mediate the growth of bulges, it is through their effect on gas dynamics rather than the stars in the bar themselves migrating to form a bulge.

Studying the colours of galaxy components using image decomposition I find that the inner region of barred galaxies (bars and bulges) are redder compared to the galaxy discs, by a median value of $\Delta(g-i) \sim 0.2$ (but with a significant spread), this colour difference increasing with stellar mass. Approximately 25% of barred galaxies have bluer bars compared to their discs and only 10% of them have bluer bulges compared to the discs, the majority of them at lower masses. Thus, in general, there is a clear colour gradient in galaxies with strong bars, with a bluer disc and increasingly red bars and bulges. It is worth noting that the estimated colours are integrated colours, measured within the same aperture (r_e) in order to be consistent between bands,

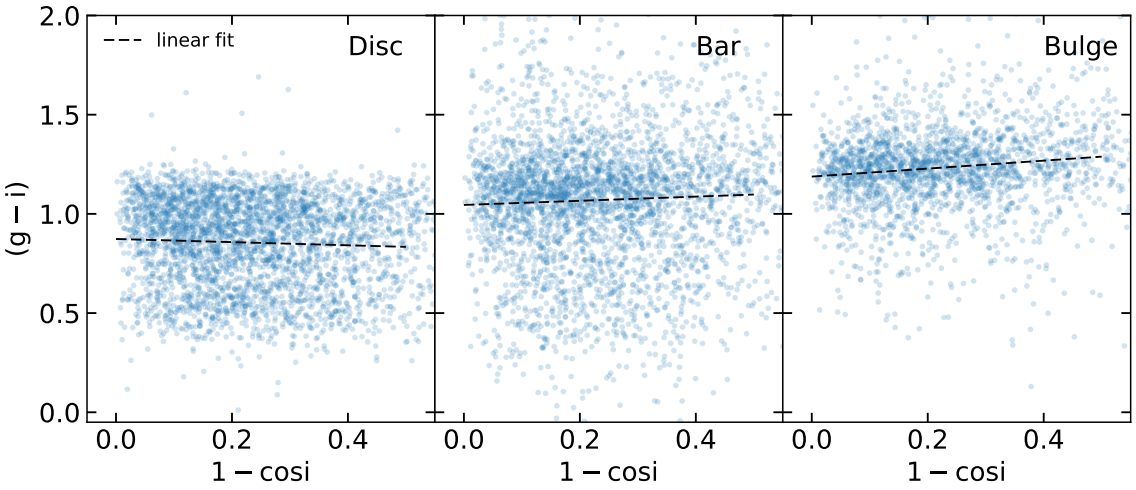

Figure 3.4: Trends of the measured colours for the discs, bars and bulges of barred galaxies with $1 - \cos i$ (where i is the inclination of the galaxy estimated using Equation 3.1; 0 corresponds to completely face-on and 0.5 to $i \approx 60°$). The lines of best fit, based on a linear regression to the data points in each panel is shown.

without taking into account colour gradients *within* components. It is possible that the colour varies smoothly with radius in these galaxies, if colour gradients within the discs, bars and bulges exist. Additionally, dust in galaxies can affect the observed colours of the components, which is discussed in the following subsection.

3.2.1 Effects of dust

The intrinsic colours are affected by reddening and extinction caused by the dust in the host galaxies. The effect of internal dust reddening should be considered when comparing the colours of different galaxy components, however these effects are hard to quantify. The colours in this thesis have already been corrected for dust extinction in the Milky Way.

In a paper on red spiral galaxies, Masters et al. (2010) showed how dust effects are systematic with the inclination of galaxies. By comparing face-on and edge-on spirals and assuming that the colour difference is only due to viewing angle, they find a total extinction for the edge-on ($i = 90°$) galaxies of 0.7, 0.6, 0.5, 0.4 and 0.3 mag for the *ugriz* wavebands. The extinction is much smaller from completely face-on ($i = 0°$) to oblique galaxies ($i = 60°$) (0.17, 0.12, 0.07, 0.04 for the *ugri* bands in Masters et al. (2010), assuming no extinction in the z band), where the inclination was calculated from the axis-ratio, assuming an intrinsic thickness of $q = 0.2$ for the

discs (Unterborn & Ryden, 2008), using

$$\cos^2 i = \frac{(b/a)^2_{\rm disc} - q^2}{1 - q^2}. \tag{3.1}$$

In this work, the effects of internal dust are not expected to be significant because the barred galaxies were selected to be moderately face-on ($i \lesssim 60°$). Nevertheless, I checked for systematic trends with inclination in the sample by converting the fitted $(b/a)_{\rm disc}$ into an inclination using Equation 3.1. I only find a small trend of colour with inclination, such that at $i \sim 60°$ (corresponding to 0.5 in Figure 3.4), the $(g-i)$ colours of the bulges, bars and discs given by the lines of best fit are 1.29, 1.10 and 0.83, while for completely face-on galaxies ($i \sim 0°$) they are 1.19, 1.04 and 0.87, respectively, as shown in Figure 3.4. Hence the colour differences between 60° and 0° are: $\Delta(g-i)_{\rm bulge} \sim 0.1$, $\Delta(g-i)_{\rm bar} \sim 0.06$ and $\Delta(g-i)_{\rm disc} \sim -0.04$. Bulges suffer from more attenuation with inclination than discs, as also shown by Pierini et al. (2004) and Tuffs et al. (2004). Perhaps counter-intuitively, I find a negative dust attenuation for the discs, such that the face-on discs are slightly redder compared to the inclined ones. This can be an optical depth effect; for the more inclined galaxies one better observes the outer stellar populations, which are likely bluer, while for the face-on galaxies one better observes the inner disc which is intrinsically redder. Gadotti et al. (2010) also found that the dust attenuation in the discs at low inclinations is negative and they suggest that this is due to scattering of photons propagating parallel to the plane of the galaxy into the line of sight. Nevertheless, it is a small effect.

Correcting for the effects of internal dust is complicated, even for face-on galaxies, because the sample in this study is made up of both late and early-type galaxies, which likely contain different amounts of dust. The effects vary with the amount and distribution of dust within the galaxy, as well as with wavelength. Furthermore, the discs, bars and bulges might have different optical depths and contain different amounts of dust, hence suffering from different dust extinction. If the galaxy is optically thick, for example, the light from the far side of the bulge would not reach us, thus increasing the extinction in the bulge (Driver et al., 2007). Driver et al. (2008) suggest that the colour excess due to dust extinction in bulges can be as high as $\Delta(g-i) \sim 0.3$, while in face-on discs $\Delta(g-i) \sim 0.1$, however they do not discuss the morphology of galaxies and the types of bulges (classical bulges, pseudobulges or inner disc regions) considered in their study. G09 estimates a smaller colour excess due to the effect of internal dust reddening (based on total galaxy dust attenuation in Kauffmann et al. 2003a) – $(g-i) = 0.08$ in classical and $(g-i) = 0.15$ in pseudobulges, in a sample selected from SDSS. Thus, the combined effect of internal dust and

inclination is to decrease the difference between the colours of the inner components (bar and bulge) and the discs. However, considering the diversity of galaxies in this study (early-types with little dust and late-types with significant dust), it is impossible to correct for internal dust extinction using a simple relation. Detailed models of how dust affects the colours of bars, discs and bulges in different types of barred galaxies would be needed to quantify the colour excess due to internal dust. This is beyond the scope of this work, and is a caveat in interpreting the colour differences. Nevertheless, the colours discussed further in this chapter are corrected for Galactic extinction (median $\Delta(g-i) \sim 0.1$), K-corrected (median $\Delta(g-i) \sim 0.05$) and the sample was selected having moderate inclinations only ($i \lesssim 60°$), so that the dust effects are minimised.

3.2.2 Comparison to other studies

I compare my measurements of component colours with other published studies. For example, Gadotti (2011) find median values of $(g-i)_{\rm disc} = 1.04 \pm 0.20$, $(g-i)_{\rm bar} = 1.27 \pm 0.42$, $(g-i)_{\rm bulge} = 1.26 \pm 0.39$ for the individual components of 291 barred galaxies, without correcting for Galactic dust. Selecting only galaxies with masses $M_\star > 10^{10} M_\odot$ and using colours from the fits directly (therefore not correcting for Galactic extinction), I find comparable colours for the discs and bars (in this study $(g-i)_{\rm disc} = 1.07 \pm 0.16$, $(g-i)_{\rm bar} = 1.27 \pm 0.27$), while the bulges are moderately redder ($(g-i)_{\rm bulge} = 1.35 \pm 0.22$). This discrepancy might arise because of the lower inclination of the galaxies in Gadotti (2011), making bulges less affected by dust extinction (as shown in the previous section it affects bulges by $\Delta(g-i) \sim 0.1$ from face-on to $i \lesssim 60°$) or measuring the colours within different apertures (different r_e), as discussed in Section 2.5.

There are not many other three component multi-band studies I can compare the measured colours with. Other authors have reported similar differences in colour between bulges and discs in disc+bulge decompositions. In a multi-band bulge+disc decomposition of 163 galaxies from SDSS, Vika et al. (2014) found a difference in the colours of discs and bulges of $\Delta(g-i)_{\rm b,d} \sim 0.3$ for late-type galaxies and $\Delta(g-i)_{\rm b,d} \sim 0.05$ for early-type galaxies, in agreement with this work. Furthermore, Kennedy et al. (2016) using bulge+disc decompositions on galaxies from the GAMA survey (Driver et al., 2009) also found that, regardless of morphology or overall colour, bulges are consistently redder than their corresponding discs in $(u-r)$ colours. Similar to this work, they also notice that the bulges and discs are closer in colour for galaxies that are bluer in overall colour. Investigating the $(g-i)$ colour profiles of barred galaxies in SDSS, Consolandi (2016) found a similar trend – the region within the bar radius is

redder by $\Delta(g-i) \approx 0.2$ compared to the disc region, and the difference increases with stellar mass, such that the most massive galaxies show the largest colour differences. Therefore, my findings are similar to studies using different methods, such as the difference in colour profiles.

3.3 Properties of bars

In addition to component colours, with the decomposition I measure the structural parameters of bars (sizes, axis ratios, luminosity ratios, and radial light profiles) in the large sample of barred galaxies.

3.3.1 Sizes

Because the Sérsic profiles of bars were not truncated (it is not possible to add a radius of truncation for the bar without inspecting the images a priori, as discussed in Section 2.4.3), I do not measure a bar length. However, one possible measure of bar size is the effective radius of the bar, $r_{\rm e,bar}$. This has been shown to correlate well with the bar semi-major axis as measured by MA17.

There exists a Galaxy Zoo project (Hoyle et al., 2011) where volunteers using a Google Maps interface were asked to measure the lengths and widths of strong bars in 3,150 galaxies from SDSS. The bar effective radius I measure in this work correlates with the visually measured average bar length in Hoyle et al. (2011). $r_{\rm e,bar}$ increases with stellar mass, but so does $r_{\rm e,disc}$. Therefore, to investigate how the size of the bar changes compared to the size of the galaxy, I define the bar scaled size as the ratio of the bar and disc effective radii and plot it as a function of stellar mass in Figure 3.5. For comparison, I also plot the scaled bar length from Hoyle et al. (2011). Although using a different measure, the length of the bar divided by two times the radius containing 90% of the Petrosian flux, $L/2R_{\rm Petro90}$, Hoyle et al. (2011) found a similar trend with stellar mass for the strong bars, suggesting that the fits are reliable.

The median bar scaled size of strong bars in Galaxy Zoo is $\sim 40-50\%$ of the size of the disc in both our measurements and those of Hoyle et al. (2011), with a peak at $\sim 10^{10.25}\ M_{\odot}$. This peak corresponds to the transition between disc dominated (low mass galaxies) and galaxies with obvious bulges (higher mass galaxies). The *bottom panel* of Figure 3.5 shows the scaled bar size for the sample split into disc dominated galaxies and galaxies with obvious bulges suggesting that the observed maximum bar size is due to the increasing prominence of bulges in the sample. Galaxies with obvious bulges have ∼25% longer bar scaled sizes when compared to disc dominated galaxies. At masses larger than $10^{10.25}\ M_{\odot}$, the median bar scaled size drops to 0.45.

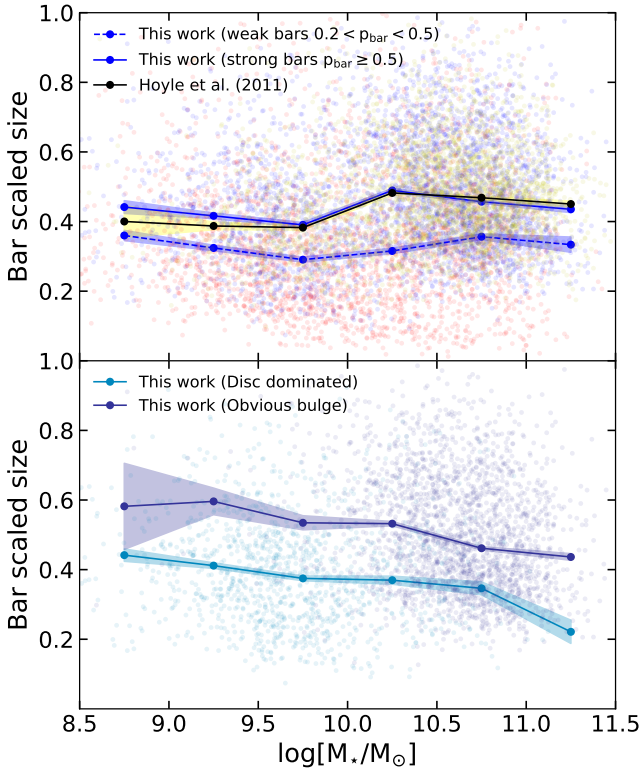

Figure 3.5: The scaled bar length, $r_{\rm e,bar}/r_{\rm e,disc}$ for weak and strong bars in this work, and $L/2r_{\rm Petro90}$ in Hoyle et al. (2011), as a function of stellar mass (*top panel*). For strong bars, the median bar size compared to galaxy size is constant at low masses and reaches a maximum of 0.5 at $M_\star \sim 10^{10.25} M_\odot$, then the scaled size declines slightly with mass. Weak bars are ~ 1.5 shorter compared to strong bars. In the *bottom panel*, the scaled bar length $r_{\rm e,bar}/r_{\rm e,disc}$ for strongly barred galaxies in this work split into DISC DOMINATED (fitted with disc+bar) and OBVIOUS BULGES (fitted with disc+bar+bulge) is shown. Galaxies with significant bulges have consistently larger bar scaled lengths. Median values in stellar mass bins of $\log(\frac{M_\star}{M_\odot}) = 0.5$ are plotted and the shaded areas represent the $1\sigma/\sqrt{N}$ error on the mean per bin.

3.3.2 Shapes

I measure bar axis ratios between 0.1 and 0.6, with a median and 1σ scatter of $b/a = 0.31 \pm 0.12$, in good agreement with the observed range of 0.2-0.4 (Kormendy & Kennicutt, 2004). This corresponds well with the measurements in other studies, although minor differences arise from different measurement methods. For example, my median axis ratio is ∼30% higher than the axis ratio found by Hoyle et al. (2011), $\langle b/a \rangle = 0.24 \pm 0.07$, but in their case the axis ratio was calculated as the ratio of the

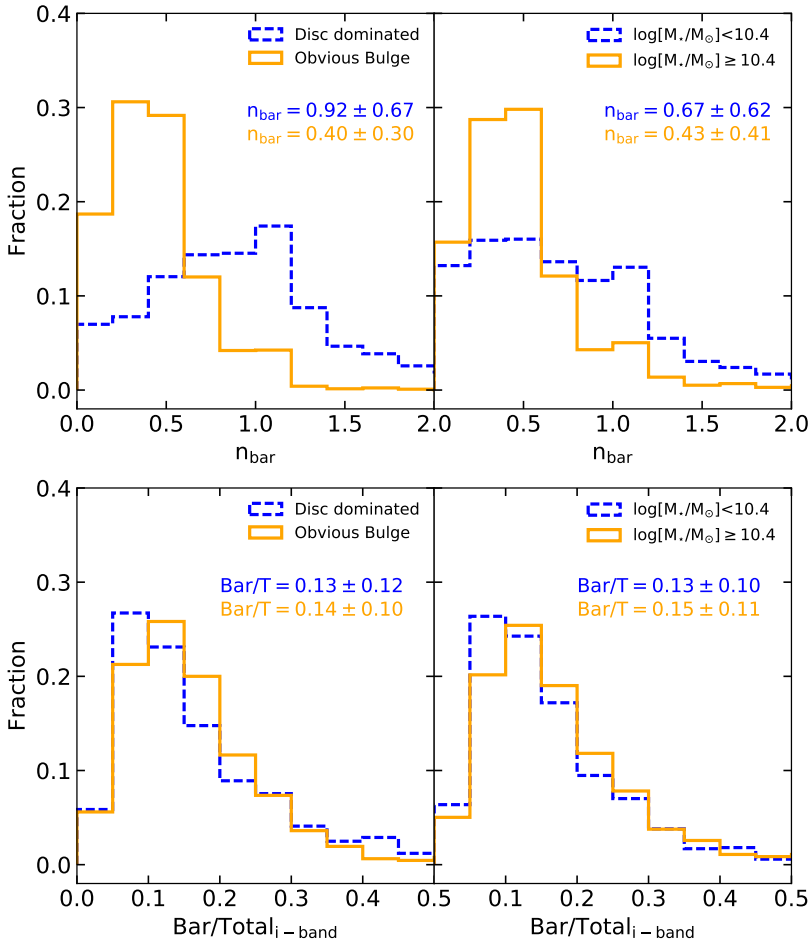

Figure 3.6: The first two figures (*top panels*) show the bar Sérsic indices split into DISC DOMINATED (modeled with disc+bar) and OBVIOUS BULGE (modeled with disc+bar+bulge) (*left*) and stellar mass bins (*right*). Low mass, disc dominated barred galaxies have bars with a broad distribution of profiles, with a large fraction of bars having exponential profiles, while high mass galaxies with prominent bulges have flatter profiles. The median Sérsic indices of the bars are represented in the plot. The bottom plots show the bar-to-total luminosity in the i-band. The bar-to-total luminosity ratio is consistent for DISC DOMINATED and OBVIOUS BULGE galaxies (*left*), as well as for low and high mass galaxies.

measured bar width to bar length. MA17 found a bar axis ratio of $\langle b/a \rangle = 0.37 \pm 0.15$ for the galaxies in the CALIFA survey. Similarly, Gadotti (2011) also found a higher axis ratio of $\langle b/a \rangle = 0.37 \pm 0.10$. These samples likely contain weak bars as well, which have been shown to have higher axis ratios (Laurikainen et al., 2004a; Díaz-García

et al., 2016) compared to the strong bars considered in my sample.

3.3.3 Bar light profiles

The bars were fitted with Sérsic profiles which were allowed to vary in the fitting process. In this section I examine their bar radial light profiles. In Figure 3.6 (*top-left panel*) I plot the Sérsic indices of the bars in the sample of strong bars, split into DISC DOMINATED (disc+bar fit) and OBVIOUS BULGE (disc+bar+bulge fit). There is a significant difference (Kolmogorov-Smirnov test $k = 0.52$, $p_{\rm KS} < 10^{-15}$) between the two samples, while a similar, but less pronounced difference (K-S test $k = 0.36$, $p_{\rm KS} < 10^{-15}$) is seen when the sample is split into low mass and high mass galaxies instead (*top-right panel*). There is a significant overlap between the DISC DOMINATED and low mass samples, and OBVIOUS BULGE and high mass, respectively.

As shown in the *top panels* of Figure 3.6, disc dominated, low mass galaxies have stellar bars with a median Sérsic index of $n_{\rm bar} = 0.92 \pm 0.67$. In contrast, high mass galaxies, many with obvious bulges, have bars with shallower, Gaussian-like, light profiles with $n_{\rm bar} = 0.40 \pm 0.30$. 80% of the galaxies with $n_{\rm bar} > 0.8$ are disc dominated, suggesting that the presence of a significant bulge is the most important discriminator in the profile of bars. Alternatively it might be possible that a faint bulge is not separable from the bar, but its presence acts to steepen the apparent bar profile. However, I find only a very weak correlation between $n_{\rm bar}$ and the measured B/T (Spearman r_s-correlation test $r_s = 0.09$, $p = 0.0001$).

3.3.4 Luminosity contribution

One important quantity that one can measure from the fits is how much each component contributes to the total light of the galaxy, and specifically the bar-to-total luminosity. In the bottom panels of Figure 3.6 I plot the Bar/T luminosity ratio of strongly barred galaxies, in the i-band. The distribution of Bar/T luminosities is consistent within all the five SDSS bands. The Bar/T ratio appears to be similar (K-S test $k = 0.07$, $p_{\rm KS} = 0.002$) for DISC DOMINATED galaxies and galaxies with OBVIOUS BULGES ($Bar/T \sim 0.14$), implying a mostly mass-independent bar growth.

As a comparison, for galaxies with $M_\star > 10^{10} M_\odot$, Gadotti (2011) found a median $Bar/T \sim 0.10$, 40% smaller than in this study, however, they truncated the bar profiles and used a boxy shape. I find a better agreement with Weinzirl et al. (2009), who used a similar decomposition method to mine, although their sample comprised of only 80 barred galaxies and the images were in the H-band.

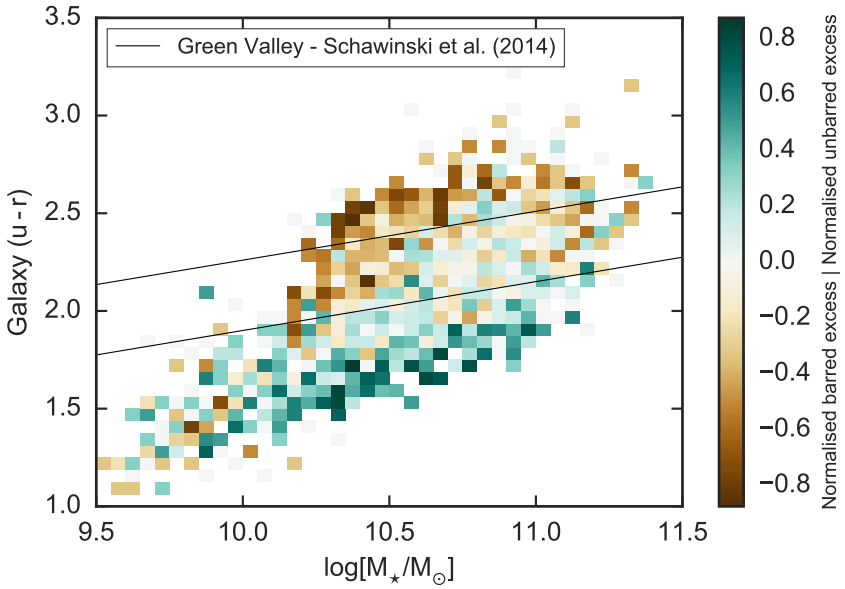

Figure 3.7: Colour-mass diagram of the mass-matched volume limited samples of BARRED and UNBARRED galaxies. Instead of overlaying the two distribution, they were subtracted and normalised by the total number of galaxies in each bin i.e. $\frac{N_{\rm unbarred}-N_{\rm barred}}{N_{\rm unbarred}+N_{\rm barred}}$. A darker red colour suggests an excess of barred galaxies, while dark blue colour an excess of unbarred ones. It is clear that the barred galaxies tend to be redder, while unbarred ones tend to be bluer, at the same stellar masses. Since the two samples were mass-matched, the main difference between them is the presence of a bar. The two lines show the definition of the 'green valley' from Schawinski et al. (2014).

3.4 Barred versus unbarred galaxies

To examine the effects bars have on their host galaxies one has to compare barred galaxies with a similar sample of galaxies without bars. For a meaningful comparison, I compare only the galaxies in the volume-limited subsamples, shown in Table 2.2. The mass-size diagram in Figure 1.5 shows how galaxy properties and morphologies change with stellar mass, size and velocity dispersion. At a fixed stellar mass, the effective radius decreases as the velocity dispersion increases. Since the velocity dispersion and determined galaxy size (r_e, from single Sérsic fits) depend on the presence of a bar, the parameter to control for is stellar mass. Therefore, to study the effects due to bars alone, I selected a mass-matched subsample of 2,435 unbarred galaxies (matched in bins of $\log\left(\frac{M_\star}{M_\odot}\right) = 0.1$ with the strongly barred galaxies).

Figure 3.7 shows the colour-mass diagram for both the mass-matched unbarred and barred galaxies (for 2,435 galaxies of each type). The plot shows a 2D binned histogram, where the numbers of unbarred and barred galaxies were subtracted in each bin and normalised by the total number of galaxies in the bin. At the same mass,

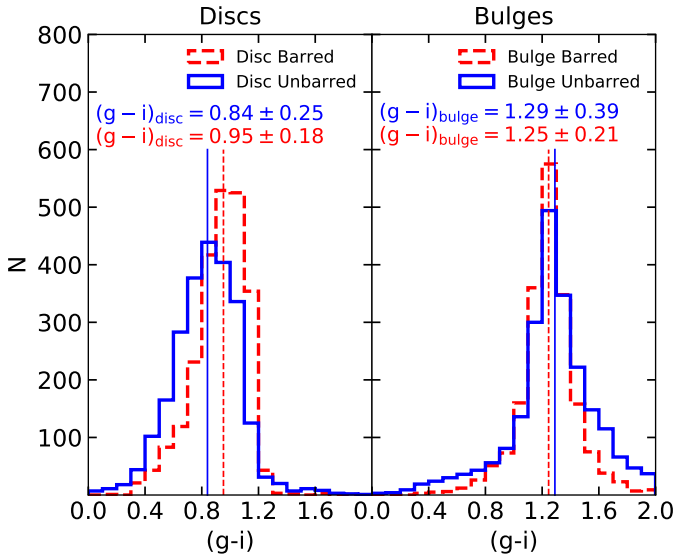

Figure 3.8: The $(g-i)$ colours of discs (*left*) and bulges (*right*) of strongly barred (with red) and mass-matched unbarred galaxies (with blue). The discs of barred galaxies are clearly redder than the ones of unbarred galaxies, while their bulges are slightly bluer compared to those of unbarred galaxies. Median values for the colours and the 1σ spread are shown.

barred galaxies (indicated by darker red colours) are more common than unbarred disc galaxies in the 'red sequence' and 'green valley' (as defined by Schawinski et al. 2014), while unbarred galaxies (indicated by darker blue colours) are more common in the 'blue cloud'.

3.4.1 Bulge and disc colours

I compare the colours of the same components (discs and bulges) of strongly barred and unbarred galaxies. As shown in Figure 3.8 (*right*), the discs of barred galaxies are clearly redder compared to the unbarred galaxies by $\Delta(g-i)_{\rm disc} \sim 0.11 \pm 0.01$ (the error is the standard error on the mean, in quadrature). This is consistent with the results of Masters et al. (2011) that barred galaxies are overall redder compared to unbarred galaxies, since the disc dominates the light from these galaxies. In contrast, the colours of bulges of barred galaxies are only moderately different to their unbarred equivalents ($\Delta(g-i)_{\rm bulge} \sim 0.04 \pm 0.01$). The colour differences are similar when comparing only barred and unbarred galaxies with obvious bulges.

The observed difference in disc colours of strongly barred galaxies is in disagreement with the study of Sánchez-Janssen & Gadotti (2013) who found the discs in barred and unbarred galaxies are closer in colour, in the sample of G09. The modes of their colour distributions actually suggest that barred discs are bluer than

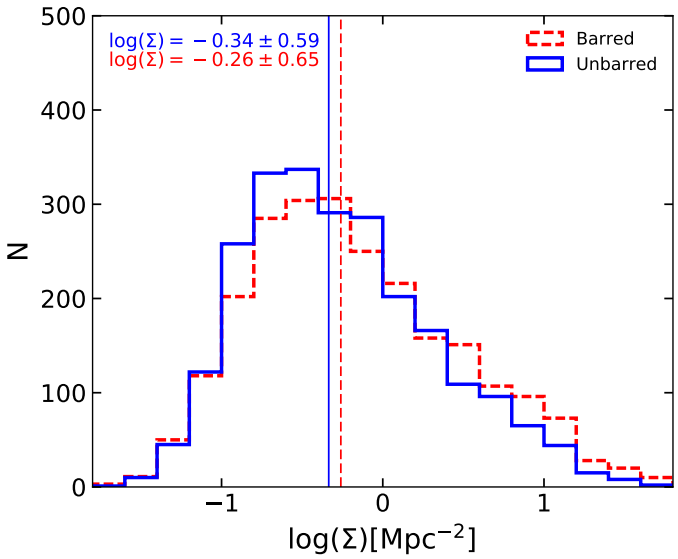

Figure 3.9: The local density of barred and mass-matched unbarred sample of galaxies, from Baldry et al. (2006). Median values for the density and the 1σ spread are shown.

their unbarred counterparts, but they also find that discs with the bluest colours $(g-i)_{\rm disc} < 0.8$ are mostly unbarred. The main difference between this work and Sánchez-Janssen & Gadotti (2013) is a significant number of unbarred galaxies in their sample having $(g-i)_{\rm disc} \sim 1.25$ (value not corrected for Galactic dust), which is not present in this sample. Investigating the differences I find that a high fraction of the unbarred galaxies (53%) in Sánchez-Janssen & Gadotti (2013) have debiased likelihoods $p_{\rm smooth} \geq 0.5$ in Galaxy Zoo, and thus were classified as 'smooth' (elliptical galaxies) rather than 'discs'; thus, they are not part of my unbarred sample.

3.4.2 Environment

As discussed in the Introduction, the environment can play an important role in quenching galaxies, through ram pressure stripping (Abadi et al., 1998), strangulation (Peng et al., 2015) or harassment (Bialas et al., 2015). To test whether the quenching observed in the barred galaxies is due to bars and not because of the environment, I compare the local environment of galaxies with and without bars. One way of quantifying the local environment of galaxies is calculating the projected neighbour density, defined as $\Sigma_N = N/\pi d_N^2$, where d_N is the distance to the $N^{\rm th}$ nearest neighbour (Baldry et al., 2006). This measure quantifies the local density of the galaxies' environment (Muldrew et al., 2012). I use the local densities from Baldry et al. (2006) for SDSS DR7 galaxies, calculated as an average between the projected distance to the nearest $N = 4^{\rm th}$ and $N = 5^{\rm th}$ neighbours that are within

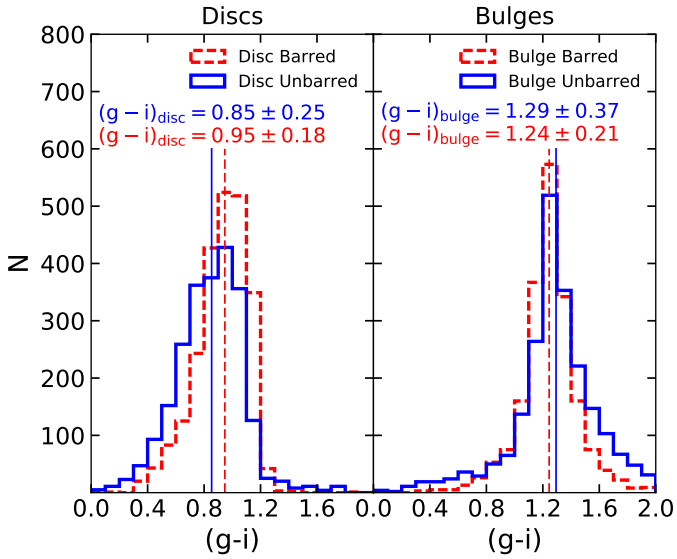

Figure 3.10: The $(g-i)$ colours of discs (*left*) and bulges (*right*) of strongly barred (with red) and unbarred (with blue) mass- and environment-matched galaxies. Median values for the colours and the 1σ spread are shown.

1000 km s^{-1}. The local density of the barred and mass-matched unbarred samples are shown in Figure 3.9. The barred galaxies live in slightly denser environments (median $\log\Sigma = -0.26 \pm 0.65$), compared to unbarred galaxies ($\log\Sigma = -0.34 \pm 0.59$), and the two distributions are slightly different (K-S test $k = 0.07$, $p_{\rm KS} = 6 \times 10^{-6}$). 384 of 2,435 (16%) barred galaxies are in the field, compared to 436 unbarred galaxies (18%), where the field (isolated) galaxies are defined as the least dense environments ($\log\Sigma < -0.8$, Baldry et al. 2006).

To assess whether the environment is driving the difference in the observed colour between the discs of barred and unbarred galaxies, I also match the two samples in environment (in bins of $\log\Sigma = 0.2$), by selecting a sample (with replacement) of unbarred galaxies that matches the environment distribution of barred galaxies shown in Figure 3.9. The distribution of disc and bulge colours for the two samples, now matched in mass and environment is shown in Figure 3.10. Matching in environment does not change the distribution of colours of the discs and bulges significantly (compare to Figure 3.8). Thus, the difference in the disc colour is mainly driven by the different morphology of galaxies (the presence of a strong bar) and not due to mass or local environment.

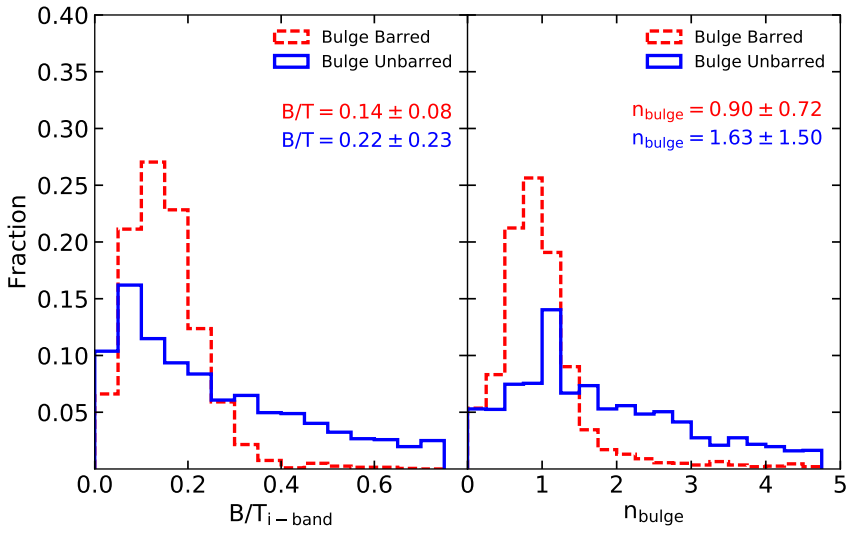

Figure 3.11: *Left*: The i-band B/T ratio for barred and unbarred galaxies. *Right*: The bulge Sérsic indices of galaxies with and without bars. The two distributions for barred and unbarred galaxies are clearly different. The bulges of barred galaxies have low Sérsic indices (exponential on average, typical of pseudobulges), while unbarred galaxies have a large spread of bulge Sérsic indices, with a higher fraction of classical bulges. The median and 1σ scatter for each distribution are given in the plot.

3.4.3 Properties of bulges

In the volume-limited subsamples, I fitted bulges to 2,040 barred galaxies and 2,435 unbarred galaxies. 92% of the bulges in barred galaxies and 99% of the bulges in unbarred ones have effective radii larger than 80% of the half width at half maximum of the PSF, which was shown by Gadotti (2008) to be a limit to properly resolve and fit bulges.

First, I look at the contribution of the bulges to the total light of the galaxies, the bulge-to-total luminosity ratios (B/T). The left-panel of Figure 3.11 shows the distribution of the i-band B/T for the barred and unbarred galaxies. The B/T increases slightly with wavelengths from the u-band to the z-band, which is expected if bulges host an older population of stars. The median B/T for the barred galaxies is 0.14 (83% barred galaxies have $B/T \leq 0.2$), while it is significantly higher for the unbarred galaxies ($B/T = 0.22$). The B/T for barred galaxies is in good agreement with other studies with smaller samples (e.g. Laurikainen et al. 2007; Weinzirl et al. 2009). The higher B/T in unbarred galaxies is, in some cases, due to a another component present in the proximity of the bulges, a 'lens' or 'oval', which was also fit by the bulge model component. I discuss this in more detail in the Section 3.5.

To check the scaling relation for the bulges, I plot the bulge effective radii, r_e, and

Sérsic indices, $n_{\rm bulge}$ against the bulge stellar mass in Figure 3.12, for both barred and unbarred galaxies. To estimate a stellar mass for each component, I used Equation (8) in Taylor et al. (2011) to convert from $(g-i)$ colours and M_i, i-band absolute magnitude

$$\log(\frac{M_\star}{M_\odot}) = 1.15 + 0.70(g-i) - 0.4M_i. \tag{3.2}$$

For both samples the measured bulge parameters are correlated with the bulge mass. This is expected since more massive bulges should be physically bigger (see e.g. Fisher & Drory 2010). Recovering the scaling relations also shows that the decompositions are reliable, however, the bulge sizes and Sérsic indices for the two samples are clearly different, some of this trend being due to the inner lenses in the unbarred sample.

The bulges should be nearly circular features when viewed face-on. I measure median axis ratios of $(b/a)_{\rm bulge} = 0.77$ for barred galaxies and $(b/a)_{\rm bulge} = 0.68$ for the unbarred galaxies. Deprojecting using the median inclination of the sample ($i \approx 40°$), the typical axis ratios for the bulges are 1.0 and 0.9, in good agreement with being circular.

The Sérsic index can be used as an indication of the nature and formation of the bulges. Low bulge Sérsic indices ($n_{\rm bulge} \sim 1$) indicate pseudobulges, believed to be formed by secular processes, while high bulge Sérsic indices ($n_{\rm bulge} \sim 4$) indicate 'elliptical-like' classical bulges, believed to be built by mergers (Kormendy & Kennicutt, 2004). The right panel of Figure 3.11 shows that $n_{\rm bulge}$ varies between 0.1 and 4, with a median of $n_{\rm bulge} = 0.90$ for the barred galaxies and $n_{\rm bulge} = 1.63$ for unbarred galaxies. Due to image co-addition, the bulge Sérsic indices are underestimated by ∼30%, as discussed in Section 2.4.8.2. Correcting for this, the median values are $n_{\rm bulge,\ barred} \sim 1.2$ and $n_{\rm bulge,\ unbarred} \sim 2.1$, suggesting a higher proportion of classical bulges in unbarred galaxies.

The low bulge Sérsic indices in the barred sample suggest that the bulges in these galaxies are overwhelmingly pseudobulges, in contrast to classical bulges, which appear to be rare. The distinction between the two types of bulges is not clear, but authors generally agree that bulges with $n \leq 2$ are pseudobulges and with $n > 2$ are classical bulges (Fisher & Drory, 2008). Some authors (e.g. Graham & Worley 2008 and Graham 2016) argue that there is no bimodality in the bulge Sérsic index, and thus one cannot reliably separate between classical bulges and pseudobulges using the Sérsic index alone. However, for the purpose of comparing the two, as well as to compare our results with the literature, I make use of this division. In this work only 10% of barred galaxies have classical bulges, while 90% have pseudobulges. In

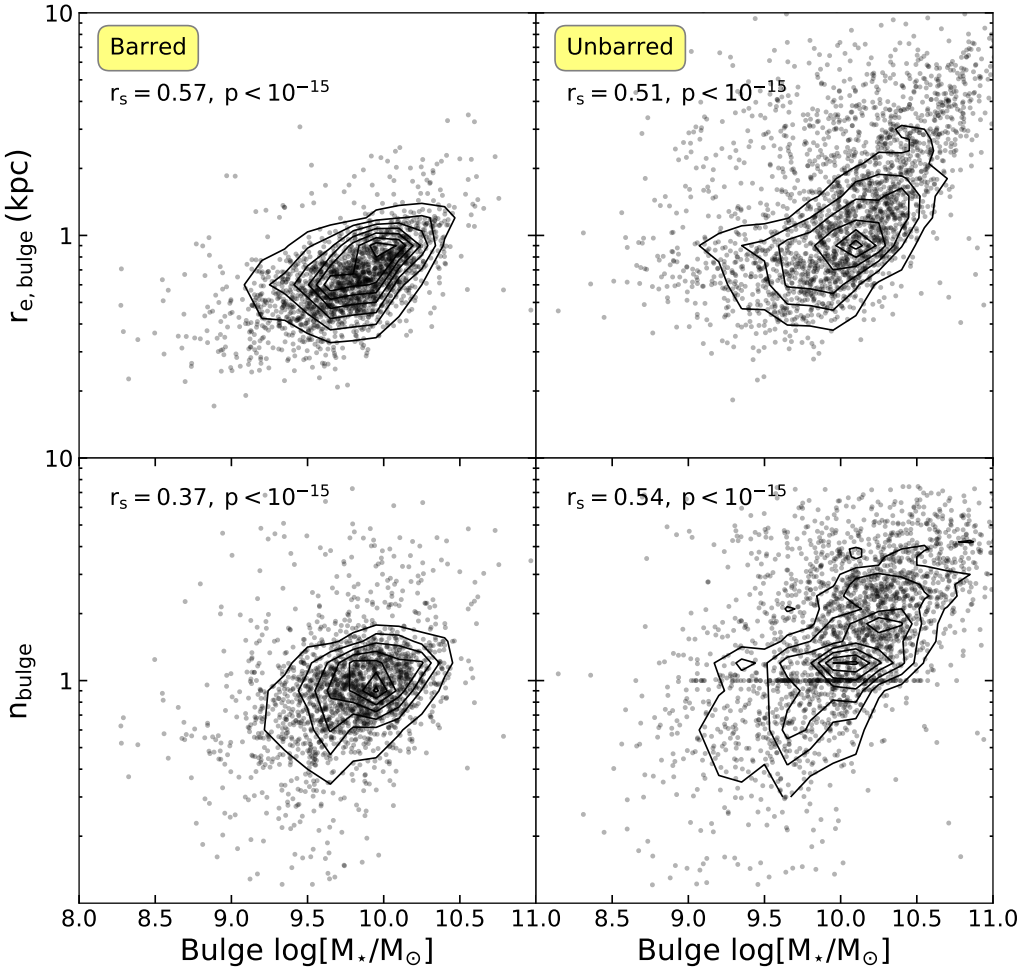

Figure 3.12: The mass-size and mass-n scaling relations for the bulges of both barred and unbarred galaxies. Although the bulge parameters for the two samples are different, they clearly increase with the bulge mass for both samples. The higher concentration of $n_{\rm bulge} = 1$ for the unbarred galaxies is due to some of the discs (fitted with a fixed $n = 1$ profile) and bulges (fitted with a free Sérsic index) interchanging in the fitting procedure. The components were identified as discs and bulges, respectively, by comparing the r_e of the components. The Spearman r_s-correlation coefficient is shown.

contrast, 40% of unbarred disc galaxies have classical bulges and 60% pseudobulges. The higher fraction of pseudobulges in barred galaxies shows a clear evidence of bars building disc-like bulges at the centre of galaxies. Nevertheless, the significant fraction of unbarred galaxies with pseudobulges suggests that gas inflow through bars is not the only mechanism in building disc-like bulges.

3.4.4 Comparison with other works

My measurements of the bulge Sérsic index are consistent with other studies. For example, Laurikainen et al. (2004b) find a typical Sérsic index of $n_{\rm bulge} = 1.4$ (74% pseudobulges, 26% classical bulges) in barred galaxies. Similarly, Weinzirl et al. (2009) found that the majority (65%) of the barred galaxies in their study had $n_{\rm bulge} \leq 2$ and mean $n_{\rm bulge} \sim 1.3$ across all Hubble types, similar to my median measurements. Furthemore, the median $n_{\rm bulge}$ for the nearby and well resolved barred galaxies in the CALIFA survey is 1.6 (MA17) (66% pseudobulges, 34% classical bulges). Finally, the median $n_{\rm bulge}$ for barred galaxies in the decomposition of a large sample of galaxies (Salo et al., 2015) from the S^{4}G survey is also 1.6 (63% pseudobulges, 37% classical bulges).

The median measured bulge Sérsic index differs significantly from the median found in G09 ($n_{\rm bulge} = 2.5$) for barred systems (39% pseudobulges, 61% classical bulges, according to the threshold by Fisher & Drory 2008[1], as shown for individual galaxies in Section 2.5. Additionally, Kim et al. (2015) also find a median of $n_{\rm bulge} = 2.1$ (37% pseudobulges, 63% classical bulges) in the decomposition of 144 barred galaxies from the S^{4}G survey. For the same galaxies, and with the same data, Salo et al. (2015) finds a lower median of $n_{\rm bulge} = 1.4$. The main difference between the two decompositions is the code used, BUDDA (in Kim et al. 2015) and GALFIT (in Salo et al. 2015). Furthermore, they used slightly different fitting procedures: Sérsic versus Ferrers bar profiles, boxy versus ellipse bar shapes, disc breaks versus single exponential disc profiles. The systematic differences between studies is probably due to a combination of using different fitting codes, different profiles and shapes for bars and including disc breaks. Comparing different softwares used for decompositions is beyond the scope of this work, however, it is a topic worth investigating in the future.

[1]G09 uses the Kormendy relationship to separate pseudobulges from classical bulges. For this work, I chose to use the simple cut of $n_{\rm bulge} \sim 2$ by Fisher & Drory (2008) to be consistent in our comparison with other studies.

3.5 Unbarred galaxies with inner lenses/ovals

While inspecting the images and the fits of unbarred galaxies with higher B/T and $n_{\rm bulge}$, I noticed a significant number of galaxies with inner lenses/ovals (or 'plateaus'), almost circular components with a shallow light profile (Buta et al., 2007) around the bulge. Lenses are frequently observed in S0 galaxies and in early-type spirals (Laurikainen et al., 2005, 2007, 2009). For example, in the Near-Infrared S0 Survey (NIRS0S), Laurikainen et al. (2011) found that 61% of the barred and 38% of the unbarred S0 galaxies host lenses. Ovals are observed in late-type galaxies and they look similar to lenses in early-types, however there is no clear evidence whether or not they are physically similar (Kormendy & Kennicutt, 2004).

Similar to the effect of not accounting for bars in disc+bulge decompositions, not accounting for the inner lenses/ovals can increase $n_{\rm bulge}$ and B/T ratio. Therefore, one should account for these components in the decompositions. Unfortunately, the Galaxy Zoo project did not ask the volunteers a question about the presence of 'inner lenses'. However, it did enquire about the presence of 'rings' in a galaxy. Nair & Abraham (2010a) noticed a correlation between rings and lenses; inner lenses are most easily and often identified when they have are accompanied by a ring. Recently, Buta (2017) also noticed that there are many inner lenses in a sample identified with outer rings in GZ2 (selected with the question *Is the odd feature a ring?*). 41.2% of the 3962 ringed galaxies identified in Galaxy Zoo 2 by Buta (2017) have inner lenses.

Therefore, the goal of this section is to compare the properties of barred, unbarred and galaxies with inner lenses. In order to select unbarred subsamples with and without inner lenses I make use of the ring question in Galaxy Zoo. Without a non-axisymmetric structure in unbarred galaxies (a lens or an oval) it is difficult to explain the presence of a ring, believed to be formed at resonances (with the exception of a collisional ring). Willett et al. (2013) discusses the ring classification in comparison with the expert classification of rings in Nair & Abraham (2010a) and suggests that rings can be reliably identified by requiring a threshold of $p_{\rm ring} \geq 0.5$. A caveat is that, because I used the ring question in Galaxy Zoo to identify lenses, I cannot fully distinguish between small inner rings and lenses. They tend to occupy similar locations in a galaxy and might be related, often a ring being a subtle enhancement at the edge of a lens, while the resolution of SDSS images makes it difficult sometimes to distinguish between the two (Buta, 2017). I cannot fully exclude the presence of a weak bar inside the inner lenses, either.

From the volume-limited unbarred sample, I identified a subsample of ringed galaxies with $p_{\rm ring} \geq 0.5$. After fitting these galaxies with disc+lens+bulge models, I

inspected and selected 394 unbarred galaxies with lenses, with physically meaningful fits (without an additional central components identified in the residuals). Compared to the disc+bulge models for these galaxies, adding a third component decreases $n_{\rm bulge}$, $r_{\rm e,bulge}$ and B/T by factors of $\sim$1.4, 1.5 and 1.8, respectively. Figure 3.13 shows four examples of galaxies with inner lenses, disc+lens+bulge fits and residuals and, for comparison, I also show the less adequate disc+bulge fits and corresponding residuals for the same galaxies. I also identified a clean subsample of unbarred galaxies with obvious bulges, but without inner lenses, by selecting only galaxies with $p_{\rm ring} = 0$, resulting in a sample of 447 unbarred galaxies with meaningful disc+bulge fits.

I compare the properties of barred galaxies (fitted with disc+bar+bulge), unbarred galaxies (fitted with disc+bulge) and unbarred galaxies with inner lenses (fitted with disc+lens+bulge). All three samples were selected to have obvious bulges as classified by Galaxy Zoo users, so that a bulge is significantly bright and included in the fit in all cases. Ideally, one would compare the properties of mass-matched samples, but due to the small sample sizes and the different mass distributions, this was not possible. I present the median values and 1σ standard deviations of the colours, Sérsic indices, axis ratios, luminosity ratios and scaled effective radii of the three components in Table 3.3.

The colours of the discs and bulges of barred galaxies and galaxies with lenses are very similar, while there is a clear difference compared to unbarred galaxies. Furthermore, galaxies with inner lenses show properties such as total stellar mass, Sérsic indices and luminosity ratios of the components that are, in general, similar to barred galaxies with obvious bulges. One small difference between the unbarred galaxies with lenses and barred galaxies is that lenses are, on average, slightly bluer than the bars, although this might be due to the presence of rings at the edge of lenses, which are usually characterized by recent star formation (Buta et al., 2007). Also, lenses are $\sim$ 40% shorter than the strong bars, in terms of their sizes normalized to the effective radius of the discs, and rounder, with an axis ratio of $\sim$ 0.67 compared to the median axis ratio of $\sim$ 0.35 of the bars. However, the median size of lenses better matches the sizes of weak bars ($r/r_{\rm e,disc} \sim 0.3$) at the median stellar mass of the unbarred galaxies with lenses, $\log(M_\star/M_\odot) = 10.7$ (see Figure 3.5), suggesting that inner lenses might be related to weak bars instead.

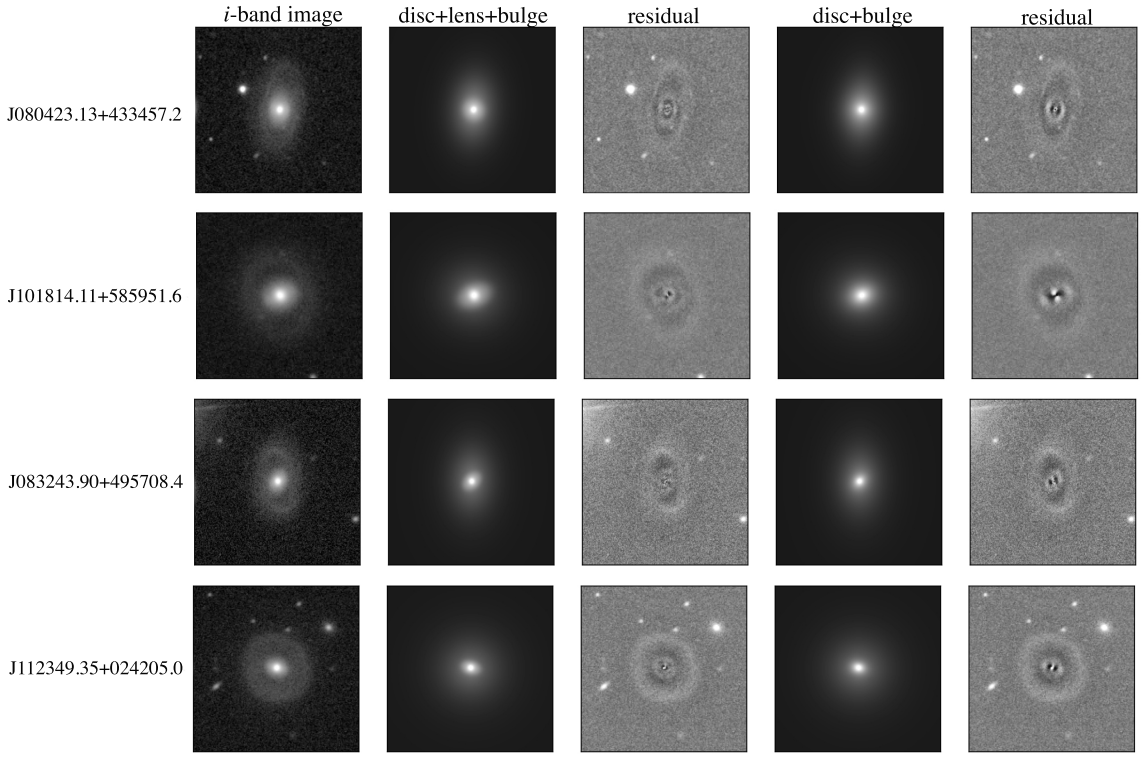

Figure 3.13: Examples of four galaxies with inner lenses which were initially part of the unbarred sample. The image on the left is the i-band SDSS image, the second and third columns are the disc+lens+bulge model and residual, while the fourth and fifth columns are the disc+bulge model and the corresponding residuals. The disc+lens+bulge models are a better representation for the light distribution of these galaxies than the simple disc+bulge models. The properties of galaxies with inner lenses are more similar to those of barred galaxies. Galaxies with inner lenses were identified using the Galaxy Zoo answers to the 'ring' question, therefore all the fitted galaxies with inner lenses show an outer ring feature in the residuals.

Parameter	bulge+disc	+lens	+bar
N_{gal}	447	394	1699
$\log(M_\star/M_\odot)$	10.42 ± 1.46	10.70 ± 1.34	10.67 ± 1.19
$(u-r)$ disc	1.65 ± 0.39	2.14 ± 0.29	2.14 ± 0.32
$(u-r)$ bar/lens	-	2.38 ± 0.52	2.55 ± 0.65
$(u-r)$ bulge	2.69 ± 1.32	2.70 ± 0.36	2.64 ± 0.48
$(g-i)$ disc	0.74 ± 0.23	1.01 ± 0.14	1.00 ± 0.14
$(g-i)$ bar/lens	-	1.11 ± 0.24	1.16 ± 0.22
$(g-i)$ bulge	1.33 ± 0.44	1.26 ± 0.17	1.24 ± 0.19
$(r-z)$ disc	0.45 ± 0.15	0.56 ± 0.09	0.57 ± 0.09
$(r-z)$ bar/lens	-	0.67 ± 0.15	0.69 ± 0.12
$(r-z)$ bulge	0.74 ± 0.19	0.72 ± 0.13	0.71 ± 0.12
Discs			
$\log(M_\star/M_\odot)$	10.07 ± 0.39	10.22 ± 0.31	10.20 ± 0.65
n	1	1	1
b/a	0.73 ± 0.16	0.71 ± 0.18	0.80 ± 0.13
$D/T_{\mathrm{i-band}}$	0.82 ± 0.18	0.58 ± 0.16	0.67 ± 0.14
r_e (kpc)	6.06 ± 2.27	7.93 ± 3.67	6.80 ± 2.87
Bar/Lens			
$\log(M_\star/M_\odot)$	-	9.88 ± 1.13	9.78 ± 0.55
n	-	0.37 ± 0.32	0.42 ± 0.26
b/a	-	0.67 ± 0.15	0.35 ± 0.11
$Bar/T_{\mathrm{i-band}}$	-	0.19 ± 0.15	0.15 ± 0.10
$r_e/r_{\mathrm{e,disc}}$	-	0.31 ± 0.12	0.46 ± 0.16
Bulge			
$\log(M_\star/M_\odot)$	9.92 ± 0.62	9.98 ± 0.47	9.83 ± 0.38
n	1.28 ± 1.23	1.00 ± 1.07	0.92 ± 0.64
b/a	0.69 ± 0.15	0.77 ± 0.14	0.78 ± 0.13
$B/T_{\mathrm{i-band}}$	0.18 ± 0.18	0.20 ± 0.09	0.15 ± 0.08
$r_e/r_{\mathrm{e,disc}}$	0.17 ± 0.11	0.08 ± 0.04	0.08 ± 0.04

Table 3.3: Median parameters and 1σ standard deviation for the fitted unbarred galaxies, unbarred galaxies with inner lenses and barred galaxies. All galaxies were selected from a volume-limited sample, based on the volunteers' classifications for the presence of bars, rings and having an obvious bulge. The total stellar masses are drawn from average values in the MPA-JHU catalogue (Kauffmann et al., 2003a), while the stellar masses of the components were calculated from the optical colours, based on Equation (8) in Taylor et al. (2011).

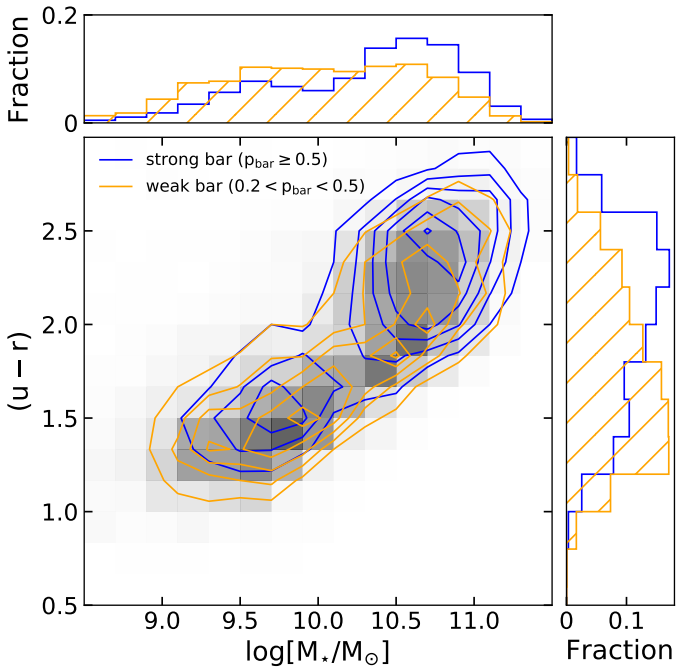

Figure 3.14: Colour-mass diagram for the weakly and strongly barred galaxies. The histograms show the normalised distributions of the stellar mass and $(u-r)$ colours for the strongly and weakly barred galaxies.

3.6 Weak bars

The work presented so far concerns galaxies with strong bars only, selected with $p_{\rm bar} \geq 0.5$ and unbarred galaxies selected with $p_{\rm bar} \leq 0.2$. As discussed in Sections 1.4.4 and 2.3.2, galaxies with intermediate bar classifications ($0.2 < p_{\rm bar} < 0.5$) correspond to weak bars when compared to expert classifications (based on their size relative to the disc and their prominence). In this section I explore the possible bias introduced by not including weakly barred galaxies in the sample. I used the successfully fitted sample of 2,617 weakly barred galaxies, 1,726 fitted with disc+bar and 891 fitted with disc+bar+bulge, as shown in Table 2.2.

Figure 3.14 shows the colour-mass diagram of strong and weak bars. When compared to galaxies with strong bars, galaxies with weak bars tend to have lower masses and are bluer in colour. Figure 3.15 shows the colours of the components of galaxies with weak bars. The discs of galaxies with weak bars have bluer colours compared to the discs of strongly barred galaxies ($(g-i)_{\rm disc} = 0.69$ versus $(g-i)_{\rm disc} = 0.90$), which reflects the overall bluer colours of these galaxies, while the bars and bulges have more similar red colours ($(g-i)_{\rm bar} = 1.04$ compared to $(g-i)_{\rm bar} = 1.10$ and $(g-i)_{\rm bulge} = 1.24$ compared to $(g-i)_{\rm bulge} = 1.23$, respectively). There is also a

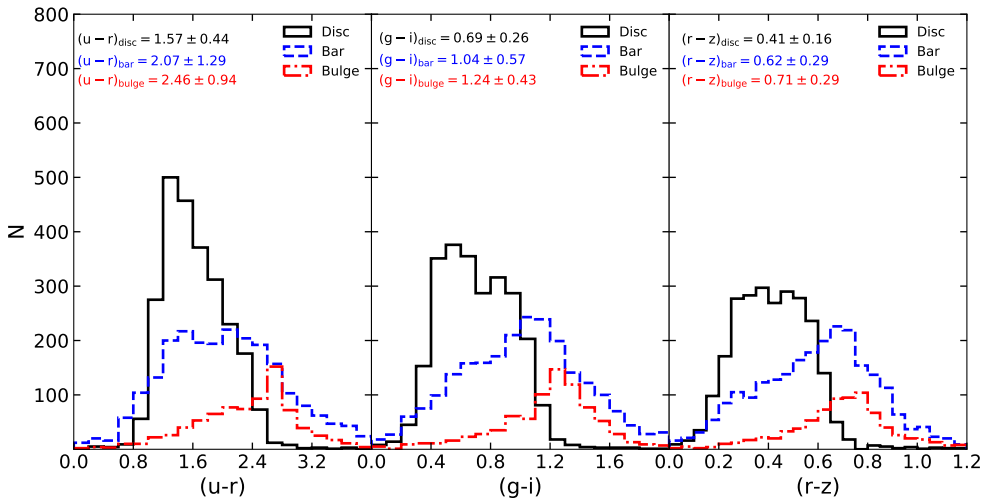

Figure 3.15: The $(u-r)$, $(g-i)$ and $(r-z)$ colours of the different galaxy components for all the fitted galaxies with weak bars (2,617 galaxies). This sample contains all the successfully fitted galaxies with weak bars and is not volume-limited. Similarly to galaxies with strong bars, the discs are bluer than the bars, which in turn are slightly bluer than the bulges. The median colours and their corresponding 1σ spreads are shown for each component.

significantly larger spread, an indication of a more diverse population of galaxies.

To compare weakly barred galaxies to unbarred galaxies, I select a volume-limited sample of galaxies with weak bars ($M_{\rm r} < -20.15$) and a new volume-limited and mass-matched subsample of unbarred galaxies (with 1,580 galaxies in each sample), shown in Table 2.2. In Figure 3.16 it can be noticed that the disc $(g-i)$ colours of galaxies with weak bars, even though they are on average bluer than the galaxies with strong bars, are still $\Delta(g-i) \sim 0.06 \pm 0.01$ redder compared to the discs of unbarred galaxies. Similarly, the bulges of weakly barred galaxies are $\Delta(g-i) \sim 0.06 \pm 0.01$ bluer compared to the unbarred counterparts, similar to the trends observed for strongly barred galaxies.

Apart from the bluer colours of the discs, as well as their lower masses in general, galaxies with weak bars show a similar bimodality in the bar Sérsic indices as galaxies with strong bars ($\langle n_{\rm bar} \rangle \sim 0.5$ for more massive galaxies, with $M_\star \geq 10^{10.4} M_\odot$ and obvious bulges, and $\langle n_{\rm bar} \rangle \sim 1$ for the disc dominated lower mass galaxies, with $M_\star < 10^{10.4} M_\odot$). The median Bar/T is only marginally lower, at $Bar/T \sim 0.10$. Figure 3.5 shows the difference in the scaled bar sizes (*top panel*) between strong and weak bars as well as the projected physical sizes of the bars (*bottom panel*). Weak bars are on average ~ 1.5 times shorter than strong bars in our sample, the largest difference being observed at $M_\star \sim 10^{10.25} M_\odot$, in both relative and absolute sizes,

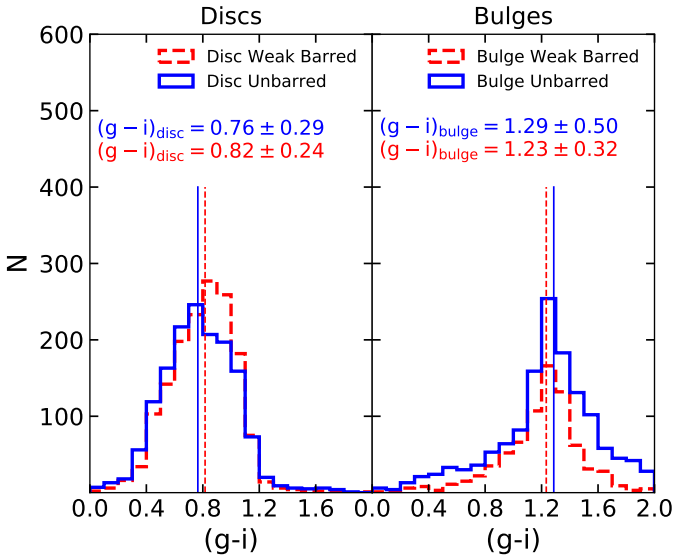

Figure 3.16: The $(g-i)$ colours of discs (*left*) and bulges (*right*) of weakly barred (with red) and unbarred (with blue) galaxies. The two samples are volume-limited and mass-matched. The discs of weakly barred galaxies are slightly redder than the ones of unbarred galaxies, while their bulges have bluer colours when compared to the bulges of unbarred galaxies. Median values for the colours and the 1σ spread are shown.

suggesting quantitatively that weak bars identified in Galaxy Zoo are indeed shorter and less prominent compared to strong bars.

3.7 Discussion

To summarise, in this Chapter I have found that the bulges of barred galaxies are predominantly pseudobulges, with a typical Sérsic index of $n_{\rm bulge} \sim 1$. I have found two types of bar Sérsic profiles: bars in low mass disc dominated galaxies have approximately exponential profiles ($n_{\rm bar} \sim 0.9$), while bars in higher mass galaxies with obvious bulges have flatter profiles ($n_{\rm bar} \sim 0.4$). With the multi-band fitting I have measured the colours of the individual components and found that the bars and bulges of barred galaxies are redder compared to the galaxy discs by $\Delta(g-i) \sim 0.2$ and $\Delta(g-i) \sim 0.3$, respectively. Furthermore, when comparing to a mass- and environment-matched sample of galaxies without bars, the discs of barred galaxies are redder by $\Delta(g-i) \sim 0.1$ than the corresponding discs, while their bulges are slightly bluer by $\Delta(g-i) \sim 0.04$ than the corresponding bulges of unbarred galaxies. Finally, I have found a subsample of galaxies with inner lenses/ovals within the unbarred sample of galaxies that have similar structural properties to barred galaxies. In this Section I discuss these findings in the context of evolution of disc galaxies

driven by bars.

3.7.1 Can bars drive the quenching of star formation in discs galaxies?

The result that the bulges and bars are redder compared to the galactic discs, across almost all stellar masses is consistent with simulations of *bar quenching* and observations of star formation ceasing from inside-out (Cheung et al., 2013; Tacchella et al., 2015). As discussed in the Introduction (Section 1.3.3), recent simulations (Fanali et al., 2015; Spinoso et al., 2017; Khoperskov et al., 2018) show that strong bars exert torques on the gas and are efficient in driving gas inflows, from within the bar corotation radius to the centre, where it is consumed in star formation, while the central region is gas depleted. Observations might identify the bar at a stage when the central regions is already quenched. Therefore, it is plausible that the star formation is suppressed in the disc region within the bar corotation radius, yielding the observed redder colours of bars and bulges. This is also supported by the work of Gavazzi et al. (2015) who found that strong bars contribute significantly to the red colors observed in the inner parts of massive galaxies. Evidence for inside-out quenching has been supplied recently by spatially resolved data from the MaNGA survey, showing a significant decrease in the central sSFR (Belfiore et al., 2018). This decrease correlates with the mass of the galaxies, such that most massive galaxies have the sSFR suppressed strongest in the cores, and Spindler et al. (2018) suggest that this is caused by morphological quenching, via bars or bulges. One caveat, though, is the presence of internal dust, which might be present in different amounts and distributed differently in bulges and bars, compared to the discs, as discussed in Section 3.2.1. Internal dust can have the effect of reddening the central region of the galaxy more compared to the discs, which can explain a redder observed colour for the discs and bulges. Nevertheless, spectroscopic observations of older stellar populations and decreased star formation in the inner region of disc galaxies (e.g. Belfiore et al. 2018; Spindler et al. 2018, etc.) suggests that the observed redder colours of bars and bulges cannot be due to internal dust alone.

One of my key findings is that the discs of barred galaxies are clearly redder compared to their unbarred counterparts, even if the two samples are matched in mass and environment. Therefore, bars either have a role in quenching the galaxies, or bar formation is suppressed in highly star forming discs. Masters et al. (2012) found that strong bars reside mainly in gas-poor discs, also consistent with the scenario in which the presence of gas makes the disc resilient to bar instabilities. Simulations by Athanassoula et al. (2013) show that large-scale bars form later in gas-rich discs

than in gas-poor ones, suggesting that bars are in place in red discs earlier than in blue spirals. This possibility can be tested by investigating the properties of barred galaxies (component colours, bar length, etc.) in higher redshift galaxies, which will be a topic for future work as discussed in Section 7.2.5.

Another possibility for the observed redder colours of barred galaxies compared to mass-matched unbarred galaxies, is that barred galaxies reside in denser environments, which is known to be effective in quenching galaxies (Smethurst et al., 2017). Skibba et al. (2012) noticed an environmental dependence of barred galaxies, such that they tend to be found in denser environments compared to unbarred galaxies. Here I also find a small preference for barred galaxies to reside in denser environments compared to galaxies of similar mass, but without bars. Smethurst et al. (2017) also found an increasing bar fraction towards the central regions in galaxy groups which coincides with an increase of the time since the galaxies were quenched. Further complication arises because bars may be triggered in interactions in denser environments (Noguchi, 1988; Moore et al., 1996; Peschken & Łokas, 2018). The process of 'strangulation' in dense environments - in which gas from the discs is stripped, removing fuel for future star formation - also contributes to galaxies growing bars (Berentzen et al., 2007). It is difficult to establish what fraction of the quenching is driven by morphology or environment since these two processes are not independent of each other, as suggested by Smethurst et al. (2017). Nevertheless, even when matching the barred and (the already mass-matched) unbarred galaxies in the density of the local environment there is a difference in the colours of galaxy discs and bulges, suggesting that the main driven for the quenching is the presence of a bar, not the environment.

Another possible reason for observing redder discs in barred galaxies is a higher dust obscured star formation compared to unbarred galaxies. Hart et al. (2017) found that two-armed spirals have an additional $\sim$ 10% obscured star formation compared to many-armed spirals, while 50% of the two-armed spirals host strong bars, compared to only 20% of the many-armed spirals. Therefore, the discs of both types of galaxies might have the same SFR, but the dust obscuration is different. However, it is improbable that the small difference in dust obscured star formation rate can account for all the observed difference in the colours of the discs.

One interesting implication for the difference in colours between the discs of barred and unbarred galaxies is whether the discs are uniform in colour, or if colour gradients are present within the discs. The galaxy discs in this work were modeled with an exponential profile, and the effective radii were fixed with wavelength, in order to measure colours consistently between the different SDSS bands. Furthermore, the measured colours are based on the integrated magnitudes of the components, thus it is

not possible to measure colour gradients within components from the decompositions in this work. In reality, colour gradients across the galaxy discs might be present. For example, galaxies with strong bars show a 'darker' region, perpendicular to the bar, within the bar corotation radius. James et al. (2009) has shown that this inner disc region swept up by the bar, referred to as the 'star forming desert' (James & Percival, 2015), is almost completely suppressed of star formation, as observed through Hα imaging. This region is not completely devoid of stars and gas though; long-slit spectroscopy reveals LINER emission, probably associated with older stellar populations (James & Percival, 2015) and low level Hα emission (James & Percival, 2016). Relatively young stellar populations have also been found in these regions $\sim$ 1 Gyr (James & Percival, 2018) (although having a considerable spread), which corroborated with the very low observed current star formation suggests a quick shutdown of star formation. Hence, given the low level star formation, this inner disc region in barred galaxies will probably have a redder colour compared to the outer disc. Without a star formation desert, the discs of unbarred galaxies might show a smoother colour gradient across the disc. Therefore, a redder integrated colour of the discs of barred galaxies might arise because of the quenched star formation desert region (that is redder), while the outer disc might be more similar in colour to the disc of unbarred galaxies. In fact, Abdurro'uf & Akiyama (2017) has recently shown that the sSFR in the outer disc in barred galaxies is similar to the sSFR in the outer disc of unbarred galaxies, the differences arising in the central regions, thus this scenario is not implausible. This view would also be consistent with simulations showing that the gas from the outer discs in galaxies cannot reach the bar corotation radius, and fall to the centre, since it is pushed by the outward transfer of angular momentum (Lynden-Bell & Kalnajs, 1972) to the outer disc where it is feeding star formation. Nevertheless, spirals which have overall redder colours have been observed to have a higher bar fraction (Masters et al., 2011) which might suggest that the entire discs of barred galaxies is quenched. The hypotheses of a colour transition in the discs of barred galaxies, or a uniform colour of the discs, need to be tested, but with a different method than decompositions, for example by averaging the colour profiles, and extracting the colours within the radius of the star formation desert and beyond it. This technique was used by Consolandi (2016) to investigate the colours of bars, however, they did not compare the discs of barred galaxies with unbarred ones to assess the role of bars in the quenching of galaxy discs.

In this chapter I also found that the bulges of barred galaxies are only moderately bluer compared to the bulges of mass-matched galaxies without bars ($\Delta(g-i)_{\rm bulge} \sim 0.04$), even when the galaxies are matched in environment. All the bulges show

red colours, compared to the corresponding discs and bars. Spectroscopic studies have shown that the current star formation is actually enhanced in the centres of barred galaxies (James et al., 2009; Ellison et al., 2011) and that the bulges of barred galaxies contain a younger population of stars compared to the bulges of unbarred galaxies (Coelho & Gadotti, 2011), which might explain the modest difference in bulge colours between the barred and unbarred populations. On the other hand, studies on quiescent galaxies have shown that there is no statistically significant difference in the stellar populations of the bulges of barred versus unbarred galaxies (Cheung et al., 2015b). The red colours of bulges compared to other components, could be explained by a higher presence of internal dust the central regions (optically thick region) or a quick formation mechanism for the bulges, for example in a starburst (Carles et al., 2016; Spinoso et al., 2017; Robichaud et al., 2017). Pérez & Sánchez-Blázquez (2011) found that the bulges of barred galaxies are more metal rich and α-enhanced, in support of a quick formation scenario.

To conclude, my observations support the idea that bars can drive the quenching of the inner region of discs galaxies. The observation that barred galaxies have redder discs compared to similar unbarred galaxies implies that bars have an effect in quenching star formation in discs as well. Investigating the colour profile of galaxy discs within the bar region, and beyond it, separately, should explain whether the quenching is effective throughout the disc, or limited to the region swept up by the bar.

3.7.2 Are bars responsible for building bulges?

Bars are believed to be efficient in transporting gas to the central regions, which can lead to the growth of bulges (Kormendy & Kennicutt, 2004). In this work I find that a large fraction ($\sim 90\%$) of the obvious bulges of galaxies with strong bars are pseudobulges, formed by, slow, secular evolution while only $\sim 10\%$ of galaxies have classical bulges believed to be formed by major and minor merger events. My results support the scenario of bulges built from the disc material. It is surprising that such a high fraction of galaxies with strong bars have pseudobulges, given the high fraction of mergers suggested by hierarchical galaxy formation, as noted before by Kormendy et al. (2010). Nevertheless, some simulations suggest that even minor mergers can lead to the formation of bulges with $n_{\rm bulge} \leq 1$ (Scannapieco et al., 2010). Furthermore, the presence of low Sérsic index bulges in unbarred galaxies is not evidence against them being formed by a bar, since the galaxies may have hosted a bar at an earlier time (see argument about inner lenses being dissolved bars).

The observation that the B/T ratio is smaller in the strongly barred galaxies compared to unbarred galaxies, which was also observed by Laurikainen et al. (2013), might suggest that bar induced bulge growth is unlikely. This is unless the bulges in barred and unbarred galaxies have different formation scenarios. I find that unbarred galaxies have a higher fraction of classical bulges, which are thought to form early in galaxy mergers (Aguerri et al., 2001), therefore, it is reasonable to believe that mergers form higher mass bulges than the bar-induced bulges. My findings agree with the idea of bars forming disc-like bulges in the majority of massive barred galaxies, which contribute to $\sim 15\%$ of the luminosity of the galaxies.

I find that both barred and unbarred galaxies start having significant bulges above a galaxy mass of $M_* \approx 3 \times 10^{10}\ M_\odot$, which corresponds to the characteristic mass in Figure 1.5 at which disc galaxies are densest (have the smallest effective radius at a given mass). Lower mass galaxies are disc-dominated with either no bulge, or only a small fraction of the light in the bulge. My observation that the bulges of barred galaxies have a lower B/T light fraction compared to the bulges of unbarred galaxies, at a fixed stellar mass (since the two samples are mass-matched), would imply that the bulges of barred galaxies have a lower velocity dispersion. This is in agreement with the finding that the majority of the bulges of barred galaxies are pseudobulges ($n_{\rm bulge} \sim 1$), since the disc-like bulges are characterised by a higher v/σ and lower velocity dispersion compared to classical bulges (Fabricius et al., 2012). Future work should seek to obtain measurements of the velocity dispersion for both barred and unbarred galaxies, which would enable the study of the dynamical scaling relations in the Mass Plane (M_*, σ_e, r_e). The observed trends in this work can be explained if at $M_* \gtrsim 3 \times 10^{10}\ M_\odot$, the bulges of barred galaxies grow via gas inflows to the centre, which ultimately leads to the quenching of star formation, and probably gas rich minor mergers in the case of unbarred galaxies.

3.7.3 How do the properties of bars change with galaxy mass?

I find that the bar profiles depend on the prominence of the bulge and the stellar mass of the galaxy. Bars in low mass disc dominated galaxies have a flatter profile and are slightly shorter compared to bars in massive galaxies. This is consistent with the findings of Elmegreen & Elmegreen (1985), although in a much smaller sample of 11 barred galaxies. They suggested that the origin of the flat profiles is the overcrowding of old and young stars at the bar ends and the difference in flat versus shallow profile is due to a difference in the bar resonance locations (Combes & Elmegreen, 1993). More recently, Kim et al. (2015) found a very similar light profiles for bars in a sample of 144 nearby galaxies (galaxies with obvious bulges have a median Sérsic index of

$\langle n_{\rm bar} \rangle \sim 0.3$, while disc dominated systems have $\langle n_{\rm bar} \rangle \sim 0.85$). They suggest that the steepness of the bar profile can be used as a bar age indicator, with younger bars having exponential profiles and older bars Gaussian profiles. My results agree well with these previous results, albeit using a much larger sample, therefore strengthening the result that bars in late- and early-type galaxies have different radial light profiles.

Bars are believed to be born out of disc material, which has an exponential profile, and in their evolution, they trap stars in the bar orbits (Sellwood & Wilkinson, 1993; Sellwood, 2014; Athanassoula et al., 2013). The mass at which the change in the light profile of bars occurs approximately coincides

with the mass at which galaxies change significantly – at $M_\star \sim 10^{10.5} M_\odot$ galaxies start growing central concentrations, their surface mass density and colour changes (Kauffmann et al., 2003b). Also, at a similar mass ($M_\star \approx 10^{10.4} M_\odot$), bars buckle and form boxy/peanut bulges (Erwin & Debattista, 2017) (see Section 6.5.3). Thus, the flat profile that I observe in higher mass galaxies can be due to the boxy/peanut structure seen face-on or moderately inclined. Bars in these galaxies are vertically thick, thus both vertical and planar orbits are seen in projection. Furthermore, the light enhancement at the end of bars (referred to as 'ansae'), commonly seen in early-type galaxies, can lead to an overall flatter profile, as suggested by Elmegreen & Elmegreen (1985).

3.7.4 What is the origin of lenses in unbarred galaxies?

There is no theoretical explanation for the origin of lenses in unbarred galaxies. Kormendy (1979) suggests that as strong bars weaken, the stars escape from the bar and migrate into lenses, therefore pointing to an evolutionary scenario leading to the formation of lenses/ovals. Stars are scattered out from the bar forming a more circular feature with a roughly flat brightness profile. His conclusion is based on observations of barred galaxies without lenses, galaxies with bars embedded in lenses and galaxies with lenses and no bars. Furthermore, simulations by Bournaud & Combes (2002) show that, in the case of an isolated barred galaxy, it may consume all its gas in stars and when the disc is hot enough, the bar weakens, leaving behind the lens it was embedded in, while the galaxy evolves to be an early-type system. The simulations of Bournaud & Combes (2002) also predict that this lens can be destroyed and a new bar can be reformed following the accretion of cosmological gas.

Laurikainen et al. (2013) suggest that inner lenses in unbarred S0 galaxies are barlenses (lens-like features embedded in bars, believed to be the vertically thick part of the bar - the boxy/peanut bulge - seen face-on) in formerly barred galaxies, where the ends of the bar evolve into ansae and slowly dissolve with time. Other studies

such as Athanassoula (1983) suggest that lenses form similarly to bars, due to an instability in the galactic discs, but in hot discs instead of cold discs.

In this work I find that the properties (stellar masses, red colours, lens Sérsic indices) of unbarred galaxies with lenses are similar to the properties of (early-type) barred galaxies, and are different from purely unbarred galaxies, suggesting that there is indeed a connection between the first two. Unless the lenses and bars are formed through exactly the same mechanism, in similar galaxies and the lenses have the same impact on the evolution of galaxies as bars do (rearranging angular momentum, transporting stars and gas), my preferred formation scenarios are the ones described by Kormendy (1979) or Laurikainen et al. (2013). The observation of a high fraction of inner lenses in S0s (believed to be evolved spiral galaxies) compared to late-type galaxies also favours the scenario in which lenses are demised bars (Gao et al., 2018) compared to a common origin of the two structures. Another possibility is that the inner lenses are bars destroyed by mergers. Indeed simulations suggest that bars can be destroyed in interactions, while the disc survives (Athanassoula, 1999; Berentzen et al., 2003). However, it is improbable that a structure with such a flat profile and a sharp edge forms after a merger.

The small differences seen, such as the bulges and lenses of unbarred galaxies having slightly larger masses (by $\sim$0.1 dex) compared to the bulges and bars of barred galaxies, are compatible with a later evolutionary stage, lenses being the remnants of bars. The higher ellipticities of lenses compared to bars might be due to the scattering of stars in the direction perpendicular to the bars. The sizes of lenses better matches the size of weak bars rather than the sizes of strong bars at the same galaxy stellar mass, in agreement with an evolutionary scenario from a strong bar to a weak bar and eventually to a lens. As the mass of the central component (the bulge) increases, bars weaken, as shown by some simulations (Shen & Sellwood, 2004; Debattista et al., 2004; Athanassoula et al., 2005; Heller et al., 2007), and over a long period of time they might dissolve into a lens feature. We see many lenses already present along the bar major axes, which might be a snapshot of this process in action (Kormendy, 2013). The observed red colour of the inner lenses, as well as their higher incidence in early-type galaxies suggests that they are old features. This is in disagreement with the scenario in which bars are destroyed and reformed multiple times in the lifetime of a disc galaxy (Bournaud & Combes, 2002), otherwise we would observe lenses being populated by younger stellar populations as well.

3.8 Conclusions

I have made use of morphological classifications from the Galaxy Zoo project and 2D photometric decomposition to study the properties of a local sample of ∼3,500 galaxies with strong bars, currently the largest sample of barred galaxies studied through image decomposition. Using a multi-wavelength galaxy fitting routine I decomposed barred galaxies into bars, discs and bulges and recovered the light from each component. Taking advantage of multi-band data, I have determined the structural parameters of each component, such as their colours, Sérsic indices, effective radii, axis ratios and the fraction of total light in each component. For completeness, I have also added a sample of $\sim 2,600$ galaxies with weak bars and investigated their properties.

Detailed studies involving large samples of nearby galaxies, such as this work, are necessary because they allow us to investigate - in a statistically reliable fashion - both the qualitative morphology via visual classifications and a more quantitative morphology by the means of photometric decompositions. Furthermore, to examine the effects of bars on their host galaxies a meaningful mass- and environment-matched comparison between galaxies with bars and galaxies without bars is needed. I summarise my main findings as follows:

(i) Weak bars, selected with lower bar likelihoods in Galaxy Zoo are shorter and less prominent than strong bars (selected with higher bar likelihoods), in agreement with expert classification of bars. They tend to be hosted by bluer and less massive galaxies. The strength of bars, how to quantify it, and their different effects on host galaxies, is nevertheless an unsettled topic in the field.

(ii) The bulges of barred galaxies are predominantly pseudobulges, with a typical Sérsic index of $n_{\rm bulge} \sim 1$, supporting the idea of bulges being formed by bars though transfer of gas to the galaxy centers, in contrast to classical bulges believed to be built by mergers. This is in good agreement with previous studies (e.g. Kormendy & Kennicutt 2004; Salo et al. 2015; Méndez-Abreu et al. 2017), and perhaps this is the strong evidence for *bar quenching* having acted in these galaxies, as suggested by Cheung et al. (2013).

(iii) There are two types of bar Sérsic profiles: bars in lower mass disc dominated galaxies (late-types) have approximately exponential profiles ($n_{\rm bar} \sim 1$), while bars in higher mass galaxies with obvious bulges (early-types) have shallower, Gaussian-like light profiles ($n_{\rm bar} \sim 0.5$), in good agreement with previous studies (Elmegreen & Elmegreen, 1985; Kim et al., 2015), albeit on much larger samples.

Considering the mass at which the transition in the light profile occurs, $M_\star \approx 10^{10.4} M_\odot$, it is possible that the flatter profile of bars in high mass galaxies is due to the boxy/peanut bulge seen moderately inclined. Boxy/peanut bulges are discussed further in Chapter 6.

(iv) The bars and bulges of strongly barred galaxies are redder compared to the galaxy discs by $\Delta(g-i) \sim 0.2$ and $\Delta(g-i) \sim 0.3$, respectively, compatible with scenarios of inside-out quenching. This colour difference steepens with stellar mass, such that the most massive galaxies show the largest difference in colour between the components.

(v) When comparing to a mass- and environment-matched sample of galaxies without bars, the discs of strongly barred galaxies are redder by $\Delta(g-i) \sim 0.1$ than the corresponding discs, while their bulges are bluer by $\Delta(g-i) \sim 0.04$ than the corresponding bulges of unbarred galaxies. A similar, only slightly smaller colour difference ($\Delta(g-i) \sim 0.06$) is observed between the discs of weakly barred galaxies and the those of mass-matched unbarred galaxies. This can be an evidence of 'bar quenching', bars depleting gas or star formation being less efficient in the disc region. The details of this process should be explored in the future, whether the entire disc is affected by bar quenching, or only the inner region.

(vi) I find a subsample of galaxies with inner lenses/ovals within the unbarred sample of galaxies that have similar structural properties to barred galaxies (especially early-type weakly barred ones), supportive of an evolutionary link between the two, in which bars weaken and eventually dissolve into lenses, compared to a common formation mechanism. Their higher incidence in early-type galaxies compared to late-type galaxies favours the bar dissolution scenario.

Chapter 4

Offset discs and bars in SDSS

I use the multi-wavelength image decompositions and Galaxy Zoo morphologies to identify a sample of 271 late-type galaxies with an off-centre bar. I measure the offsets between the photometric centres of the stellar disc and stellar bar, and the lopsidedness of these galaxies, and compare them to predictions from simulations of dwarf-dwarf tidal interactions producing off-centre bars. I investigate the physical properties of these galaxies and the types of galaxies most susceptible to disc-bar displacements. I conduct a search for companions to test the hypothesis of tidal interactions, comparing the fraction of offset galaxies with companions, with a mass- and redshift-matched sample of galaxies with centred bars. Finally, I suggest alternative scenarios that might lead to an offset bar.

4.1 Motivation and background

Offsets between discs and bars are seen in Magellanic spirals (de Vaucouleurs & Freeman, 1972), defined by their prototype, the Large Magellanic Cloud (LMC; de Vaucouleurs 1955). Historically, in literature these galaxies are referred to as 'offset bars' (de Vaucouleurs & Freeman, 1972; Odewahn, 1996) and previous studies have focused on a small sample of objects. Examples of nearby galaxies with offset bars can be seen in Figure 1.3. The only galaxies studied in greater detail are the LMC and NGC 3906. The LMC hosts a bar that is offset from the centre of the outer disc isophotes by ∼0.4 kpc, and a single prominent spiral arm. NGC 3906 hosts a bar that is off-centre by ∼0.9 kpc from the photometric centre of the disc (de Swardt et al., 2015), and multiple spiral arms, being classified as an SBd, rather than a Magellanic barred spiral (SBm). In the case of NGC 3906 the bar centre coincides with the dynamical centre of the galaxy (the centre of the dark matter potential), determined

through HI observations. In the LMC the kinematic centre of the HI disc is offset from both the photometric centre of the bar and of the stellar disc by as much as 0.8 kpc (van der Marel, 2001). Because it is still unclear which of the two components, the disc or the bar, is offset from the dynamical centre, I refer to such galaxies as 'offset galaxies'. The relation between the bar and disc photometric centres and the star and gas kinematic centres is discussed in Chapter 5.

The origin of such offsets is not well understood. Numerical simulations of barred galaxies have shown that a bar may become offset from the disc following a fly-by[1] or an impact of a companion, while the disc of the galaxy becomes lopsided (Athanassoula, 1996; Athanassoula et al., 1997; Besla et al., 2012; Yozin & Bekki, 2014; Pardy et al., 2016). Athanassoula (1996) managed to reproduce the one arm morphology and off-centre bar in a Magellanic type galaxy following an impact of a companion galaxy (their Figure 3). Athanassoula et al. (1997) noticed the transient displacement of the bar in an oblique impact of a galaxy, which is associated with a change in the size and pattern speed of the bar. A recent tidal interaction with the Small Magellanic Cloud (SMC) or the Milky Way has been suggested as an explanation for the off-centre bar in the LMC (Zhao & Evans, 2000). More recently, Besla et al. (2012) and Yozin & Bekki (2014) suggested a dwarf-dwarf galaxy interaction being responsible for the offset bar, rather than the interaction with the Milky Way. On the contrary, the other well-studied offset galaxy, NGC 3906, appears to be relatively isolated (de Swardt et al., 2015), with no evidence of on-going interaction with nearby galaxies; a possible explanation for the observed offset is an interaction with a dark matter satellite, or an unidentified fast moving companion. Bekki (2009) suggested that dark satellites with masses of $10^8 - 10^9 M_\odot$ (dark matter subhalo) and either no or very little observable matter can create an offset bar in a collision with a Magellanic type galaxy. Another explanation for the offsets might be the cosmological accretion of gas in galaxies (Bournaud et al., 2005b). Alternatively, the modeling of lopsided galaxies suggests that long-lived off-centre bars and asymmetries may be a consequence of misalignments between the stellar disc and halo (Levine & Sparke, 1998; Noordermeer et al., 2001), or due to a perturbation to the potential, for example a lopsidedness (Jog, 1997, 2002) or triaxiality (Jog, 2000) of the dark matter haloes. Nevertheless, with a sample of two galaxies it is impossible to establish whether interactions are responsible for the off-centre bars and discs in galaxies.

Despite the availability of large surveys, observationally, the origin of offsets and the asymmetries in Magellanic type galaxies has not yet been established. There

[1] interactions without an impact, but in which galaxies are approaching sufficiently close that the gravitational field of one galaxy influences the gravitational field of the other

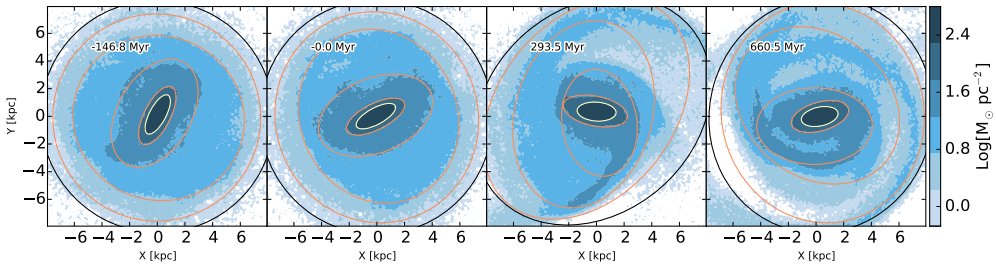

Figure 4.1: Face-on stellar disc surface density map from Pardy et al. (2016). The inner yellow ellipse shows the bar component and the outer black ellipse outlines the disc. The four panels illustrate four different time steps in the simulation, from the time before the companion is introduced to 660.5 Myr after the interaction. The morphology of the galaxy becomes distorted and asymmetric. This particular model is a prograde interaction with an inclination of 45° and a cored density model for the halo.

has been contradictory evidence about the frequency of companions of Magellanic galaxies (with and without bars). In a large survey of local Magellanic type galaxies, Odewahn (1994) found that 71 out of 75 galaxies have a nearby neighbour, within a projected separation of 120 kpc. In contrast, in an HI follow-up study of a subset of the Magellanic type barred galaxies observed by Odewahn (1994), Wilcots & Prescott (2004) found that only 2 of 13 were interacting with their neighbour, clearly affecting their morphologies. One aim of this work is to establish whether interactions can account for the observed offsets and asymmetries in galaxies.

4.2 Offsets in detailed simulations

Recently, Pardy et al. (2016) (hereafter P16) followed up on the idea of a tidally induced offset in barred Magellanic type galaxies using N-body and hydrodynamic simulations[2] of dwarf-dwarf galaxy interactions. The morphologies of the dwarf galaxy before, during and after the interaction are shown in Figure 4.1. They investigated the relation between the dynamical, stellar, and gas rotation and disc and bar photometric centres, following a 1:10 mass ratio interaction, characteristic of the interaction between the SMC and the LMC (the stellar mass of the LMC is $3 \times 10^9 M_\odot$; van der Marel et al. 2002, while that of the SMC is $3 \times 10^8 M_\odot$; Stanimirovic, S. and Staveley-Smith, L. and Jones, P. A. 2004). The bar in the simulations was grown out of disc instabilities and not induced by the encounter.

[2]using the GADGET3 SPH code

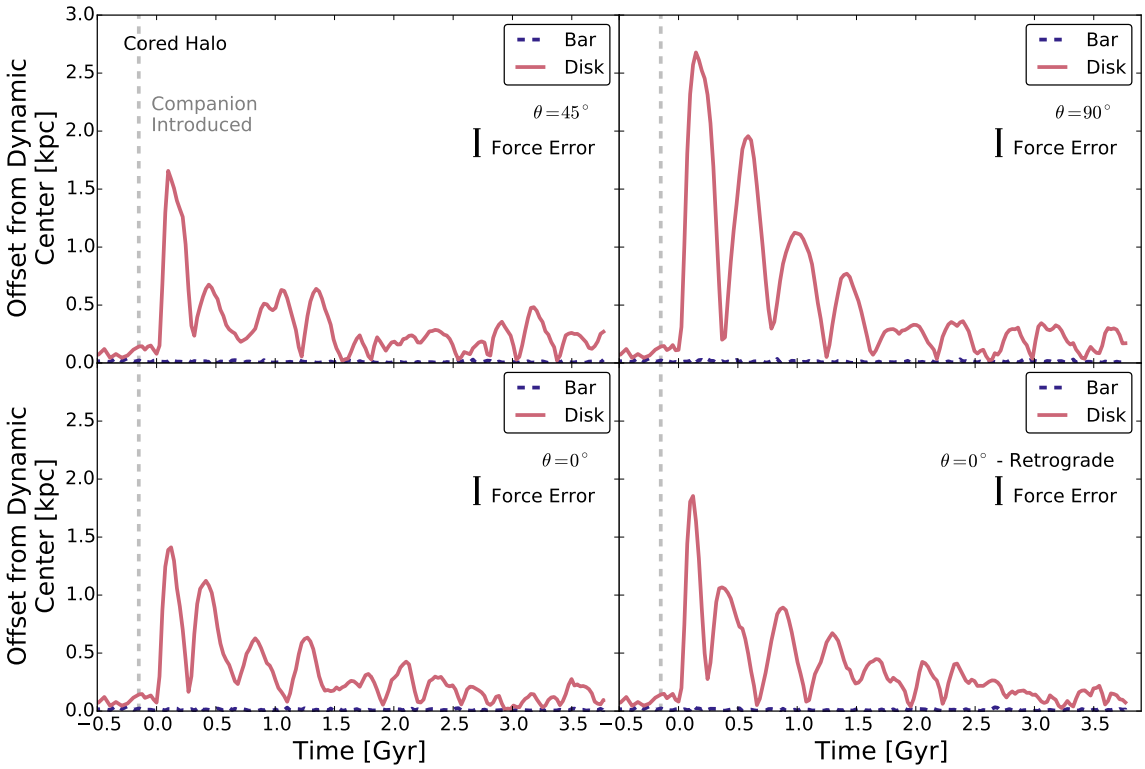

Figure 4.2: Time evolution of the offsets between the photometric centre of the disc (red line) and of the bar (blue line) and the dynamical centre of the galaxy (centre of gravitational potential), in the cored density model for four orbital configurations, from Pardy et al. (2016). The bar is always centred on the dynamical centre, while the disc is offset.

Investigating various orbital parameters for the interaction and two types of dark matter halos ('cusp' versus 'cored' density models), they conclude that an offset between the photometric centre of the bar and of the disc is produced, with a predicted shift of at most 1.5-2.5 kpc, as shown in Figure 4.2, for four different orbital inclinations (this example is for the 'cored' density model in particular). The largest offsets are produced for smaller impact parameters and large inclination angles of the passing galaxy with respect to the plane of the primary galaxy. Surprisingly, they find that the bar is always coincident with the dynamical centre (defined as the location where the galaxy potential well is deepest) and it is the disc that is displaced from the dynamical centre. P16 find that the impact parameter and the orientation of the orbital plane with respect to the rotation plane of the galaxy are the most important parameters in determining the magnitude of the offsets. The amplitude of the offsets is strongly correlated with the distorted asymmetry (lopsidedness) of the disc ($R^2 \geq 0.68$ for all orbital configurations), measured using $m = 1$ Fourier decomposition. Both the offsets and lopsidedness decrease with time and vanish after

2 Gyr, when the disc-bar alignments are restored.

In this chapter I test the predictions from P16 on the largest sample of galaxies with off-centre discs and bars identified so far. I measure the magnitude of the offsets, the masses of the offset galaxies, the correlation of offsets with lopsidedness and the hypothesis that interactions with companion galaxies such as the SMC are the origin of the observed offsets.

4.3 Identifying the offsets

While inspecting the sample of successfully fitted galaxies with strong bars I realised that the bars in a notable fraction of galaxies appeared to be offset from the photometric centre of the galaxy discs. One example of a disc+bar fit of such a galaxy, in five bands, is shown in Figure 4.3.

To fit the galaxies with disc+bar or disc+bar+bulge models I used the Galaxy Zoo volunteer's classification of bulges, as discussed in Section 2.3.3. This is slightly different from the previous chapter. In the work in Chapter 3, I based the distinction between two component and three component fits on my visual inspection of the images and residuals, as discussed in Section 2.4.7. The difference between the galaxies categorised into 'disc dominated' and 'obvious bulges' between this chapter and Chapter 3 is only 15%, though. This is mostly due to galaxies fitted with disc+bar+bulge components being classified by the volunteers as being disc dominated (10%) and 5% of galaxies fitted with two components being identified as having obvious bulges. This causes the final number of successfully fitted galaxies with strong bars to be slightly different, 3,461 in Chapter 3 and 3,357 in this chapter. The small difference might arise because placing the prominence of bulges into four categories ('No bulge', 'Just noticeable', 'Obvious' and 'Dominant') can be subjective. Nevertheless, an agreement of 85% between my classifications, based on residuals and the volunteers' classification of bulges based on colour images, suggests that the average classification of the volunteers is reliable in estimating the prominence of a bulge. The volunteers' classification of bulge prominence is surprisingly well correlated with the measured B/T, as shown in Figure 2.6. There are only $\sim$ 100 fewer successful fits in this chapter compared to the previous one. This fraction is insignificant ($\sim$ 3%) and is not expected to influence the results. In what follows, I use the sample of 3,357 successfully fitted galaxies as published in Kruk et al. (2017).

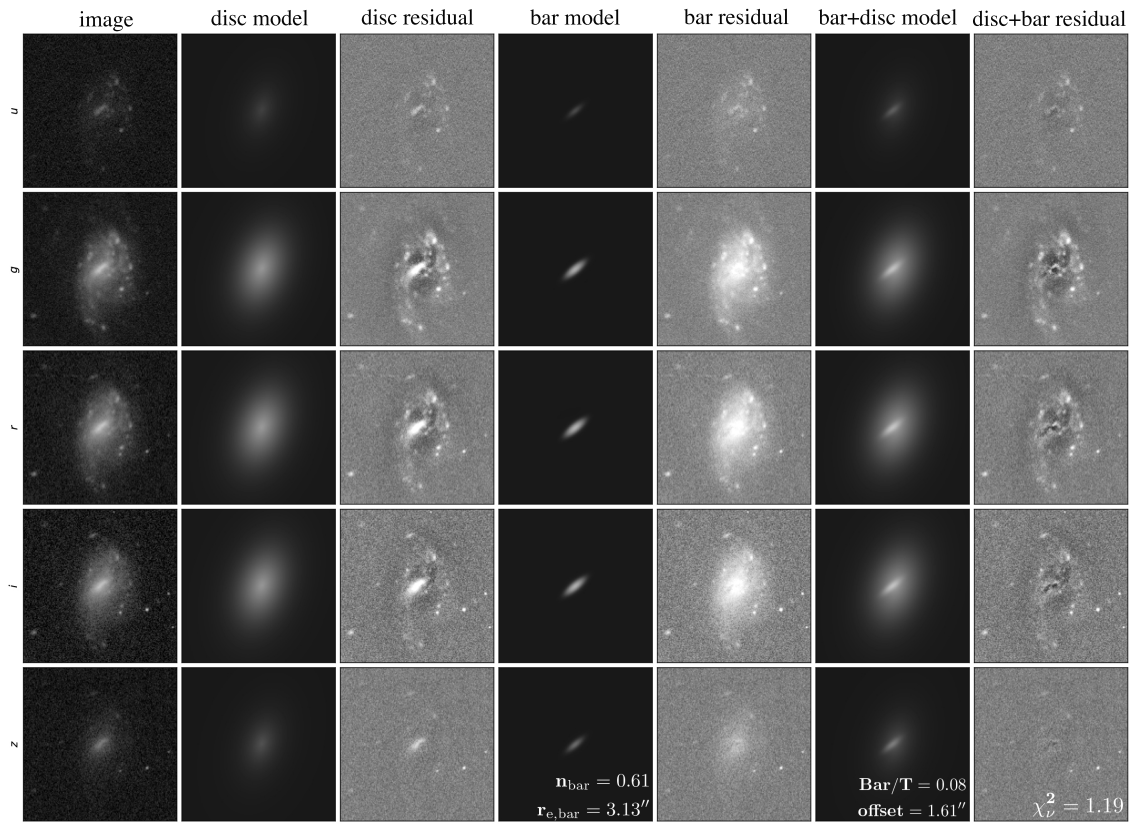

Figure 4.3: Images of galaxy J143758.75+412033.0 in *u, g, r, i, z* bands. Example of a GalfitM disc+bar fit, model and residuals, used to identify galaxies with offset bars. The 1st column shows the original images, the 2nd and 3rd show the model for the exponential disc and the residual from this model. The 4th and 5th columns show the model for the bar, fitted with a free Sérsic profile, and the associated residual. The 6th column is the combined bar+disc model and the last column shows the residual and the reduced χ^2. The projected offsets were measured as the separation on the sky between the centres of the two components. The legend shows the Sérsic index, the effective radius for each component and the bar-to-total luminosity ratio.

4.4 Offset Sample

The galaxies were fitted with GalfitM. In the fitting procedure, I allowed offsets between the centres of the bar and of the disc components, a novelty compared to previous studies in which they were kept fixed to the same location. I measured the projected distance on the sky between the photometric centres of the two components. Because galaxies do not have sharp edges, it is difficult to establish where galaxies end (this also depends on the depth of the images), which introduces uncertainties in measuring the shape and centre of the outer disc. Moreover, it is easier to distinguish offsets in more extended galaxies, compared to galaxies having small angular sizes, as shown in the offset bar galaxies in Figure 4.4. Additionally, it is easier to identify

Figure 4.4: Examples of galaxies with offset discs and bars in SDSS, *gri* composite colour images, ordered in increasing angular size. The images are $1' \times 1'$.

offsets in galaxy images with better resolution, which, amongst other factors, is determined by the astronomical seeing – the atmospheric turbulence on the night of the observations. Thus, one needs to choose a (conservative) threshold value above which a galaxy is considered to belong to the class of offset galaxies. A reasonable choice for such an offset threshold is the seeing measured as the FWHM of the PSF. If the measured offset between the photometric centres of the bar and disc components is larger than the FWHM of the PSF, I consider the galaxy to be an offset galaxy. In the images used from SDSS, the FWHM of the PSF varied between different fields and bands (Bramich & Freudling, 2012), ranging between $0.83''$ and $2.33''$ in the u-band, (with a median of $1.34''$), and between $0.56''$ and $1.99''$ in the i-band (with a median of $1.06''$). Since there were five bands fitted simultaneously, I considered a galaxy to be offset if the projected offset was larger than the smallest FWHM of the PSF in the five bands. In the vast majority of cases, this was the i-band. This cut for identifying galaxies with off-centre bars in five bands is probably conservative since the bar is not a round feature like the PSF, but rather an extended, linear feature, in which offsets are easier to measure. Nevertheless, the identified offset galaxies are those showing the largest offsets in the sample of strongly barred galaxies.

Figure 4.5 illustrates the effects of resolution on identifying offsets in galaxies. I compare an SDSS image of an offset galaxy situated at $z = 0.07$ (only slightly further away than the redshift limit considered in this study) with an image of the same

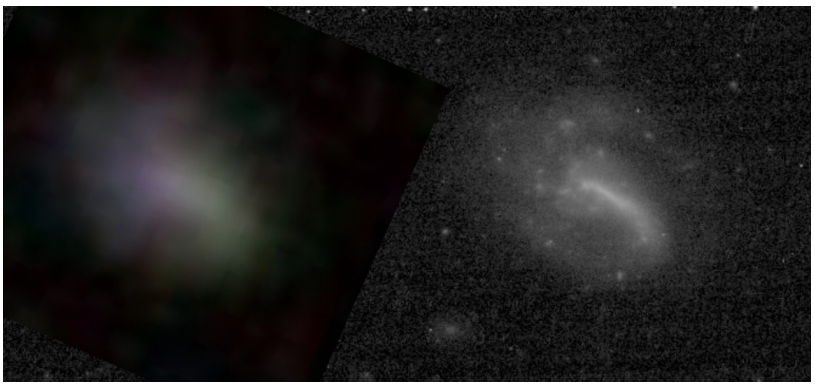

Figure 4.5: An SDSS image of a galaxy at z=0.07 (*left*) and a Hubble Space Telescope image of the same galaxy (*right*) (Credit: Brooke Simmons), showing the effect of resolution in blurring the galaxy image.

galaxy taken by the *HST*, with a resolution of 0.09″. The physical resolution of the SDSS image, 1.1″ or 1.5 kpc at the redshift of the galaxy, is clearly inferior to that of the *HST* image, 0.13 kpc. While an offset bar is clearly noticeable in the *HST* image, it is difficult to distinguish an offset bar feature in the SDSS image. This is the reason for selecting a sample of nearby galaxies (up to $z = 0.06$) and an even closer (up to z=0.04) volume-limited sample in this chapter.

To study the physical properties of galaxies, the measured projected offsets were converted into a physical offset, at the redshift of the galaxy and deprojected, adopting a simple analytical 1D approximation used to deproject bars (Martin, 1995; Gadotti et al., 2007)

$$d_{\rm offset}^{\rm dep} = d_{\rm offset}^{\rm proj} \sqrt{\sin\alpha^2 \sec i^2 + \cos\alpha^2}, \tag{4.1}$$

where α is the angle between the projected direction of the disc-bar offset and the major axis of the inclined disc, $\sec i \sim 1/(b/a)_{\rm disc}$ (where i is the inclination) and $d_{\rm offset}^{\rm proj}$ is the projected physical offset. According to the work of Zou et al. (2014) in deprojecting bars, the uncertainties in the deprojections are small (∼20%), since the galaxies were selected such that $i \lesssim 60°$ and the sizes of the offsets are small compared to the sizes of bars and discs.

There are 271 galaxies satisfying the set condition for the offset galaxies. Inspecting the galaxy images with projected offsets > FWHM, the majority of these galaxies are blue (median $u-r \sim 1.6$), with one or more spiral arms and with an offset between the stellar bar and disc clearly noticeable. Figure 4.6 shows the absolute magnitude versus redshift of the offset galaxies in comparison to the successfully fitted barred sample. The first noticeable aspect is that offset galaxies tend to be fainter and at lower redshift than the general population of barred galaxies. The former is due to

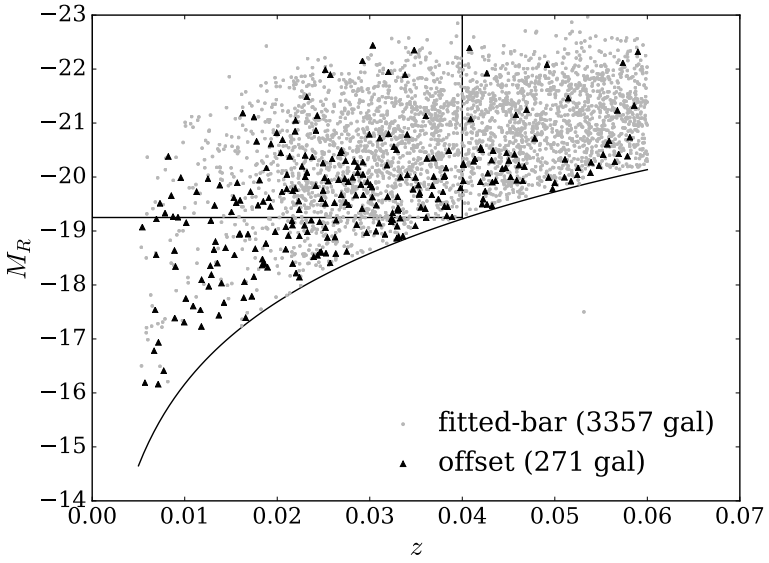

Figure 4.6: The r-band Petrosian absolute magnitudes of the samples used in the paper: the FITTED-BAR sample and the OFFSET sample, as defined in Section 3.2. The box contains the galaxies in the volume-limited sample (1,583 galaxies) as defined in Section 4.3. The curved line corresponds to the GZ2 completeness limit of 17 magnitudes, at a particular redshift.

offset galaxies being intrinsically smaller and dimmer and thus harder to observe at higher redshifts, while the latter is a resolution effect. 87% of the offset galaxies have projected offsets larger than $1''$, which corresponds to 0.1 kpc at $z = 0.005$ and to 1.1 kpc at $z = 0.06$.

One concern when identifying offset bars in galaxies is whether the offset bar is a stable structural feature (a linear bar) or a star forming clump, since the majority of these galaxies are observed to be blue and star forming. If the offset bars are indeed only regions of enhanced star formation, populated by young stars, they will be most prominent in the blue SDSS bands (u and g), whereas if they are real bars they should be identifiable in older stellar populations as well (tracing the mass distribution of the galaxy) – thus visible in the near-infrared SDSS bands (i and z). Inspecting images of offset systems in multiple bands, the bars in these galaxies stand out in both the blue bands, suggesting that they contain young stars, but also in the near-infrared bands, tracing older stellar populations. Furthermore, if they were clumps of star formation, one would expect them to have a different morphology to a bar, which is a linear feature. Therefore, the offset bars do appear to be real, stable features, and the offsets are identifiable in the i-band images as well as in the bluer bands. In fact, the prominent offset bar in the LMC is revealed in both the B-band, dominated by a

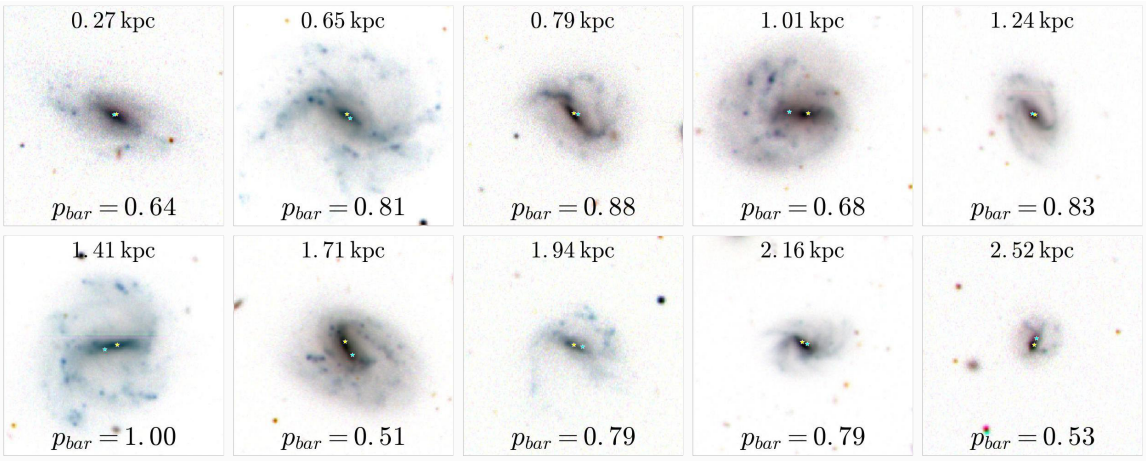

Figure 4.7: Examples of galaxies with offset discs and bars in SDSS; inverted colour *gri* composite images. The measured deprojected photometric offset between the bar and the disc is given at the top of each image. The GZ2 debiased likelihood that the galaxy has a bar is given at the bottom of each image. The centre of the bar component, according to the best fit model, is marked with a yellow star, while the photometric centre of the disc is marked with a cyan star. The images are $1' \times 1'$.

distribution of younger stellar populations (de Vaucouleurs & Freeman, 1972) and in the intermediate-age stellar populations (Holtzman et al., 1999; van der Marel, 2001). The bar in the LMC is not seen in HI (Kim et al., 1998), and nor it is a site of current star formation in Hα imaging (Kim et al., 1999).

As discussed in Section 2.4, in the multi-wavelength fitting with GALFITM, the best fit model (based on χ^2 minimisation) is weighted by the noise in the images, with the i-band being the least noisy. Therefore, the i band has, on average, a higher weight compared to the u and g bands in the decomposition. The offsets, thus are genuine and trace the underlying stellar mass distribution rather than the distribution of star formation.

Henceforth I refer to this sample of 271 offset galaxies as the OFFSET sample. This is currently the largest sample of such galaxies. Examples of galaxies with offset bars and the measured deprojected offsets are shown in in Figure 4.7, while the results from the parametric fitting are summarized in Table 4.2. For comparison, I also select a mass and redshift-matched COMPARISON sample of 271 galaxies with centred bars (selected such that the projected offset is smaller than the PSF FWHM).

As shown in Figure 4.6, the survey is incomplete for fainter galaxies at higher redshifts, therefore in order to study the statistical properties of the offset population in greater detail I selected a volume-limited sample. From the FITTED-BAR sample I selected only galaxies in the redshift range $0.005 < z < 0.04$, brighter than $M_r \leq -19.22$ (inside the box in Figure 4.6), which is the r-band absolute magnitude

Desciption	Criteria	No.
FITTED BAR	successfully fitted	3,357
OFFSET	offset > PSF FWHM	271
COMPARISON[a]	offset > PSF FWHM	271
volume-limited FITTED BAR	$M_r < -19.22$ & $z < 0.04$	1,583
volume-limited OFFSET	$M_r < -19.22$ & $z < 0.04$	131
volume-limited COMPARISON[a]	$M_r < -19.22$ & $z < 0.04$	131

[a]Mass- and redshift-matched with the OFFSET sample.

Table 4.1: Definitions of the samples used in this chapter.

SDSS Name	Redshift	m_r	Disc		Bar		Bulge		$\log(M_\star)$	A_1	Offset	Offset
		[mag]	r_e [kpc]	n	r_e [kpc]	n	r_e [kpc]	n	$[M_\odot]$		[arcsec]	[kpc]
J001723.39-003112.8	0.032	16.71	3.13	1.00	1.25	0.49	-	-	9.40	0.20	2.80	1.98
J163037.96+272744.2	0.059	14.96	11.35	1.00	6.33	0.48	0.77	1.03	11.07	0.09	0.97	1.24
J023356.29+005525.2	0.022	15.17	5.27	1.00	1.24	0.51	-	-	9.59	0.08	1.19	0.58
J102003.64+383655.9	0.007	13.87	2.60	1.00	0.80	0.87	-	-	9.05	0.28	6.84	1.01
J074951.23+184944.3	0.016	14.78	6.11	1.00	1.22	0.25	-	-	9.34	0.07	1.08	0.38
J132743.83+624559.6	0.022	13.93	8.93	1.00	4.23	0.70	0.49	1.38	10.54	0.04	1.90	1.19
J155946.42+371437.9	0.057	16.74	8.56	1.00	1.46	2.56	-	-	9.91	0.17	1.22	1.34
J111041.31+585646.5	0.046	16.42	5.02	1.00	3.10	0.97	-	-	9.93	0.18	1.23	1.19
J134308.83+302015.8	0.035	13.66	12.61	1.00	7.19	0.26	0.96	0.43	11.09	0.07	1.16	1.00
J165214.37+635738.9	0.017	14.71	3.75	1.00	0.91	0.10	-	-	9.77	0.18	3.25	1.22

Table 4.2: Properties for 10 out of the 271 galaxies in the OFFSET sample, fitted with disc+bar or disc+bar+bulge components. The redshifts and r-band apparent Petrosian magnitudes are drawn from SDSS DR7 and the stellar masses are drawn from the MPA-JHU catalogue (Kauffmann et al., 2003a). The disc component was fitted with an exponential profile ($n = 1$), while the bar and bulge with a free Sérsic profile. The offsets were measured between the photometric centres of the disc and of the bar and the physical offsets were deprojected using Equation 4.1. Full table is available in the electronic version of Kruk et al. (2017).

corresponding to the GZ2 completeness magnitude of 17, at a redshift of $z = 0.04$. I chose this redshift cut as a compromise between including fainter galaxies, typical for offset galaxies, having a sufficiently large sample, as well as to limit the resolution effects, as discussed earlier. This volume-limited sample consists of a subset of 1,583 barred galaxies from the FITTED-BAR sample. 8% of the galaxies in the volume-limited sample are offset systems. I summarize the sample definitions used in this chapter in Table 4.1. In Sections 4.5.2 - 4.5.5 I use the volume-limited sample of barred galaxies and the corresponding subsample of offset systems to discuss their properties: distribution of stellar masses, stellar bar properties and the lack of bulges. In Sections 4.5.1, 4.5.6 and 4.5.7 I use the entire sample of 271 offset galaxies to study the distribution of offsets, lopsidedness and companions.

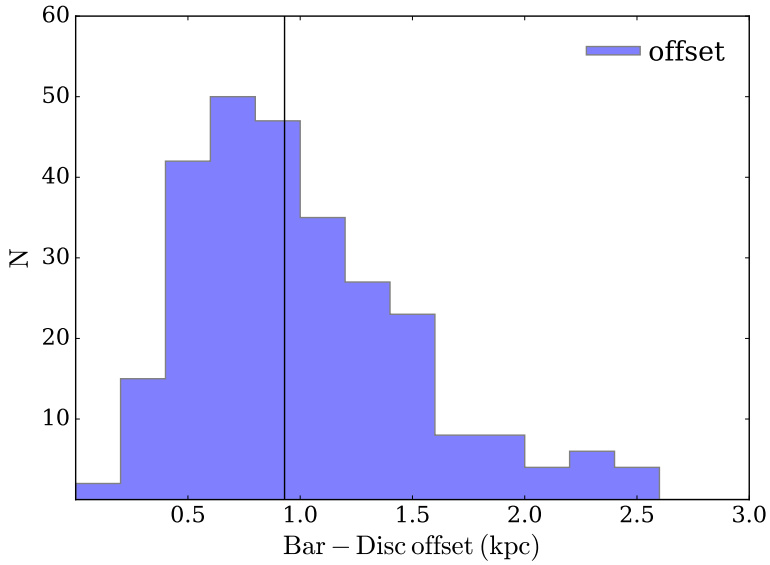

Figure 4.8: Distribution of the measured offsets between the photometric centres of the discs and bars, corrected for inclination effects, in the OFFSET sample. The criterion for a galaxy to have an offset bar is that the projected offset is larger than the FWHM of the PSF.

4.5 Results

4.5.1 Bar-Disc Offsets

The measured offsets between the geometric centre of the exponential disc component and the centre of the bar component were deprojected using Equation 4.1. For the 271 galaxies in the OFFSET sample the measured physical offsets varied between 0.2 and 2.5 kpc (with a median offset of 0.93 kpc and a standard deviation of 0.50 kpc), as shown in Figure 4.7, a similar range as predicted by P16, for different parameters of dwarf-dwarf interactions (up to 1.5-2.5 kpc). These offsets correspond to 10-40% the effective radii of the disc (median 16% and 1σ =10%).

4.5.2 Mass distribution

The distribution of stellar masses for the 131 offset galaxies in the volume-limited sample, as well as for the entire volume-limited sample of fitted barred galaxies, can be seen in Figure 4.9. The two distributions are clearly different; the barred galaxies in the sample have a median mass of $10^{10.3}\,M_{\odot}$, while the offset galaxies have a lower median mass of $10^{9.6}\,M_{\odot}$. A K-S test gives a value of $k = 0.49$ and $p_{KS} < 10^{-15}$; therefore, the two distributions of stellar masses are different, suggesting that offsets between the discs and bars are properties of lower mass barred galaxies only.

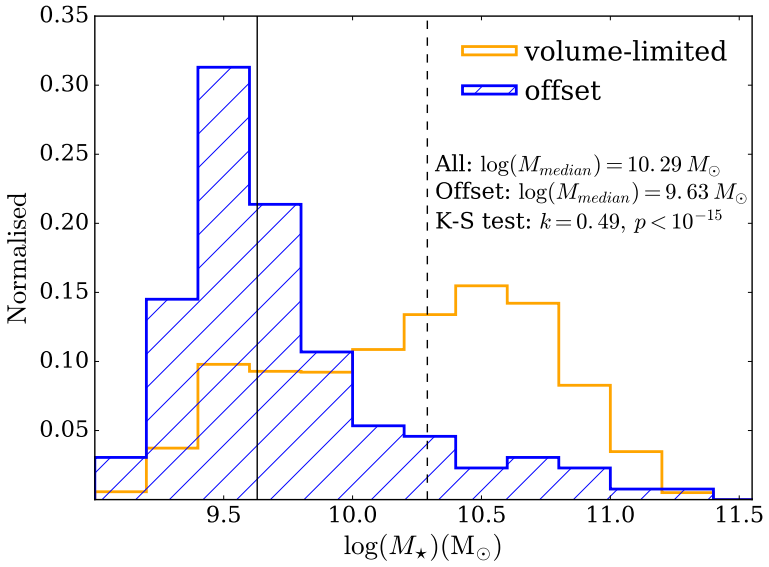

Figure 4.9: Normalized histograms of the mass distribution of galaxies with offset bars in the volume-limited sample (131 galaxies) and the volume-limited sample of barred galaxies (1,583 galaxies). The median mass of galaxies with off-centre bars is $10^{9.63} M_\odot$ (as shown by the vertical solid line), while the median mass of barred galaxies is $10^{10.29} M_\odot$ (as shown by the vertical dashed line). Only 12 galaxies with $M > 3 \times 10^{10} M_\odot$ are seen to have off-centre bars.

The majority of offset systems have stellar masses between $10^9 - 10^{10}$ $M_\odot$, in agreement with being Magellanic type dwarfs, with a typical (median) mass of 4×10^9 $M_\odot$. 103 galaxies (∼20%) of all the dwarf galaxies (with $M < 10^{10}$ $M_\odot$) of the volume-limited barred sample have offset discs and bars. The peak of the mass distribution of offset galaxies is at $\sim 10^{9.5}$ $M_\odot$, where 32% of the barred galaxies show offsets. In contrast, only 12% of the offset galaxies have masses larger than $10^{10.3}$ $M_\odot$, even though this is the median mass of the volume-limited sample and only five offset galaxies are as massive as the Milky Way, with a mass of $\sim 10^{10.8}$ $M_\odot$ (Licquia & Newman, 2015). Moreover, inspecting the higher mass galaxies (with $M > 3 \times 10^{10}$ $M_\odot$) with offsets suggests that these offsets might be due to recent minor mergers as they show signs of tidal debris. An important result is that Milky Way-like and more massive barred galaxies ($M_* \gtrsim 10^{10.3}$ $M_\odot$) are unlikely to have offsets between the discs and the bars. This poses a challenge to simulations of interacting galaxies producing the offsets, as a 1:10 mass ratio interaction can be scaled up from a SMC - LMC to a LMC - Milky Way type interaction. The lack of massive galaxies with offsets suggest that such an interaction does not affect the relative position of the bar and disc significantly in a Milky Way-like galaxy.

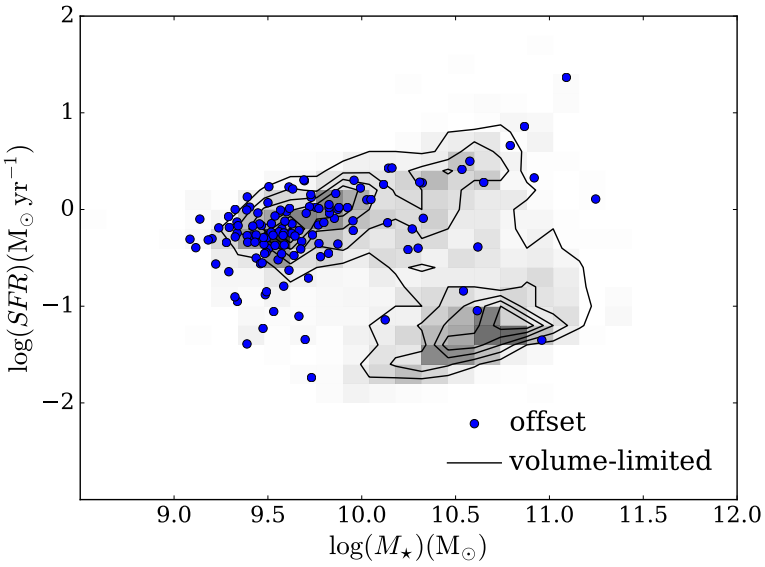

Figure 4.10: The location of the offset systems on a SFR-mass plot, overlaid on the volume-limited sample of barred galaxies. Galaxies with offset bars are located almost entirely on the star forming main sequence.

4.5.3 Star formation

In Figure 4.10 the SFR (drawn from Brinchmann et al. 2004) is plotted against the stellar mass. The first aspect to notice is that most offset galaxies are young, blue and star-forming, being situated on the star forming main sequence (Brinchmann et al., 2004), in contrast with the majority of the barred galaxies, which are red in colour, as shown in Figure 3.7 and in Masters et al. (2011). 21 out of the 131 offset galaxies (16%) have SFRs below $\log(\mathrm{SFR}) = -0.5\,M_\odot\,\mathrm{yr}^{-1}$, and are below the main sequence. Within the volume-limited OFFSET SAMPLE, at $M_\star < 10^{10} M_\odot$, barred galaxies are typically star forming. There is no significant difference in the SFR of galaxies with offset and centred bars. Nevertheless, it is worth noting that the volume-limited sample is incomplete for red (and so likely passive) galaxies at $M_\star \lesssim 10^{10} M_\odot$ and, therefore, one cannot rule out differences in star formation fractions at low masses.

4.5.4 Bar properties

The best fits from GALFITM suggest that the stellar bars in the offset systems are characterized by a median axis ratio of $b/a = 0.28 \pm 0.10$ (error bars are 1σ) and they contain $B/T = 0.15 \pm 0.09$ of the total light of the galaxy in the r-band. The median axis ratios and flux ratios are not dissimilar to the those of the general population of

strongly barred galaxies, presented in Section 3.3.2 ($b/a = 0.31 \pm 0.12$ and $Bar/T = 0.14 \pm 0.12$ in the r-band).

The bars in offset galaxies have an almost exponential light profile, of median Sérsic index $n = 0.93 \pm 0.70$, which is typical for a population of low-mass late-type barred galaxies, as shown in Figure 3.6. These observations suggest that the main determinant of the structure of these galaxies is the stellar mass, rather than the physical process that is causing the bar and discs to be off-centre from each other.

The disc and bar components of the offset galaxies have similar blue colours, with a median $(u - r) \sim 1.5$. Therefore, it is reasonable to assume that the stellar populations of the bar are the same as those in the disc, while their blue colours suggest mostly young stellar ages. This is in agreement with the work of Monteagudo et al. (2018) who find that the stellar bar in the LMC has the same star formation history as the rest of the disc, suggesting that the bar formed as a redistribution of disc material when the LMC disc became bar unstable.

Converting to stellar masses using Equation 3.2, I find that the median mass of the stellar bars is $\sim 6 \times 10^8 M_\odot$, which is comparable to the mass of the bars in other Magellanic type galaxies ($3 \times 10^8 M_\odot$ for NGC3906, de Swardt et al. 2015, for example).

4.5.5 Bulge properties

Only 10% of the offset galaxies (14 out of 131) have obvious bulges (as identified by the Galaxy Zoo volunteers), while 90% (117 out of 131) have just noticeable or no bulges. This is in striking contrast with the distribution of bulge types of the volume-limited sample of barred galaxies, of which 56% have obvious bulges and 44% are disc dominated, suggesting that the presence of an offset is also related to the absence of a considerable bulge. However, the disc dominated and obvious bulge fractions are similar to the fractions in barred galaxies of similar mass, $M_\star \lesssim 10^{10} M_\odot$ (13% and 87%). Therefore they are not unusual for the galaxies of similar mass in what the bulges are concerned; at these masses the vast majority of galaxies are disc dominated.

4.5.6 Lopsidedness

The lopsidedness or asymmetry of galaxies, as measured by the normalised amplitude A_1 of the $m = 1$ Fourier modes, has been known for a long time and has commonly observed in spiral galaxies (Baldwin et al., 1980; Rix & Zaritsky, 1995; Zaritsky & Rix, 1997; Bournaud et al., 2005b). The simulations by P16 suggests that following

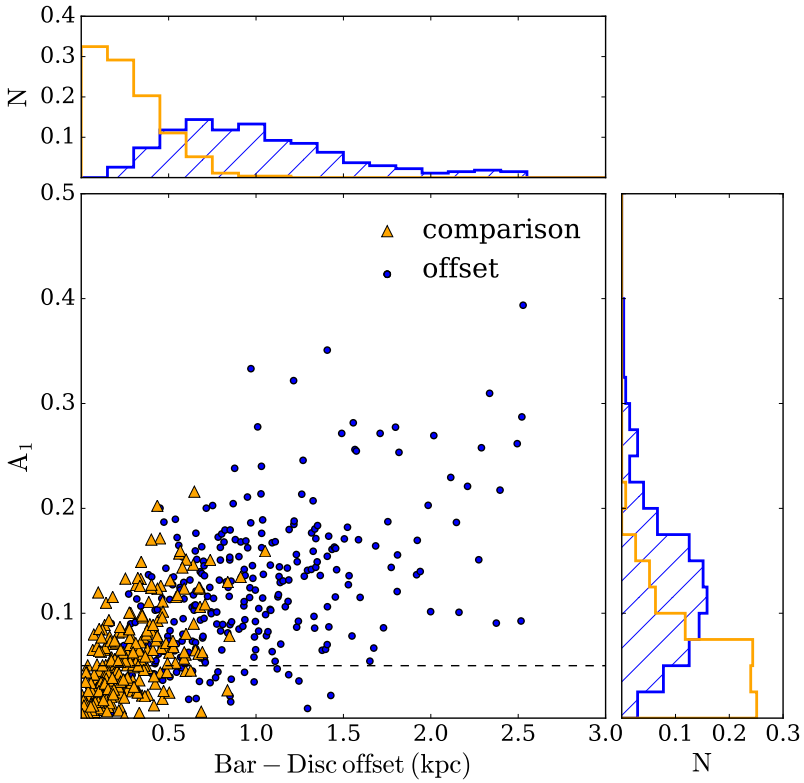

Figure 4.11: The Fourier $m = 1$ mode amplitude, A_1, correlates with the offset between the disc and the bar. $A_1 > 0.05$ is an indicator of lopsidedness, shown by the dotted line in the plot. The normalized histograms show the distributions of A_1 for the OFFSET sample and COMPARISON sample (on the vertical) and the distribution of the deprojected offsets for the two data sets (on the horizontal).

the interaction in which the bar becomes offset from the disc, the disc also becomes highly asymmetric.

Here, I measure the lopsidedness of the 271 offset systems and of the 271 mass- and redshift-matched comparison sample. For this I fit a Fourier mode to an exponential profile used to model the galaxy disc, using GALFITM, as explained in Section 2.4.5. I find that A_1 varies between 0 and 0.40, with a median of 0.12 in the OFFSET sample. In contrast, the COMPARISON sample has a median A_1 of 0.05. $A_1 > 0.05$ is an indicator of lopsidedness (unlikely to result from internal mechanisms), according to the numerical simulations by Bournaud et al. (2005b). As expected, I find a moderate, but significant correlation between the measured A_1 and the magnitude of the disc-bar offsets (Spearman rank correlation test $r_s = 0.4$, $p < 10^{-11}$), as shown in Figure 4.11. Almost all the offset galaxies are lopsided, with 90% of them having $A_1 > 0.05$, while 63% of them show strong lopsidedness with $A_1 > 0.10$. This result matches the simulation prediction in Figure 6 of P16 and suggests that the strongest asymmetry in

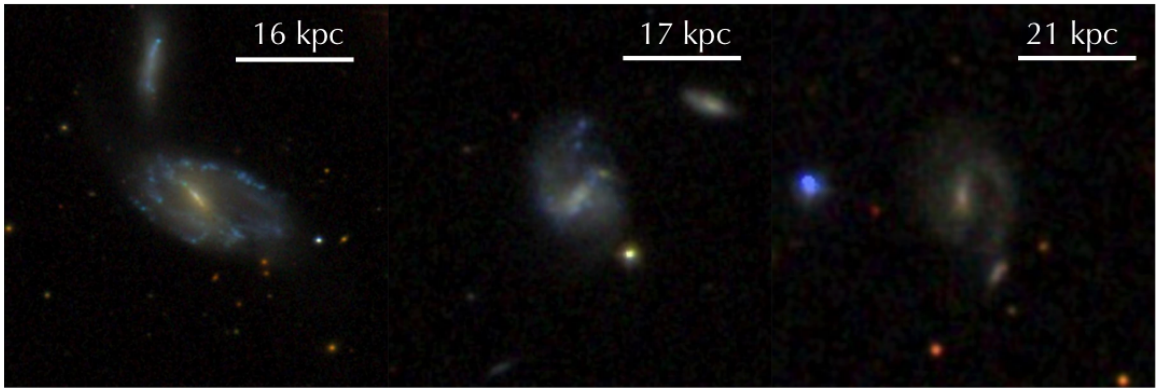

Figure 4.12: Examples of offset galaxies that have close neighbours (< 100 kpc).

the central regions of the galactic disc is produced by the off-centre bar. A K-S test on the OFFSET sample and the COMPARISON sample of galaxies with centred bars gives $k = 0.53$ and $p_{KS} < 10^{-15}$, suggesting that offset galaxies are indeed more lopsided than the galaxies with centred bars. Nevertheless, many galaxies with centred bars are also lopsided (with $A_1 > 0.05$), suggesting that lopsidedness is common at these low stellar masses.

4.5.7 Companions

To investigate the proposed origin of offsets in tidal interactions I conduct a search for companion galaxies in SDSS. In this section I use the FITTED-BAR sample, the OFFSET sample of 271 galaxies and the similar sized mass- and redshift-matched COMPARISON sample of galaxies with centred bars, as defined in Section 4.4.

I identify the closest companion in SDSS for each galaxy in the two samples by using a similar method to identify pairs as in Patton et al. (2016), Barton et al. (2000), Ellison et al. (2008) and Patton et al. (2013) – considering as potential companions only those galaxies which have measured spectroscopic redshifts by SDSS and with Δv within 1,000 km s^{-1} of the galaxy in question. The closest companion is the one with the smallest projected separation, r_p. I consider all the possible companions, without requiring any mass ratio cut.

642 out of the 3,357 galaxies (∼19%) in the FITTED-BAR sample have close companions, defined as those within a projected separation of r_p <100 kpc. With a similar fraction, 17%, 46 galaxies in the OFFSET sample have a close companion, some examples of which can be seen in Figure 4.12. An even higher percentage, 24%, or 64 galaxies out of the 271 galaxies in the COMPARISON sample have close companions, within r_p <100 kpc.

Simulations by P16 suggest that distortions in the disc can persist for 2 Gyr after the companion fly-by. Assuming a typical relative velocity of 375 km s^{-1} ($\sim$ LMC-SMC relative velocity), the offset galaxy and companion could be separated by 750 kpc at 2 Gyr after the interaction. Therefore, I check for companions within this projected distance. There are 199 offset galaxies (or 82% of the OFFSET sample) which have at least one spectroscopically confirmed companion within 750 kpc. Similarly, 86% of the galaxies with centred bars in the COMPARISON sample have at least one companion within 750 kpc. Since the separation can be used as a proxy for the time after the interaction, I plot the disc-bar separation versus the separation from the nearest companion in Figure 4.13. There is no significant anti-correlation of the offset with separation (Pearson correlation coefficient $r = 0.17$). Perhaps surprisingly, there are more galaxies with centred bars with companions within 750 kpc. However, the slight differences in close or distant companion fractions between the offset-bar sample and centred-bar comparison sample are not statistically significant. Thus, offset galaxies do not have more companions compared to similar mass and redshift barred galaxies within 750 kpc, nor more companions within 100 kpc. There are many cases of isolated offset galaxies without any apparent companion and the origin of offsets in these galaxies is puzzling.

It is important to note that there is high incompleteness in galaxies with small separations due to fibre collisions. Fibers cannot be placed closer together than 55″ which biases the mass and redshift distribution of close pairs (Ellison et al., 2008). This corresponds to 5-45 kpc separations in the redshift range of the galaxies considered here. The nearest companion search is also incomplete because of the flux limits of the survey. The limiting magnitude for the spectroscopic survey in SDSS is $m_r = 17.77$ (Strauss et al., 2002), where m_r is the Galactic extinction-corrected Petrosian magnitude. The r-band magnitudes of the galaxies in the OFFSET sample range between $12.55 < m_r < 17$, suggesting that towards the faint end limit, one is strongly biased against finding less massive companions.

Based on the limiting magnitude of the SDSS spectroscopy survey ($m_r = 17.77$) and the median magnitude of the offset galaxies ($m_r \sim 16$), the lowest luminosity of a companion that can be detected is $10^{-1.77/2.5}\ L \sim 0.2L$, where L is the luminosity of a typical offset galaxy. Assuming a similar mass-to-light (M/L) ratio for the offset galaxy and the companion (not unreasonable if both are dwarf systems, for example for the LMC and SMC have $M/L \sim 2-5$, Alves 2004; Bekki & Stanimirović 2009), the maximum mass an unseen companion can have is $10^{8.9}\ M_\odot$ (considering that the typical mass of an offset galaxy is $10^{9.6}\ M_\odot$), corresponding to a median mass ratio of 5:1. It is possible to find a 10:1 mass ratio companion only for galaxies brighter

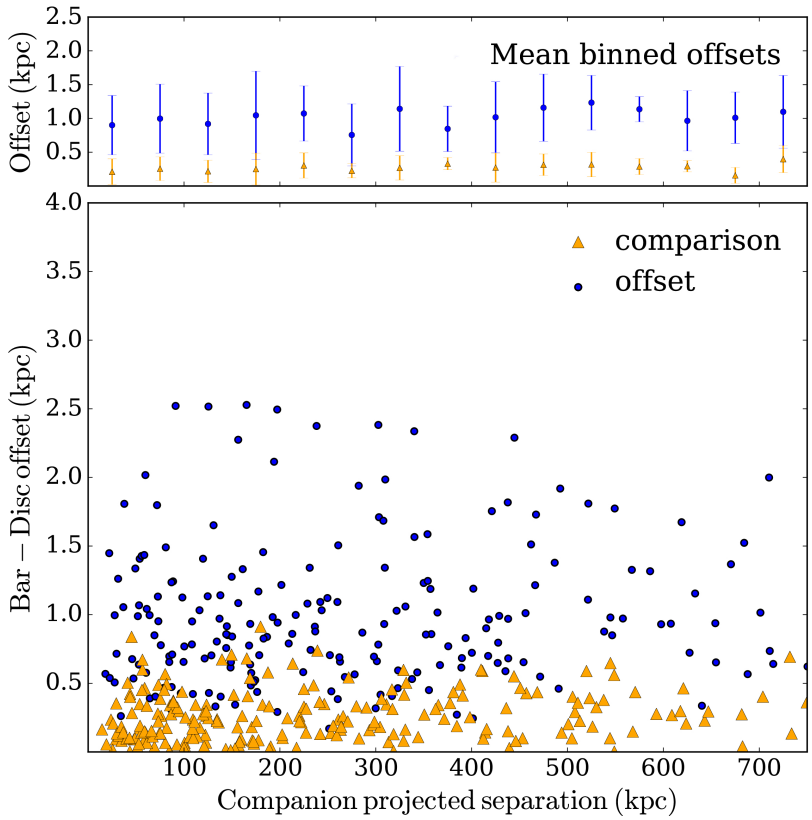

Figure 4.13: Bar-Disc offset versus the projected separation to the nearest neighbour with spectroscopic redshifts from SDSS. The top plot shows the same offset binned in separations of 50 kpc for the OFFSET sample and the COMPARISON sample. There is no clear evidence for declining offset with projected separation for the sample of galaxies with off-centre bars, the r-coefficient for a correlation being $r = 0.17$, $p = 0.01$. The mean disc-bar offset is $\sim$1 kpc across all bins for the OFFSET sample. The error bars represent 1σ in each bin.

than $m_r \lesssim 15.27$. Thus, it is likely that companion galaxies which are 10 times less massive than the offset galaxies are missed.

Possible signs of interactions can be identified if there are tidal tails or debris in the galaxy images. Inspecting the SDSS *gri* composite images for the offset galaxies I find evidence for tidal tails/debris for 59 out of 271 galaxies (22%) at the depths of the SDSS images ($m_r = 22.2$). However the SDSS images are not deep enough to reliably identify tidal debris. Deeper surveys such as SDSS Stripe 82, DECaLS (Schlegel et al., 2015) or GAMA (Driver et al., 2009) are needed to identify possible low mass companions and search for tidal features as potential evidence of interactions.

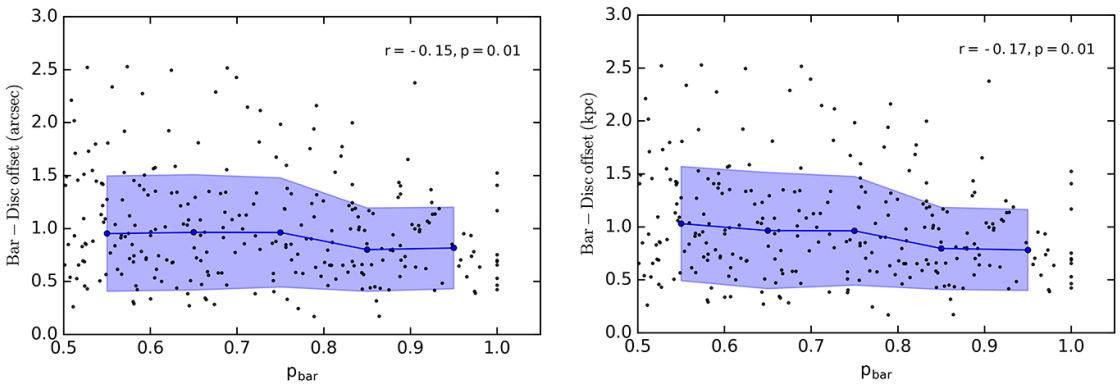

Figure 4.14: (*Left*): Projected angular offsets against $p_{\rm bar}$. (*Right*): Deprojected physical offset between the discs and the bars against $p_{\rm bar}$. The median values binned in $p_{\rm bar} = 1$ is represented with blue dots and the blue shaded area represents the 1σ spread. There is only a weak negative trend (Spearman rank correlation test $\rho = -0.15$, $p = 0.01$).

4.6 Possible biases

As shown in Figure 4.5, the image resolution plays an important role in identifying offset systems and measuring the offsets accurately. Images with better physical resolution would be useful, preferably in the infrared since this waveband better traces the underlying mass distribution of the galaxies, for a more accurate measurement of the offsets. In Section 7.2.3 I discuss how I plan to achieve this with data from the S^{4}G survey.

One caveat for this work is that the galaxies discussed in this chapter were selected with $p_{\rm bar} \geq 0.5$ and thus correspond to strong bar cases. One might worry that, since the offset galaxies have lower masses and might host weak bars, a significant fraction of these galaxies might be missed by imposing such a high threshold and, therefore, the selection might be biased against very offset systems. I checked for possible correlations of the offsets with $p_{\rm bar}$ and found only a weak negative correlation (Spearman rank correlation coefficient $r_s = -0.15$, $p = 0.01$) for both the projected angular offsets and deprojected physical offsets (Figure 4.14). The offset trends are relatively flat with $p_{\rm bar}$ up until $p_{\rm bar} \sim 0.8$, where the median offset declines slightly. The galaxies with the largest bar likelihood are the ones having unambiguously strong and long bars, and these galaxies usually have the highest masses and are bulge dominated. I previously found that there are very few high mass galaxies with offsets (only 12% of the galaxies with offset have masses larger than $10^{10.3} M_{\odot}$), therefore this explains the negative trend at large $p_{\rm bar} \geq 0.8$. The trend of the disc-bar offsets below $p_{\rm bar} < 0.8$ is relatively flat, suggesting that there is no bias against galaxies with very large offsets, otherwise there would be a clear negative correlation, peaking

at $p_{\rm bar} \approx 0.5$ - the threshold of this sample. Nevertheless, this does not mean that there are no galaxies with offsets at $p_{\rm bar} < 0.5$. It is very probable that the flat trend continues below this threshold, however selecting a sample with a lower bar likelihood cutoff (for example weak bars $0.2 \leq p_{\rm bar} < 0.5$), would produce a sample which included many galaxies without bars, as discussed in Section 2.3.2.

4.7 Discussion

4.7.1 What are the properties of offset galaxies?

In this study, I find that offsets between discs and bars are characteristic to low mass galaxies, with a typical mass of $10^{9.6}$ $M_{\odot}$ (which is similar to the mass of the Large Magellanic Cloud). 32% of barred galaxies at this mass show offsets. Only a small percentage (2%) of barred galaxies with stellar masses $M_{*} > 10^{10.3}$ $M_{\odot}$ (which is the median of the sample of barred galaxies) show offsets, and these galaxies have probably undergone minor mergers recently. Furthermore, only 10% of the offset galaxies have an obvious bulge suggesting a correlation between the offsets and the lack of a significant bulge.

The lack of significant bulges in the offset galaxies suggests that the growth of bulges and, thus the increase in stellar velocity dispersion (as discussed in Section 1.1), stabilises the disc, preventing it from moving around the centre of mass of the galaxy, and it can be an explanation for the observed distribution of stellar masses of the offset galaxies. In high mass galaxies, a significant fraction of the galaxy mass is in the bulge and in the bar ($B/T \sim 0.14$ and $Bar/T \sim 0.14$, as found in Sections 3.4.3 and 3.3) which will produce a steeper potential well. Being highly concentrated, the inner components will reduce the self-gravity of the disc and it will prevent the disc from shifting significantly due to an interaction. This transition from a rotation supported stellar disc to one having a concentrated central component might be sufficient to stabilise the disc.

It would be possible to find the same distribution of stellar masses for offset galaxies if low mass galaxies have a much higher interaction rate compared to high mass galaxies, assuming that the offsets between discs and bars are truly caused by interactions. Robotham et al. (2012) showed in the GAMA survey (and similarly Liu et al. (2011) in the SDSS survey) that there is a ∼12% chance for a galaxy with a similar mass to the Milky Way to have a companion at least as massive as the LMC (thus with a 10:1 mass ratio), at a distance corresponding to the Milky Way-LMC distance. In this volume-limited study, I have shown that only 2% of the galaxies with the mass of the Milky Way (between $10^{10.5} - 10^{11.1}$ $M_{\odot}$) have offset bars, and

even these are disturbed and show signs of recent minor mergers, while the fraction of galaxies with masses $10^9 - 10^{10}$ $M_\odot$ having offset bars is as much as 30%. If an interaction with a lower mass galaxy is equally likely to cause an offset, regardless of the mass of the main galaxy, it is very improbable that the interaction rate for low mass galaxies is ~ 10 times higher (basically all LMC-like galaxies would need to be in pairs). In fact, in the same study, (Robotham et al., 2012) finds only a $\sim 5\%$ chance of finding an LMC-SMC close pair analogue, twice smaller than finding a Milky Way-LMC pair. Therefore, the observed lack of high mass galaxies with offsets is very unlikely to be explained by a lower interaction rate compared to low mass galaxies.

The low mass tail of the distribution $< 10^9$ $M_\odot$ can be explained by a combination of the magnitude limit of SDSS, missing low mass galaxies (with measured spectroscopic redshifts) at increasing redshifts and by the lack of bars in low mass galaxies. In Chapter 3, I find that bars are only identified in galaxies with stellar masses $> 10^8$ $M_\odot$, similar to the mass of the Small Magellanic Cloud, thus placing a constraint on the minimum stellar mass a galaxy can have to form a bar. Deeper observations are needed to confirm whether galaxies with masses $< 10^8$ $M_\odot$ host bars and further simulations are need to investigate whether such low mass dwarfs are sufficiently cold dynamically to undergo bar instabilities.

In this chapter I find that offset galaxies are significantly lopsided, 90% of them having $A_1 > 0.05$, and the lopsidedness correlates with the disc-bar offsets. Similar mass galaxies with centred bars are also lopsided, but less so compared to offset galaxies. Other authors have also found significant lopsidedness in stellar discs, but correlations with a bar or offset bar are contradictory. For example, using a sample of 149 galaxies observed in the infrared, Bournaud et al. (2005b) show that a large fraction of disc galaxies are lopsided and that the the presence of $m = 2$ spiral arms and bars correlates with the $m = 1$ amplitudes. Similar to this work, they find that strong lopsidedness is not correlated with the presence of interacting companions. In the absence of perturbers, they attribute at least a fraction of the observed lopsidedness to cosmological accretion of gas. More recently, Zaritsky et al. (2013) found, using late-type galaxies in the S^{4}G survey, that lopsidedness is a generic feature of galaxies that does not depend on rare events such as the accretion of a satellite, otherwise the incidence of accretion or fly-bys (1 every 100 Myrs) would be larger than what we expect. They found an average value of lopsidedness of $\langle A_1 \rangle = 0.15$ in local barred galaxies in the S^{4}G survey, in good agreement with the median lopsidedness of the offset bars, but higher compared to the lopsidedness of galaxies with centred bars. They suggest that the lopsidedness is not correlated with the presence and strength

of a bar, as many non-barred galaxies are also lopsided, however they did not make a distinction between galaxies with off-centre bars and those with centred bars.

4.7.2 What is the origin of the offsets between disc and bars?

A widely suggested origin for the offsets is galaxy interactions. An interaction between the LMC and the SMC has been used to explain the offset bar in the LMC (Besla et al., 2012; Yozin & Bekki, 2014; Pardy et al., 2016). There is evidence that the two galaxies have been interacting and that the disturbed appearance of the LMC is not due to an interaction with the MW, for example in the observations of the Magellanic Bridge (bridge of HI gas between the two Magellanic Clouds, Kerr 1957) and of the leading and trailing streams of gas (Leading Arm and Magellanic Stream, Wannier & Wrixon 1972, although the origin of these streams has been debated, e.g. Bekki & Chiba 2005; Besla et al. 2010). Choi et al. (2018) attributes the ring-like structure observed in the intermediate-age stars in the LMC to either repeated encounters with the SMC (forming a one-armed spiral that is wrapped around the body of the LMC) or a direct collision with the SMC. Such a ring, although star forming, is observed in NGC 922, a galaxy which also shows evidence for an offset bar (Elagali et al., 2018). The formation of this ring is attributed to a collision with a companion galaxy situated at a projected distance of 102 kpc from NGC 922. In this study, only 10 out of the 271 offset galaxies show evidence for a ring-like morphology in the SDSS *gri* images, indicating mergers. Furthermore, $\sim 20\%$ of offset galaxies show evidence for tidal debris/tails in the *gri* composite SDSS images, however deeper images are needed to reliably identify tidal tails.

In this work I do not find a correlation between the offsets and the presence of companion galaxies. Galaxies with centred bars have a similar number of companions as those with offsets, within 100 kpc or 750 kpc. Still, tidal interactions between the galaxies and small companions, as suggested by P16, cannot be ruled out. The incompleteness due to the flux limit of SDSS and fiber collisions at the smallest separations make the closest spectroscopic companion hard to identify. Future spectroscopic observations of potential candidate companions should be able to help identify physical companions. Another possible explanation for the missing companions are high velocity dwarfs on eccentric orbits that are now too far away to appear associated with the primary galaxy, especially if the timescales in which the offset is restored is long (~ 2 Gyr), as suggested by the simulations of P16.

Furthermore, these simulations concern only the case of the LMC-SMC interaction (or of galaxies of similar masses). Further simulations of galaxy interactions that better explore the parameter space (mass ratios of the galaxies, relative velocities and

impact parameters) and constrain how long the offset lasts in different galaxy interactions, how far can the companion galaxy can reach while the offsets are still visible and whether star formation is enhanced in such an interactions are needed. Interactions might explain the offset bar in a fraction of the offset galaxies, for which companions are detected or those showing tidal features, including the Large Magellanic Cloud.

Despite not being able to identify all the physical companions, the large number of isolated offset and lopsided galaxies in this study and other studies (Feitzinger, 1980; Wilcots & Prescott, 2004) is puzzling. Different explanations for the offsets seen in some galaxies should be considered. One suggested origin is the interaction with 'dark' satellites, with no or very few stars (Bekki, 2009). This could produce an offset bar seen in the older stellar populations, as is observed in the case of the LMC. Some simulations of the SMC-LMC interaction do predict the formation of an offset bar in the LMC, but with young stars formed from asymmetric gas due to star formation being enhanced in the interaction (Bekki & Chiba, 2007). Cosmological simulations predict the existence of many dark matter subhaloes with masses $10^6 - 10^8\,M_\odot$ (Madau et al., 2008), but which are not detected because of the possible lack of visible matter (referred to as the 'missing satellite problem', Moore et al. 1999; Klypin et al. 1999). Dark matter subhaloes with masses $\sim 10^8\,M_\odot$ with no or little matter could in theory exist, as a minimum mass of $10^9\,M_\odot$ was found to be needed for gravitational collapse to form galaxies (Strigari et al., 2008). Deep observations indeed reveal ultra faint dwarf galaxies that can populate $\sim 10^9\,M_\odot$ dark matter haloes (Simon & Geha, 2007). Interactions with dark matter subhaloes could be the origin of offsets in galaxies with unidentified companions.

Another plausible explanation is the asymmetry of the dark matter haloes, manifested as a lopsided (Jog, 1997, 1999) or a triaxial halo (Jog, 2000). The dark matter halo is far more extended than the galactic disc, thus it is susceptible to distortions. If galaxy interactions are common, one should expect them to primarily have an effect on the dark matter haloes, perturbing the distribution of the dark matter (Weinberg, 1995). If the halo becomes displaced, one would expect the baryonic matter to trail and re-centre in the new centre of the halo. As suggested by simulations, the bar would centre faster in the centre of the potential compared to the disc. Lopsided haloes may also form via the accretion of dark matter following cosmological perturbations. The dynamics of stars in a galactic disc as a response to a perturbed halo potential has been studied by Jog (1997) and Jog (1999) and has been shown to lead to lopsided discs, such as the discs of M101 and NGC 1637 (Sandage, 1961). Since lopsidedness is so commonly observed in the Universe, it implies that asymmetries are long lived. In this work I find a correlation between the off-centre bars and the

galaxies being lopsided. The asymmetries in the dark matter halo could also lead to the observed offsets and this might explain the missing companions. In the following chapter I discuss this possibility further, by studying the kinematics of gas and stars in offset galaxies using spatially resolved integral field spectroscopic data from the MaNGA survey (Abolfathi et al., 2018).

A last possibility is that the $m = 1$ modes and offset bar arise naturally in galaxies of these stellar masses, and external perturbation or global asymmetry in the mass distribution explanations are not needed. Zasov & Khoperskov (2002) find in N-body simulations of collisionless discs that a long-lived offset bar is produced as a result of the $m = 1$ mode interfering with an $m = 2$ mode, if the mass of the disc dominates over the mass of the halo throughout the disc. However, these simulations predict only a small offset ($\sim 5\%$ of the size of the disc), while the typical offsets observed in this work are three times larger. Therefore, this is not a preferred scenario for the origin of most of the offset bars.

4.8 Conclusions

In this study using morphological classifications from the Galaxy Zoo project and photometric decomposition I identified a sample of 271 barred galaxies with a bar that is offset from the photometric centre of the discs (out of ∼3,500 galaxies with strong bars), in a first systematic search for such systems in SDSS data. This has been an understudied topic and the origin of such offsets is unknown. Below I summarise the results of this study:

(i) The vast majority of these galaxies have similar properties to the Large Magellanic Cloud: similar masses, optical colours and measured bar offsets. These galaxies are highly asymmetric, and the offsets between the disc and the bar are an explanation of their lopsidedness.

(ii) My observations show that offsets are characteristics of low mass systems only, with typical masses between $10^9 - 10^{10}\ M_\odot$. 30% of galaxies at these masses show offsets. Only very few (2%) high mass barred galaxies (for example with a similar mass as the Milky Way) show offsets, which suggests that high mass galaxies are stable against disc-bar displacements. I suggest that the growth of bulges and thus the increase in velocity dispersion stabilises the discs and bar from shifting with respect to each other. This hypothesis should be tested in future simulations.

(iii) It is believed that these offsets trace minor interactions, however, I do not find statistically significant evidence of a correlation with the nearest companions, even though the measured physical offsets match the predicted values from simulations of tidal interactions. This could be due to the incompleteness of the SDSS spectroscopic survey at the faint flux limit and observations of possible companion candidates should be done in order to confirm their spectroscopic redshifts.

(iv) Many isolated galaxies show evidence of an offset bar, which cannot be attributed to a dwarf-dwarf interaction. Other possible explanations for the offset should also be considered, such as an interaction with a dark matter subhalo or a perturbation in the dark matter halo potential.

There are still many questions related to the appearance of Magellanic Irregulars and other dwarf systems, for example what gives rise to the lopsidedness in these galaxies? is lopsidedness long-lived or transient phenomena? how do bars form in these galaxies? Although they got the attention of the astronomical community in the 80's-90's, they have not been in the focus of astronomical reseach in the last few decades. Yet, there is an increasing prospect to study such systems since they are frequent in the Universe and they are good laboratories to study the properties of dark matter.

Chapter 5

Kinematics of barred galaxies

One puzzle regarding the galaxies with offset discs and bars identified in Chapter 4 is identifying which of the two components is centred on the dark matter halo that dominates the galaxy potential. Here, I study the Hα gas and stellar kinematics of galaxies with offset and centred discs and bars, using data from the MaNGA survey. I model the kinematics of these galaxies using a harmonic decomposition with DISKFIT. I investigate the relation between the gas and stellar kinematic centres and the bar and disc photometric centres. I measure the asymmetries in the rotation curves and determine the possible perturbations in the potential due to a lopsided dark matter halo. Finally, I measure the non-circular distortions in the gas velocity fields and place constraints on the ellipticity of the dark matter haloes.

5.1 Motivation and background

In Chapter 4 I studied the photometric offsets between discs and bars in barred galaxies in SDSS and found that offsets between 0.2 and 2.5 kpc are identified predominantly in lower mass galaxies (with masses $M_* \sim 10^9 - 10^{10}\ M_\odot$), and that interactions might not be the only cause of the offsets since many offset galaxies appear to be isolated. The questions that arise, since the bar and the disc are offset from each other in these galaxies are: (1) which, if any, of the two components is located at the dynamical centre of the galaxies (the location where the galaxy potential is deepest, corresponding roughly to the centre of the dark matter halo)? and (2) what is the origin of the offsets?

Dark matter is the dominant mass component in galaxies, thus it affects how stars and gas rotate. The shape of the dark matter profile has been the subject of

ongoing debate. Simulations predict that the dark matter haloes are triaxial (Frenk et al., 1999; Hayashi et al., 2004) and have profiles that fall off as r^{-1} (known as a 'cusp' profile, Hernquist 1990; Navarro et al. 1996). However, observations of the kinematics of galaxies, especially of dwarf galaxies which are believed to be dark matter dominated[1](Carignan & Freeman, 1988; de Blok & McGaugh, 1997), suggest a flat density of dark matter at the centre of galaxies (a 'core' profile, McGaugh & de Blok 1998).

As presented in Section 4.2, Pardy et al. (2016) (hereafter P16) investigated the relation between the dynamical, stellar and gas kinematic centres in N-body+SPH simulations of offset galaxies during an encounter with a lower mass galaxy. The dynamical centre in the simulations was measured as the centre of mass of the 100 particles with the most negative potentials. The fraction of dark matter, stellar or gas particles within these 100 particles depends on the model chosen for the dark matter potential. In both 'cusp' and 'core' models, the centre of the dark matter halo (measured as the centre of mass of dark matter particles only) realigned rapidly with the dynamical centre after the interaction (within $\sim$ 100 Myr), thus the two centres are consistent with each other. In this work, I consider that the location where the potential is deepest corresponds to the centre of the dark matter halo and refer to it as the 'dynamical centre'. As P16 mentions, the offsets between the two are minimal, except during the encounter. As shown in Section 4.5.7, only few offset galaxies are seen during the encounter, and many show offsets without a nearby companion, suggesting that the offsets are long lived.

P16 showed that following the fly-by of a lower mass galaxy, the bar centre (as measured from ellipse fitting) always coincides with the dynamical centre of the galaxy, while the stellar disc is offset. As shown with the dotted lines in Figure 5.1 the gas initially becomes offset from the dynamical centre and undergoes damped oscillations, similarly to the stellar disc, but realigns faster (within $\sim$ 0.5 Gyr) with the dynamical centre (and thus with the bar) compared to the stars (which realign only after $\sim$ 2 Gyr). The physical reason for the offsets and subsequent damped oscillations is that both the offset disc of stars and gas feel a torque in the gravitational potential of the galaxy, this torque being larger at smaller radii. The difference in the torques makes the orbits at smaller radii precess faster than at outer radii and since the orbits of gas and stars in the offset disc are no longer circular, this leads to orbits crossing (van de Voort et al., 2015). Gas is collisional, thus when orbits intersect the gas will lose energy and will change its velocity, falling faster to the bottom of the potential

[1]Although see the latest debate about the an ultra diffuse galaxy allegedly lacking dark matter (van Dokkum et al., 2018; Martin et al., 2018; Trujillo et al., 2018).

well. The motion of stars in the disc, on the other hand, is collisionless, thus, once disturbed, it will take longer to align with the dark matter halo than the gas.

In the simulations of P16, the centre of the gas velocity field was measured by fitting a bisymmetric model (since the gas can be susceptible to distortions caused by a bar potential at the galaxy centre) using the two-dimensional velocity fitting code DiskFit (Spekkens & Sellwood, 2007; Sellwood & Sánchez, 2010). The velocity field of the stellar component was found to be displaced by $\sim 0.5-1$ kpc (although the 1σ error range is considerable) from the dynamical centre (shown by the brown line in Figure 5.1), as measured by fitting a linearly rising function up to a turnover radius and a flat velocity beyond this radius.

In this chapter I use the following definitions for the different centres investigated:

- **dynamical centre** - centre of the potential (corresponding roughly to the centre of the dark matter halo for the dark matter dominated dwarf galaxies)
- **gas kinematic centre** - centre of the Hα rotation curve, as measured from the MaNGA Hα kinematic maps
- **stellar kinematic centre** - centre of the stellar rotation curve, as measured from MaNGA maps
- **bar centre** - the photometric centre of the bar (peak of stellar distribution), as measured from the multi-band decompositions of SDSS images, described in Chapter 2
- **disc centre** - the photometric centre of the disc, also measured in the decompositions and described in Chapter 2.

In reality it is difficult to measure the location of the dynamical centre in galaxies since the dark matter is not directly observable. Usually, it is assumed that the dynamical centre of galaxies is traced by the HI gas, since the gas is most susceptible to the underlying potential. In theory, for an unperturbed galaxy, the dynamical centre, the kinematic centre of gas and stars and the photometric centres should all coincide. Therefore, the gas and stars should have the same centre as they both orbit in the same potential.

In the nearest example of an offset galaxy, the LMC, the different centres (kinematic centre of gas, as measured from HI rotation curves, Kim et al. 1998; kinematic centre of stars, traced by line of sight velocity measurements of carbon stars, van der Marel et al. 2002, or stellar proper motions, Kallivayalil et al. 2006; photometric centres of the disc and bar components, Cole et al. 2005), are not spatially coincident,

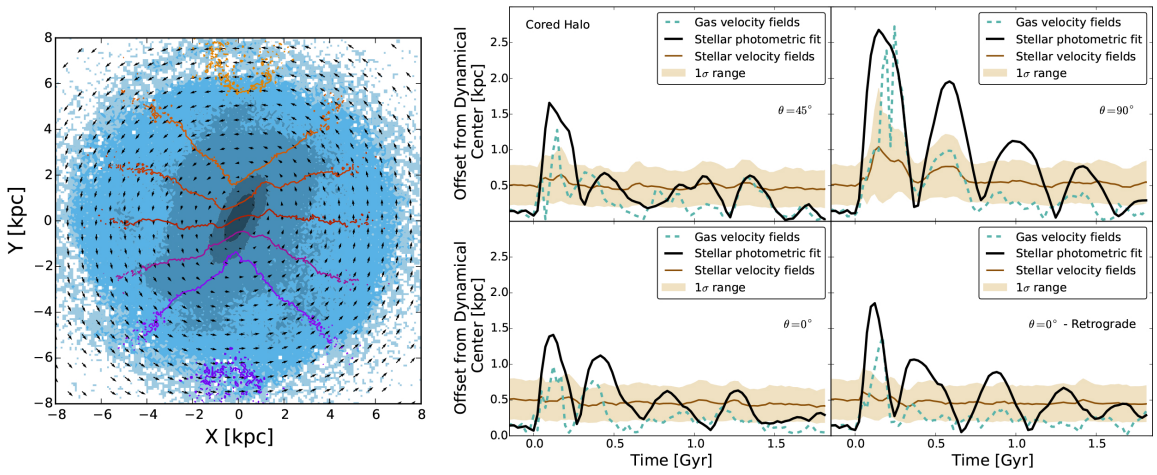

Figure 5.1: *Left*: Velocity fields of the stellar components (plotted with arrows) and gas components (coloured contours) before the collision from P16 (original Figure 7). *Right*: The time sequence of the offsets between the gas kinematic centre (dotted line), stellar velocity fields (brown line), the disc photometric centre (black line) and the dynamical centre for four encounters with different orbital configurations from P16 (their Figure 8).

although some recent studies suggest that the gas and stellar kinematic centres are closer than previously thought (van der Marel & Kallivayalil, 2014). The HI gas was found to be centred on the bar component and offset from the disc in other offset galaxies, for example in NGC 3906 (de Swardt et al., 2015) and NGC 4027 (Pence et al., 1988).

Many galaxies show a lopsided morphology (Rix & Zaritsky, 1995), suggesting that asymmetry is a long-lived phenomenon, not necessarily linked to interactions. A more general phenomena, the existence of lopsided dark matter haloes, has been used to explain the asymmetric appearance of galaxies such as M101 (Jog, 1997). Jog (1999) has shown that a lopsided ($m = 1$) halo potential can disturb an axisymmetric disc, imprinting a lopsidedness that is 0.5-0.7 smaller than that of the halo, especially in the outer parts, if the disc self-gravity is small. Jog (2000) also argues that a similar lopsidedness can be imprinted in the discs by an ($m = 2$) elliptical perturbation in the potential, which is reduced by a factor of 0.75-0.9 in the potential of the disc, since the disc self-gravity resists the imposed potential.

In Chapter 4 I found that offset galaxies have, in general, low masses and lack large bulges with significant self-gravity that can stabilise the discs. In addition, the offsets are correlated with the lopsidedness of galaxies; the offset galaxies are more asymmetric than other galaxies with similar masses. Thus, it is plausible that a perturbed dark matter halo is the origin of the observed asymmetry in the offset galaxies and of the offsets between the disc and the bar. Jog (2002) predicts that

such an $m = 1$ lopsided halo can give rise to large scale asymmetry in the rotation curve of galaxies, such that there is a measurable difference between the approaching and receding sides of the rotation curves, referred to as kinematic lopsidedness. The rotation velocity is maximum in the direction of the maximum of the halo perturbation and minimum along the opposite direction. The perturbation parameter, $\epsilon_{\rm kin}$, of the lopsided potential can be estimated from the difference in the two sides of the rotation curves (Jog, 2002) as

$$\epsilon_{\rm kin} = \frac{V_{\rm app} - V_{\rm rec}}{2V_{\rm c}}, \tag{5.1}$$

where $V_{\rm app}$ and $V_{\rm rec}$ are the velocities on the approaching and receding sides of the rotation curve, respectively, and $V_{\rm c}$ is the circular velocity, calculated as the average between the two opposite sides, in the flat part of the rotation curve (see Jog 2002 for the derivation). Swaters et al. (1999) found that the HI kinematics of two photometrically lopsided spiral galaxies (DDO 9 and NGC 4395) are also lopsided, suggesting that a 5%-10% perturbation of the potential can give rise to a 10-20% difference between the rotation curves of the approaching and receding sides.

Alternatively, if the halo is triaxial (having an elliptical $m = 2$ perturbation), it is possible to estimate the ellipticity of the halo based on the higher order moments in the velocity field in the outer regions of the galaxies. Schoenmakers et al. (1997) showed, by expanding the velocity field in higher order harmonics, that if the potential has a distortion of harmonic number m, the velocity field as seen on the sky will show $m' = m - 1$ and $m' = m + 1$ distortions. Therefore, a lopsided $m = 1$ halo will result in $m' = 0$ and $m' = 2$ modes in the line of sight velocity field, while an elliptical $m = 2$ halo will show $m' = 1$ and $m' = 3$ terms. Thus, non-spherical dark matter haloes give rise to mild deviations from circular motions in the outer disc regions (Jing & Suto, 2002; Hayashi et al., 2007). The observations of these motions is complicated by the fact that $m = 2$ distortions in the potential are induced by bars or spiral arms as well, and superimposed on (weaker) oval perturbations of the halo.

If, on the other hand, the halo is round but an offset between the dark matter halo and disc exists, as suggested by Levine & Sparke (1998), the gas kinematics will be affected, such that, in case of a retrograde rotation of the disc relative to its orbit around the halo, one side (towards the centre of the halo) of the rotation curve will be rising, while on the other side, the rotation curve is flat, as shown by Noordermeer et al. (2001). In both models, of a lopsided halo or a halo misalignment, the largest (long-lived) kinematic lopsidedness is in systems where the dark halo dominates the mass distribution, thus it is expected for dwarf galaxies to show higher kinematic lopsidedness.

In this chapter I investigate the relation between the photometric centres of the bar and of the disc, measured from the SDSS imaging, and the centres of the stellar and gas rotation measured from the SDSS MaNGA survey, for a sample of offset galaxies and a sample of galaxies with centred bars, with the aim of testing the kinematic predictions from the fly-by simulation of P16. If the gas disc re-centres on the dynamical centre, in a relatively short time, while the stellar disc is still 'sloshing', one would expect the centre of the gas kinematics to trace the centre of the bar component, while the stellar kinematics to be offset from both in the offset systems.

Furthermore, I test if the dark matter haloes of these galaxies are $m = 1$ or $m = 2$ lopsided. For galaxies that show asymmetric rotation curves, I estimate the perturbation of the lopsided potential by comparing the approaching and receding sides of the rotation curves. By measuring the amplitude of the non-circular motions in the gas kinematics in the outer regions of galaxies, I measure the ellipticity of the dark matter haloes, for both offset galaxies and galaxies with centred bars. Evidence for a perturbation in the halo being the cause of offsets would be a difference in the estimated perturbation or halo ellipticity for the two types of galaxies.

To investigate these effects, I model the Hα gas and stellar kinematics for a representative sample of barred galaxies observed in the MaNGA survey, with both offset and centred bars. I first illustrate the method in quantifying the kinematic lopsidedness and fitting the kinematic centres in Section 5.2. I then discuss the modeling of kinematics with DiskFit in Section 5.3, where I also quantify the departures from circular motions in the gas velocity fields which can be produced by non-axisymmetric structures such as bars, spiral arms or an oval halo. I apply all these techniques for a sample of barred galaxies selected based on the photometric decompositions described in Chapter 2 and integral field spectroscopic observations from the MaNGA survey. The sample selection is discussed in Section 5.4. In Section 5.5 I present measurements of the alignment between gas, stellar and photometric axes, the offsets between the kinematic and photometric centres, the perturbation in the potential and the amplitude of non-circular motions in the velocity fields. Finally, in Section 5.6 I compare the results to other studies and simulations.

5.2 Case study - J161931.90+413945.2

In order to demonstrate the method in determining the kinematic centres of galaxies and the lopsidedness parameter ($\epsilon_{\rm kin}$) for a possible $m = 1$ perturbation, I consider the case study of a typical galaxy with an offset disc and bar. J161931.90+413945.2

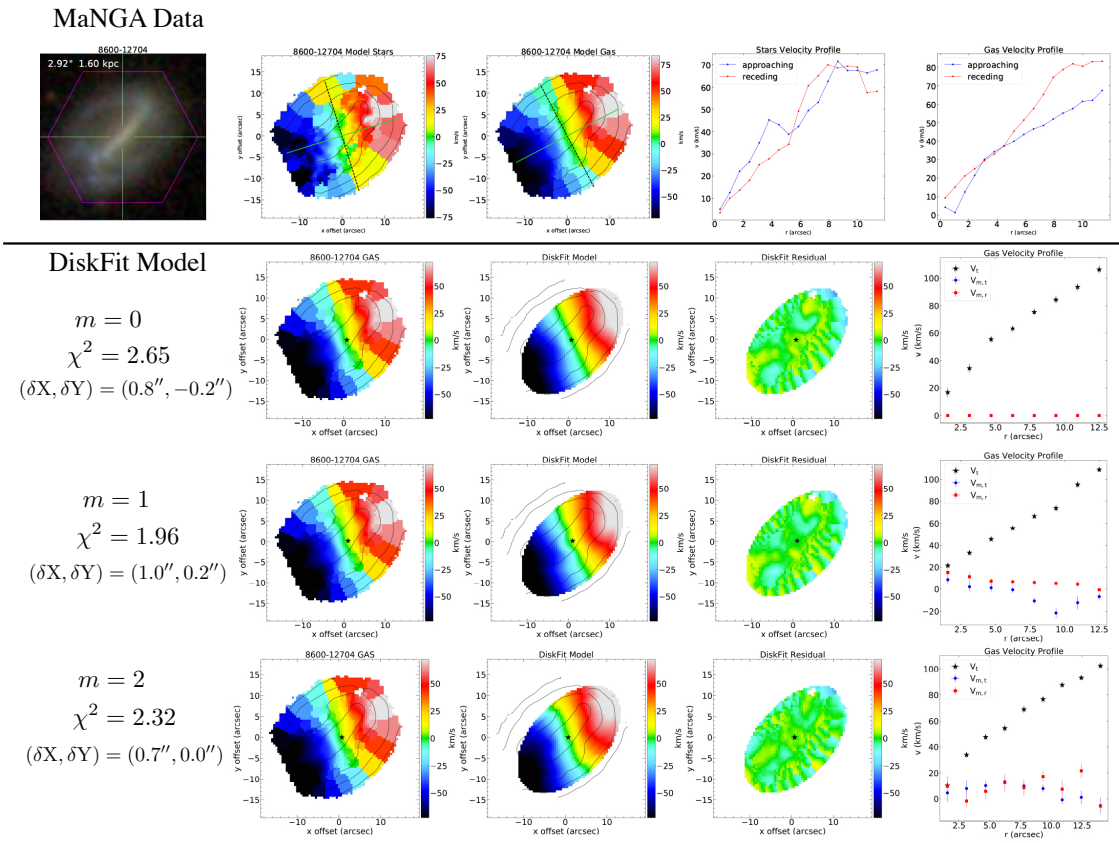

Figure 5.2: *Top panel*: The stellar and Hα kinematics of 8600-12704, identified to have an offset between the disc and the bar. The galaxy shows lopsided kinematics, one side of the galaxy rising faster than the other and flattening out at large radii. *Bottom panels*: Different harmonic models ($m = 0$ - pure rotation, $m = 1$ - lopsided and $m = 2$ - bisymmetric model) for the gas velocity fields of 8600-12704 and the corresponding residuals. The centres of the velocity maps are shown with a star on the velocity maps, and the reduced χ^2 is shown on the left.

(shown in the *top left panel* of Figure 5.2) is a galaxy at redshift $z = 0.027$, with a stellar mass of $M_* \sim 10^{9.9}\, M_\odot$ which was found in Chapter 4 to have a bar offset from the disc centre by $2.92''$, corresponding to a projected offset of 1.6 kpc. The two-dimensional stellar and Hα gas kinematics of this galaxy as observed by MaNGA (*id* 8600-12704, shown within the MaNGA IFU hexagon), and reduced by the MaNGA Data Analysis Pipeline, are shown in the *top panel* of Figure 5.2.

Both the stellar and Hα gas kinematics show regular rotation, typical for disc galaxies, with one side of the galaxy receding and the other one approaching (*top right panel* of Figure 5.2). The stellar kinematics map is noisier than the gas kinematics, the galaxy being gas-rich. The MaNGA IFU was approximately centred on the optical centre of the bar component, where the peak of the stellar distribution of

the galaxy (brightest pixel) is located. Observing the gas rotation curve on either side of the kinematic axis (*top right* panel of Figure 5.2), it is evident that this galaxy is kinematically lopsided. It shows an asymmetric rotation curve since the approaching side does not match the receding side. Also, the rotation on the receding side of the galaxy rises more slowly than that on the approaching side, and it does not flatten out. Such an asymmetry in the kinematics can be typical for low mass galaxies.

Determining the location of the kinematic centre is not possible from the velocity profile alone. It is, however, possible to fit the velocity field with models in which the residual is minimised, thus the asymmetry between the two halves of the rotation curves is minimised as well, and determine the centre of such a model. I fit the gas velocity field with a pure rotation ($m = 0$) model, a lopsided model with $m = 1$ perturbations to the potential and a bisymmetric model with $m = 2$ perturbations to the potential. The fitted model is based on Equation 5.3 and is described further in Section 5.3. The different models are shown in the lower panels of Figure 5.2. The model with the lowest reduced χ^2 is the $m = 1$ model ($\chi^2 = 1.96$), as expected given the asymmetry in the rotation curve. The kinematic centre in this model is located at $(\delta X_{\rm k,g}, \delta Y_{\rm k,g}) = (1.0'', 0.2'')$, corresponding to a distance of $1''$ from the centre of the IFU, or 0.6 kpc. For simplicity, given the noise in the stellar kinematics, I fitted the stellar velocity map with pure rotation $m = 0$ model (I have found this model to be adequate for the stellar velocity fields of the majority of galaxies, within the noise in the data). I measure a stellar kinematic centre located at $(\delta X_{\rm k,s}, \delta Y_{\rm k,s}) = (-0.5'', -0.8'')$, also corresponding to $\sim 1''$ from centre of the IFU, or 0.6 kpc. Re-centering the data on the newly determined kinematic centre for Hα gas, the difference between the approaching and receding sides of the rotation curve is $\Delta V \approx 13$ km s^{-1}, which, considering a circular velocity of $V_{\rm c} \approx 77$ km s^{-1}, corresponds to a perturbation of the potential of $\epsilon_{\rm kin} \approx 0.084$.

Therefore, in this particular galaxy, both the gas and stellar kinematic centres are offset from the IFU pointing centre, and thus offset from the bar component, by 0.6 kpc, similar to the case of the LMC.

As illustrated for J161931.90+413945.2, it is possible to determine the centres of gas and stellar kinematics by fitting adequate models to the velocity fields and to calculate the possible ($m = 1$) distortion of the dark matter halo, from the difference between the receding and approaching velocity sides (normalised by the circular velocity). This method is applied to ~ 200 barred galaxies, the selection of which is described in Section 5.4, while the kinematic modeling is described in Section 5.3.

5.3 Kinematic model

5.3.1 DiskFit

To model the kinematics of galaxies I used the publicly available DiskFit code[2] (Sellwood & Sánchez, 2010), which is an extension of the original *velfit* routine (Spekkens & Sellwood, 2007). Sellwood & Sánchez (2010) has shown that DiskFit can be used to estimate the magnitudes of non-circular motions in galaxies, from strong distortions due to strongly barred galaxies to mild bar-like distortions and mild distortions in the outer regions of galaxies, which can place bounds on the ellipticity of the dark matter haloes. Since the galaxies considered in this study are barred and the aim is to estimate the non-circular motions, it is the ideal tool to use.

DiskFit creates physically motivated models from the observed rotational velocities using a χ^2 minimization technique (Barnes & Sellwood, 2003). The simplest kinematic model for a galaxy is a pure rotation ($m = 0$) model:

$$V_{\rm model}(r) = V_{\rm sys} + V_{\rm c}(r) \sin i \cos\theta \tag{5.2}$$

where $V_{\rm model}(r)$ is the modeled rotation , $V_{\rm sys}$ is the systemic velocity (due to Hubble flow and the peculiar velocity of the galaxy), $V_{\rm c}$ is the mean rotation velocity, i is the inclination of the disc and θ is the angle made with the kinematic major axis.

DiskFit is designed to fit non-circular models of galaxy kinematics, such as those produced by bars and is therefore able to fit the twists and distortions in the centre of the kinematic maps of some galaxies, as shown in Figure 5.4. The assumption for non-axisymmetric or non-circular motion is that the circular orbit of stars and gas is affected by perturbations to the potential, for example an $m = 1$ mode produced by a lopsided potential or an $m = 2$ mode corresponding to bisymmetric perturbations such as those produced by bars or by a triaxial halo (Schoenmakers et al., 1997). A model with mode m perturbations to the potential can be expressed as:

$$V_{\rm model}(r) = V_{\rm sys} + \sin i[\bar{V_t}\cos\theta - V_{m,t}\cos m(\theta-\phi_b)\cos\theta - V_{m,r}\sin m(\theta-\phi_b)\sin\theta] \tag{5.3}$$

where ϕ_b is the phase relative to a convenient axis (for example, the position angle of the bar), $\bar{V_t}$ is the average tangential circular velocity, $V_{m,t}$ and $V_{m,r}$ are the tangential and radial components of the non-circular motions and m is the harmonic order.

The inputs to DiskFit are a two dimensional FITS file containing the observed velocity field, a FITS file containing the velocity uncertainties in each pixel and an

[2]Available online at https://www.physics.queensu.ca/Astro/people/Kristine_Spekkens/diskfit/

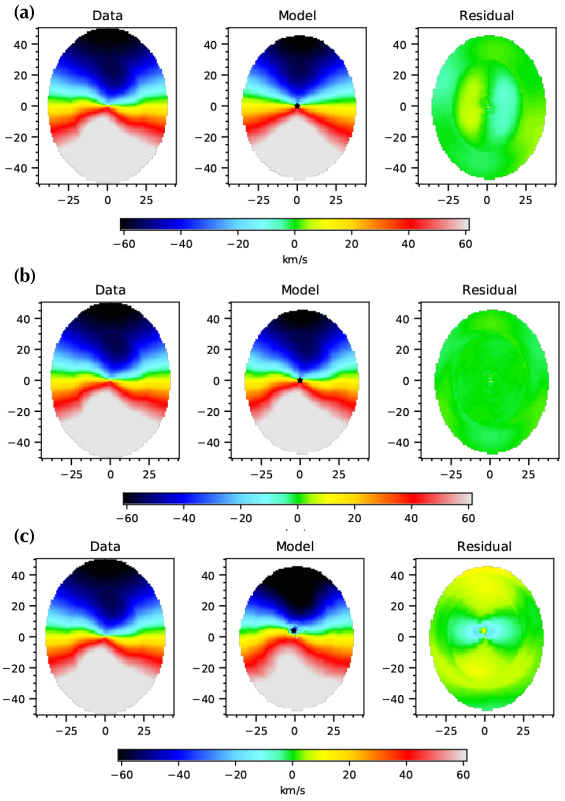

Figure 5.3: Artificially generated data of the kinematics of a barred galaxy with non-circular flows and fitted by DiskFit using: (a) an $m = 0$ pure rotation model; (b) an $m = 2$ model with a bar-like flow; (c) an $m = 2$ model with a bar-like flow, but with fixed $V_{\rm sys} = 0$. A model with non-circular flows is a better model for barred galaxies than a pure rotation model, as shown by the residual in (b). Not fitting the residual systemic velocity results in estimating an inaccurate kinematic centre as shown by the residuals in (c).

input file containing the initial guesses for the position angle (P.A.) of the kinematic major axis, ellipticity, kinematic centre, the systemic velocity, and the elliptic radii at which to extract the fitted velocities. It also requires an 'ISM turbulence' (in km s^{-1}; typically a few km s^{-1}), which is a measure of the errors introduced by turbulent motion in the discs. This is usually not known, but can be treated as a free parameter. Other parameters are needed to sample the input data - the user has the choice of sampling every pixel, or every n_{th} pixel outside some specified radius, to deal with correlated pixels, and ensure statistical independence. Finally, DiskFit corrects for Gaussian distortions to the kinematics due to seeing and beam smearing by providing the FWHM of the observations or the angular resolution of the velocity field. Beam smearing can blur the inner velocity gradients and has the effect of smearing the light and increasing the uncertainty on each model point. DiskFit minimises the residuals

in N spaxels using

$$\chi^2 = \sum_{n=1}^{N} \frac{[V_{\rm obs}(x,y) - V_{\rm model}(x,y)]^2}{\sigma_n^2(x,y)} \tag{5.4}$$

where $\sigma_n(x,y)$ is the velocity uncertainty in the each pixel, expressed as

$$\sigma_n(x,y) = \sqrt{\Delta_D^2(x,y) + \Delta_{\rm ISM}^2} \tag{5.5}$$

where $\Delta_D(x,y)$ is the velocity uncertainty from the input file and $\Delta_{\rm ISM}$ is the ISM turbulence. DiskFit returns the kinematic centre (x_k, y_k), the inclination (i), systemic velocity $(V_{\rm sys})$, the position angle (P.A.) of the kinematic major axis, the P.A. of the modeled distortion and $V_{\rm c}$, $V_{m,t}$ and $V_{m,r}$ at the specified radii in the input. Furthermore, it provides a model map of $V_{\rm model}(x,y)$ and a residual map with $V_{\rm res}(x,y) = V_{\rm obs}(x,y) - V_{\rm model}(x,y)$, where (x,y) are the coordinates of each spaxel.

To get uncertainties in the best-fitting parameters at each spaxel, DiskFit uses the bootstrap technique described in Sellwood & Sánchez (2010) (Appendix B). To estimate the true uncertainty in each quantity, the bootstrap repeats the kinematic fits a specified number of times to resampled data obtained by adding to the predicted velocity from the best-fit model at every spaxel a residual from another spaxel chosen at random. I ran the bootstrap 100 times for each galaxy.

Although higher order harmonic components exist, the $m = 1$ and $m = 2$ components dominate in barred galaxies and are sufficient to model the physical properties of the kinematics in this chapter. DiskFit does not allow fitting $m = 1$ and $m = 2$ modes simultaneously, because of degeneracies. These harmonics can only be fitted independently. Therefore, I fitted three independent models to the Hα gas velocity fields ($m = 0$, 1 and 2), with otherwise exactly the same input parameters. I determine the best model based on the lowest χ^2 and my visual inspection, in order to ensure the reliability of the fits. The centre of this model is adopted as the kinematic centre.

Many barred galaxies show characteristic position angle twists at their centres (an 'S' - shape perpendicular to the major axis; Emsellem et al. 2006; Fathi et al. 2009). This is mostly noticeable in their gas kinematics (therefore the need for higher order harmonic decompositions), but not in the stellar ones. For the stellar kinematics, I found that a pure rotation model describes the data well in most cases. In some cases the stellar velocity fields are noisy and, including higher order modes, results in unphysical fits. Therefore, the stellar kinematics were modeled with an $m = 0$ model, and the centre of this model was adopted as the stellar kinematic centre.

When measuring the kinematic centres, P16 also used a non-axisymmetric model for the gas kinematics and a simple rotation model for the stellar kinematics.

To investigate the amplitude of non-circular flows due to ($m = 2$) oval distortions in the halo, one needs to keep the kinematic centre fixed, otherwise the free centre would drift in such a way as to minimise $V_{2,r}$ and $V_{2,t}$ (Schoenmakers et al., 1997). Therefore, as a final step of the kinematic modeling, I fixed the centre of the Hα gas velocity field to the previously determined value, and refitted all the galaxies with an $m = 2$ mode, measuring the $V_{2,r}$ and $V_{2,t}$ amplitudes at various radii.

5.3.2 Testing on artificial data

I first tested DiskFit with artificial data on a (100 $\times$100) grid centred on $(x_k, y_k) = (0, 0)$, inclined at $i = 40°$ with $V_{\rm sys} = 10\,{\rm km\,s^{-1}}$, $V_{\rm c} = 100(\frac{r}{30})^{0.3}$ and a bar with $\phi_b = 30°$ introducing non-axisymmetric velocity components $V_{m,t} = 20\sin(\frac{r}{10})\,({\rm km\,s^{-1}})$ and $V_{m,r} = 0.75 \times V_{m,t}$ at radii $r < 30$. Figure 5.3 (a) shows a pure rotation DiskFit model for this generated data of a barred galaxy. While the centre (shown by the black star) converges close to the true value of (0,0), the residual shows structure due to the non-axisymmetric components. Figure 5.3 (b) shows a model with a bar, initially set to have $\phi_b = 45°$. The model quickly converges to the real values and is an accurate representation of the artificial data, as shown by the low level residuals. In Figure 5.3 (c) I have fixed the systemic velocity $V_{\rm sys} = 0$ instead of leaving it as a free parameter in order to study the effect of allowing $V_{\rm sys}$ to vary on the position of the kinematic centre. As expected the fitted kinematic centre is no longer at (0,0), but at (-1, 4). The residuals in Figure 5.3 (c) also show a significant amount of structure, suggesting that the fit is inadequate. Therefore DiskFit should be allowed to fit the systemic velocity, even if the value is small, in order to derive an accurate kinematic centre.

Subsequently, I tested the effect of beam smearing due to seeing on the kinematic centre and modeled velocities by convolving the artificial data with a Gaussian filter with a standard deviation σ = FWHM/2.355, corresponding to a FWHM of 1.2, 2.4, 4.8 and 7 spaxels (0.6″, 1.2″, 2.4″ and 3.5″ respectively, assuming a 0.5″/spaxel scaling). The kinematic centre (x_k, y_k) does not change significantly between the models with different FWHM. The fitted rotation velocities, on the other hand, change in the inner $r < 10$ pixels. This was also shown by Cecil et al. (2016) for SAMI IFU observed galaxies who found that the PSF smearing changes the linear rise of the circular rotation curves to higher values especially for galaxies with the smallest rotation velocities (thus lower mass galaxies) (see their Figure 3).

These tests on generated data show that DiskFit can fit non-circular motions in the discs and determine the kinematic centre. Fitting real data will result in increased uncertainty due to the noise in the kinematic maps. Nevertheless, an advantage of DiskFit over other routines such as *rotcur* (Begeman, 1987) is that DiskFit uses all the data in a single fit, making it easier to identify mild distortions in noisy data (Sellwood & Sánchez, 2010). Other codes such as *kinemetry* (Krajnović et al., 2006), on the other hand, assume a fixed kinematic centre.

5.3.3 Input parameters for MaNGA data

The data used in this chapter are taken from the MaNGA MPL-6 Data Analysis Pipeline (DAP; Westfall et al, in prep.), as discussed in Section 2.2. In the DAP, the data cubes are background subtracted and the penalized Pixel-Fitting algorithm (pPXF; Cappellari & Emsellem 2004; Cappellari 2017) was applied to determine the best fit stellar continuum model and stellar kinematics. In the DAP, the emission lines were fitted separately with Gaussian profiles to determine the gas velocities. Here I make use of the Voronoi binned (to S/N>10; Cappellari & Copin 2003) stellar velocity maps and Hα gas velocity maps. The MaNGA DAP data are redshift subtracted, therefore the measured values for $V_{\rm sys}$ in DiskFit corresponds to the mean (residual) velocity in the MaNGA IFU.

As discussed in the previous subsection, the position of the kinematic centre does not change significantly with the FWHM of the observations. Even though the median r-band FWHM of MaNGA is $\sim 2.5''$ I have chosen a FWHM of $1''$ in the DiskFit models to increase the number of ellipses at which the rotation velocity is extracted. DiskFit requires the spacing between the ellipses to be larger than the input FWHM in order to do the deconvolution, thus a lower FWHM value increase the number of ellipses fitted. A FWHM of $\sim 2.5''$ would lead to only $3-5$ elliptical rings, which are too few for a reliable χ^2 estimation.

Another input of DiskFit is an initial guess for the ellipticity of the galaxies, which can either be a free parameter or based on photometry. Since the galaxies often extended past the MaNGA IFU, I have chosen to fix the ellipticity to the values provided in the NSA catalogue, measured at the half-light radius. Fitting the ellipticity with DiskFit either results in a similar value or a fixed value of 0.05 for the galaxies with lowest ellipticities. The bar can also bias the determination of the inclination from the kinematics. The initial position angle of the galaxies was also set to the value in the NSA catalogue.

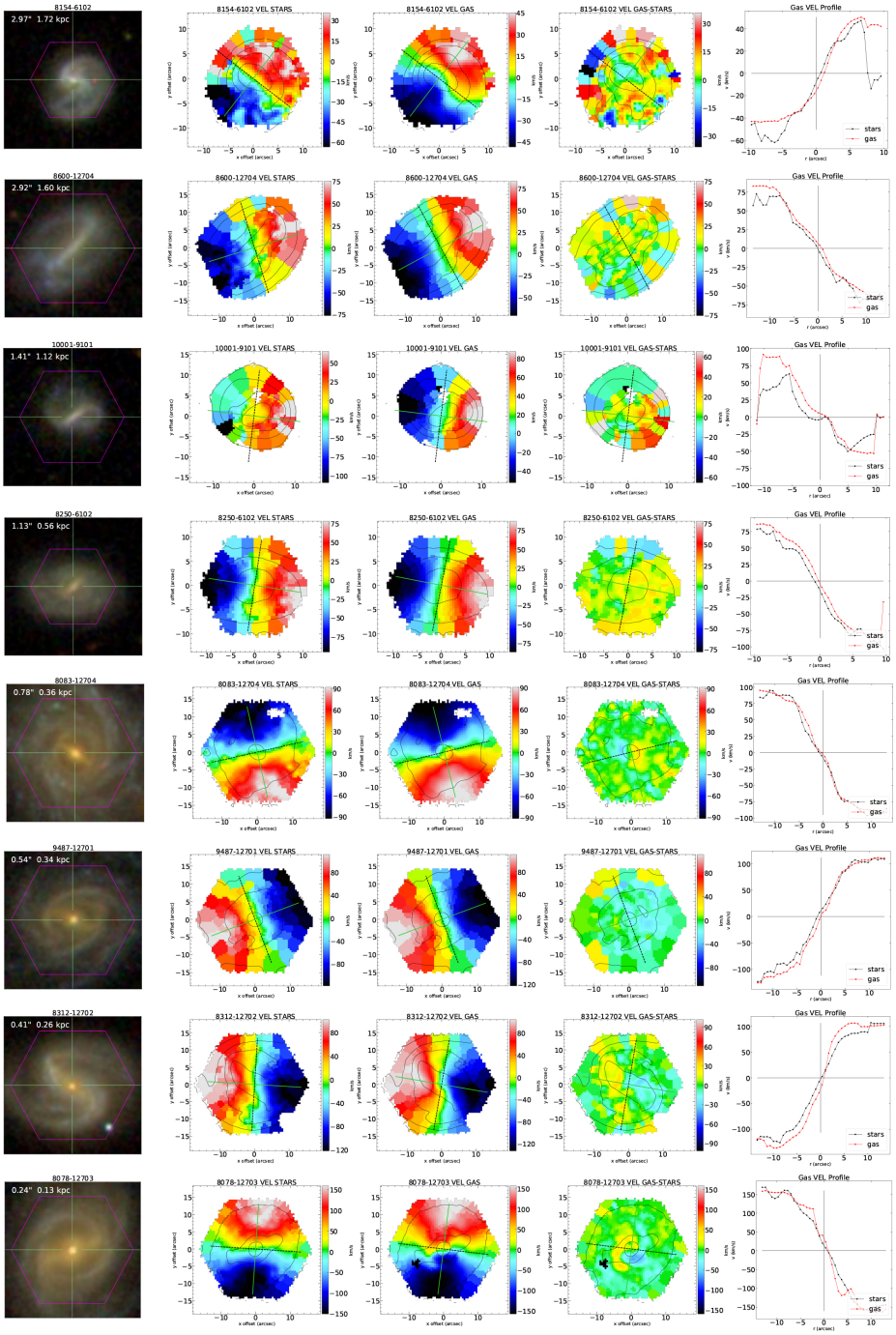

Figure 5.4: The SDSS *gri* composite image of eight out of the 214 galaxies in this study, with the hexagon illustrating the MaNGA IFU bundle (first column), stellar and gas kinematic maps (second and third columns), the difference between the two kinematic maps (fourth column) and the gas and stellar velocity profile along the two kinematic major axes (gas and star). The green line shows the kinematic major axis, and the dotted line the perpendicular to it (the $v = 0$ axis). The offset on the sky (in arcsec) and the projected physical offsets are shown at the top left of the SDSS image.

In order to properly estimate χ^2, as described in Equation 5.4, DiskFit requires uncertainties in the measured velocities, $\Delta_D(x, y)$, and an estimate for the ISM turbulence $\Delta_{\rm ISM}$. For the velocity uncertainties I have used the inverse variance ($IVAR$) maps provided by MaNGA for the gas and stellar kinematics, binned in Voronoi bins, similarly to the kinematic maps. I converted the $IVAR$ maps to σ maps, dividing by $\sqrt{IVAR}$. For the ISM turbulence $\Delta_{\rm ISM}$ I used values from 0 km s^{-1} to 3 km s^{-1} in increments of 0.5 km s^{-1}. Since the goal of this work is to determine the kinematic centre and not to measure the ISM turbulence, I have set $\Delta_{\rm ISM} = 2.5$ km s^{-1} for all the galaxies, which was found to provide a reasonable normalisation for χ^2 for most galaxies.

For all the fitted galaxies I used 9 concentric ellipses of varying radii, depending on the IFU size. The ring spacing is the radius of the IFU divided by 9, therefore ranging from 1″ for the smallest IFU (37 fibers) to 2″ for the largest IFU (127 fibers). The initial guess for the perturbation position angle ϕ_b was arbitrarily set to 45°.

The initial guess for the kinematic centre is taken to be centre of the IFU. According to Wake et al. (2017), the centering on the targets was based on the spectroscopic centre from the SDSS DR7 fiber. In cases where the photometric centre (obtained from single Sérsic fits) differed by more than 1″ from the SDSS fiber centre, the galaxies were inspected and a new correct centre was provided. The inspection showed that 1,227 galaxies had bad centres out of the $\sim 40,000$ possible targets ($< 3\%$), and 1,189 were recentred. The uncertainty in centering the IFU in different exposures is $\sim$0.5″ as noted by Law et al. (2016) and shown in their Figure 15. Therefore, I consider this value to be an error estimate in determining accurately the kinematic centres of the galaxies.

5.4 MaNGA sample

The sample of galaxies with offset and centred bars studied in this chapter is drawn from the SDSS-IV MaNGA integral field spectroscopic survey. The survey, as well as the MaNGA data products are described in detail in Section 2.2.

There are 4,692 galaxies observed by MaNGA in the latest internal data release (MPL-6). 4,188 of these galaxies have been classified in the Galaxy Zoo 2 project (3,841 as part of the SDSS spectroscopic survey and 347 as part of the photometric survey). Morphological classifications for 504 galaxies are missing because of the different sample selection in Galaxy Zoo 2, where only galaxies brighter than $r = 17$ were classified.

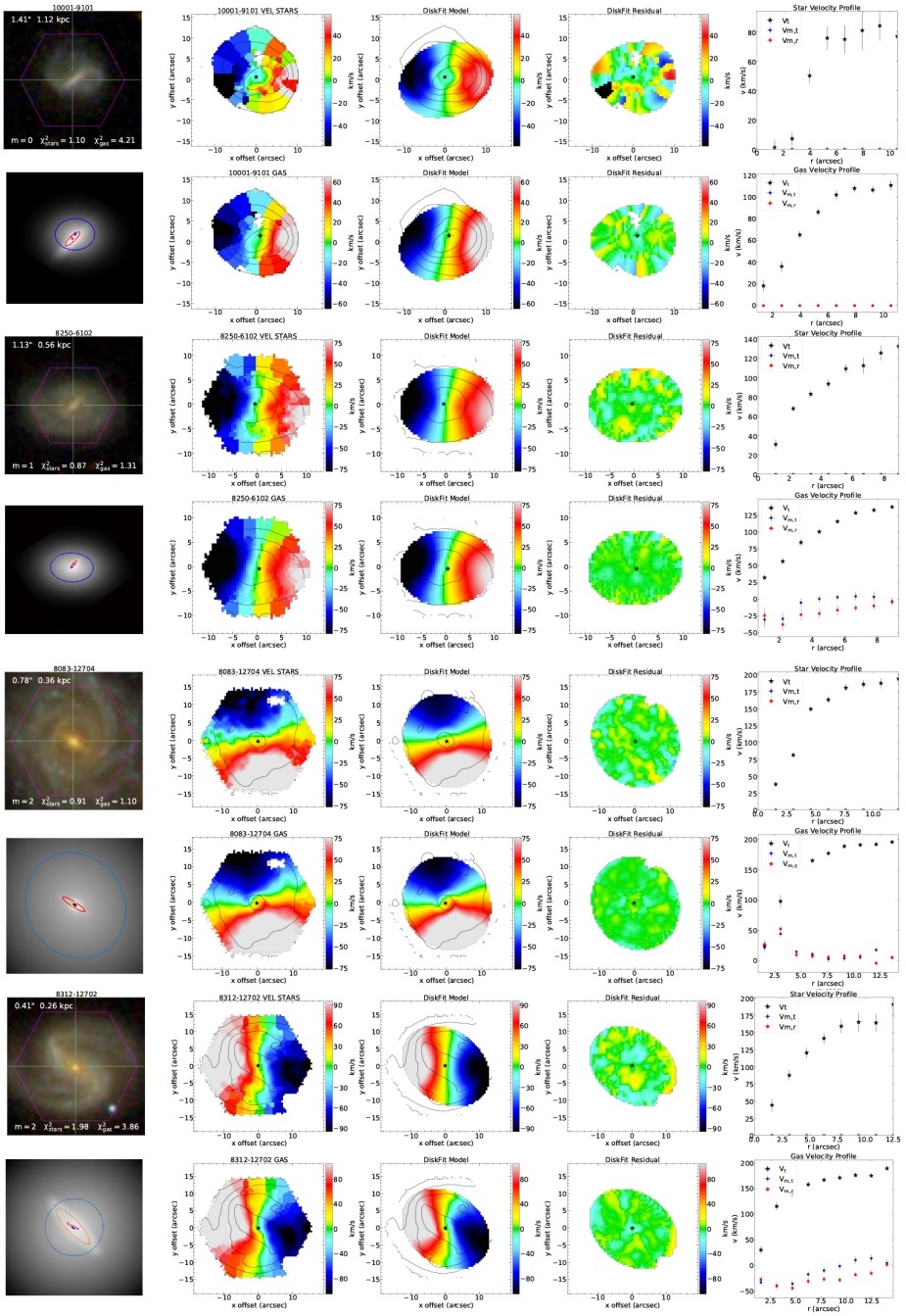

Figure 5.5: The columns show (in 2 rows): SDSS *gri* image, photometric decomposition, MaNGA kinematic maps for star/gas and DiskFit models, residuals and in-plane velocity radial profiles (corrected for galaxy inclination) for two galaxies with off-centre disc and bars (*top* 4 rows) and two galaxies with centred discs and bars (*bottom* 4 rows). The black star shows the position of the kinematic centre in the velocity maps, while the blue and red crosses in the photometric models show the photometric centres of the disc and bar components, respectively.

Out of the 3,841 galaxies with spectroscopic redshifts and Galaxy Zoo classifications (from the same large catalogue used in Chapters 2-4), 1,173 are moderately inclined discs ($N_{\rm bar} \geq 10, i < 60^{\circ}$) and 569 are barred - 287 have strong bars ($p_{\rm bar} \geq 0.5$) and 282 have weak bars ($0.2 < p_{\rm bar} < 0.5$). I have successfully fitted 358 of these barred galaxies (as described in Section 2.3.1), 194 with strong bars and 164 with weak bars. The techniques used to fit these galaxies and their measured parameters are described in Section 2.4.

I consider both strongly barred galaxies and weakly barred galaxies in this study in order to increase the number statistics of offset galaxies (only ∼10% of these galaxies show offsets between discs and bars). Out of the 358 galaxies, I removed 22 galaxies which based on my visual inspection were not barred galaxies, but post-mergers or systems with unclear morphology. I further removed 72 galaxies which were Hα gas-poor and showed no rotation in the gas kinematic maps, making it impossible to extract a kinematic centre. These galaxies were mostly massive early-type systems. In what follows I refer to individual galaxies using their *plateifu* designation in MaNGA which consists of the IFU plate number (e.g. 8154) and the IFU bundle size (e.g. 127) followed by a dummy variable giving the number of the galaxy with the same IFU bundle size on the sample plate (for example 8154-12703).

50 barred galaxies were further discarded either because the outer spaxels in the MaNGA IFUs were contaminated by the sky, which resulted in erroneous estimates of the non-circular motions in the outer disc, or because the bar was orientated too close to the major axis of projection, yielding unphysical large estimates for the velocities as noted by Sellwood & Sánchez (2010). The final sample of barred galaxies in this study contains 214 galaxies, 27 with offsets and 187 with centred bars.

The kinematic maps of the 214 remaining barred galaxies show clear rotation in both the stellar and Hα components. Eight are shown in Figure 5.4, the top four with off-centre discs and bars and the bottom four with centred components. The photometric and kinematic centres, calculated as offsets from the IFU pointing, are shown in Table 5.1 for the eight galaxies. Some low mass galaxies show rising velocity profiles, characteristic of solid-body rotation, which flatten out at large radii $\sim 1.5r_e$ ($\sim$ size of the MaNGA IFU hexagon). The velocity profiles of high mass galaxies, in contrast, have a steeper rise and flatten out at smaller radii. The kinematic maps show twists in the central regions, especially in the gas kinematics, which are characteristic of non-circular bar flows. For example, this is obvious in the gas maps of galaxies 8154-6102, 8083-12704 and 8312-12702 and perhaps in the stellar kinematic maps of 8312-12702. The twists in the kinematic maps complicate the determination of the kinematic centres of the galaxies, hence a pure rotation model for these galaxies

Plateifu	SDSS Name	IFU		Bar (″)		Disc (″)		Gas (″)		Stars (″)		$\epsilon_{\rm kin}$	m	$\chi^2_{\rm gas}$	$\chi^2_{\rm stars}$
		RA(°)	DEC(°)	δX	δY	δX	δY	δX	δY	δX	δY				
8154-6102	J025640.69-001444.3	44.16959	-0.24566332	-0.7	0.8	1.5	-1.1	-1.0	0.0	0.4	0.0	0.043	1	1.01	1.22
8600-12704	J161931.90+413945.2	244.88292	41.662464	1.3	1.6	-1.5	-0.5	1.0	0.2	-0.5	-0.8	0.084	1	1.96	0.93
10001-9101	J085530.75+573352.3	133.8781	57.564545	0.3	-0.5	2.1	0.6	2.0	1.5	0.5	0.2	0.272	0	4.21	1.10
8250-6102	J091536.62+420926.0	138.90262	42.157223	0.2	0.4	-0.6	-0.5	0.6	-0.5	-0.5	0.0	0.017	1	1.31	0.87
8083-12704	J032247.22+000857.6	50.696785	0.14936614	-0.2	0.1	0.5	-0.3	-0.2	-0.1	0.2	-0.4	0.011	2	1.10	0.91
9487-12701	J081005.48+461134.8	122.52287	46.193024	-0.1	-0.2	0.3	0.3	0.1	0.1	0.5	0.0	0.045	0	4.07	1.30
8312-12702	J162105.00+395502.6	245.27087	39.917393	0.0	-0.2	0.5	-0.3	0.1	-0.1	0.0	-0.1	0.120	2	3.86	1.98
8078-12703	J025016.86+000531.1	42.570267	0.09199015	0.0	0.0	-0.2	-0.1	0.0	0.2	0.1	0.0	0.014	2	2.62	2.17

Table 5.1: Table showing the offsets of the bar and disc photometric centres, and gas and stellar kinematic centres from the IFU pointing centre for the eight galaxies in Figure 5.4. The measured $m = 1$ perturbation to the potential, $\epsilon_{\rm kin}$, the mode m chosen to model the Hα gas kinematics (the stellar kinematics were modeled with $m = 0$) in order to determine the kinematic centre, and the corresponding reduced χ^2 are also shown.

is largely inadequate. Furthermore, the relatively shallow gradients in the rotation curves of some low mass galaxies, characteristic of solid-body rotation, introduce further uncertainties in the determination of the kinematic centres.

5.5 Results

As discussed in Section 5.3, I choose the best fit model ($m = 0, 1$ or 2) based on the lowest χ^2 and my visual inspection of the fits and residuals. When the model with lowest χ^2 was not a good physical representation of the velocity field, I choose the model with the second lowest χ^2. In cases where the differences in χ^2 between the three models were small and no bar-like flows were present, I chose the simplest model ($m = 0$). Therefore, the gas kinematics of 47 (22%) barred galaxies were modeled with $m = 0$, 60 (28%) with $m = 1$ and, the majority of 107 galaxies (50%) with $m = 2$. Of the offset galaxies, the proportions are comparable, 7 (26%) with $m = 0$, 10 (37%) with $m = 1$ and 10 (37%) with $m = 2$, being slightly in favour of $m = 1$ models. Figure 5.5 shows the output of DiskFit for four galaxies (two offset galaxies and two centred galaxies): the SDSS *gri* images, photometric decompositions (with photometric centres), MaNGA star and gas velocity maps, DiskFit models, residuals and in-plane velocity profiles (corrected for galaxy inclination) extracted at 9 radii from the kinematic centres. The harmonic decompositions with DiskFit are good models for the MaNGA kinematic maps, as they are able to model the twists due to bars and other non-circular motions in the discs.

5.5.1 Kinematic-photometric centres

I define the magnitude of the projected offsets between the relevant centres as: $d_{\rm bar-disc}$ – the photometric offset between the centre of the bar and disc components; $d_{\rm gas-bar}$,

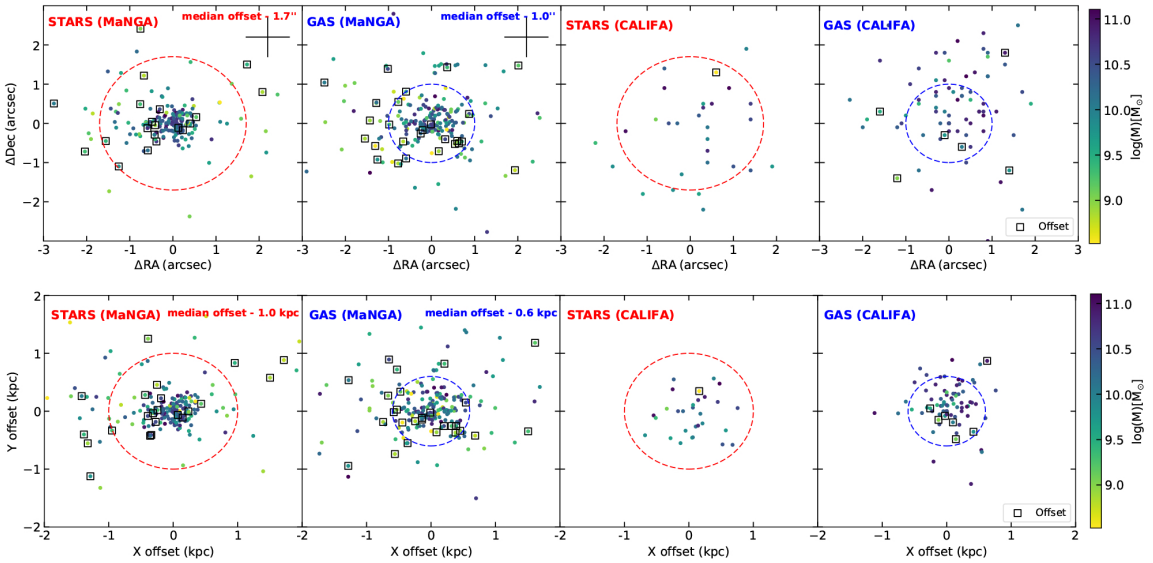

Figure 5.6: *Top*: R.A. and Dec. offsets between the IFU pointing centre and the stellar kinematic centre (*first panels*) and between the IFU centre and the gas kinematic centre (*second panels*). 0.5″ error in measuring the offsets, corresponding to the size of a spaxel, is shown. The third and fourth panels show published offsets between the same quantities from the CALIFA survey, stellar kinematics from Barrera-Ballesteros et al. (2014) and gas kinematics from García-Lorenzo et al. (2015). The red circles and blue dotted circles mark the median of the offset for the photometrically offset galaxies. *Bottom*: The same offsets converted to physical offsets in kpc at the redshift of the galaxies in the samples. In all panels the squares denote the galaxies with significant photometric offsets between discs and bars.

$d_{\mathrm{gas-disc}}$ – the offset between the Hα gas kinematic centre and bar (disc) photometric centre; $d_{\mathrm{stars-bar}}$, $d_{\mathrm{stars-disc}}$ – the offset between the stellar kinematic centre and bar (disc) photometric centre.

The easiest offsets to compare are those between the stellar/gas kinematic centres and the IFU pointing centre, since these are outputs of DiskFit. The MaNGA IFUs were positioned on the spectroscopic and photometric centre of the galaxies based on previous SDSS data (as discussed in Section 5.3.3). The photometric centre of galaxies roughly corresponds to the centre of the bar component in the offset galaxies. In Figure 5.6 I plot the position of the star/gas kinematic centres relative to the R.A. and Dec. position of the IFU. From the first two plots (*top panel*) it is evident that the IFU-gas offsets are smaller than the IFU-star offsets, and the IFU-star offsets are larger for the photometrically offset galaxies than for the centred galaxies, on average. The *bottom panels* show the same quantities, but converted to physical offsets at the redshift of the galaxies. The panels on the right hand side show a comparison with offsets published in the literature, from the CALIFA survey (from

the studies of García-Lorenzo et al. 2015 and Barrera-Ballesteros et al. 2014).

The quantities of interest in this study are the offsets between the stellar and gas kinematic centres and the disc and bar photometric centres. The projected $d_{\rm stars-disc}$, $d_{\rm gas-disc}$, $d_{\rm gas-bar}$, $d_{\rm stars-bar}$ plotted against $d_{\rm bar-disc}$ are shown in Figure 5.7 (a-d). The first aspect to notice in Figure 5.7 panels (a) & (c) is an obvious anti-correlation of the offsets with mass; lower mass galaxies show the largest offsets in both photometry and stellar kinematics. The mass trend is not surprising; it reflects the mass trend of the offset galaxies found in Chapter 4. Furthermore, there is a correlation between $d_{\rm stars-disc}$, $d_{\rm stars-bar}$ and $d_{\rm bar-disc}$ (Spearman $r_s = 0.42$ and $r_s = 0.38$, respectively). On the other hand, panels (b) & (d), show only a very weak correlation between $d_{\rm gas-disc}$, $d_{\rm gas-bar}$ and $d_{\rm bar-disc}$ (Spearman $r_s = 0.29$ and $r_s = 0.26$, respectively).

The $1''$ grey dotted lines in Figure 5.7, corresponding to the median resolution of the SDSS i-band images, split the four panels into four quadrants representing in a clockwise direction from the top left: (1) galaxies that are offset in their kinematic centres, but not photometrically offset; (2) galaxies that are offset in both kinematics and photometry; (3) galaxies offset in photometry, but not in kinematics and (4) galaxies which are not offset in neither the kinematics nor in photometry. The number of galaxies in each quadrant is shown with red in the panels of Figure 5.7. 17 galaxies are offset in both stellar kinematics and photometry (out of the 27 offset in photometry, 63%), while 15 are offset in gas kinematics and photometry (55%), suggesting again that photometrically offset galaxies tend to be offset mostly in stellar kinematics, rather than in gas kinematics. Only $\sim 20\%$ of the galaxies with centred bars show offsets in kinematics (shown in the first quadrant). Typically only low mass galaxies are offset in stellar kinematics, and both low and high mass galaxies can be offset in gas kinematics. The small fraction of galaxies with centred bars, but with offset kinematics suggests that the kinematic offsets are characteristic mainly to photometrically offset galaxies, although it is important to note the two samples of offset and centred-bar galaxies were not mass-matched.

The physical offsets (projected offsets converted using the physical distances of the galaxies) show similar trends as the offsets measured in the sky (Figure 5.8 panels a-d). The median $d_{\rm stars-disc}$ and $d_{\rm stars-bar}$ (shown with the blue dotted lines) for the offset galaxies are 0.94 and 0.84 kpc, respectively, while the gas kinematic centre is considerably closer to the photometric centres (median $d_{\rm gas-disc} = 0.71$ kpc and $d_{\rm gas-bar} = 0.56$ kpc). It is important to note that centre of gas rotation is located nearer to the bar centre than to the disc photometric centre. There is an evident trend for the stellar kinematics to be more misaligned in low mass galaxies than in high mass systems, trend which is not obvious in the gas kinematics.

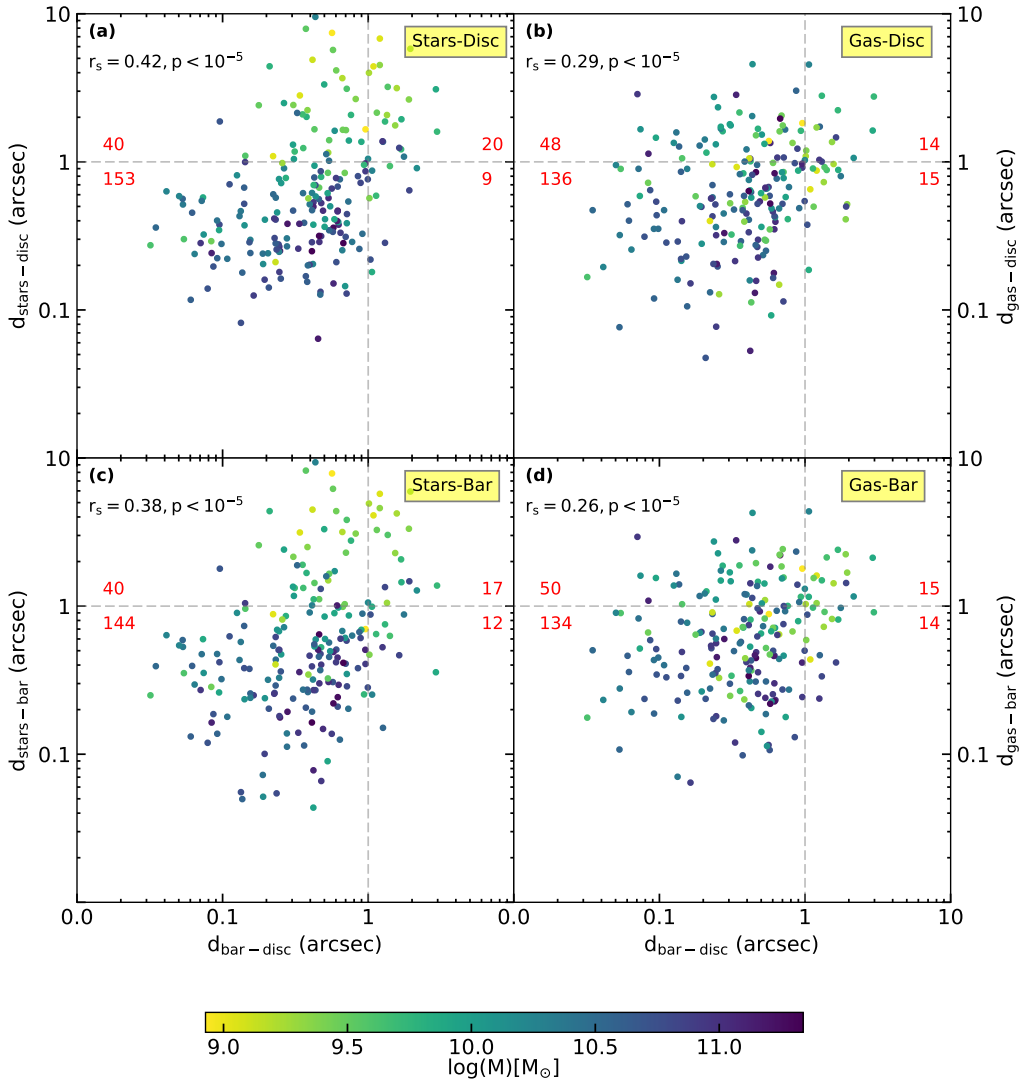

Figure 5.7: (a) The offset between the centre of the disc component and the stellar kinematic centre; (b) The offset between the centre of the disc component and the gas kinematic centre; (c) The offset between the centre of the bar component and the stellar kinematic centre; (d) The offset between the centre of the bar component and the gas kinematic centre versus offset between the bar and disc photometric components as measured from the decompositions on SDSS imaging. The kinematic offsets were measured in the MaNGA data using DiskFit. The grey dotted lines show the delimitation of galaxies identified to be offset, with offsets larger than 1″. The error in measuring the offsets is 0.5″. The Spearman r_s-rank correlation coefficient and p value are shown in the top left of each figure. The numbers in red represent the number of galaxies in each of the four quadrants made by the 1″ dotted lines.

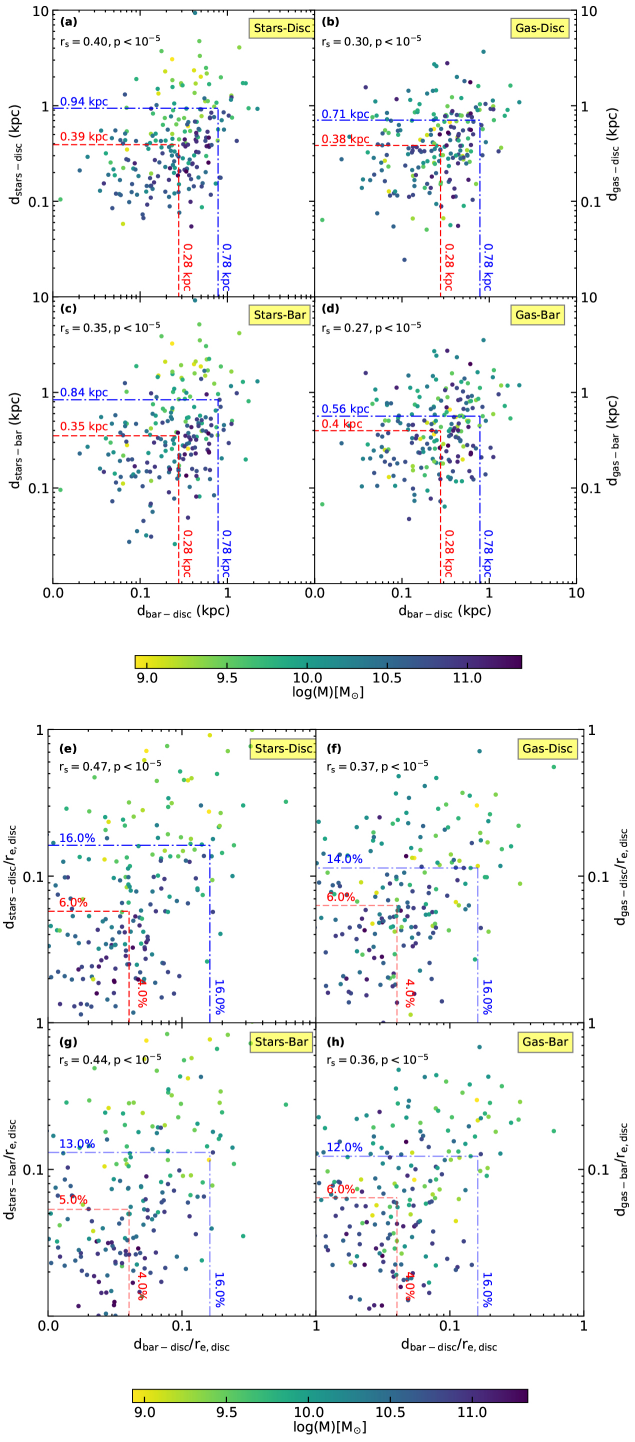

Figure 5.8: The same offsets as in Figure 5.7, but *Top panels*: converted to physical offsets in kpc at the distance of the galaxies in the sample. *Bottom panels*: scaled by the effective radius of the disc, r_e. The red dotted lines show the median values (red numbers) for the different offsets for the entire sample, while the blue dotted line shows the median offsets (blue numbers) for the offset galaxies only. The Spearman r_s-rank correlation coefficient and p value are shown in the top left of each figure.

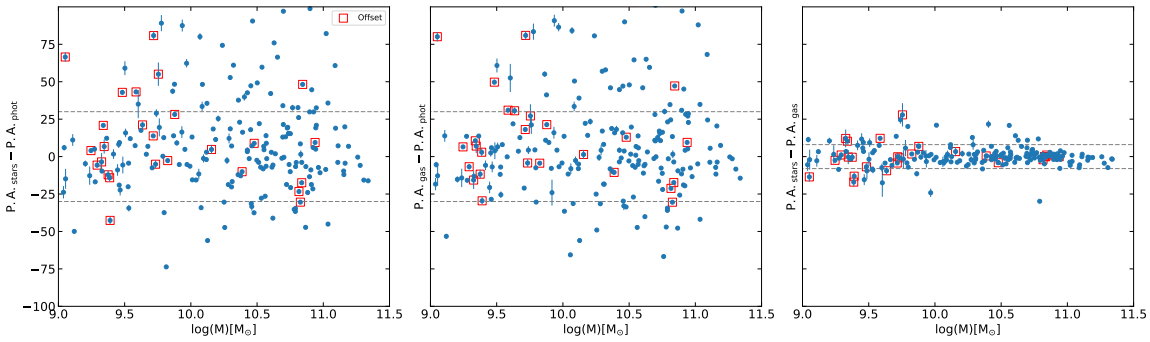

Figure 5.9: Difference between the stellar (*left*) and gas (*middle*) kinematic P.A. and the photometric P.A. as measured by the NSA half-light radii and between the star and gas kinematic P.As (*right*) against stellar mass. The dotted lines show the $1\sigma = 30$ km s^{-1} standard deviation (*left* and *middle*) and the tighter $1\sigma = 7$ km s^{-1} distribution. Offset galaxies are shown with a red square.

These trends are also noticeable when scaling the offsets with the size (r_e) of the discs, as shown in the panels e-h of Figure 5.8. For the offset galaxies, the median stellar kinematic offsets are 13% of the r_e of the discs, while for the gas, they are only slightly lower, 12%. Again, an even stronger correlation with mass is noticeable, since low mass galaxies have smaller effective radii.

The median kinematic offset for all the barred galaxies is 0.4 kpc (6% of the r_e of the disc), which approximately corresponds to the accuracy in determining the position of the kinematic centres (0.5″). This implies, that for the majority of the galaxies, both the stars and gas are centred on the photometric centres and follow the gravitational potential.

Now that I have established the relative positions of the gas and stellar kinematic centres with respect to the photometric ones, it is worth exploring the kinematic signatures of the possible origins of offsets.

5.5.2 Kinematic-photometric misalignments

The line-of-sight velocity distributions of rotationally supported disc systems are expected to show regular rotation with a kinematic axis (the axis along the greatest velocity gradient) that is aligned with the photometric major axis of the galaxies (Sofue & Rubin, 2001) unless the galaxy has undergone a recent major merger event (Naab & Burkert, 2003).

If these offset systems have recently undergone major mergers that produced the offsets, one might expect significant misalignments between the kinematic axes of the different components, as well as between the kinematic and photometric axes. The difference between the kinematic and photometric position angles (as measured by

the NSA half-light ellipticity), and the star and gas kinematic major axis are shown in Figure 5.9. The median P.A. offset between the photometric axis and the star/gas kinematic axis is 15°, but with a significant scatter rms $\approx \pm 30°$. Some of this scatter can be explained by the presence of strong bars in these galaxies, with the strong bar flows twisting the measured P.A. of the kinematic axis of the galaxies, misaligning it with the photometric axis. The offset galaxies do not show a different photometric-kinematic misalignment compared to the other galaxies with centred components.

The *right* hand side panel of Figure 5.9 shows a significant alignment between the kinematic axis of the stellar and gas components (median $\sim 3°$ and rms $1\sigma = 7\,\mathrm{km\,s^{-1}}$). For 90% of the 214 galaxies in the sample, the stellar and gas kinematic position angles are within 20°. Two barred galaxies show more significant counter-rotating gas and stars (8717-3703 and 8319-3702) and deserve further attention.

Major mergers are, therefore, not the cause of the observed offset bars. However, this does not exclude potential minor mergers or fly-bys which should not cause kinematic misalignments. Interactions might also perturb the dark matter haloes first, since these galaxies are dark matter dominated. This is investigated in the following section.

5.5.3 Halo lopsidedness

Jog (1999) suggested that an $m = 1$ lopsided dark matter halo can imprint its lopsidedness onto the hosted disc, which can be observed as an asymmetry in the kinematics of galaxies, with a discrepancy between the receding sides and the approaching sides of the rotation curve. The perturbation in the potential ($\epsilon_{\rm kin}$) due to a lopsided halo can be calculated from the two sides of the rotation curves, using Equation 5.1 (Jog, 2002). As illustrated in Section 5.2, once I determined the gas kinematic centre of galaxies, I extracted the rotation curve of the galaxy along the kinematic major axis, and calculated the difference between the two sides in the flat part of the curve (at largest possible radii). In order to determine $\epsilon_{\rm kin}$, I also estimated the circular velocity $V_{\rm c}$ as the average between the approaching and receding sides in the flat part of the curve. This was not always possible, as some galaxies, especially those with low masses, show a steadily rising rotation curve typical of solid-body rotation, even at the edge of the IFU. In these cases the calculated $\epsilon_{\rm kin}$ is a maximum value.

An important fraction of galaxies show asymmetries in the kinematics ($\sim$5-15 km s^{-1}, the median difference between the two sides is ΔV =12 km s^{-1} for the galaxies in the sample), with differences between the approaching and receding sides as large as 50 km s^{-1} for four galaxies.

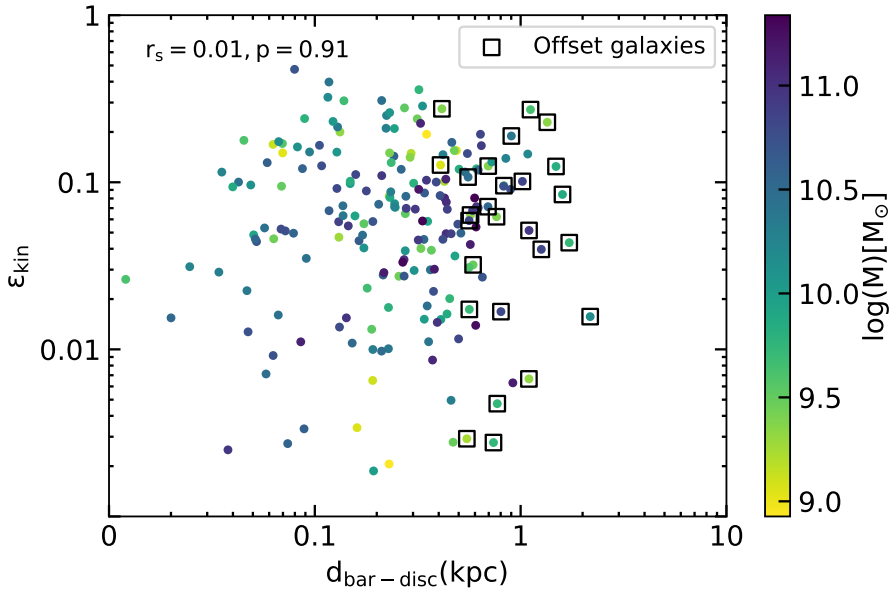

Figure 5.10: The perturbations in the potential ($\epsilon_{\rm kin}$) calculated from the difference in the velocity curve on the approaching and receding sides, normalised by the circular velocity of the galaxies, against the disc-bar photometric offsets. The Spearman r_s-rank correlation coefficient and p value are shown in the top left.

I have shown in Section 4.5.6 that there is a correlation between the offsets and morphological lopsidedness (A_1) and Jog (2002) argues that $\epsilon_{\rm kin}$ and, thus, the kinematic lopsidedness is related to A_1. Hence, if $m = 1$ perturbations in the dark matter potential are responsible for the observed offsets, one might expect larger perturbations to produce larger offsets. The measured perturbations to the potential are plotted against the photometric offsets in Figure 5.10. The values of $\epsilon_{\rm kin}$ range between 0 and 0.4, for both galaxies with offset and centred bars, and there is no obvious trend of $\epsilon_{\rm kin}$ with $d_{\rm bar-disc}$ (Spearman $r_s = 0.01$ and $p = 0.91$). The median $\epsilon_{\rm kin}$ for the barred sample is 0.066 and for the offset galaxies it is 0.063. There is no clear trend with stellar mass either, both low and high mass galaxies have similar $\epsilon_{\rm kin}$ estimates. Therefore, if perturbations in the halo potential exist, they are of the order 6%, for both types of galaxies considered.

5.5.4 Halo triaxiality

Measuring the amplitudes of non-circular motions in the gas velocity fields in the outer region of galaxies allows us to study whether the dark matter haloes are triaxial ($m = 2$ lopsided). However, in the potential, a weak $m = 2$ mode due to an oval halo is superimposed on a stronger $m = 2$ signal which is due to non-circular bar flows.

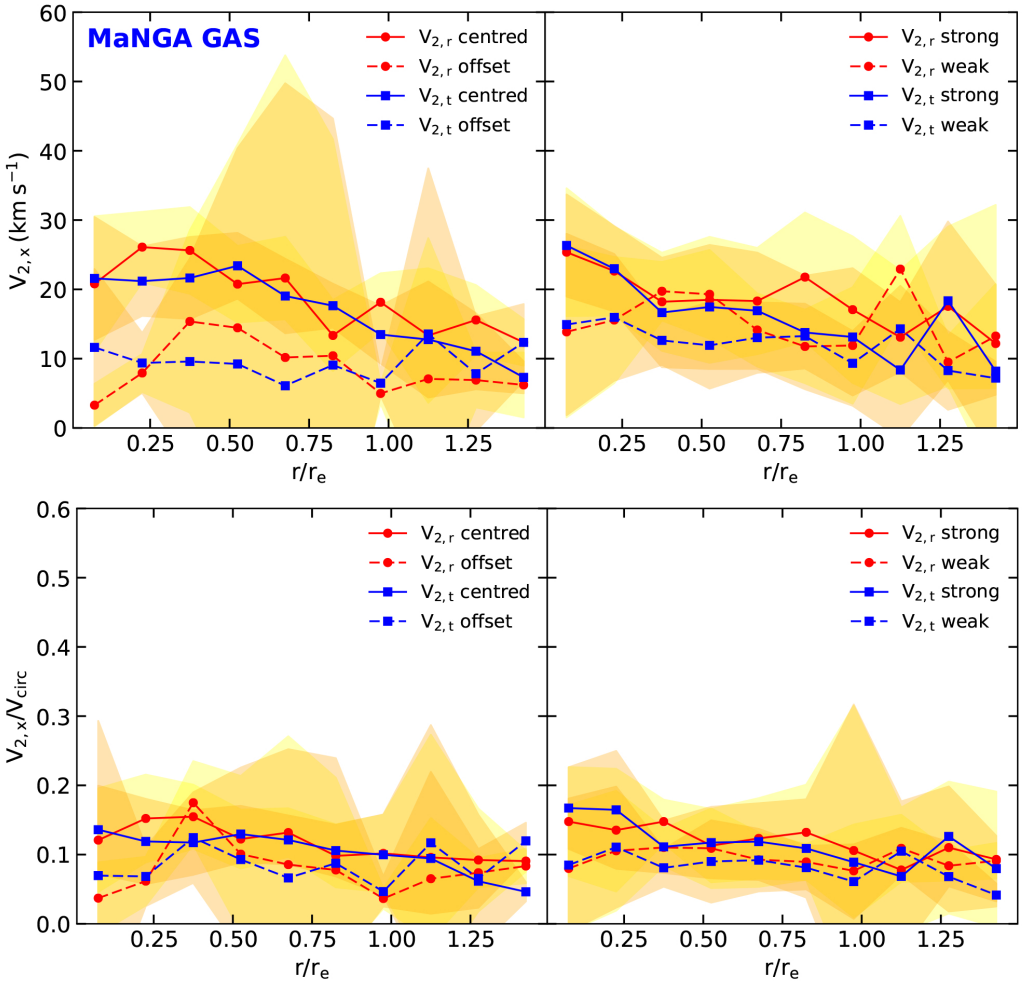

Figure 5.11: Gas kinematics of barred galaxies fitted with non-circular models in DiskFit stacked by radius scaled by the effective radius. Top two panels show the gas non-circular motions for galaxies with offset (27 galaxies) and centred (187 galaxies) discs and bars and weak and strong bars. Bottom panels show the same measurements, but scaled by the circular velocity. The shaded area show the 1σ spread.

Nevertheless, I attempt to distinguish between bar and halo effects for offset galaxies in what follows.

It is difficult to assess the overall trends of the non-circular velocity components with offsets by inspecting individual velocity curves since they are noisy and the error bars are significant. Therefore, to study overall trends, one needs to stack the galaxies in the sample. One way to achieve this is by scaling the extracted $V_{2,t}$ and $V_{2,r}$ by the effective radius of the galaxies r_e, taken from the NSA catalogue. The size of the MaNGA IFUs chosen to observe the galaxies is either $1.5r_e$ or $2.5r_e$, thus for consistency, I investigate the non-circular velocity trends up to $1.5r_e$. Figure 5.11 (*top panels*) shows $V_{2,t}$ and $V_{2,r}$ in bins of r/r_e for the photometrically offset and centred

galaxies, as well as for strongly and weakly barred galaxies, while the *bottom panels* show the same values scaled by the circular velocity (which is roughly equivalent to a scaling by mass, since more massive galaxies have higher circular velocities). Since the errors on the measurements are significant I assume a detectability limit of $V \sim 10$ km s^{-1}, which is the mean error in the measured quantities from DiskFit. The *top left panel* of Figure 5.11 shows that galaxies with centred bars have relatively high non-circular velocity components, with a median of $V_{2,x} \sim 25$ km s^{-1} at the centre, whereas the offset galaxies have small non-circular components, comparable to the smallest value that it is possible to measure. This result suggests that galaxies with centred bars have significant non-circular gas flows at the position of the bar, while offset galaxies show only weak $m = 2$ distortions. This is evident when inspecting velocity maps of barred galaxies – strongly barred galaxies show twists and distortions at the centres of their gas velocity fields. Nevertheless, at larger radii ($> r_e$), the amplitude of the non-circular motions is similar for the offset and centred barred galaxies. The non-circular amplitudes scaled by the circular velocity show even more similar trends for the two types of galaxies, in both the bar region (within $0.5r_e$) and outside the bar region.

Sellwood & Sánchez (2010) suggest that it is possible to quantify the distortion of the potential, by relating its axis ratio (q_ϕ) to the strength of the non-axisymmetric perturbations in the outer disc, induced by the halo (see Sellwood & Sánchez (2010) for a full derivation)

$$q_\phi = \left(\frac{V_\mathrm{c}}{V_\mathrm{c} + 2V_{2,r}} \right)^{1/2}. \tag{5.6}$$

Assuming that the non-circular flows in the inner region of the galaxies are due to the bar only, while the distortions in the outer disc ($r > r_e$) are solely due to the perturbations in the halo, it is possible to calculate the axis ratio of the potential. The median radial component of the non-circular velocity ($V_{2,r}$) in the outer region is 6.7 km s^{-1} for the offset galaxies and 13.7 km s^{-1} for the galaxies with centred bars. The median circular velocity for the offset galaxies is 117 km s^{-1} and 164 km s^{-1} for the galaxies with centred bars, respectively. Using Equation 5.6, this implies that the axis ratios of the potentials are $q_\phi \sim 0.97$ for the offset galaxies and $q_\phi \sim 0.96$ for galaxies with centred bars. In reality, this is an overestimate since the spiral arms also contribute to non-circular motions in the outer disc regions in addition to the halo, and were not considered in these calculations. Also, as mentioned before, for galaxies with solid-body rotation it is only possible to estimate a lower value for the circular velocity, given the radial extent of the MaNGA data. Therefore the axis ratio

of the potential is likely to be larger than $q_\phi \sim 0.96$. The results suggest that for both offset galaxies and galaxies with centred bars, the dark matter haloes are consistent with being round, with no evidence for significant asphericities.

One byproduct of fitting bisymmetric models with $m = 2$ distortions is being able to study the magnitude of the bar-like flows in the kinematic maps of galaxies. This can help us measure the dynamic importance of gas in a galaxy: whether weak bars have indeed a smaller dynamical impact compared to strong bars and whether an offset bar has a dynamical effect on the non-circular flows in a galaxy. Therefore, by studying the strength of the non-circular velocity components one can establish the correspondence between the photometric properties of a bar and their kinematic features.

In order to investigate the relation between the visually characterised bar strength, through $p_{\rm bar}$, I plot the $m = 2$ non-circular amplitudes ($V_{2,x}$) for galaxies split into 90 weakly barred ($0.2 < p_{\rm bar} < 0.5$) and 124 strongly barred galaxies ($p_{\rm bar} > 0.5$) in the *right* hand side panels of Figure 5.11. The gas velocity fields of strongly barred galaxies show stronger distortions with radial components of the non-circular flows up to $V \sim 25$ km s^{-1} at the centre, while weak bars show bar gas flows of $V \sim 15$ km s^{-1} at the centre. This difference in amplitudes at the centre of the galaxies is seen even when normalising by the circular velocity. This suggests that the strength of bars, measured in Galaxy Zoo with $p_{\rm bar}$ as a proxy, is a good measure of the influence of bars on their host galaxies.

5.6 Discussion

In what follows I discuss the results in the context of the two questions posed in Section 5.1: what is the relation between the photometric centres of the discs and bars, and the gas and stellar velocity fields and what is the origin of the offsets in these galaxies?

5.6.1 Kinematic-photometric centre offsets

Simulations by P16 suggest that offsets between the kinematic centre and the photometric components of a galaxy arise following an interaction, with the gas centering on the bar component (and the dynamical centre) ~ 0.5 Gyr after the interaction, and the disc settling only after ~ 2 Gyr.

In this work, for all the barred galaxies studied, I find an average offset of 0.4 kpc between the gas, stellar kinematic centre and the photometric centres, which is within the errors of the measurements. Therefore, for a typical barred galaxy,

all the components are centred and both the gas and stars follow the underlying potential. For the photometrically offset galaxies, the median offset between the stellar kinematic centre and the bar component is 0.8 kpc, while the gas kinematic centre is situated closer to the bar, at 0.5 kpc. I find that the offsets between kinematic centres and photometric centres correlate with the disc-bar offsets; galaxies with larger photometric offsets also shown large kinematic offsets. I also find a significant mass trend; low mass galaxies tend to show larger offsets in both bar-disc offsets and in the stellar rotation, which is expected given the lower self-gravity of the discs and their higher lopsidedness.

The stellar kinematic centre in the simulations of P16 was offset by 0.5-1 kpc from the bar, however they did not find a significant correlation with the disc-bar offsets (the displacement of the stellar velocity field is roughly constant with the time since interaction, see Figure 5.1). It is not clear why the stellar kinematics in the simulations do not undergo damped oscillations similarly to the disc. My observations suggest, given the correlation with the bar-disc offsets, that the stellar kinematics should oscillate, similarly to the stellar disc.

For all the barred galaxies, the Hα gas rotation is offset by 0.4 kpc, on average, from the bar centre. For the offset galaxies, the centre of the gas velocity field is located closer to the centre of the bar compared to the centre of the stellar velocity field (median 0.56 kpc compared to 0.84 kpc). In fact, the results suggest that the gas kinematic centre is located nearer to the bar than to the centre of the disc (median 0.56 kpc compared to 0.71 kpc). This is in good agreement with P16, where the gas re-centers faster than the disc to the dynamical centre. The gas relaxation time, defined as the time taken for particles in a system to lose completely the memory of their initial velocity once disturbed (Binney & Tremaine, 2008), and thus re-align with the underlying potential can be estimated. According to Lake & Norman (1983), the relaxation time depends on the shape of the potential: $t_{\rm relax} \approx \frac{t_{\rm dyn}}{\epsilon}$, where t_{dyn} is the dynamical timescale (roughly the disc crossing time $t_{dyn} \approx R/v$) and ϵ is the ellipticity of the dark matter potential. Considering an initial offset of 2 kpc and a rotation velocity of 100 km s^{-1} for the offset galaxies, and the measured ellipticity of the potential $\epsilon = 1 - q_\phi \approx 0.03$, the gas relaxation time is ~ 0.7 Gyr, in agreement with the one predicted in simulations of P16 (~ 0.5 Gyr, see Figure 5.1). The observation of some offset galaxies with $d_{\rm gas-bar} > 0.5$ kpc (the average for the offset sample), suggests that the gas is not relaxed in some of these galaxies, and, if interactions are responsible for the offsets, they should have occurred in the last 0.7 Gyr. This timescale can be sufficiently large for the perturber to escape undetected if it has a high velocity.

There are not many studies in the literature which investigate the offsets between kinematic and photometric centres in galaxies, probably because of the lack of integral field spectroscopic data for a large sample of galaxies. This has changed in the last few years with the advent of IFS surveys such as CALIFA, MaNGA and SAMI. The studies investigating the kinematic centres of currently the largest sample of galaxies use data from the CALIFA survey (Walcher et al., 2014). García-Lorenzo et al. (2015) obtained the kinematic centres of the Hα velocity fields by determining the position where the velocity gradient is largest. Their catalogue provides the R.A. and Dec. offsets between Hα kinematic centre and the optical nucleus (placed at the centre of their IFU) for 84 weakly and strongly barred galaxies. Although the photometric decomposition of CALIFA galaxies does not provide the centers of the individual components, I inspected the images and 6 galaxies show some degree of offset between the disc and bar components (UGC 00312, UGC 03944, NGC 3057, UGC 08727, NGC 7321, UGC 12864, NGC 7800). Also using CALIFA data, Barrera-Ballesteros et al. (2014) published offsets on the sky between the star kinematic centre and the centre of the IFU for 30 galaxies with weak and strong bars, with only one showing a disc-bar offset (UGC 03944). As shown in Figure 5.6, the median gas-IFU offsets for the CALIFA data is $1.05''$ (rms $1\sigma = 0.87$), which at the distance of the galaxies corresponds to 0.32 kpc. For the 7 offset galaxies, the median offset is similar: 0.3 kpc. In this work I found comparable gas-bar offsets: 0.3 kpc for the entire sample studied and 0.5 kpc for the offset galaxies. The median stellar kinematic centre - IFU centre for the 30 CALIFA galaxies is $1.4''\pm0.6''$ (0.46 ± 0.22 kpc). This matches well our median result for the whole sample of 214 barred galaxies: 0.4 kpc for the star-IFU centre, while the offset galaxies show significantly larger offsets (0.8 kpc).

The simulations of P16 predict that the bar is always located at the dynamical centre of galaxies (measured as the location where the potential is deepest). The location of the dynamical centre is not trivial to determine in observations, as dark matter is not directly observable, but kinematics have often been used to infer its position. In general, authors (e.g. Trachternach et al. 2008; van Eymeren et al. 2011, etc.) assume that the kinematic centre of the HI gas is a good proxy for the dynamical centre in dwarf galaxies, since these galaxies have large amounts of gas that traces the underlying potential. Furthermore, studies show that the HI and Hα gas rotation curves are consistent in dwarf galaxies (Marchesini et al., 2002; Swaters et al., 2009). In this work, I find that the kinematic centre of Hα gas is located closer to the bar component than to the centre of the disc, while the centre of the stellar velocity field is displaced from the bar as well. If the Hα gas indeed traces the HI atomic gas,

this suggests that the bars are near the dynamical centre of galaxies, not the discs. Trachternach et al. (2008) also find that the position of the centre of HI gas kinematics and optical centres are in good agreement. Since the optical centre in offset galaxies is located in the bar, it would suggest that the bar is indeed at the dynamical centre. The HI gas centre has been observed to be coincident with the bar component in particular cases of offset galaxies, for example in NGC 3906 (de Swardt et al., 2015) or NGC 4027 (Pence et al., 1988). Therefore, these are galaxies with offset discs, not offset bars. Nevertheless, small offsets between the bar and the dynamical centre might exist in some galaxies, as the Hα rotation curves show different rotations on either side of the axis - flat rotation on one side, and rising on the other, for example in the case study of J161931.90+413945.2 (Section 5.2). This has been suggested by Noordermeer et al. (2001) to be a signature of the stellar distribution being offset from the dynamical centre, the rotation curve rising in the direction of the dynamical centre. In fact, the HI gas kinematic centre was found to be slightly offset from the bar in the LMC (van der Marel et al., 2002) as well.

If the gas is centred on the bar component for most of the offset galaxies, the stellar velocity field is not. I find an offset of 0.8 kpc between the bar and centre of stellar kinematics in the offset galaxies. In fact, latest observations of individual stars rotating (peculiar motion measurements) in the Large Magellanic Cloud by the *Gaia* mission (Gaia Collaboration, 2016) show clearly that the centre of stellar rotation does not match the centre of the bar component (Figure 5.12), confirming my findings for Magellanic type galaxies.

5.6.2 Kinematic-photometric misalignments

In this chapter I investigated, using kinematics, the possible origin of the off-centre discs and bars in recent major mergers (with a mass ratio from 1:1 to 3:1). Note, that galaxies that currently are photometrically disturbed, as identified by Galaxy Zoo, were discarded. By fitting the kinematic major axis for the star and gas velocity fields and measuring the difference from the photometric major axis I find a median of 15°, but with a significant rms scatter ±30°. The large scatter in this relation is probably due to selecting moderately inclined galaxies only, for which the P.A. determination is difficult, and some of the measurements might be biased because of strong bars which can change the observed kinematic P.A within the extent of the MaNGA data. There is a degeneracy between ellipticity and kinematic alignment at small inclinations - flatter galaxies show larger misalignments because the uncertainties in measuring the photometric major axes in face-on galaxies is large (the position angle can take

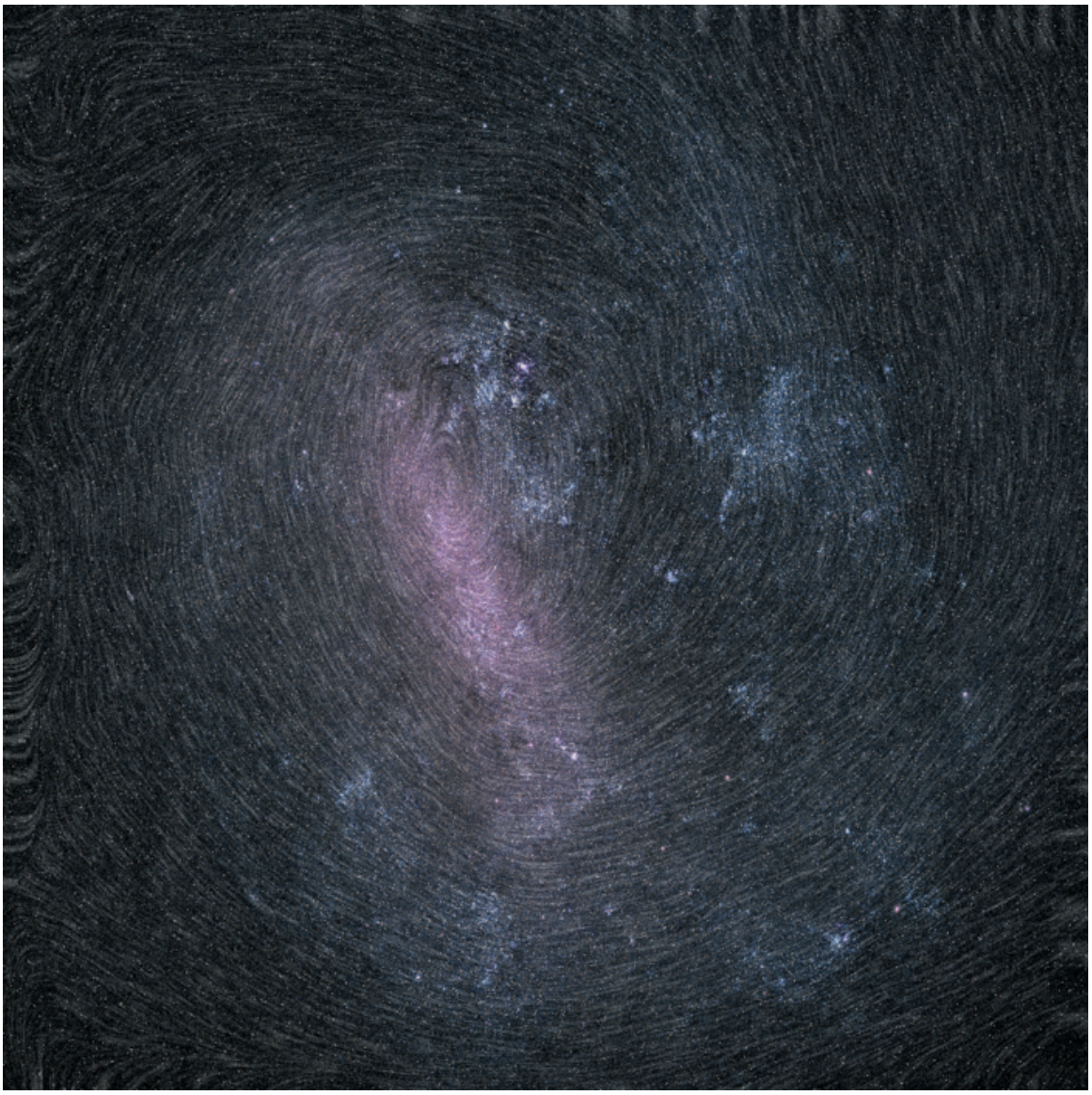

Figure 5.12: Rotation of the Large Magellanic Cloud as observed from the peculiar motions of stars by the *Gaia* mission (Gaia Collaboration, 2016). Credit: ESA, Gaia Data Processing and Analysis Consortium (DPAC); A. Moitinho / A. F. Silva / M. Barros / C. Barata, University of Lisbon, Portugal; H. Savietto, Fork Research, Portugal; P. McMillan, Lund Observatory, Sweden.

any value for exactly face-on galaxies). Graham et al. (2018) show this ellipticity-kinematic alignment degeneracy for fast rotators (spirals and early type galaxies with regular rotation) in their Figure 12. They find kinematic misalignment between the stellar velocity field and photometric axis of up to $\sim 30^\circ$ in MaNGA data for fast rotators of similar ellipticity, therefore my results are in agreement with their findings, for similar galaxies from the same survey.

Additionally, I found a very tight relation between the gas and stellar position angles $\sim 3^\circ$ with a scatter of $\sim 7^\circ$. This is similar to the value found by Barrera-Ballesteros et al. (2014), ($\sim 1^\circ$ and $1\sigma = 7^\circ$) who studied the kinematic misalignment in disc galaxies, including galaxies with weak and strong bars, in the CALIFA survey. They have used a different method in measuring the kinematic axis, by following the largest gradient on both the receding and approaching sides of the galaxies. In a sample of ~ 80 barred galaxies they find differences between the photometric and kinematic axes of both gas and stars less than 22° for 90% of the sample. They find similar misalignments for strongly, weakly and non-barred galaxies. Therefore, my results are consistent with other studies, though note that the galaxies considered in this work are more face-on than the ones considered in other studies.

One important distinction made in this work is between galaxies with significant offsets in photometry between disc and bar and galaxies with centred bars. I find similar alignments between the gas/stellar kinematics and the disc major axes, as well as between the stellar and gas kinematic axes, for offset galaxies and galaxies with centred components. This suggests that the offset galaxies in the sample did not undergo a major merger recently and thus the offset bar is not due to a recent major collision. Note that this does not exclude minor mergers (of mass ratio 10:1 for example), interactions or fly-bys. However, in the previous chapter, Section 4.5.7 I did not find a significant correlation of the offsets with companion galaxies.

5.6.3 Halo lopsidedness and triaxiality

Another possible scenario that can lead to an off-centre bar is if the dark matter halo is distorted, which can imprint the asymmetries onto the disc. This will result in an observed kinematic lopsidedness, where the two sides of the rotation curve are asymmetric (Jog, 2002). After the kinematic centre was estimated, I measured the difference between the approaching and receding sides of the rotation curve and calculated the perturbation in the potential, $\epsilon_{\rm kin}$ that could give rise to such an asymmetry in the kinematics. I found no correlation of $\epsilon_{\rm kin}$ with the disc-bar offsets, suggesting that the observed offsets are not due to their haloes being more lopsided, compared to the haloes of galaxies with centred bars. My observations that the haloes

are perturbed by ∼6% is consistent with the findings of van Eymeren et al. (2011), who for 70 nearby spiral and irregular galaxies found a similar, mean, $\epsilon_{\rm kin} = 0.056$ in HI data. In fact, for 6 of the galaxies showing the largest offsets in the sample of van Eymeren et al. (2011) (NGC 3274, NGC 2719, NGC 4242, NGC 4395, UGC 12732, NGC 7741) the measured $\epsilon_{\rm kin}$ is between 0.01 and 0.06, suggestive of their haloes not being significantly perturbed compared to the haloes of galaxies with centred bars.

Another possibility for the origin of offsets is if the haloes are not spherical, but triaxial. I have also estimated the axis ratio of the potential, q_ϕ from the non-circular velocities in the outer regions of the galaxies, assuming that these distortions are due to an oval dark matter halo. I find non-circular motions up to 5-15 km s^{-1}, on average (translating to $\sim 5-10\%$ of the circular velocity), at a distance of $1.5r_e$ from the centre in galaxies. These values result in an axis ratio of the haloes of $q_\phi \approx 0.96$, for both offset and galaxies with centred bars. This value is an upper estimate as well, since I considered all the distortions in the outer regions to be caused by the halo alone. Using a similar analysis, Sellwood & Sánchez (2010) found an axis ratio of the halo of 0.98 for two galaxies with centred bars, NGC 3198 and NGC 2403. Trachternach et al. (2008) found similarly small distortions (7-9 km s^{-1}) using HI data, suggesting ellipticities of only 0.983. These measurements of the halo axis ratios are in disagreement with cosmological ΛCDM simulations which suggest that dark matter haloes are triaxial (Frenk et al., 1999; Hayashi et al., 2004), and are significantly higher than predictions, $\epsilon = 0.7 - 0.9$ (Hayashi et al., 2007).

Non-circular motions are most evident at the centre of galaxies, where bars are present. I find significant bar-like flows, with an average of $V_{2,max} = 25$ km s^{-1}, in the MaNGA gas velocity maps of strongly barred galaxies. Weak bars show bar flows with a slightly smaller amplitude of $V_{2,max} = 15$ km s^{-1}. This implies that the bars shape the local potential and influence the kinematics of gas in the central regions of galaxies, rather than the dark matter halo.

The incidence of bar-like kinematic flows causing the twists was studied before in IFS data from the CALIFA survey by Holmes et al. (2015), also using the DiskFit software. They find 25 out of the 37 disc galaxies fitted to be well characterized by pure rotation models and 12 galaxies to show significant radial and tangential components characteristic of bar-like flows (> 15 km s^{-1}). Out of the 12 galaxies with non-circular flows, 11 are barred. They show an average $V_2 \sim 16$ km s^{-1} over the central 4.5 kpc, which is similar to the values found in this work for strongly barred galaxies, if V_2 is averaged over half the r_e of the disc. Cecil et al. (2016) also discusses fitting non-circular motions to 13 barred galaxies, with similar morphologies to those in this work. They find distortions to the circular motion of gas of the order

$V = 10 - 30$ km s^{-1}, similar to the values found in this work, suggesting that the measurements are robust.

Excluding major mergers and lopsided halos as the possible origins of off-centre discs and bars in some galaxies, the scenarios left to explore are interactions with dark matter subhaloes (Bekki, 2009) or interactions with small companions which I did not detect either because they are too faint or because they are fast moving. A search for companions, or tidal tails might be successful in determining the cause of offsets.

5.6.4 Kinematic-photometric offsets as tests for alternative theories to GR

One idea deriving from the work in this chapter is that studying the kinematics of dwarf galaxies has been suggested to be useful in testing alternative theories of General Relativity, such as the existence of a 'fifth' force that acts like the Newtonian force at large scales. Since this force is excluded by measurements on Solar System scales, it must be 'screened', effectively acting differently at different scales. Because of the high local potential in stars, stars are screened from this fifth force, while gas and dark matter are not. This screening mechanism may cause the stars to lag behind the gas and dark matter, which can lead to a separation between the disc centre, gas centre and centre of dark matter halo (Jain & VanderPlas, 2011; Desmond et al., 2018). This would be most effective in lower density environments such as low mass dwarf galaxies, which have a lower potential than Milky Way size galaxies. It is possible to measure the effect of this fifth force by measuring the distance between the stellar and gas mass centroids, for example between the photometric centres and the gas (HI in special) kinematic centres (Desmond et al., 2018). The results showing that the gas and bars trace the dynamical centre, while the stellar discs do not, suggests that these offset galaxies might be good targets to test such alternative theories of General Relativity.

5.7 Conclusions

In this chapter I investigated the spatial relation between the photometric components of galaxies (discs and bars) and the kinematic components (gas and stars), as well as the origin of the observed visual offsets between discs and bars in a sample of galaxies, using data from SDSS and the MaNGA IFU survey. Even though the small sample of offset galaxies (27), the relatively low spatial resolution of MaNGA and the selection

effects of relatively face-on galaxies prevent drawing definitive conclusions, below I summarise the results of this study:

(i) I find evidence that, in offset galaxies, the rotation of Hα gas better traces the bar component compared to the disc component, hinting towards the bar component being situated closer to the dynamical centre of the these galaxies, as predicted by the simulations of P16.

(ii) The stellar velocity fields are offset by 0.8 kpc from the bar, on average, and these offsets correlate with the disc-bar offsets suggesting that the stellar disc is 'sloshing around'. A mismatch between the bar centre and centre of stellar rotation in the Large Magellanic Cloud is also seen in the latest *Gaia* observations.

(iii) The kinematic and photometric major axes are aligned for both stars and gas, and the alignment does not differ between galaxies with offset or centred components. This excludes recent major mergers to be the cause of the offsets.

(iv) From the asymmetry in the kinematics I find that, if the dark matter haloes are $m = 1$ lopsided, the perturbations in the potential are small, $\epsilon_{\rm kin} = 0.063$ for the offset galaxies and $\epsilon_{\rm kin} = 0.066$ for galaxies with centred bars. Furthermore, there is no correlation between the perturbation in the potential and offsets, implying that a lopsided dark matter halo imprinting its lopsidedness onto the galaxy discs is not the origin of off-centre discs and bars.

(v) By fitting $m = 2$ modes to the gas and stellar velocity maps I find strong non-circular gas motions at the centre of strongly bar galaxies with centred components, typical of bar-flows. The amplitude of the bar flows increases with bar strength as measured from Galaxy Zoo bar classifications.

(vi) By measuring the amplitude of the non-circular motions in the outer region of galaxies, I find only small $m = 2$ radial and tangential flows ($\sim 5 - 15$ km s^{-1}) for offset galaxies, at the measurement limit. This is consistent with the dark matter haloes being approximately round ($q_\phi \approx 0.97$).

Chapter 6

Boxy/Peanut Bulges

Many edge-on galaxies show a vertically extended structure with a boxy, peanut or an X-shaped appearance, referred to as a 'boxy/peanut bulge'. One of the outstanding puzzles in the evolution of barred galaxies is how and when bars thicken out of the plane of the galaxy to form these structures. In this chapter I investigate, for the first time, the fraction of boxy/peanut bulges in barred galaxies from $z \approx 0$ to $z = 1$, using two mass- and resolution-matched samples of moderately inclined galaxies with masses $M_* > 10^{10}\,M_\odot$, from SDSS and from the *Hubble Space Telescope* COSMOS survey. The boxy/peanut bulges are classified based on the morphology of their inner bar isophotes by three expert astronomers. I examine the redshift evolution of the fraction of boxy/peanut bulges, as well as its dependence on stellar mass and bar length. A mechanism proposed to be responsible for the vertical thickening of bars is bar buckling. By comparing the observed isophotes with those predicted from simulations of bar buckling, I identify galaxies in the process of buckling, at both low and high redshifts. I investigate when bar buckling occurs, how long this phase lasts and if it can account for the observed fraction of boxy/peanut bulges.

6.1 Motivation and background

There is now clear evidence that many galaxies appear vertically thickened in the inner part when viewed edge-on, appearing as 'boxy', 'peanut' or even 'X'-shaped (e.g. Bureau & Freeman 1999; Lütticke et al. 2000a,b; Laurikainen & Salo 2016). Collectively known as 'boxy/peanut bulges' (B/P bulges), these features are the same basic structure, with morphology differing due to differences in strength and orientation (Combes & Sanders 1981; Combes et al. 1990; Athanassoula & Misiriotis 2002).

They are referred to as 'bulges' following the standard definition of a bulge being a component extending above the plane of the disc; however the boxy/peanut feature is actually part of the bar, so the name 'boxy/peanut bulge' is a misnomer that unfortunately stuck in astronomical nomenclature. This topic has received increased interest lately since our own galaxy, the Milky Way, is now believed to have a boxy/peanut structure (Dwek et al., 1995; Freudenreich, 1998; Shen et al., 2010; Wegg & Gerhard, 2013; Wegg et al., 2015; Shen & Li, 2016; Debattista et al., 2017).

The vertical structure of B/P bulges is thought to be supported by complex orbits referred to as the x_1 tree, arising from stable x_1 bar orbits forming vertical bifurcations such as 'banana' (x_1v_1) orbits (Skokos et al., 2002). But other orbits might also contribute to this vertical structure, such as box orbits (Valluri et al., 2016; Abbott et al., 2017), 'brezel' orbits (Portail et al., 2015) or unstable chaotic orbits (Contopoulos & Harsoula, 2008). The superposition of these orbits gives an overall thick structure appearance of the bar when viewed in 3D, with the inner part being thicker than the outer part.

N-body simulations have shown that after a galaxy forms a bar, it can shortly be followed by a violent vertical instability in the inner part that causes the bar to thicken asymmetrically in the vertical direction, a mechanism referred to as *bar buckling* (Raha et al., 1991; Merritt & Sellwood, 1994; Martinez-Valpuesta & Shlosman, 2004; Debattista et al., 2004, 2006; Saha et al., 2013). A driver of buckling is the coupling between the vertical and radial motions of stars which results in increasing the random motion in the vertical direction (σ_z), until it is comparable to the random motion in the galaxy plane (σ_r) (Toomre, 1966). Despite bar buckling appearing frequently in simulations (Martinez-Valpuesta & Shlosman, 2004; Debattista et al., 2004), leading to the formation of B/P bulges, so far only three galaxies have been observed in the process of buckling (NGC 3227 and NGC 4569, Erwin & Debattista 2016, and ESO 506-G004, Li et al. 2017). The lack of many observations of ongoing bar buckling suggests that either this process occurs rapidly, so that the chances of observing a galaxy buckling are low, or that another mechanism is responsible for the formation of B/P bulges. The other mechanism suggested for forming boxy/peanut bulges is a slower, symmetric thickening due to the trapping of disc stars at vertical resonances (Combes et al., 1990; Pfenniger & Friedli, 1991; Quillen, 2002; Debattista et al., 2006; Quillen et al., 2014). Although bar buckling has now been observed, it is not yet clear how frequent it is and whether it can lead to the formation of the observed fraction of B/P bulges.

In this work I would like to establish if bar buckling is common, when it occurs, what its cause is and if it can explain the observed fraction of B/P bulges in the local

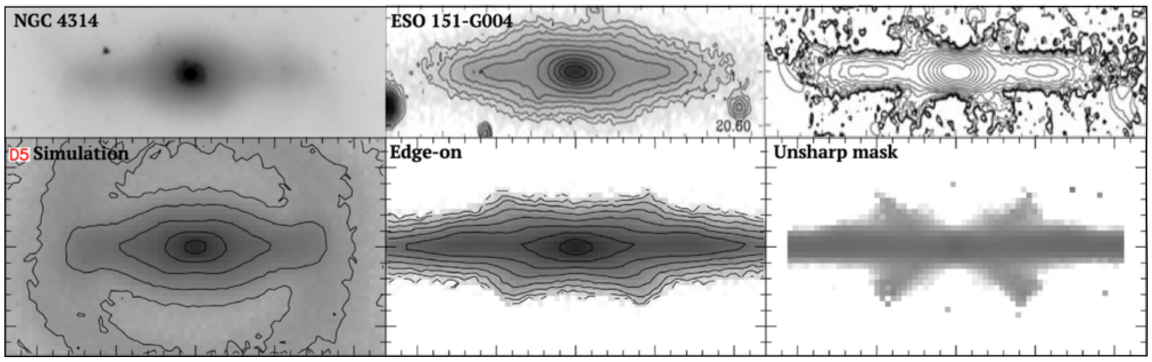

Figure 6.1: *First row*: Observations of a face-on 'barlens' (Laurikainen et al., 2011) in NGC 4314, 3.6μm image from the S^{4}G survey; an edge-on view showing the boxy/peanut structure of ESO 151-G004 and an unsharp mask revealing the X-shaped feature of the galaxy (K-band image from Bureau et al. 2006). *Second row*: Face-on and edge-on views of a galaxy from the N-body simulation of Debattista et al. (2017) (at t =5 Gyr).

Universe. To achieve this, I select a sample of barred galaxies at different redshifts ($0.15 < z < 1$), observed by the *Hubble Space Telescope (HST)*, and a sample of local barred galaxies ($z \approx 0$) from SDSS for comparison. The SDSS survey is ideal for the selection of a comparison sample, since the resolution of SDSS from the ground for galaxies at $z < 0.05$ is similar to the resolution of *HST* for galaxies at $0.15 < z < 1$. Therefore, I study the redshift evolution of B/P bulges in the Universe, its dependency on galaxy properties (stellar mass and bar length), and identify buckling bars at various redshifts. To identify these structures based on their morphology, I compare the observations with N-body simulations of galaxies undergoing bar buckling and forming B/P bulges, by Debattista et al. (2006, 2017), Sellwood & Debattista (2009), Erwin & Debattista (2013) and Cole et al. (2014).

There have been many attempts to study the fraction of B/P bulges in edge-on galaxies, where these structures are most easily identifiable. Lütticke et al. (2000a) found a local fraction of B/P bulges in edge-on galaxies of 45%, in both optical and infrared, when inspecting a large sample of $\sim 1,350$ galaxies. In a more recent study using SDSS data, Yoshino & Yamauchi (2015) found a lower fraction of 22%. The Galaxy Zoo 2 project also asks a question about the shape of the bulge if the galaxy is initially classified as being edge-on. However, studies of edge-on galaxies suffer from an important problem: it is relatively easy to identify a galaxy hosting a B/P bulge, but it almost impossible to identify if an edge-on galaxy without a B/P bulge hosts a bar. Therefore, it is difficult to assess the fraction of *barred* galaxies hosting B/P bulges by studying edge-on galaxies. In addition, the orientation of the bar in an edge-on galaxy is important, since a bar viewed end on will appear to have an elliptical shape, while bars with intermediate orientations and edge-on bars will appear to have

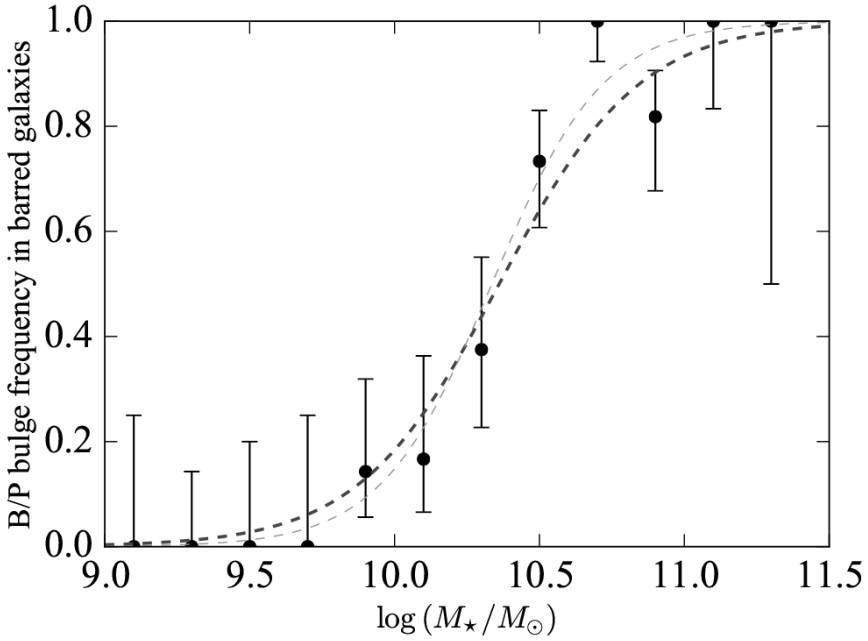

Figure 6.2: Frequency of B/P bulges in barred galaxies as a function of stellar mass (from Erwin & Debattista 2017). The thick line shows the best-fitting logistic regression.

boxy and peanut shapes, respectively (Lütticke et al., 2000a). Recently, Laurikainen et al. (2014) suggested that boxy/peanut bulges can also be identified in face-on galaxies, appearing projected as 'barlenses' (lens like structures embedded inside bars, Laurikainen et al. 2011, 2013). Athanassoula et al. (2015) confirmed this view by comparing numerical simulations from different viewing angles with observations. The observed morphology of boxy/peanut/X-shaped bulges in face-on view (identified as a 'barlens') and edge-on view, and the morphology of boxy/peanut bulges from N-body disc galaxy evolution simulations by Debattista et al. (2017) are shown in Figure 6.1. Erwin & Debattista (2013) showed that it is possible to recognise B/P bulges in moderately inclined galaxies ($i \sim 40° - 70°$) by identifying boxy shaped isophotes and offset spurs (as shown in Figure 6.6), in a sample of 78 local galaxies observed mostly in the infrared. They compare the observations with N-body simulations of B/P bulge formation via bar buckling (Debattista et al., 2006) to demonstrate that it is possible to identify both galaxies *with* B/P bulges and *without* B/P bulges using this method. Therefore, if galaxies have an ideal orientation (moderately inclined with a bar with a position angle $< 60°$ measured from the galaxy major axis) it is possible to identify *both* B/P bulges and bars in galaxies, thus allowing us to confidently compute a fraction of barred galaxies with B/P bulges.

Erwin & Debattista (2017) (hereafter E&D17) investigated the fraction of galaxies

hosting B/P bulges in 84 moderately inclined local galaxies, selected to have well resolved bars and suitable orientations. The galaxies were selected from the catalogue of de Vaucouleurs et al. (1991), situated at a distance < 25 Mpc and with diameters $D_{25} \geq 3.0'$, with available optical and near-infrared imaging. They found that B/P bulges are very common in the local Universe, with $\sim 50\%$ of barred galaxies hosting B/P bulges, and a strong dependence of the B/P bulge fraction on mass: $\sim 80\%$ of galaxies with $M_* > 10^{10.4} M_\odot$ have B/P bulges compared to only $\sim 20\%$ of lower mass galaxies, as shown in Figure 6.2. A similarly strong dependence on stellar mass was found by Li et al. (2017) in the I-band imaging of a sample of 264 local disc galaxies from the Carnegie-Irvine Galaxy Survey. They used the same method of identifying boxy/peanut bulges in moderately inclined galaxies as in Erwin & Debattista (2013), and further identified 'barlenses' as boxy/peanut bulges in face-on galaxies.

In this chapter I refer to boxy, peanut- or X-shaped bulges and their face-on barlens counterparts collectively as B/P bulges. In Section 6.2 I describe the selection of a sample of barred galaxies from the *HST* COSMOS survey and a comparison sample from SDSS. In Section 6.3 I discuss the simulations of boxy/peanut bulges and bar buckling, and compare the morphologies of these features with observations. In Section 6.4, I discuss the method used in identifying B/P bulges and buckling bars and the expert classifications of Erwin, Debattista and myself. In Section 6.5 I present the results of this project: the B/P bulge fraction with redshift, the B/P bulge fraction with inclination, the B/P bulge fraction with mass and bar length and the identification of a sample of buckling bars and the fraction of buckling bars in the Universe. Finally, in Section 6.7 I discuss the implication of my results in the context of the evolution of barred galaxies, and, in particular, for the buckling mechanism in forming B/P bulges.

6.2 Data

6.2.1 *Hubble Space Telescope* - COSMOS

The higher redshift barred galaxies were selected from the *HST* Cosmic Evolution Survey (COSMOS) (Koekemoer et al., 2007; Scoville et al., 2007), covering an area of 1.8 deg^2, centred at $\alpha = 10^h00^m$ and $\delta = +02°12'$. COSMOS is the largest wide-field survey ever undertaken by *HST*, designed to probe the evolution of galaxies, star formation, AGN and dark matter with the large-scale structure up to $z \lesssim 3$ (Scoville et al., 2007). The *HST* images were taken with the Advanced Camera for Surveys (ACS), with the I-band F814W filter, during 590 orbits consisting of 590 pointings

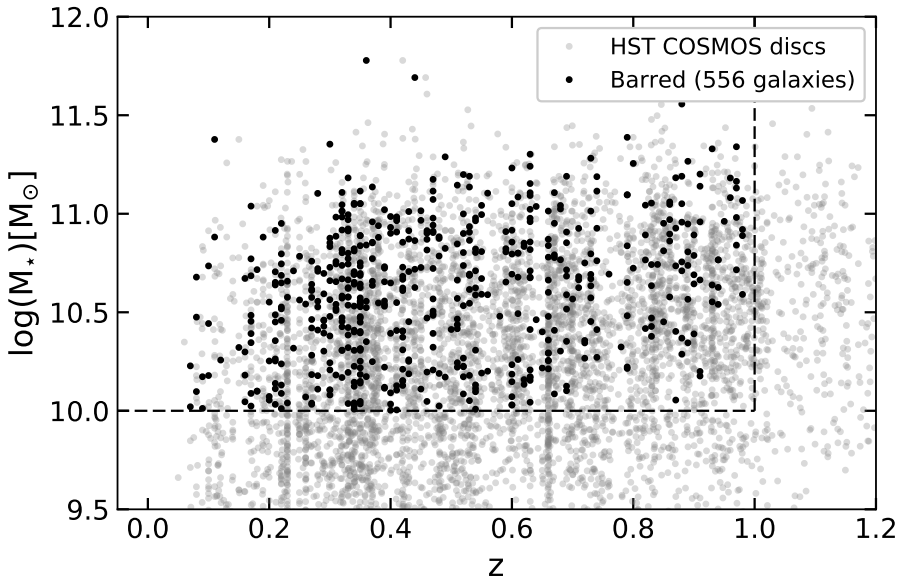

Figure 6.3: Mass-redshift relation for the selected *HST* galaxies in this study. The gray points show the disc galaxies identified in *HST* COSMOS and the black points show the moderately inclined barred galaxies with $p_{\rm bar} > 0.5$ as identified in the Galaxy Zoo: Hubble project. Masses and redshifts are from the COSMOS2015 catalogue (Laigle et al., 2016).

with an exposure time of 2028 s each (Koekemoer et al., 2007). The resolution of the ACS images is 0.05 arcsec pixel^{-1}, and the PSF FWHM is 0.09".

85,000 images of galaxies from COSMOS were classified in the third incarnation of the Galaxy Zoo project, Galaxy Zoo: Hubble (GZH, Willett et al. 2017). Although the COSMOS survey provides only I-band F814W images, in GZH pseudo-colour images were created based on Subaru telescope B_J, r_+ and i_+ filters (see Griffith et al. 2012). To correct for redshift bias (galaxies appearing dimmer and fainter at higher redshifts) in the classifications, the GZH project (Willett et al., 2017) used simulated *HST* images of 288 nearby galaxies, based on lower-redshift SDSS images and redshifted to $0.3 < z \leq 1$ using the FERENGI code (Barden et al., 2008) (see Section 4.1 in Willett et al. 2017 for more details).

The question tree was similar to the one in GZ2 (seen in Chapter 2, Figure 2.2), with the exception of a second tier question (after the *smooth/features/artifact* question and in parallel with the bar question), asking if the galaxy has a clumpy appearance.

The redshift debiasing was only applied to the top tier question in GZH, as the lower tier questions had, on average, fewer classification than required for a reliable debiasing. Therefore, the vote fractions weighted by the users' performance are used for the lower tier questions to select a barred sample. Following the recommendations

of Willett et al. (2017) (in their Section 6.1), to select a sample of barred galaxies I selected galaxies with $p_{\rm features} > 0.23$, $p_{\rm edge-on,no} > 0.25$, $p_{\rm clumpy,no} > 0.30$, $N_{\rm bar} \geq 20$ and $p_{\rm bar} > 0.5$. Due to the more complex decision tree (with the addition of the '*does the galaxy have a mostly clumpy appearance?*' question) in GZH compared to GZ2 and the increased difficulty in classifying higher redshift galaxies, the median number of individual classifications per image was 122, compared to 40 (in GZ2) (Willett et al., 2017). Thus, I selected galaxies from the COSMOS survey with a higher bar classification threshold compared to SDSS (20 votes compared to 10 votes), to ensure that $p_{\rm bar}$ is well-sampled. Nonetheless, selecting galaxies with $N_{\rm bar} \geq 10$ instead does not change the sample due to the large number of classifications and the requirement that $p_{\rm bar} > 0.5$. The selection of $p_{\rm edge-on,no} > 0.25$ removes edge-on galaxies from the sample ($i \gtrsim 75$). The $p_{\rm clumpy,no} > 0.30$ threshold in GZH guarantees the exclusion of galaxies that have mostly a clumpy appearance, frequently observed at high redshifts (Elmegreen et al., 2007) and for which the bar identification is difficult. The barred sample is nevertheless insensitive to the 'clumpy' question; increasing this threshold to $p_{\rm clumpy,no} > 0.50$ removes only 1% of the galaxies. Selecting bars with $p_{\rm bar} > 0.5$ corresponds to selecting a sample of galaxies with strong bars, as these are most easily identifiable in galaxy images.

In addition, I selected only galaxies with stellar masses $M_* > 10^{10} M_\odot$ and in the redshift range $0 < z < 1$. This mass threshold is motivated by the findings of E&D17 that galaxies with stellar masses $M_* < 10^{10} M_\odot$ are observed to have a very low fraction of B/P bulges ($f_{\rm B/P} \lesssim 0.1$). The upper redshift limit of $z \approx 1$ is set by the F814W band shifting to the rest-frame u-band, where bar detection has proved to be difficult due to clumpy star formation and lower signal-to-noise (S/N) (Sheth et al., 2008; Melvin et al., 2014). This selection yields a total of 556 barred galaxies, which are shown in the mass-redshift diagram in Figure 6.3 compared to disc galaxies in *HST* COSMOS (selected similarly to barred galaxies, but without the requirement $p_{\rm bar} > 0.5$).

The FITS images are downloaded from the STScI Hubble Legacy Archive[1]. The stellar masses are taken from the COSMOS2015 catalogue (Laigle et al., 2016) and are based on the BC03 (Bruzual & Charlot, 2003) synthetic spectrum fitting (best-fit template, minimum χ^2, value *mass best* in their catalogue) using multiwavelength $YJHK_s$ imaging and assuming a Chabrier IMF (Chabrier, 2003). The photometric redshifts of the galaxies obtained by fitting spectral templates to the galaxy SEDs are also taken from the COSMOS2015 catalogue. The accuracy of the photometric

[1] https://hla.stsci.edu/hlaview.html/

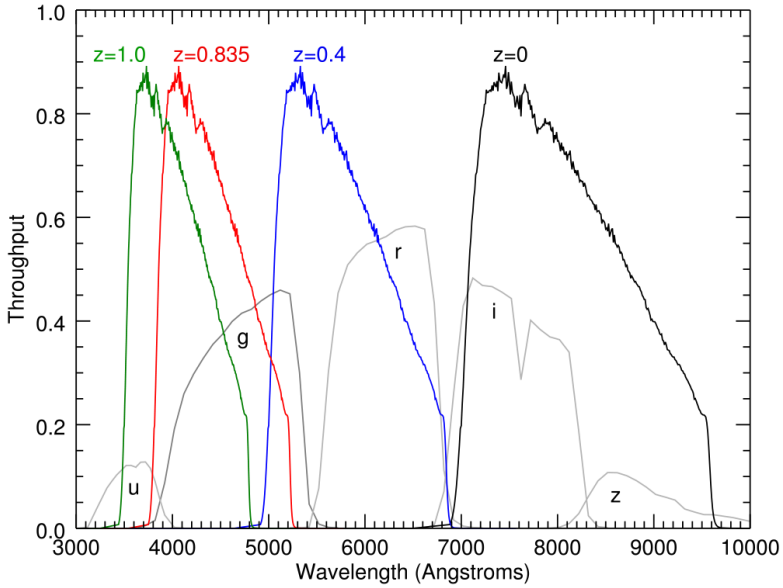

Figure 6.4: Illustrating the band shifting effects of the ACS F814W filter to the SDSS *griz* rest-frame filters for galaxies at redshifts $0 < z < 1$. F814W images of galaxies situated at $z > 1$ have rest-frames corresponding to the u-band and are not included in this study. The throughput values include detector, instrumental effects, as well as effects due to the atmosphere (for SDSS). Original plot from Melvin et al. (2014).

redshifts is high: $\sigma = 0.007$ (dispersion measurement compared to the measured spectroscopic redshifts of a subsample of galaxies) and $\eta = 0.5\%$ (fraction of catastrophic errors $|z_{phot} - z_{spec}|/(1 + z_{spec}) > 0.15$) (Laigle et al., 2016). Structural parameters from one component Sérsic fits for the COSMOS galaxies are available from Griffith et al. (2012). The physical resolution of the COSMOS galaxies is calculated assuming a FWHM of 0.09" and using the photometric redshift of the galaxies, and, to account for band shifting, the corresponding SDSS *gri* rest-frame band of the *HST* F814W filter was determined, as shown in Figure 6.4.

6.2.2 SDSS comparison data

To study the redshift evolution of the B/P bulge fraction, from the local Universe to $z \sim 1$, I selected a local ($z \approx 0$) mass- and resolution-matched sample from SDSS DR10, with morphological classification from Willett et al. (2013). From the initial sample of 243,000 Galaxy Zoo 2 galaxies with available spectroscopic redshifts (GZ2 *specz* sample), I selected galaxies with $M_* > 10^{10} M_\odot$, $p_{\rm features} > 0.23$, $p_{\rm edge-on,no} > 0.25$, $N_{\rm bar} \geq 10$ and $p_{\rm bar} > 0.5$ giving a total of 14,104 galaxies. This selection is very similar to the selection of higher redshift galaxies from COSMOS, with the exception

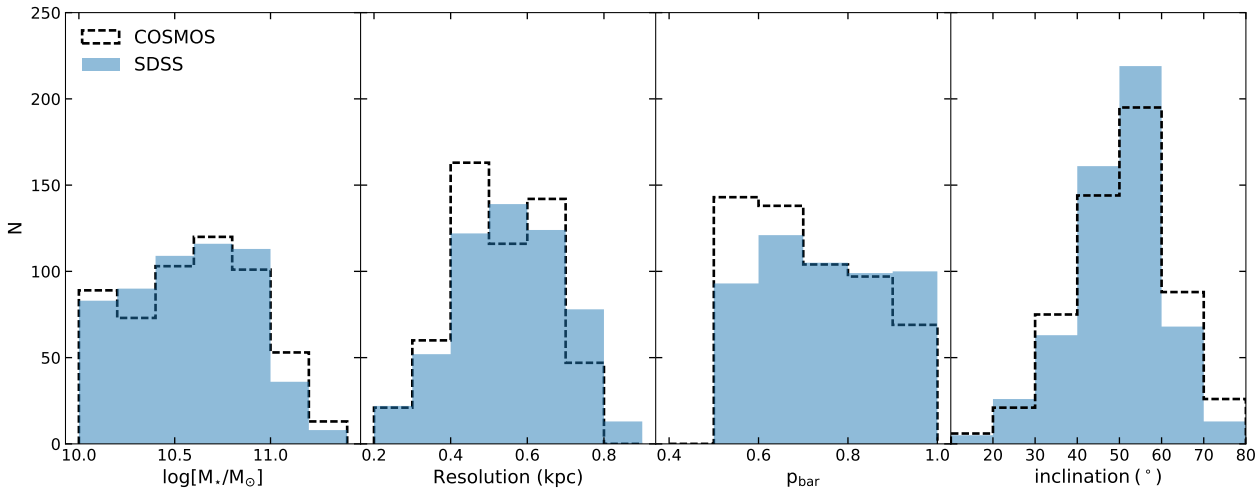

Figure 6.5: Histograms showing the matching in stellar mass, physical resolution and bar likelihood ($p_{\rm bar}$) for the HST and SDSS samples.

for the threshold for the 'clumpy' question in GZH question which did not appear in GZ2, and which did not affect the final sample selection of COSMOS galaxies.

The mean resolution of the SDSS imaging, of the selected galaxies, in the g, r, i bands is 1.2", 1.13", 1.06", respectively. This resolution was converted to a physical resolution, in kpc, at the redshift of the SDSS galaxies. The resolution ranges from 0.1 kpc to ∼5 kpc (which is much larger than the resolution of *HST* at $z \sim 1$, ∼0.8 kpc/arcsec). In order to obtain similar resolution with SDSS, one needs to select galaxies with $z \lesssim 0.04$.

Thus, in order to compare COSMOS galaxies with SDSS galaxies, from the superset of 14,104 SDSS barred galaxies, I selected a random sample of 556 unique (without replacement) SDSS galaxies such that the stellar mass of each SDSS galaxy is within ±0.2 dex of the mass of a COSMOS galaxy, $p_{\rm bar}$ is within ±0.2 and the physical resolution (in kpc) of the *gri* band of the SDSS observation corresponding to the rest frame of the F814W image of the COSMOS galaxy is within 20% of the physical resolution (in kpc) of *HST*. This selection resulted in sample containing 556 high redshift galaxies and a control sample of 556 $z \approx 0$ galaxies, as shown in Figure 6.5. Small differences arise because of (1) binning - individual galaxies in the two samples are matched in the parameters described above, rather than matched in bins, and (2) there are insufficient high mass SDSS barred galaxies with comparable resolution to *HST*, as the more massive galaxies in SDSS are situated at higher redshifts (due to the smaller volume probed). A better match between the two stellar mass distributions could be achieved by sampling with replacement, however this would be at the expense of introducing further discrepancies in the distribution of

physical resolutions, since the highest mass SDSS galaxies have the worst resolution images. Nevertheless, I have investigated matching the COSMOS mass distribution by sampling with replacement and all the results are similar to those presented in this chapter. Thus, in the analysis I used the SDSS comparison sample matched without replacement, since all the 556 SDSS galaxies were inspected and classified.

Axis ratios for the SDSS galaxies are available from r-band exponential fits. The distribution of galaxy inclinations, calculated from the apparent axis ratios ($\cos i \approx b/a$), are shown in Figure 6.5 (4^{th} panel). Both the higher redshift COSMOS and local SDSS galaxies in this chapter are selected to have moderate inclinations (95% of galaxies have inclinations $i \sim 30^\circ - 75^\circ$), but both samples also include a small fraction (5%) of face-on galaxies with $i \lesssim 30^\circ$. The two distributions are similar, even though matching the two distributions was not a selection criterion. The small differences are due to a slightly different measure for the axis ratios (Sérsic fits for COSMOS and exponential fits for SDSS), and the fading of the outer discs in the imaging of COSMOS galaxies (Sheth et al., 2008; Melvin et al., 2014), causing the discs to appear rounder and, thus, less inclined.

To mitigate the potential biases of B/P classifications with wave band, the SDSS galaxies were classified in one of the g, r, i bands corresponding to the rest-frame wavelength of the F814W image of the analogous COSMOS galaxy. This depends on the redshift of the COSMOS galaxies, the band shifting being illustrated in Figure 6.4.

6.3 Simulations

In this chapter I used four simulations to show the projection effects on galaxy isophotes in order to compare the visual morphologies of B/P bulges and buckling bars with the morphologies of simulated galaxies undergoing bar buckling. Three of the simulations (A, B and E), shown in Figure 6.6 compared to real galaxies, are taken from and described in further detail in Erwin & Debattista (2013, 2016) (A and B), in Sellwood & Debattista (2009) (B) and in Debattista et al. (2017) (E). Simulations A and B are pure N-body simulations using 300,000-500,000 stellar particles in the disc and have softening lengths between 50-60 pc. In simulation A, the disc of mass $M_* = 7 \times 10^{10} M_\odot$ has an exponential scale length of 6 kpc and a scale height of 0.3 kpc. In contrast, simulation E contains gas. It is an N-body+SPH simulation (described in Ness et al. 2014; Cole et al. 2014; Debattista et al. 2017) with a spatial resolution of 50 pc, and a stellar mass resolution $M_* \sim 10^4 M_\odot$. All simulations develop a strong bar (shown in simulation B before buckling), undergo

bar buckling (shown in Figure 6.7) and form B/P bulges (shown in simulations A and E). Simulation E has undergone recurrent buckling.

The fourth simulation (C), showing a buckling bar in Figure 6.7, taken from Erwin & Debattista (2016) (and also described in Sellwood & Debattista 2009), is run with similar initial parameters to simulation B, but with a different initial seed to explore the stochasticity of disc galaxy evolution. It illustrates the morphology before buckling (*left panel*), during the buckling stage (*middle panel*) and post-buckling (*right panel*).

Therefore, it is possible to identify B/P bulges and buckling bars in COSMOS and SDSS data by comparing the appearance of real galaxies with the morphologies from N-body simulations shown in Figure 6.7.

6.4 Classification method

6.4.1 Identification

The visual identification of B/P bulges is based on the method outlined in Erwin & Debattista (2013). At moderate inclinations, the B/P bulge projects to form thicker, often box-shaped, isophotes, and the outer part of the bar projects to form thin offset isophotes referred to as spurs, as illustrated in galaxies NGC 1808, NGC 1617, NGC 3992 and simulations A and E in Figure 6.6 (from E&D17). Figure 6.6 shows the projection effects of the inclination i and difference in position angle between the bar and disc ($\Delta\mathrm{PA}_{\mathrm{bar}}$) on the isophotes. If the galaxy does not have a B/P bulge, the projected isophotes are ellipses and the spurs are not distinguishable, as in the case of IC 676.

Buckling bars can be identified based on their trapezoidal isophotes in contrast with the boxy isophotes of B/P bulges, as illustrated in Figure 6.7.

6.4.2 Panoptes Project

To classify B/P bulges more efficiently I set up a project using the Zooniverse Panoptes Project Builder. The interface used for classifications is shown in Figure 6.8. Instead of a *Yes/No* answer for the question *'Does the galaxy have a B/P bulge?'*, I decided on five possible answers: 'Definitely', 'Probably', 'Maybe', 'No' and 'No bar' to capture our confidence in classifying the galaxy isophotes. The 'No bar' option was added in the case of galaxies without bars that were misclassified in GZ2 or GZH. Each answer was assigned a score: -1 ('No bar'), 0 ('No B/P'), 1 ('Maybe B/P'), 2 ('Probably B/P') and 3 ('Definitely B/P').

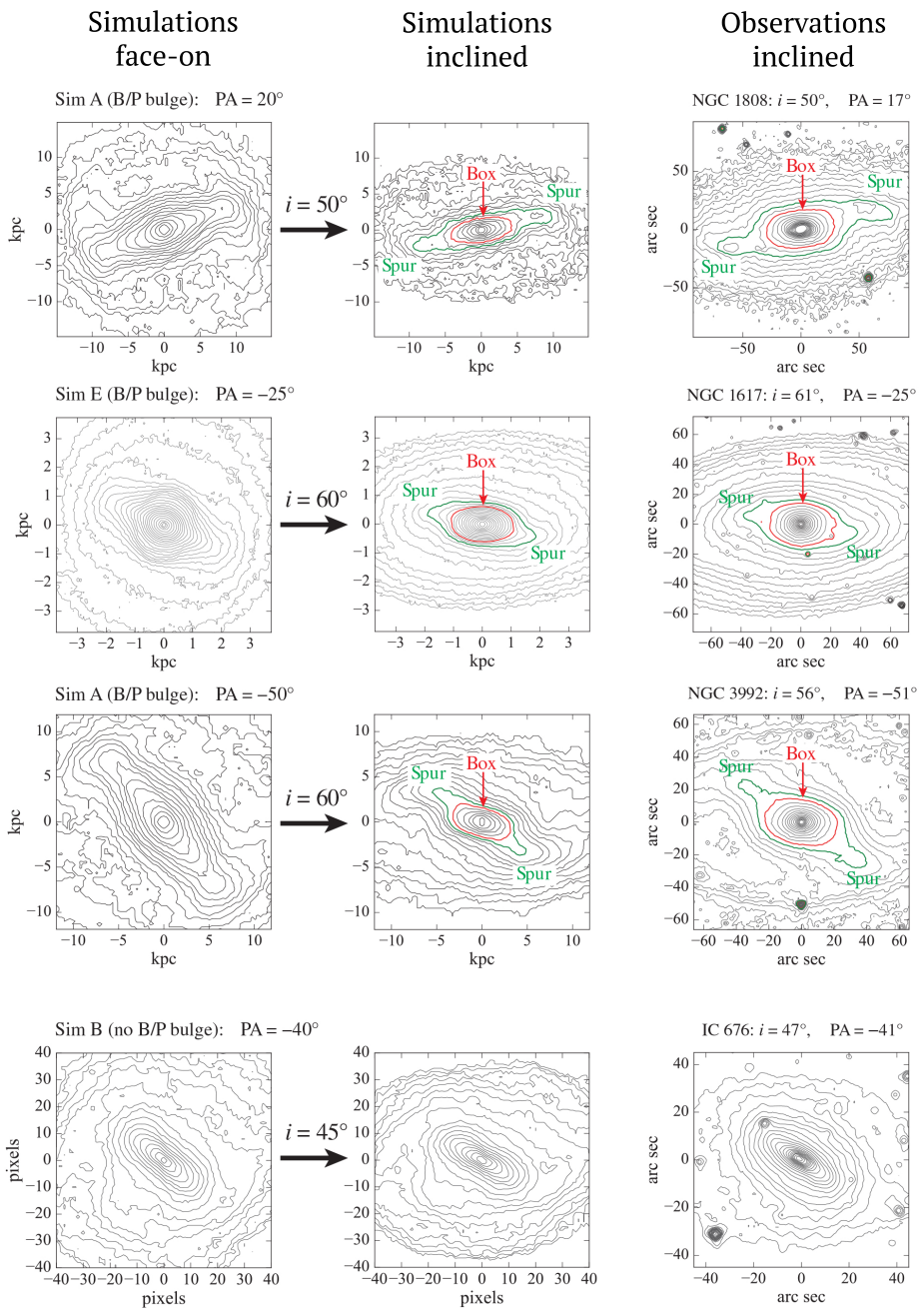

Figure 6.6: Original Figure 1 from Erwin & Debattista (2017). Projection effects on the isophotes for galaxies with and without B/P bulges, used for B/P identification in this chapter. B/P bulges show boxy isophotes and offset spur morphology. Galaxies without B/P bulges show elliptical isophotes and do not show spurs (last row). The *left* and *middle panels* show two simulations of galaxies with B/P bulges (A and E) and one without a B/P bulge (B) projected face-on (*left*) and inclined at the inclination of real galaxies (*middle*). The galaxies on the right hand side are *H*-band images from the S^{4}G survey, except for NGC1808 which is from Eskridge et al. (2002).

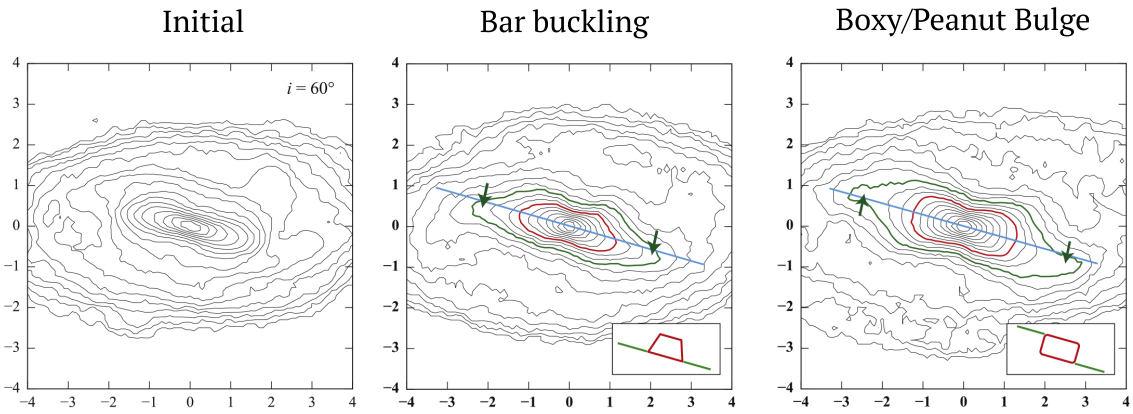

Figure 6.7: N-body simulations before, during and after buckling showing how it is possible to identify buckling bars and B/P bulges using isophotes. Buckling bars show trapezoidal inner isophotes with the outer-bar spurs offset in the same direction, to the base of the trapezium (*middle panel*). B/P bulges show boxy isophotes and spurs offset on the symmetrically opposite sides of the box (*right panel*). Original Figure 1 in Erwin & Debattista (2016).

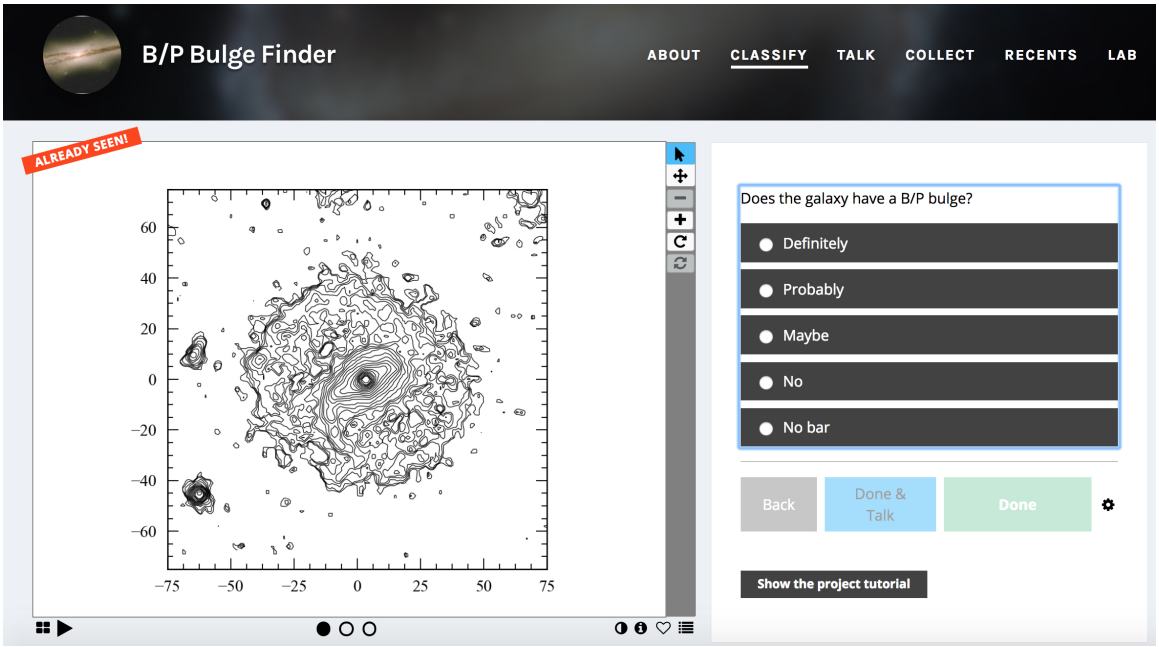

Figure 6.8: The project interface with the Zooniverse Panoptes project builder to classify the 1,112 COSMOS and SDSS galaxies. Instead of colour images, the galaxy isophotes were shown, and, to avoid any possible bias, the galaxies were anonymised by removing the ids and redshift from the images.

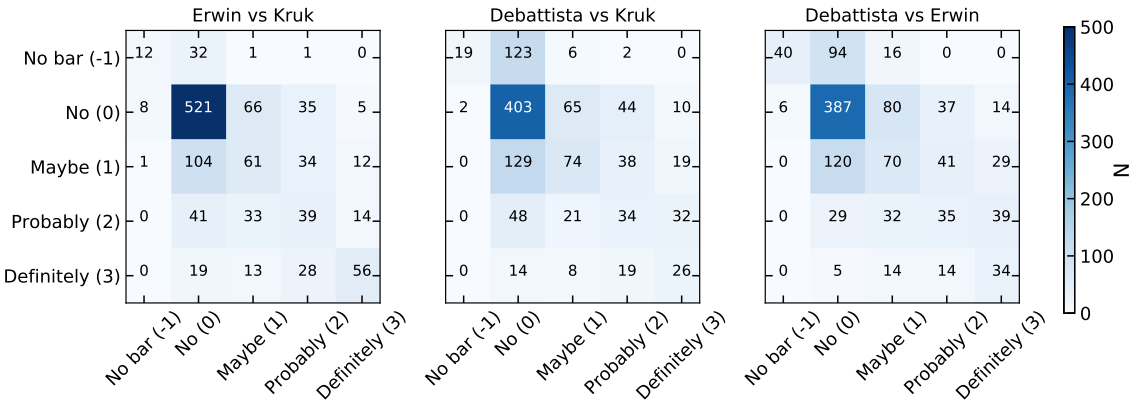

Figure 6.9: Agreement between the three classifiers for the 1,112 classified galaxies. The first name in the title is for *classifier 1* (y-axis) and the second for *classifier 2* (x-axis). The 2D histogram is colour coded by the number of galaxies in each bin, with the number displayed in each bin.

The 556 higher-z from *HST* and 556 low-z from SDSS galaxies were classified by three experts (myself, Debattista and Erwin). Apart from answering the *'Does the galaxy have a B/P bulge?'* question, we tagged galaxies that we considered to have buckling bars and other interesting features, for example nuclear discs or offset bars. Figure 6.9 shows the agreement between the classifiers for the five categories. The majority of the classifications ($\sim 400 - 500$) were for the 'No B/P' category. In general, there is a good agreement between the three of us for most answers, shown by the darker colours along the diagonal. Most of the scatter is explained by a one step difference in classifications, for example one classifier selecting 'Maybe' (or 'Probably') and another 'No' or 'Probably' (or 'Definitely'). The largest discrepancies are for the 'No ' and 'No bar' answers: Debattista has been more conservative than me or Erwin, classifying more galaxies as having 'No bar' and fewer galaxies as 'Definitely' having B/P bulges. For 128 galaxies (11% of the sample) we disagree on the classifications, i.e. each of us chose a different answer for the B/P question. Nevertheless, this is a small fraction given the subjectivity of the possible answers. Examples of galaxies for each of the five possible options, for which at least 2 of us agreed on an answer, are shown in Figure 6.10.

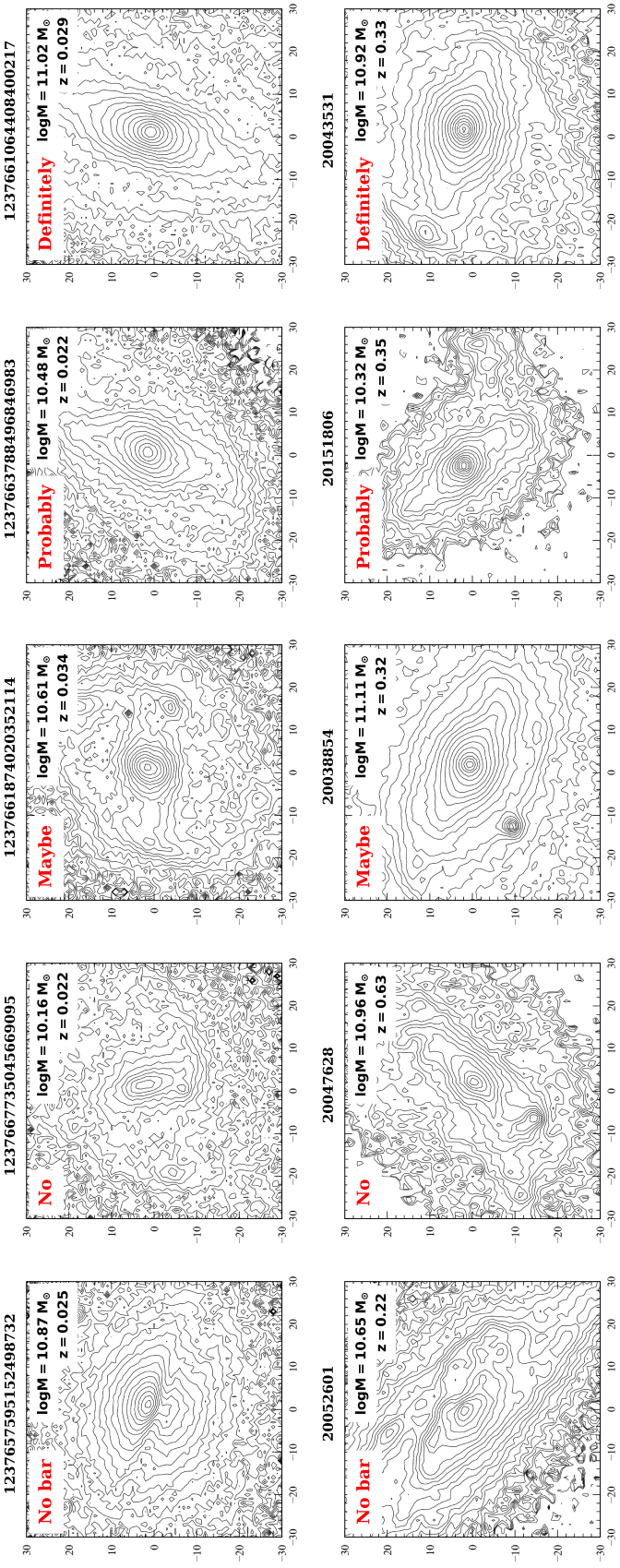

Figure 6.10: Examples of SDSS (*top row*) and COSMOS (*bottom row*) galaxies classified by at least 2 of us as having 'No bar', 'No', 'Maybe', 'Probably' and 'Definitely' boxy/peanut bulges. The B/P bulges were identified based on the boxy isophotes and the offset spurs on one side and the other of the rectangle, as shown in Figure 6.10.

The scores from each of the three expert classifications are added together ($\Sigma_{\rm score}$) for each galaxy and the galaxies are split into three categories, depending on the total score: galaxies without bars ($\Sigma_{\rm score} < -1$), barred galaxies without B/P bulges ($-1 \leq \Sigma_{\rm score} \leq 3$) and barred galaxies with B/P bulges ($\Sigma_{\rm score} > 3$). This distinction between galaxies with B/P bulges and without B/P bulges ($\Sigma_{\rm score} = 3$) corresponds to all three classifications for a galaxy being 'Maybe' (which was considered to be a negative answer in this chapter). Galaxies with two classifications of 'Maybe' and one of 'Probably' or any combinations with 'Probably' and 'Definitely' are considered to have B/P bulges. Out of the 1,112 classified galaxies (556 COSMOS and 556 SDSS galaxies) there are 259 galaxies classified as having B/P bulges (89 COSMOS and 170 SDSS galaxies), 816 without B/P bulges (436 COSMOS and 380 SDSS galaxies) and 37 having no bars (31 COSMOS and 6 SDSS). In the analysis that follows, the 37 galaxies classified as not being barred were removed, leaving a total of 525 COSMOS galaxies and 550 SDSS galaxies. Additionally, since in the analysis it is important to have an equal number of COSMOS and SDSS galaxies in order to consistently compare the two datasets, I removed an extra 6 COSMOS galaxies whose analoguous (same mass, $p_{\rm bar}$ and resolution) SDSS galaxy was classified as having 'No bar', and similarly, the 31 SDSS galaxies whose analoguous COSMOS galaxies were without bars, leaving a total of 519 COSMOS and 519 SDSS galaxies.

6.5 Results

6.5.1 Boxy/Peanut bulge fraction with redshift

The measured fraction of barred galaxies having boxy/peanut bulges, $f_{\rm B/P}$ is plotted as a function of redshift in Figure 6.11. This plot shows some interesting trends with redshift. The mean $f_{\rm B/P}$ for SDSS galaxies is 0.31 (at $z \approx 0$), followed by higher fractions in the first two COSMOS bins (0.33 and 0.37 at $z = 0.15$ and $z = 0.25$) and a decline to $f_{\rm B/P} = 0$ at $z \sim 1$. A higher $f_{\rm B/P}$ for the first two COSMOS bins (considering the uncertainties) is expected because at these redshifts ($z < 0.3$), *HST* has better spatial resolution compared to the mean spatial resolution of SDSS. Nevertheless, it is a noteworthy aspect that the SDSS and COSMOS B/P bulge fractions at $z < 0.3$ are similar. Even though the classifications were done on different imaging, the continuity at the lowest redshifts suggests that the observed evolution of the B/P bulge fraction with redshift is real.

A general trend of decreasing $f_{\rm B/P}$ with redshift is what one would expect if the resolution of the images affects the identification of B/P bulges. Low-redshift *HST* data have better spatial resolution than higher redshift *HST* data. Since the SDSS

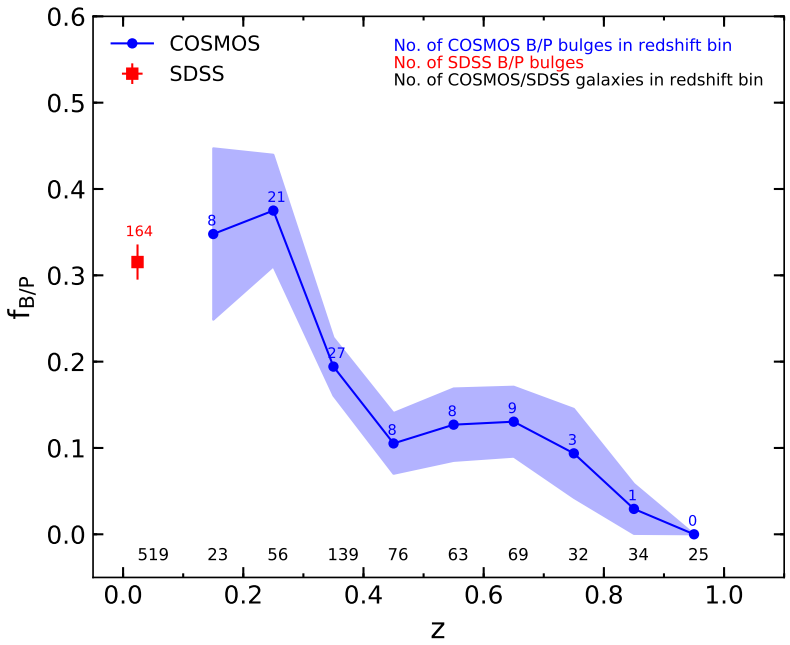

Figure 6.11: The B/P bulge fraction against redshift for the SDSS and COSMOS barred galaxies, as measured by the expert classifications of Erwin, Debattista and myself. The blue points represent the mean B/P bulge fraction of COSMOS galaxies in each redshift bin and the shaded area the standard error on the mean in each bin, σ_m. The red square shows the local B/P bulge fraction as measured for the SDSS galaxies. The numbers in blue (red) represent the number of B/P bulges in each bin for the COSMOS (SDSS) galaxies, while the numbers at the bottom of the figure represent the total number of galaxies in each bin.

images were selected to have roughly the same spread of spatial resolution as the COSMOS data, one would expect $f_{\mathrm{B/P,SDSS}}$ to be approximately the mean of all $f_{\mathrm{B/P,COSMOS}}$. However, the fact that this is not the case, the mean $f_{\mathrm{B/P,SDSS}}$ being actually $> f_{\mathrm{B/P,COSMOS}}$ everywhere, apart from the first two COSMOS bins, is an indication that the observed trend is a genuine evolution of the B/P bulge fraction with redshift.

In order to verify whether the observed trends are real, I compute the excess of B/P bulges in the COSMOS data, compared to SDSS, by dividing the $f_{\mathrm{B/P}}$ fraction for each COSMOS redshift bin by the $f_{\mathrm{B/P}}$ fraction of the comparison resolution- and mass-matched SDSS galaxies in that bin (Figure 6.12). This result demonstrates that there is indeed an evolution of the B/P bulge fraction with redshift and that changes in resolution are not responsible for the observed trends. Present day B/P bulge fractions are reached at $z \sim 0.3$ (3.5 Gyr ago), then the B/P bulge fraction declines steeply with redshift up to $z \sim 0.5$, followed by a more gentle decline to $z \sim 1$. The SDSS B/P bulge fraction is relatively constant with image resolution,

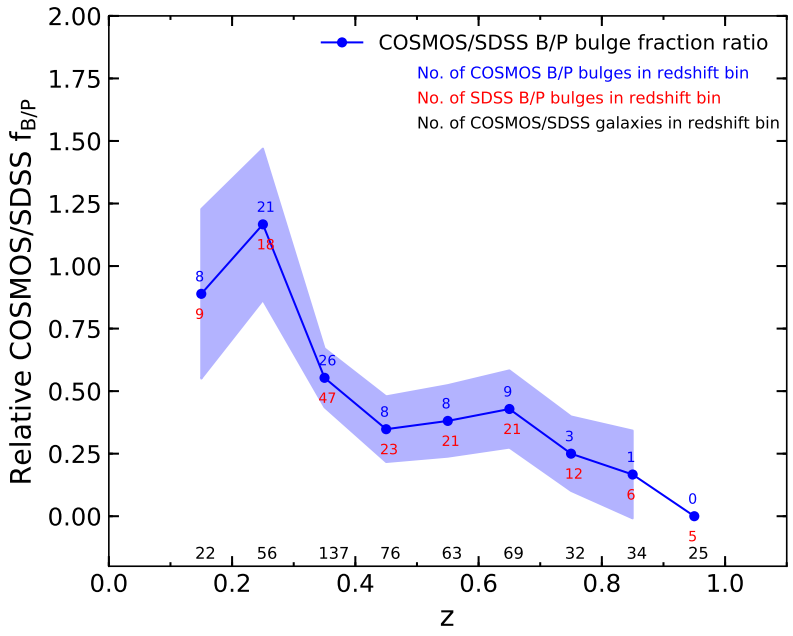

Figure 6.12: The ratio of COSMOS $z > 0.15$ and SDSS $z \approx 0$ B/P bulge fractions with redshift. The COSMOS and SDSS galaxies are matched in mass and resolution in each redshift bin, so that similar galaxies are being compared. The numbers in blue (red) represent the number of B/P bulges in each bin for the COSMOS (SDSS) galaxies, while the numbers at the bottom of the figure represent the total number of galaxies in each bin.

fluctuating between $f_{\rm B/P,SDSS} \sim 0.3$ and $f_{\rm B/P,SDSS} \sim 0.4$ and declining to $f_{\rm B/P} \sim 0.2$ at a physical resolution ~ 0.8 kpc. This suggests that the image resolution does not significantly affect the B/P classification, as long as the resolution of the images is reasonably high ($\lesssim 0.8$ kpc).

6.5.2 Boxy/Peanut bulge fraction with inclination

Erwin & Debattista (2013) showed that B/P bulges can be detected in moderately inclined galaxies, with inclinations between 40° and 70°, in few cases down to $i \sim 30°$. Figure 6.13 shows the fraction of galaxies having boxy/peanut structures ($f_{\rm B/P}$) as a function of inclination. The fraction is relatively constant (within uncertainties) for both SDSS and COSMOS galaxies with inclinations $45° \lesssim i \lesssim 75°$, similar to the findings of E&D17 (see their Figure 4). The mean $f_{\rm B/P}$ value for SDSS galaxies having moderate inclinations is only slightly smaller compared E&D17 ($f_{\rm B/P} \sim 0.4$ compared to $f_{\rm B/P} \sim 0.5$). However, $f_{\rm B/P}$ drops for lower inclinations, more steeply for SDSS (to $f_{\rm B/P} \sim 0.15$) than for COSMOS galaxies. This suggests that it is indeed difficult to identify B/P structures using isophotes in face-on galaxies. Nevertheless, 83% of the galaxies have inclinations ($i > 40°$) over which the B/P bulge fraction is roughly

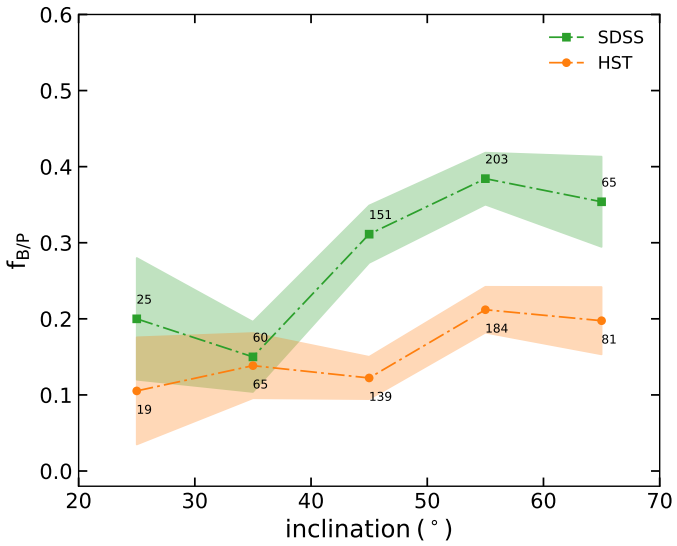

Figure 6.13: The boxy/peanut fraction with inclination for the SDSS and COSMOS galaxies in the sample. The numbers above (below) the mean $f_{\rm B/P}$ represent the number of galaxies in each bin for the SDSS (COSMOS) galaxies.

constant. Furthermore, the mean inclination of COSMOS galaxies is constant with redshift ($i \sim 50°$), suggesting that galaxies having different inclination at different redshifts cannot be the cause of the observed evolution of the B/P bulge fraction.

6.5.3 Boxy/Peanut bulge fraction with mass

E&D17 showed that there is a strong trend of the B/P bulge fraction ($f_{B/P}$) with mass (Figure 6.2), with a steep transition from $f_{B/P} \sim 0.2$ at $M_* < 10^{10.4} M_\odot$ to $f_{B/P} \sim 0.8$ at $M_* > 10^{10.5} M_\odot$. Therefore, I investigated whether the same trend is observed in the SDSS data and whether the trend is maintained for the COSMOS data, or if there is a redshift evolution of the dependence of $f_{B/P}$ on stellar mass.

The calculated $f_{\rm B/P}$ increases with stellar mass for the local SDSS data, similar to the trend observed in E&D17 and Li et al. (2017), as seen in Figure 6.14 (*left panel*). As found by E&D17, there is a strong turnover in the B/P bulge fraction at $M_* \sim 10^{10.4} M_\odot$, where $f_{\rm B/P}$ doubles. The important new result is the $f_{\rm B/P}$ dependence on stellar mass for the higher redshift COSMOS galaxies, shown in Figure 6.14 for two redshift bins ($z < 0.5$ and $0.5 < z < 1$). The observed dependency of $f_{\rm B/P}$ on stellar mass for the COSMOS data is similar to the one for the local SDSS data - $f_{\rm B/P}$ increases with stellar mass. As shown earlier, the decrease of the B/P bulge fraction with redshift is also noticeable. In the $0.5 < z < 1$ redshift bin, $f_{\rm B/P}$ is 0.3 times as large as for the local barred galaxies. Only the local SDSS and highest COSMOS bin

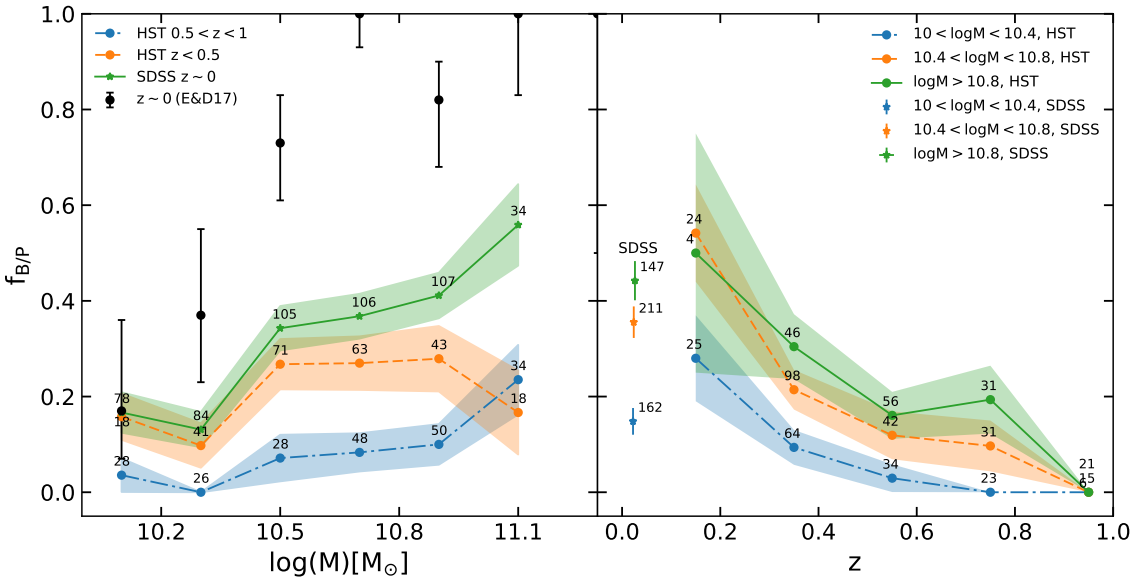

Figure 6.14: *Left panel*: The trend of the B/P bulge fraction with stellar mass for SDSS galaxies (green) and COSMOS galaxies in two redshift bins (orange and blue). The black points show the observed local fraction from Erwin & Debattista (2017), for galaxies preferentially selected with ideal orientation to identify B/P bulges. The points show the mean $f_{\rm B/P}$ in each mass bin, and the shaded area shows the standard error on the mean in each bin. The numbers illustrate the number of barred galaxies in each bin. *Right panel*: The redshift evolution of $f_{\rm B/P}$ for three COSMOS mass bins and the value of the local B/P bulge fraction for the SDSS galaxies, for the same three mass bins.

show a 'jump' in $f_{\rm B/P}$ at the largest masses $M_* \sim 10^{11} M_\odot$, although this mass bin at mid-redshifts in COSMOS contains the fewest galaxies, so it might be affected by small number statistics.

Compared to the B/P bulge fraction found in E&D17, the local B/P bulge fraction in SDSS data found in this chapter is $\sim 0.5 - 0.7$ times as large: $f_{B/P} \sim 0.15$ at $M_* < 10^{10.4} M_\odot$ and $f_{B/P} \sim 0.4$ at $M_* > 10^{10.5} M_\odot$. The galaxies in E&D17 are preferentially selected with favourable inclinations ($i = 40° - 70°$) and bar position angle within 60° of the major axis of the galaxy ($\Delta {\rm PA}_{\rm bar} \lesssim 60°$) to maximise the possibility of B/P bulge identification. In this chapter, some COSMOS and SDSS galaxies have inclinations $i \lesssim 40°$ (Figure 6.5), where the B/P bulge identification is more challenging, which might explain the lower B/P measured fraction. Furthermore, because measurements of the bar and disc position angles are not available, the galaxies are selected having all possible relative disc-bar orientations, including the less favourable orientation of bars along the minor axis of the galaxy ($\Delta {\rm PA}_{\rm bar} = 90°$). Assuming that the projected orientation of the bar in a galaxy is equally probable at all position angles ($\Delta {\rm PA}_{\rm bar}$ has a uniform distribution), it is 1.5 times more likely to

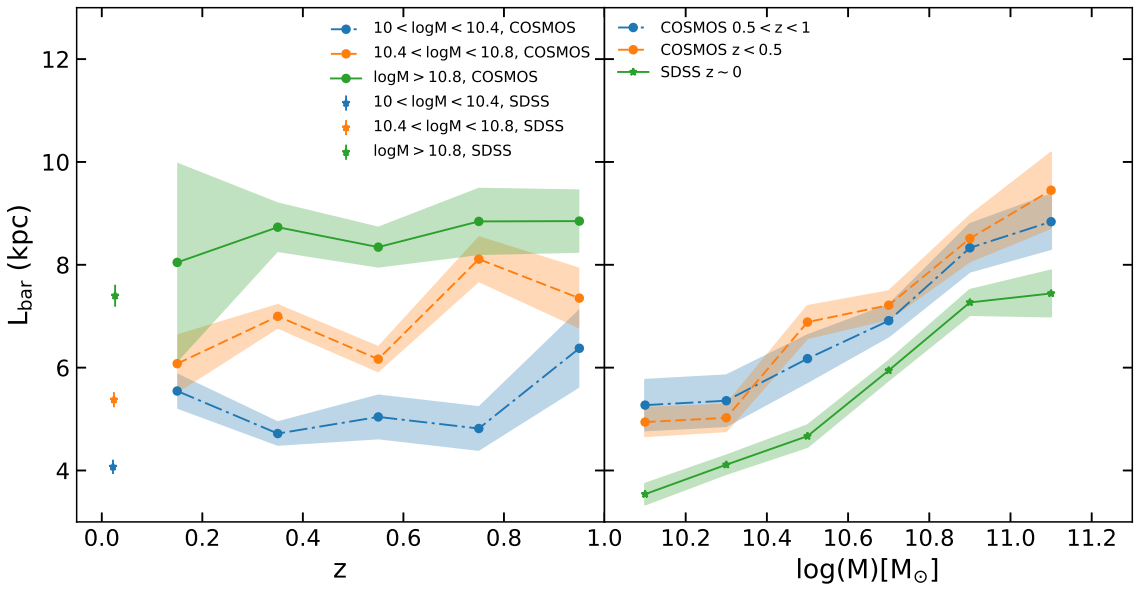

Figure 6.15: *Left panel*: The median bar length of COSMOS and SDSS galaxies for three mass bins. The lengths were measured by Galaxy Zoo volunteers, by drawing a line on top of the bar. There is no obvious evolution of bar length with redshift in this sample for galaxies of the same stellar mass. *Right panel*: The strong dependence of bar length on galaxy mass for COSMOS and SDSS galaxies. The points show the median L_{bar} in each bin, and the shaded area shows the standard error on the median in each bin.

randomly select galaxies with $\Delta\mathrm{PA}_{\mathrm{bar}} = 0^\circ - 90^\circ$ than with $\Delta\mathrm{PA}_{\mathrm{bar}} = 0^\circ - 60^\circ$. Thus, one would expect a factor of ~ 1.5 difference between a preferentially selected sample, and one with random orientations. Nonetheless, this factor is probably an underestimate as well, since the sample in E&D17, containing galaxies at $D < 25$ Mpc, has a much better physical resolution (~ 0.1 kpc) than SDSS (~ 1 kpc). Additionally, the galaxies in E&D17 are analysed using near-infrared images (whenever possible), which might also increase the B/P bulge detection rate. Hence, it is reasonable to observe a local B/P bulge fraction $\sim 0.5 - 0.7$ as large as that in a preferentially selected sample.

The right panel of Figure 6.14 shows the redshift evolution of $f_{\mathrm{B/P}}$ for three mass bins. The three mass bins show similarly decreasing B/P bulge fractions with redshift, and the first *HST* bin roughly matches the local SDSS values. The similar trends for galaxies of different masses suggest that the B/P bulge fraction indeed decreases with redshift, rather than the mass at which galaxies buckle to form B/P bulges changes. The highest mass bin is more noisy because of the smaller number of galaxies.

6.5.4 Boxy/Peanut bulge fraction with bar length

Bar length measurements for the COSMOS galaxies are available through the Galaxy Zoo Hubble: Bar Lengths project (GZH:BL, Hutchinson-Smith et al., in prep.), where volunteers were asked to measure the length and width of bars by drawing lines over the full length of the bar. The bar length measurements reported in this chapter are bar diameters, twice the semi-major axis of the bar commonly reported in other works. The bars in the COSMOS galaxies are measured by at least 10 volunteers and their measurements are aggregated by Hutchinson-Smith et al. (in prep.) using a clustering algorithm. Out of the 519 barred COSMOS galaxies, 488 have measured bar lengths due to the slightly different sample selections. The bar lengths of COSMOS galaxies vary between 4 kpc and 11 kpc (10^{th} and 90^{th} percentile), with a median of 6.7 kpc and a standard deviation of 2.8 kpc. Bar lengths for SDSS galaxies are available from the GZ2: Bar Lengths project (GZ2:BL, Hoyle et al. 2011) for 364 out of the 556 SDSS galaxies. There are fewer SDSS galaxies with measured bar lengths because the original GZ2:BL project (Hoyle et al., 2011) was carried out before the Galaxy Zoo 2 project finished collecting all the classifications, thus a smaller sample of barred galaxies went into GZ2:BL. The SDSS barred galaxies have bar lengths varying between 3.3 kpc and 9 kpc (10^{th} and 90^{th} percentile), with a median of 5.6 kpc and a standard deviation of 2.3 kpc. The difference in bar lengths between the SDSS and COSMOS (the higher redshift galaxies having, in median, 15% longer bars) is partly due to the smaller sample size of SDSS galaxies with measured bar lengths, compared to the COSMOS sample. The two samples with measured bar lengths, having different sizes, are no longer resolution and mass-matched. It is worth mentioning that the galaxies have moderate inclinations (too highly inclined galaxies are excluded) and the measured bar lengths are the projected bar lengths. The real, physical, lengths of the bars are larger.

There is a strong dependence of bar length on stellar mass (*right panel* of Figure 6.15), as noticed by Hoyle et al. (2011), Díaz-García et al. (2016) and Erwin (2018): more massive galaxies are larger in size and, in turn, have longer absolute bar sizes. The median length of bars for the COSMOS galaxies shows no evolution with redshift from $z = 0.15$ to $z = 1$ (*left panel* of Figure 6.15); the observed trends are either consistent with being flat (within uncertainties) or perhaps with a weak increase with redshift, from $z = 0.15$ to $z = 1$. It is likely that this is a resolution effect - the sample is missing galaxies with small bars at high redshifts due to the deteriorating spatial resolution. At $z = 1$, the resolution is 8 kpc/arcsec, which at the FWHM of HST (0.09") suggests that bars with absolute bar lengths smaller than $2\times$ FWHM=1.5 kpc might be missed (Erwin, 2018), thus driving the median bar lengths to higher values.

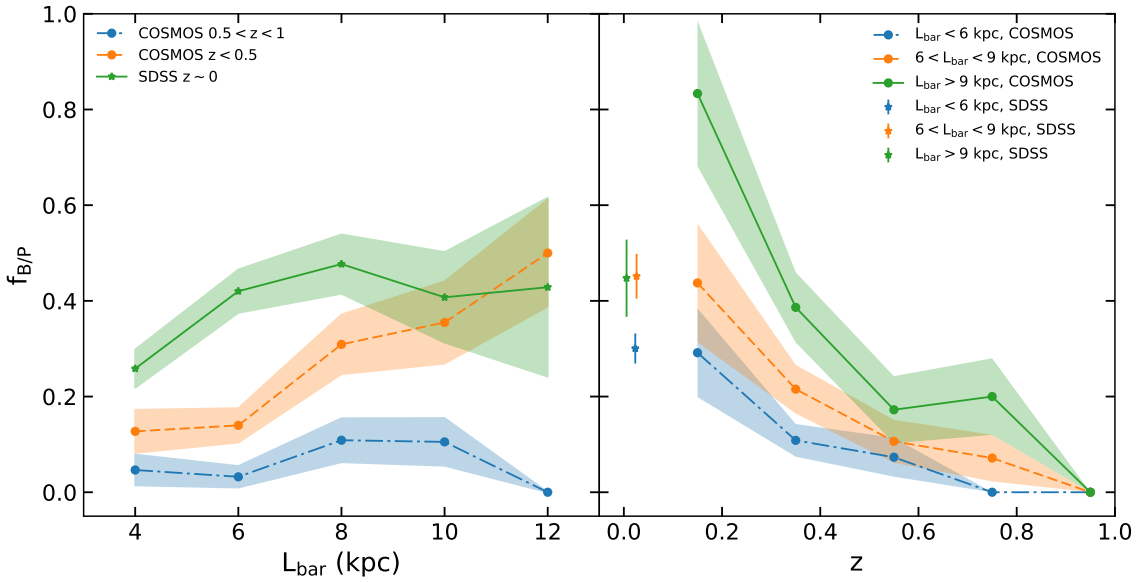

Figure 6.16: *Left panel*: The dependency of the measured fraction of barred galaxies with B/P bulges ($f_{\mathrm{B/P}}$) on bar length for SDSS and COSMOS galaxies. *Right panel*: The B/P bulge fraction with redshift for three bar length bins: small bars ($L_{\mathrm{bar}} < 6$ kpc), intermediate bars ($6 < L_{\mathrm{bar}} < 9$ kpc) and long bars ($L_{\mathrm{bar}} > 9$ kpc). The points show the mean $f_{\mathrm{B/P}}$ in each bin, and the shaded area shows the standard error on the mean in each bin. The largest bar length SDSS bin has been displaced slightly in redshift for a better view of the plot.

Nevertheless, it is surprising that the length of bars does not *increase* significantly in the last 8 Gyr, as some simulations suggest (simulations by Debattista & Sellwood 2000 and Martinez-Valpuesta et al. 2006 predict that bars double in size since $z \sim 1$).

Similar to the steep increase of the B/P bulge fraction with mass (Figure 6.14, *left panel*), there is an increase of $f_{\mathrm{B/P}}$ with the bar length L_{bar}, as shown in the *left panel* of Figure 6.16. In the local Universe, the fraction of B/P bulges in barred galaxies reaches a value of $\sim 40\%$ when the bars have a length of 6 kpc, then the fraction is roughly constant with bar length. This is in good agreement with the findings of E&D17 (their Figure 9, lower *left panel*). The novel result in this work is the redshift evolution of the dependency of $f_{\mathrm{B/P}}$ on bar length. Although there is a trend of $f_{\mathrm{B/P}}$ with bar length (Figure 6.16, *left panel*), longer bars being more likely to have buckled, there is a clear drop in the fraction of B/P bulges with redshift (Figure 6.16, *right panel*), irrespective of bar size.

The dependency of $f_{\mathrm{B/P}}$ on L_{bar} with redshift is similar to the dependency of $f_{\mathrm{B/P}}$ on M_* with redshift (Figure 6.14, *right panel*). Thus, it is possible that the trend of $f_{\mathrm{B/P}}$ with L_{bar} is entirely explained by the strong dependence of bar length on stellar mass. To check for secondary correlations of the B/P bulge fraction with absolute bar

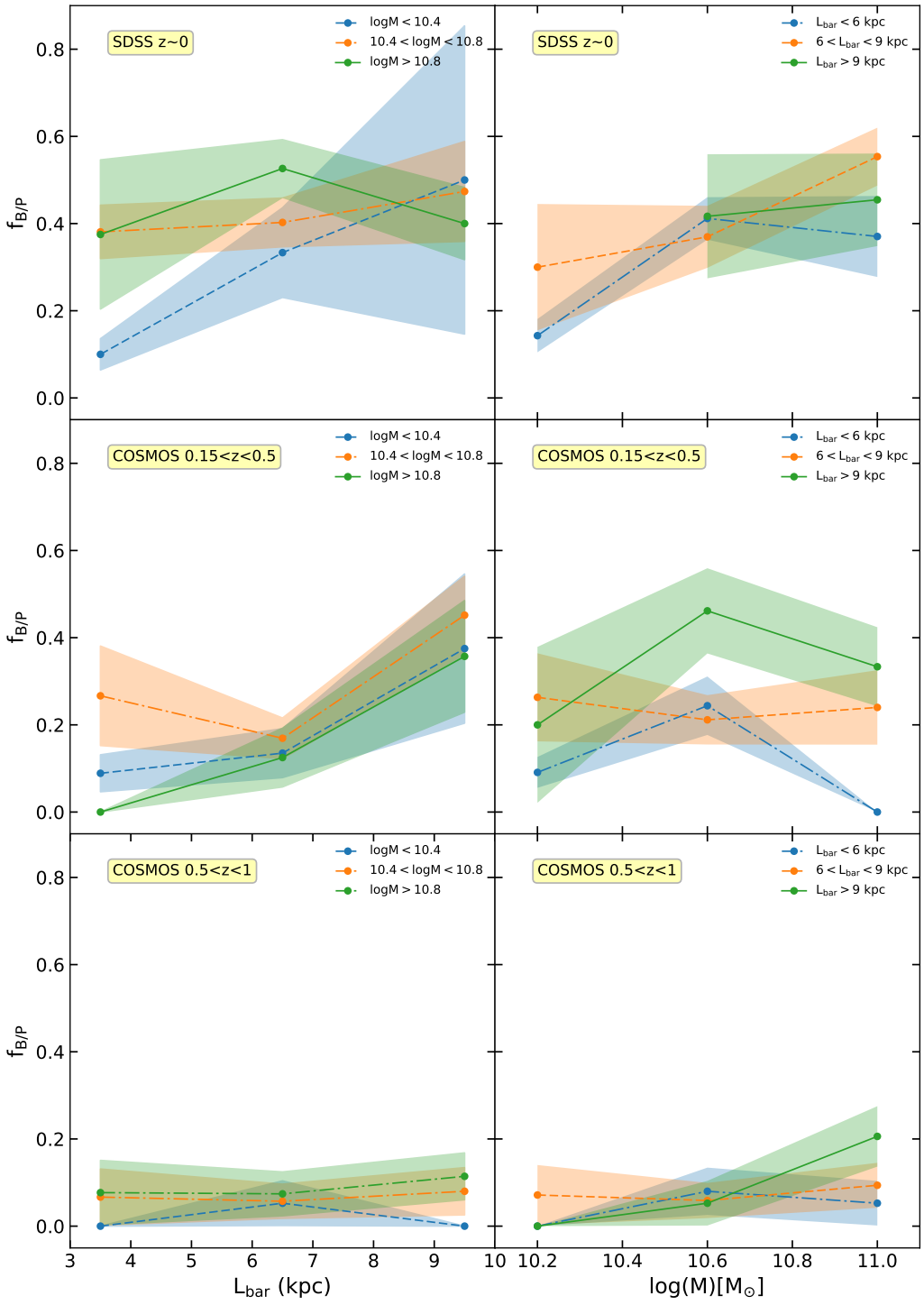

Figure 6.17: Secondary correlation of the fraction of boxy/peanut bulges in barred galaxies with bar length, for three redshift bins: SDSS, $z \sim 0$, COSMOS $0.15 < z < 0.5$ and COSMOS $0.5 < z < 1$ (from top to bottom). *Left panels*: $f_{\mathrm{B/P}}$ against measured bar length, binned in three mass bins (low, intermediate and high mass). *Right panels*: $f_{\mathrm{B/P}}$ against stellar mass, binned in three bar length bins (short, intermediate and long bars). The points show the mean $f_{\mathrm{B/P}}$ in each bin, and the shaded area shows the standard error on the mean in each bin.

size I plot the frequency of $f_{\rm B/P}$ against $L_{\rm bar}$ in three bins of stellar mass and in three redshift bins (SDSS, $z \sim 0$, COSMOS $0.15 < z < 0.5$ and COSMOS $0.5 < z < 1$) in the *left panels* of Figure 6.17. Similarly, I plot the frequency of B/P bulges in barred galaxies against stellar mass in three bins of different bar lengths (short, intermediate and long bars), in the same three redshift bins in the *right panels* of Figure 6.17. These plots show complex behaviour, when controlling for either M_* or $L_{\rm bar}$. The *top panels* of Figure 6.17 suggest that for the local SDSS galaxies, $f_{\rm B/P}$ depends mostly on stellar mass rather than on bar size. Similar trends can be seen at the highest redshifts (COSMOS $0.5 < z < 1$), but with fewer galaxies having B/P bulges ($f_{\rm B/P} \lesssim 0.1$). The *middle panels* (for the mid-redshift bin, COSMOS $0.15 < z < 0.5$) show a secondary correlation of the B/P bulge fraction on bar length - $f_{\rm B/P}$ increases with bar length (for $L_{\rm bar}$ >6 kpc) in a similar way for the three mass bins. Some of this trend is perhaps expected, since the lengths of the bars are not deprojected. B/P bulges are easier to identify when they are aligned with the major axis of the galaxy, and thus the measured bar size is maximised (being closer to the real length of bars) rather than when the bar is aligned along the minor axis of the galaxy, having the smallest projected size. Additionally, it might be intrinsically easier to observe B/P bulges in longer bars due to resolution effects. Finally, it is important to note that binning the data in eight different bins (two redshift bins, three mass bins and three bar length bins) for 488 COSMOS galaxies results in only a small number of galaxies per bin and, therefore, in an increased uncertainty.

6.5.5 Buckling bars

Besides classifying boxy/peanut bulges, the three expert classifiers individually flagged objects which appear to show trapezoidal isophotes, suggestive of bar buckling. These galaxies are classified as not having boxy/peanut bulges. The galaxies which at least two of the classifiers considered to be buckling (32 candidates) were inspected by Erwin using DS9 (Smithsonian Astrophysical Observatory, 2000), slowly varying the level of the isophote contours to better reveal the trapezium shape. Finally, 26 were considered to be buckling, 11 classified as 'Good' and 15 as 'Plausible', with uncertainty introduced due to possible dust obscuration. Out of the 26 galaxies, 15 are *HST* galaxies (8 'Good' and 7 'Plausible') and 11 are SDSS galaxies (3 'Good' and 8 'Plausible'). The buckling bars are in a COSMOS : SDSS ratio of ~ 1.4 (2.7 if only counting the ones classified as 'Good'), already suggesting that buckling occurs predominantly at higher redshifts. The properties (stellar masses, absolute bar lengths) of the identified buckling bars are shown in Table 6.1. Bar lengths are available from the GZH:BL and GZ2:BL projects for 17 galaxies. I measure the other bar lengths

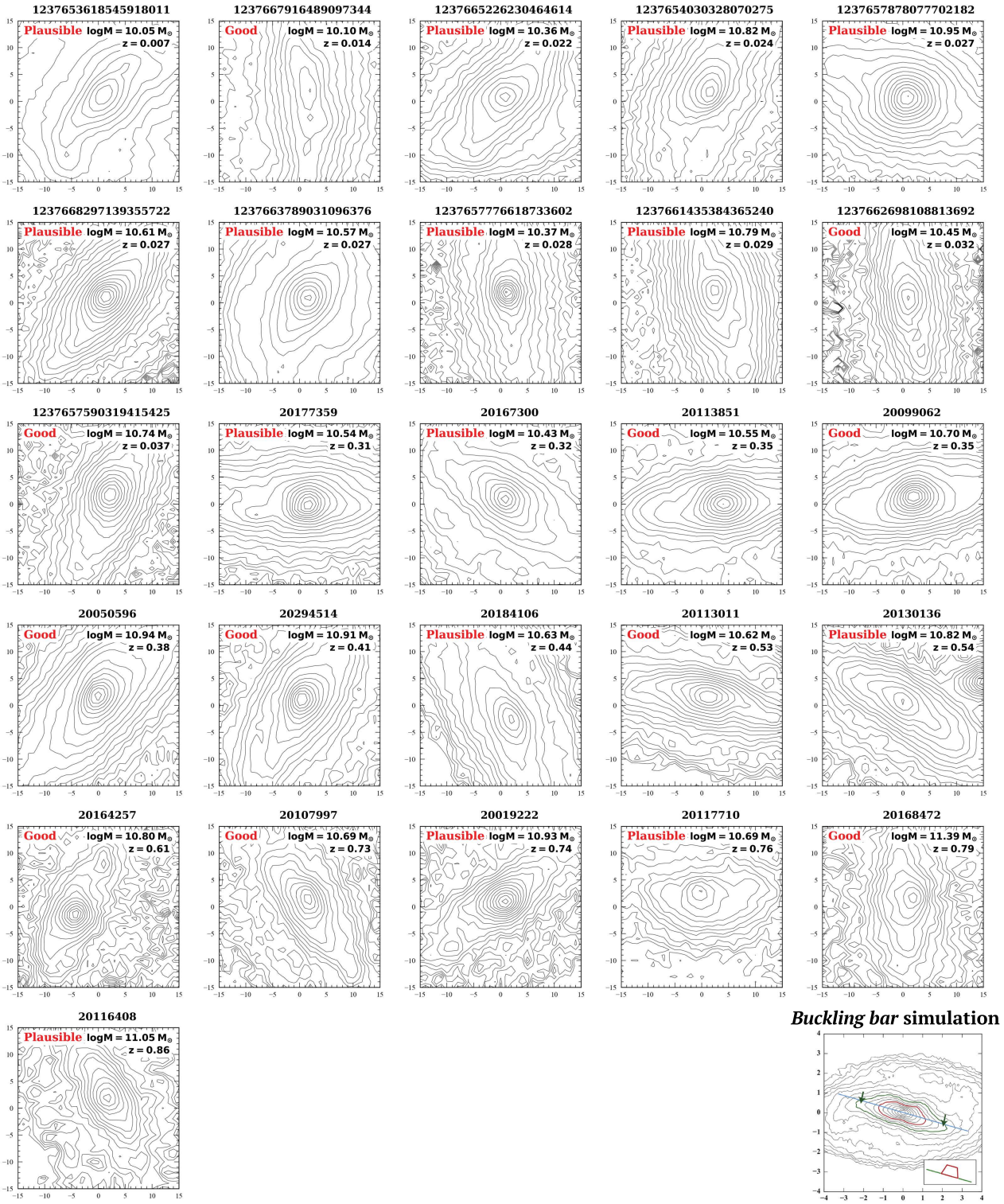

Figure 6.18: The 26 barred galaxies (11 SDSS and 15 COSMOS) visually identified as being in the stage of buckling based on the trapezoidal isophotes (as illustrated in the *Buckling bar* simulation in the bottom right panel). The buckling bar galaxies are labelled as 'Plausible' or 'Good', based on the confidence in identifying them as being buckling. The stellar masses and redshifts are shown in the top right of each panel.

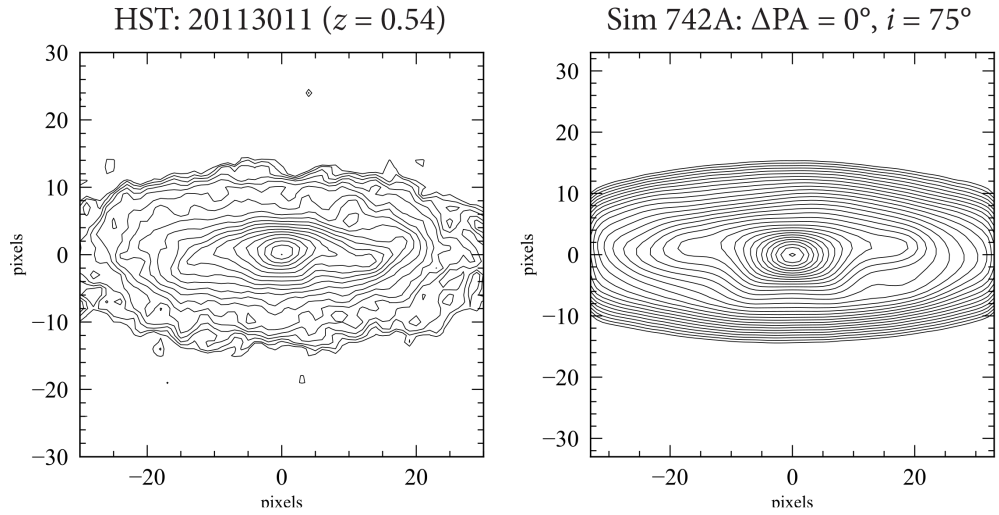

Figure 6.19: The morphology of *HST* galaxy 20113011 (at $z = 0.54$), one of the best cases of buckling bars found in this work, compared to simulated galaxy with a buckling bar at time step $t = 780$), convolved with a PSF approximating the HST PSF (same FWHM).

myself. Comments based on the inspection of the isophotes are also given in the last column of the table. The trapezoidal isophotes of the 26 barred galaxies identified as being in the stage of buckling are shown in Figure 6.18. The highest redshift buckling bar galaxy is at $z = 0.86$, while the median redshift of the buckling bars in COSMOS galaxies is $z = 0.53$. The median mass of galaxies with buckling bars in COSMOS is $\log(M_*) = 10.7\, M_\odot$, while the median in SDSS is slightly lower, $\log(M_*) = 10.6\, M_\odot$. This difference is not statistically significant, given the small number of buckling bars. Additionally, there is no obvious correlation of the buckling with the length of the bar. The bar lengths for buckling galaxies range between 2 kpc and 15 kpc, and the median values of SDSS and HST are similar: median $L_{\mathrm{bar,\,SDSS}} = 8.4$ kpc and $L_{\mathrm{bar,\,COSMOS}} = 8.9$ kpc.

The appearance of the buckling galaxies can be well reproduced by simulations, by selecting similar viewing angles. For this work, new N-body simulations of isolated galaxy evolution were produced by Victor Debattista, illustrating galaxies in their buckling phases. For example, simulation 742A, with a bar at ΔPA=0° and inclined at $i = 75°$ is a good match to the general appearance of HST galaxy 20113011 (Figure 6.19), one of the best cases of galaxies found in the buckling stage. Both the simulations and 20113011 show trapezoidal isophotes, with the spurs on the long side of the trapezium.

(1)	(2)	(3)	(4)	(5)	(6)	(7)	(8)	(9)	(10)
id	Common Name	survey	RA J2000	Dec J2000	z	$\log(M_*)[M_\odot]$	$L_{\rm bar}$ (kpc)	Confidence	Comment
1237653618545918011	NGC 3471	SDSS	164.78749	61.53067	0.007	10.05	1.87	Plausible	-
1237667916489097344	J113103.69+201408.2	SDSS	172.76539	20.23562	0.014	10.10	9.25	Good	pinched isophotes for trapezoid
1237665226230464614	J120615.62+315804.3	SDSS	181.56509	31.96786	0.022	10.36	5.20	Plausible	-
1237654030328070275	NGC 3644	SDSS	170.38697	2.810440	0.024	10.82	5.35	Plausible	slightly disturbed morphology
1237655678077702182	IC 486	SDSS	120.08743	26.61352	0.027	10.95	11.41	Plausible	possibly problematic dust lanes
1237668297139355722	J134628.78+175748.7	SDSS	206.61991	17.96353	0.027	10.61	12.14	Plausible	could be interpreted as symmetric offset spurs
1237663789031096376	J080844.70+563532.4	SDSS	122.18625	56.59234	0.027	10.57	8.40	Plausible	somewhat small, poorly resolved
1237657776618733602	J091652.87+434249.5	SDSS	139.22030	43.71377	0.028	10.37	5.17	Plausible	-
1237661435384365240	J125039.83+475600.3	SDSS	192.66595	47.93341	0.029	10.79	8.22	Plausible	-
1237662698108813692	J153541.87+272231.0	SDSS	233.92448	27.37528	0.032	10.45	9.29	Good	highly inclined
1237657590319415425	J111743.50+534736.2	SDSS	169.43128	53.79340	0.037	10.74	12.79	Good	-
20177359	zCOSMOS 845890	COSMOS	150.11788	2.66899	0.31	10.54	14.98	Plausible	left spur is broad/diffuse
20167300	J100206.66+024515.2	COSMOS	150.52774	2.75421	0.32	10.43	6.72	Plausible	large, well-resolved inner part of trapezoid
20113851	J100132.26+022328.7	COSMOS	150.38441	2.39126	0.35	10.56	8.72	Good	very lopsided outer disk
20099062	J095929.71+021120.7	COSMOS	149.87379	2.18904	0.35	10.70	8.22	Good	possible confusion on one side from partial ring
20050596	J095810.73+015643.0	COSMOS	149.54471	1.94527	0.38	10.94	13.07	Good	large, well-resolved dust lane on one side weakens trapezoid
20294514	J095847.62+023643.9	COSMOS	149.69846	2.61217	0.41	10.91	9.65	Good	possible confusion on one side from partial ring
20184106	J095907.51+024015.7	COSMOS	149.78132	2.67097	0.44	10.63	10.81	Plausible	potential dust obscuration
20113011	J100137.94+022203.3	COSMOS	150.40811	2.36753	0.53	10.62	6.16	Good	large, well-resolved
20130136	J095827.87+022549.8	COSMOS	149.61612	2.43049	0.54	10.82	14.51	Plausible	-
20164257	J100235.46+024339.8	COSMOS	150.64768	2.72776	0.61	10.80	8.11	Good	large, well-resolved
20107997	J100242.35+022058.6	COSMOS	150.67648	2.34955	0.73	10.69	9.21	Good	large, well-resolved
20019222	J095923.58+014537.7	COSMOS	149.84826	1.76046	0.74	10.93	8.76	Plausible	-
20117710	zCOSMOS 831270	COSMOS	150.19137	2.40647	0.76	10.69	6.64	Plausible	relatively low inclination, not as well-resolved
20168472	J100150.18+024400.2	COSMOS	150.45910	2.73338	0.79	11.39	11.28	Good	not as highly inclined, large, well-resolved
20116408	J100124.67+022135.4	COSMOS	150.35283	2.35978	0.86	11.05	8.93	Plausible	not as well-resolved, could be standard box offset spurs

Table 6.1: Properties of galaxies with *buckling bars* visually identified in this work. The first column shows the SDSS DR8 and *HST* COSMOS survey ids, followed by the common name in the second column. 4^{th} and 5^{th} *columns*: RA and dec, 6^{th} *column*: redshifts, as measured by SDSS spectroscopy or photometric redshift from COSMOS2015 catalogue (Laigle et al., 2016). 7^{th} *column*: stellar masses for SDSS from the MPA-JHU catalogue and for *HST* from the COSMOS2015 catalogue (Laigle et al., 2016). 8^{th} *column*: bar length as measured by GZH:BL, GZ2:BL and Sandor Kruk. 9^{th} *column*: confidence in identifying the buckling bar and 10^{th} *column*: comments on the isophote appearance.

Though small, this is currently the largest sample of buckling bars (26 buckling bars, 2.3% of 1,112 galaxy images inspected), 10 times larger than previous samples (Erwin & Debattista 2016 – 2 buckling bars, also 2.3% of the 88 galaxies inspected, and Li et al. 2017 – 1 buckling bar). Thus, it is worth computing the fraction of barred galaxies that are buckling at different redshifts. In what follows I consider both the 'Plausible' and 'Good' cases as barred galaxies undergoing bar buckling. In the SDSS sample, I find a local fraction of 2% of barred galaxies currently buckling, and in the COSMOS sample a peak of 6% at $z = 0.75$, followed by a decline in the buckling fraction, as shown in Figure 6.20 (*left panel*). Similar to the technique used in studying the B/P bulges, I divide the buckling fraction in each redshift bin by the buckling fraction at $z = 0$ of the analogous SDSS galaxies in that bin, thus matched in mass and resolution (Figure 6.20, *right panel*). I find that, at the peak redshift of buckling ($z = 0.75$), 4 times more barred galaxies buckle than at $z = 0$.

6.5.6 Summary of results

As a summary, I plot all the COSMOS barred galaxies in the $\log M - z$ space, coloured by the presence or the absence of a B/P bulge and with buckling bars represented by a star symbol in Figure 6.21. The likelihood that a galaxy hosts a B/P bulge increases strongly with mass and decreasing redshift. Higher mass galaxies are more likely to have B/P bulges earlier (at higher z) than lower mass galaxies. This trend can also be seen in the barred galaxies undergoing buckling instability: buckling occurs earlier (at higher z) in more massive galaxies and later in less massive ones (as shown by the linear fit to the data). The linear fit to the $\log M - z$ values for buckling bars is at slightly lower values than a similar linear fit for the B/P bulges, suggesting a redshift and mass offset between the B/P bulges and buckling bars. At a fixed redshift, the B/P bulges have, on average, larger masses, while the buckling bars are at lower masses. This suggests that there is a time delay between the buckling and the formation of a B/P bulge.

6.6 Potential biases

In this study, I tried to minimise the potential biases arising in the classification of B/P bulges and buckling bars. In order to determine whether the observed trends with redshift are real, I selected a comparison sample of local galaxies from SDSS, having the same stellar masses and bar likelihood, selected in a similar manner based on Galaxy Zoo classifications. Furthermore, to ensure that the quality of the data is

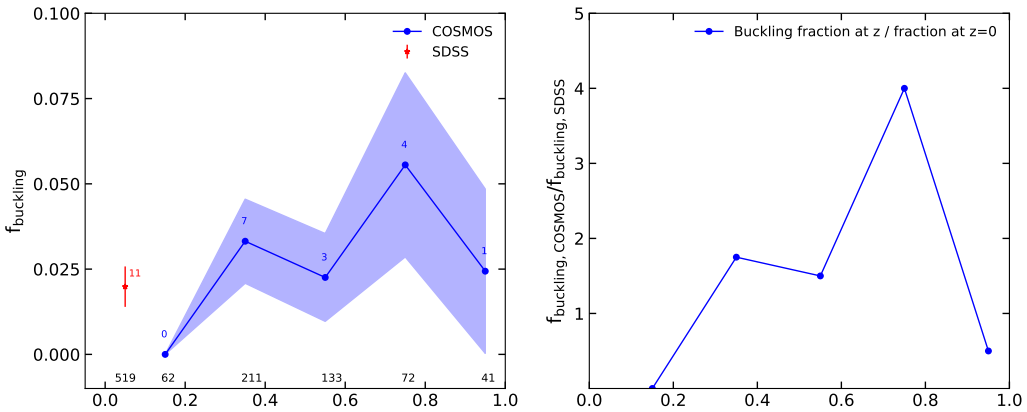

Figure 6.20: *Left panel*: The fraction of barred galaxies buckling in the local Universe (SDSS) and at higher redshifts (COSMOS). *Right panel*: The ratio of the fraction of buckling galaxies at redshift z and at $z \approx 0$ for galaxies matched in mass and resolution in each bin.

similar, I matched the SDSS and COSMOS galaxies in image resolution and consistently classified the SDSS galaxies by accounting for bandshifting. Nevertheless, the SDSS and COSMOS datasets differ in one more quantity – signal-to-noise. Images of higher redshift galaxies suffer from lower S/N due to cosmological surface brightness dimming, because of its strong evolution with redshift, for example $\propto (1+z)^{-4}$, in the case of the bolometric surface brightness. This can introduce two effects: missing a large fraction of bars in the sample due to misclassifications and changing the isophotes, making the B/P bulges harder to classify.

The first effects were studied before by Sheth et al. (2008), Melvin et al. (2014) and Willett et al. (2017). As discussed in Section 6.2.1, artificially redshifted SDSS galaxies were used to calibrate the classifications in the GZH project and to account for the redshift bias in the classifications, however the debiasing was limited to the top tier question (*features* versus *smooth*) and not to the bar question. In general, the disc has a lower mean surface brightness than the bar, therefore it can fade away due to the surface brightness dimming (Jogee et al., 2002), and so the barred galaxies might be classified as smooth or inclined discs. If this is the case, there should be a drop of the bar fraction with the surface brightness of galaxies. However, this is not observed by either Sheth et al. (2008) or Melvin et al. (2014). Sheth et al. (2008) argues that the COSMOS data is sufficiently deep to detect the outer edges of a high mass galaxy disc to $z \sim 1$ and to identify bars in galaxies. Additionally, by artificially redshifting SDSS images to $z = 0.84$ they find that their bar classifications remain unchanged for $\sim 90\%$ of the galaxies (Appendix B of Sheth et al. 2008).

The second potential effect, that the deterioration of the signal-to-noise in *HST* images at higher redshifts hinders the identification of B/P bulges based on isophotes,

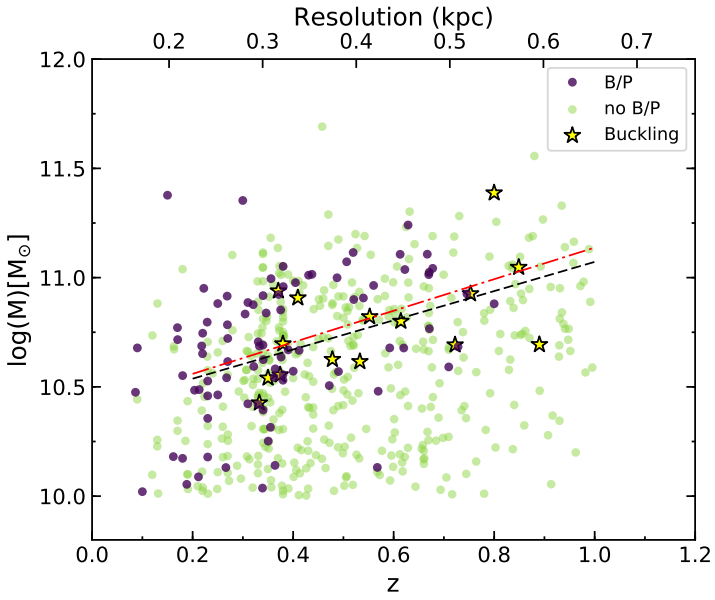

Figure 6.21: A $\log M - z$ plot of the COSMOS barred galaxies in this work, coloured by the presence of a B/P bulge (dark blue) and the absence of a B/P bulge (light green), as identified in this chapter. The stars show the 15 *HST* galaxies identified as being in the phase of buckling, while the black (red) dotted line shows a linear fit to the mass and redshift of the buckling bars (B/P bulges, respectively).

is worth exploring. For the SDSS dataset, I found a similar B/P bulge fraction across the g, r and i bands that were investigated, and these bands have slightly different signal-to-noise. Exploring the effect of S/N on B/P bulge identification will be done in future work by adding Poisson noise, mimicking the noise in *HST* images, to the SDSS images and reclassifying the SDSS comparison sample based on the isophotes of the images with added noise. This correction will be more important for higher redshift studies and for less massive galaxies which are expected to be dimmer.

Another potential problem is missing smaller bars at higher redshifts due to the deteriorating resolution. As shown in Figure 6.15, the bar length for the galaxies in the COSMOS sample is roughly constant with redshift. Many numerical simulations of bar formation and evolution (e.g. Shen & Sellwood 2004; Debattista et al. 2006; Berentzen et al. 2007; Athanassoula et al. 2013) suggest that bars are long-lived (∼5-10 Gyr) and grow with time, thus one would expect an increasing mean bar size with decreasing redshift. This implies that small bars, possibly with sizes < 2 kpc, as suggested by as Erwin (2018), might indeed be preferentially missed from the COSMOS sample at high redshifts. The barred galaxies in this work were selected with $p_{\rm bar} > 0.5$, which has been shown to correspond to strong bars, thus it is likely that small bars are missed at high redshifts with this selection. Alternatively, a constant

bar length with redshift would imply that bars can be short-lived and recurrent (on timescales of ∼1-2 Gyr, as suggested by Bournaud & Combes 2002; Bournaud et al. 2005a), since in this scenario one would expect, on average, a similar bar size at all redshifts. It is unlikely though that bars can be destroyed and reformed so efficiently, given the relatively large fraction of bars that we observe. The destruction of a fraction of bars might explain the origin of inner lenses in galaxies, as discussed in Section 3.7.4, but their red colours suggest that they are much older than 1-2 Gyrs.

The lifetime of bars is not yet a settled issue and it is certainly worth investigating with both observations and more simulations. Nevertheless, the strong correlation between the B/P bulge fraction with bar length suggests that even if small bars are missed at higher redshifts, including more galaxies with small bars in the sample would further decrease the observed B/P bulge fraction, not increase it. Therefore, the decrease in the B/P bulge fraction cannot be explained by missing small bars at high redshifts. Still, observations with higher resolution than currently possible with the *HST* are needed, in the infrared, to confirm whether smaller bars are present at high redshifts, and to establish when the majority of the bars were formed.

6.7 Discussion

6.7.1 Do boxy/peanut bulges form via the buckling instability?

I have shown in this study that the fraction of boxy/peanut bulges increases from $f_{\rm B/P} = 0\%$ at $z \sim 1$ to $f_{\rm B/P} \approx 30\%$ at $z = 0$, using two samples of barred galaxies selected from SDSS and COSMOS. I have also quantified the fraction of barred galaxies that are in the phase of buckling: 2% at $z = 0$ and a peak of 5% at $z \sim 0.75$. For similar mass galaxies seen at the same resolution, buckling is 4 times more likely to occur at $z \sim 0.75$ than at $z = 0$. Erwin & Debattista (2016) found two buckling galaxies in a sample of 84 local barred discs, thus deriving a similar buckling fraction of 2.3%. Both of their buckling galaxies had stellar masses $M_* > 10^{10.4} M_\odot$, thus the buckling fraction for galaxies with masses above this threshold is $f_{\rm buckling} = 4.5^{+4.3}_{-2.3}\%$. 85% of the buckling bars in SDSS and COSMOS have $M_* > 10^{10.4} M_\odot$ (4 SDSS galaxies and none of the COSMOS galaxies are below this threshold). Thus, I find only a sightly smaller fraction of buckling bars $f_{\rm buckling} = 3\%$ for the SDSS and COSMOS galaxies with $M_* > 10^{10.4} M_\odot$; the two studies are consistent.

Erwin & Debattista (2016) considered a simple galaxy evolution model to test whether the frequency of buckling bars is consistent with many or all B/P bulges being the result of the buckling instability. In this model they considered the fraction

of disc galaxies with visible bars ($f_{\rm bar}$) to be a linear function of redshift and to be decreasing with redshift, as suggested by various observational studies (Sheth et al., 2008; Melvin et al., 2014; Simmons et al., 2014) and cosmological simulations of bar formation (Kraljic et al., 2012). Their model also considers the redshift at which bars form (z_i), the local fraction of B/P bulges ($f_{\rm B/P}$) and the fraction of bars currently buckling ($f_{\rm buckling}$). Simulations suggest that there is a delay between bar formation and buckling ($\Delta T_{\rm non-B/P}$) and a duration for the buckling phase ($\delta T_{\rm buckling}$) before a B/P bulge is formed. Performing a Markov Chain Monte Carlo (MCMC) analysis and computing the likelihoods for observing the $z = 0$ fractions, they determined the evolution of $f_{\rm buckling}$ and $f_{\rm B/P}$, as well as the timescales ($\Delta T_{\rm non-B/P}$ and $\delta T_{\rm buckling}$), which gives rise to the local observed fractions in Erwin & Debattista (2016) of $f_{\rm buckling} = 4.5\%$ (above $M_* > 10^{10.4} M_\odot$) and $f_{\rm B/P} \approx 80\%$.

In this chapter, by observing the redshift evolution of B/P bulges and buckling I can directly compare their model to the real Universe. Figure 6.22 left panel shows my measurement of the COSMOS/SDSS relative fraction of B/P bulges (peaking at $z \approx 0$) and buckling bars (peaking at $z \approx 0.75$, buckling 4 times more likely to occur than at $z \approx 0$). The simple galaxy evolution model by Erwin & Debattista (2016) predicts surprisingly similar buckling bar and B/P bulge fractions, peaking at similar redshifts (Figure 6.22, *right panel*, plot courtesy of Peter Erwin). This plot shows the prediction for 200 samples of parameter values (z_i, $f_{\rm bar}$, $\Delta T_{\rm non-B/P}$, $\delta T_{\rm buckling}$) from the MCMC computation, with the thick red and blue lines representing the median of the MCMC runs. There is a significant spread in the model for $f_{\rm buckling}$ and $f_{\rm B/P}$ evolution with z, however, the median values are consistent with my observations. The model which matches the observations suggests median values of $\Delta T_{\rm non-B/P} = 2.2^{+1.3}_{-1.1}$ Gyr and $\delta T_{\rm buckling} = 0.8^{+0.7}_{-0.4}$ Gyr (Erwin & Debattista, 2016) (the $\pm$ limits represent the 68% confidence intervals). As noted by Erwin & Debattista (2016), these values are in excellent agreement with predictions from N-body simulations, $\Delta T_{\rm non-B/P} = 1 - 2$ Gyr and $\delta T_{\rm buckling} = 0.5 - 1$ Gyr (Martinez-Valpuesta & Shlosman, 2004; Martinez-Valpuesta et al., 2006; Saha et al., 2013). Additionally, observations of stellar ages in NGC 6032 with integral field spectroscopy (Pérez et al., 2017) suggest that the bar formed 10 Gyrs ago, and it buckled ~ 8 Gyr ago (at $z \sim 1$) to form a B/P bulge, in good agreement with my findings.

This study directly confirms that, as simulations suggest, the buckling instability can be responsible for the formation of B/P bulges and it can account for most, if not all of the B/P bulges observed today. The relatively short duration of the buckling phase, $\delta T_{\rm buckling} = 0.8$ Gyr, suggests that a relatively rapid and violent buckling mechanism is preferred, as suggested by Martinez-Valpuesta & Shlosman (2004) and

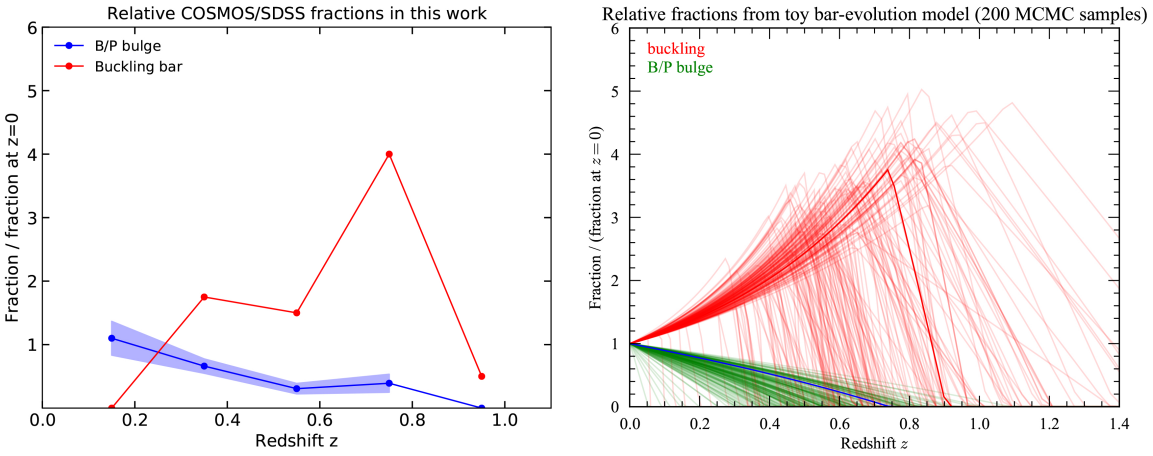

Figure 6.22: *Left panel*: The observed COSMOS/SDSS relative fractions of B/P bulges and buckling bars for galaxies of similar mass and imaged with similar resolution in each bin in this work. This plot is a combination of Figures 6.12 and 6.20, with fewer redshift bins. *Right panel*: Simple galaxy evolution model predicting the relative fraction of B/P bulges and buckling bars with redshift compared to the local fraction ($z = 0$), following 200 MCMC realizations with different initial parameters (plot courtesy of Peter Erwin). The thick red line and blue line represent the median values from the MCMC runs.

Saha et al. (2013) compared to a slower mechanism in which the bar is vertically thickened by the trapping of stars at resonances (Combes et al., 1990; Quillen et al., 2014). One caveat to note, though, is that some simulations predict that bars can buckle more than once (Martinez-Valpuesta et al., 2006). The secondary buckling is milder and persists for a longer time ($\sim$ 3 Gyr), but it is not yet clear how one can detect a secondary buckling in galaxy isophotes. If bars buckle multiple times and the buckling instability has the same appearance in the isophotes (trapezium shape with spurs on the same side), this would affect the buckling fraction determined in this study ($f_{\rm buckling}$ would be overestimated). Further simulations are needed to explore secondary buckling and how they affect the galaxy isophotes in order to recognise them in observed galaxies and to study their effect on the formation of B/P bulges.

6.7.2 What causes the buckling instability?

It is not yet established what determines the vertical instability commonly seen in simulations and now seen in observations as well. N-body simulations predict that the formation of a bar increases the radial velocity dispersion of the stars in the discs which leads to a vertical destabilization of the bar (Merritt & Sellwood, 1994). Rapid growth of bars (Martinez-Valpuesta et al., 2006), reduced gas content (Berentzen et al., 2007) and small vertical thickness of the disc have been suggested to cause bar

buckling in simulations.

This study (and E&D17 and Li et al. 2017) shows that there is a strong stellar mass dependence of the fraction of barred galaxies having B/P bulges. There is a rapid transition around a stellar mass of $\log(M_*) \sim 10.4\, M_\odot$ from $f_{\rm B/P} = 0.1$ to $f_{\rm B/P} = 0.4$ at the highest masses, and this transition can also be seen at higher redshifts, although at lower $f_{\rm B/P}$ values due to the observed redshift evolution of the B/P bulge fraction. It is well-known that the absolute bar length has a strong dependence on stellar mass —the most massive galaxies host, on average, the longest bars. It is worth therefore exploring if the rapid growth in bar size since $z \sim 1$ can be responsible for the bar buckling. In this work, however, I find very little evolution of bar size with redshift for fixed stellar mass (Figure 6.15). The distribution of length of bars of the COSMOS sample is consistent with being flat between $z = 0.15$ and $z = 1$. Furthermore, I only find a weak secondary correlation of the B/P bulge fraction with bar length when mass is controlled for in Figure 6.17 (between redshifts $0.15 < z < 0.5$). Both in the local and $z \sim 1$ Universe, the B/P formation is entirely explained by a strong dependence on stellar mass. E&D17 also found only a weak secondary correlation with absolute bar length: for galaxies of similar mass, the B/P bulge hosts tend to have longer bars by 1 kpc (median value). Why we only observe a correlation for the mid-redshift bin is puzzling; this result might be affected by small number statistics in each bin. Nevertheless, the absolute bar length of buckling bars has a large range of values, between 2 kpc and 15 kpc, therefore it is likely that rapid bar growth does not have a significant effect on bar buckling. Both small and large bars have been observed to be buckling, in the process of forming a B/P bulge.

Assuming that the gas content does not suppress bar buckling (as found by E&D17), the only still unexplored parameter that can control the buckling instability is the vertical thickness of the disc, which may have an important effect on the morphological evolution of galaxies. If the discs are dynamically too hot, with significant vertical velocity dispersions, bar buckling might be suppressed (Raha et al., 1991). A possible investigation of this scenario is discussed further in Section 7.2.4.

6.8 Conclusions

In this chapter I have investigated the presence of boxy/peanut bulges in the local and higher redshift Universe ($z \sim 1$) using a sample of 519 barred galaxies from the HST COSMOS survey and a mass- and resolution- matched sample of 519 barred galaxies from the SDSS survey, with morphologies from the Galaxy Zoo project. The selected barred galaxies are moderately inclined, such that both the identification of bars and

boxy/peanut bulges is possible based on the shapes of the inner isophotes, using a method devised by Erwin & Debattista (2013, 2017). 26 galaxies currently in the phase of buckling, being vertically unstable to form B/P bulges, were also identified. The galaxy isophotal contours were classified by three experts (Peter Erwin, Victor Debattista and myself) and the votes were aggregated to identify barred galaxies hosting B/P bulges or buckling bars. Finally, the local and higher redshift fraction of barred galaxies having B/P bulges, as well as the fraction of buckling bars was determined. I summarise the findings in this study as follows:

(i) The fraction of barred galaxies hosting boxy/peanut bulges decreases steeply with redshift, from 30% at $z = 0$ to 0% at $z = 1$.

(ii) Boxy/peanut bulges can be identified in moderately inclined galaxies (with inclinations $i = 40° - 70°$) by inspecting the boxy isophotes and offset spur morphology. They are more difficult to identify in face-on galaxies ($i \lesssim 30°$), as also shown by Erwin & Debattista (2013, 2017).

(iii) The boxy/peanut fraction depends primarily and strongly on stellar mass, with $> 40\%$ of barred galaxies with masses $\log(M_*) > 10.4\ M_\odot$ hosting B/P bulges and $< 20\%$ of barred galaxies lower than this mass hosting B/P bulges.

(iv) I identified 26 buckling bars in our sample (15 HST and 11 in SDSS), ~ 10 times more than previously found in the literature. The buckling rate in the local Universe is $\sim 2\%$ and the peak of buckling occurred at $z \sim 0.75$, where it was 4 times larger than it is now.

(v) A simple galaxy evolution model that matches the observed fraction of B/P bulges and buckling bars in the local Universe predicts that the buckling occurs ~ 2 Gyr after bar formation and lasts for ~ 0.8 Gyr. This model suggests that with the observed fractions of buckling bars with redshift it is possible to explain that most, if not all, of the B/P bulges were formed rapidly via bar buckling.

(vi) The cause of bar buckling is still uncertain. E&D17 showed that the atomic gas content is unlikely to suppress the formation of a B/P bulge and in this work I have shown that rapid bar growth is also unlikely to cause bar buckling. Galaxies with different bar lengths are observed buckling, and the bar size does not change significantly with redshift. A parameter still left to explore is the thickness of the discs, which is not possibly to study with this sample because the selected galaxies are not edge-on.

Chapter 7

Conclusions and Future Work

7.1 Summary of main results

In this thesis I have explored the structural properties with image decompositions of what is currently the largest sample of barred galaxies, examining the effects of bars on the properties and evolution of galaxies. With the decompositions I identified a curious sample of low mass galaxies with the bars offset from the centre of the discs, and investigated their statistical properties and their origin, a topic which has received insufficient attention in the recent astronomical literature. In addition, I have studied the formation and evolution of structures associated with bars, the 3D vertically thick boxy/peanut shaped part of the bar, from $z \approx 1$ to the local Universe, using a novel method of identification in galaxies with intermediate inclinations. I summarise my findings in this thesis below.

7.1.1 Properties of barred galaxies in the local Universe

In Chapter 3, I have investigated the properties of a large sample of barred galaxies in the local Universe, with data from the Sloan Digital Sky Survey, morphological classifications from the Galaxy Zoo project and 2D multi-wavelength and multi-component image decompositions with the GALFITM software. This sample of $\sim 3,500$ barred galaxies is currently the largest sample of galaxies decomposed with a model which includes a bar component. Using a multi-wavelength approach I found that the bulges and bars of strongly barred galaxies are redder in colour compared to their disc counterparts by $\Delta(g-i) \approx 0.3$ and $\Delta(g-i) \approx 0.2$, respectively, in good agreement with simulations of secular evolution driven by bars, leading to the quenching of the inner regions of galaxies. Furthermore, by comparing this sample with a mass-matched sample of galaxies without bars, fitted with a disc and a bulge component, I have

found that the discs of barred galaxies are redder compared to their unbarred counterparts by $\Delta(g-i) \approx 0.1$, while the bulges are slightly bluer by $\Delta(g-i) \approx 0.04$. I have found a similar colour difference even when matching the density of the local environment of the two samples, therefore the colour difference is not due to environmental effects such as ram pressure stripping or strangulation. This again points to a secular evolution scenario whereby the gas from the inner disc (probably within the bar co-rotation radius) is brought in by the bar to the galaxy centre where it triggers star formation, leaving the inner disc region devoid of the gas necessary to form new stars. This results in the redder colour of the discs of barred galaxies compared to the discs of galaxies without bars. Another piece of evidence strongly in favour of secular evolution is that barred galaxies have an overwhelming fraction ($\sim 90\%$) of disc-like pseudobulges (with a Sérsic index of $n_{\rm bulge} \approx 1$), suggestive of them being built by the infall of gas rather than by galaxy mergers.

Additionally, I have found that there are two types of bars in disc galaxies, confirming the early work of Elmegreen & Elmegreen (1985): bars with an exponential profile ($n_{\rm bar} \approx 1$) in late-type, lower mass ($M_* < 10^{10.4}\,M_\odot$) disc dominated galaxies, and bars with a shallower, Gaussian-like light profile ($n_{\rm bar} \approx 0.5$) in earlier type, higher mass ($M_* \geq 10^{10.4}\,M_\odot$) galaxies with larger bulges. The shallow light profile of bars in massive galaxies might be an indication of the vertically extended boxy/peanut structures observed at moderate inclinations. Moreover, galaxies with larger bulges tend to have longer bars when compared to the size of the galaxies (by about $\sim 40\%$), at all stellar masses. This implies that the light profile of bars can be used as an age indicator – lower mass, bulgeless galaxies with exponential bars have grown their bars relatively recently from the disc material, retaining the exponential profile of the discs, while more massive galaxies with longer bars and shallower light profiles have already grown their bars while building up a disc-like bulge at the galaxy centre.

Finally, within the sample of galaxies without bars selected with Galaxy Zoo morphologies I identified a significant fraction of galaxies which have inner lenses or ovals, morphological components with shallow light profiles and with yet unclear origins. Fitting these galaxies with models including an additional 'lens' component, I have found that the structural parameters of lenses (Sérsic indices, colours) as well as the properties of the galaxies hosting them (stellar masses, colours) are similar to those of early-type bars and early-type barred galaxies, respectively, suggestive of an evolution between bars and lenses (Kormendy, 1979).

7.1.2 Galaxies with offset discs and bars in the local Universe

In the first systematic search for galaxies with 'offset bars', I have found a sample of 271 such galaxies with offsets in a range 0.2-2.5 kpc between the stellar bar and the disc, measurements in good agreement with the predictions from simulations. I found that offsets are characteristic to lower mass galaxies, with a median mass of $M_* \approx 10^{9.6}\,M_\odot$ (which is also the mass of the LMC) and asymmetric discs ($A_1 \gtrsim 0.05$), with the asymmetries correlating with the disc-bar offsets. Simulations of dwarf galaxy interactions (Pardy et al., 2016) suggest that the discs and bars can become offset from each other following a flyby of a lower mass galaxy, with offsets up to 2.5 kpc which are restored in ~ 2 Gyrs. Investigating the correlation between these galaxies and companion galaxies, I did not find a higher fraction of galaxies with companions compared to a redshift- and mass-matched sample of galaxies with centred bars. However, this might be due to the shallowness of the SDSS spectroscopic survey ($m_r < 17.77$) missing fainter companions or the companions having high velocities and reaching large distances making their identification difficult. Deeper surveys can reveal missing companions or signs of interaction and higher resolution data will allow a more precise measurement of the offsets.

Using integral field spectroscopic field data from the SDSS-IV MaNGA survey I investigated the kinematics of gas and stars of offset galaxies in Chapter 5, by modeling their kinematics with a rotation model including non-circular motions with the DISKFIT software. Interestingly, the simulations of Pardy et al. (2016) predict that it is the disc that becomes offset from the centre of the dark matter halo and oscillates, not the stellar bar. Analysing the kinematic centres of stars and gas I found tentative evidence that the gas kinematics follows the bar component, while the stellar kinematics are offset, in agreement with simulations. Thus, these galaxies should be referred to as 'offset discs' rather than 'offset bars'. Another possible origin for the offsets is the lopsidedness or triaxiality of the dark matter haloes surrounding these galaxies which might imprint their asymmetries onto the galaxy discs. I have shown in Chapter 4 that these galaxies are largely asymmetric, thus it is a plausible scenario. By measuring the kinematic lopsidedness of the offset galaxies, I have found that the perturbations in the potential due to a lopsided halo are small, $\sim$6%, and are similar for galaxies with offset discs and those with centred components. The ellipticity of the dark matter haloes can be estimated by measuring the departures from circular motions at large radii in galaxies. The measured non-circular amplitudes at distances $\gtrsim r_e$ in these galaxies suggest that the haloes are approximately round (axis ratios $\gtrsim 0.96$), with only minor departures from axisymmetry, implying that perturbations in the potential due to a lopsided or triaxial halo cannot be the cause of the observed

offsets. Nevertheless, deep and well-resolved imaging of a sample of galaxies with offset discs and bars with gas measurements are needed to definitively establish the origin of offsets and the relation between the components and the dark matter haloes.

7.1.3 Bar buckling and evolution of galaxies with boxy/peanut bulges

In contrast to the galaxies with offset discs and bars which tend to have low masses, higher mass barred galaxies show bars with vertically extended boxy or peanut shaped structures (known as boxy/peanut bulges). In Chapter 6 I investigated the fraction of local (SDSS survey) and higher redshift (from the *HST* COSMOS survey) barred galaxies with intermediate inclinations having boxy/peanut features, using a novel visual expert classification method of the projected boxy/peanut structures. I found a sharp increase in the boxy/peanut fraction (from $\sim 15\%$ to $\sim 40\%$ for local galaxies) around $M_* \approx 10^{10.4}\ M_\odot$, in agreement with previous work by Erwin & Debattista (2017). I have also found an evolving fraction of boxy/peanut bulges from 30% at $z \approx 0$ to 0% at $z \approx 1$, which is not due to observational biases such as the degrading resolution of *HST* imaging data or band shifting.

Simulations suggest that the bar buckling instability is responsible for forming the boxy/peanut bulges now commonly seen in both edge-on and moderately inclined galaxies. Buckling has been seen frequently in simulations, however only three galaxies have previously been caught in the buckling phase (Erwin & Debattista, 2016; Li et al., 2017). In Chapter 6 I have presented 26 galaxies in the buckling phase (11 in the local Universe and 15 in higher redshift COSMOS data). The local fraction of galaxies currently undergoing bar buckling is 2% and in the past it reached a peak at $z \approx 0.75$, where the frequency of buckling was ~ 4 times higher than it is now. A simple evolutionary model considering the local observed fraction of boxy/peanut bulges and the evolution of the fraction of barred galaxies with redshift that matches the observations of bar buckling suggests that buckling occurs ~ 2 Gyr after bar formation and lasts for ~ 0.8 Gyr, in good agreement with simulations. The observed evolution of the fraction of buckling bars implies that most, if not all boxy/peanut bulges are formed via the buckling instability.

Nevertheless, the cause of bar buckling is not yet clearly established. I have found that the rapid growth of bars cannot be the origin of bar buckling since the bar lengths of the galaxies in the COSMOS sample do not evolve significantly with redshift (for fixed stellar mass). Furthermore, the galaxies currently buckling have a large range of bar lengths. Additionally, Erwin & Debattista (2017) found no correlation of the boxy/peanut bulge fraction with the lack of gas in galaxies (after controlling for the

strong stellar mass trends), suggesting that the gas fraction does not suppress bar buckling. One other possibility is that the disc thickness, related to the random motion of galaxies in the vertical direction, is responsible for buckling. This will be explored in future work as it was not possible to measure the galaxy thickness in moderately inclined galaxies.

7.2 Future work

The research in this thesis has provided insight on how the presence of large-scale bars in a large proportion of galaxies affects the evolution of their host galaxies, how they can lead to the formation of associated structures (disc-like bulges, 3D boxy/peanut structures) and to the off-centering between the discs and the bars. Still, my work raises new questions: (1) how can we quantify the impact of bars on galaxies with spectroscopy? (2) is there a limit on the sizes of the disc-like bulges built by bars and can they destroy the bars? (3) what is the redshift evolution of the offsets and what is the origin of offsets? (4) can the thickness of the galaxy discs cause the vertical buckling of bars? and (5) how do the structural properties of bars evolve with time, and how can we measure these in the upcoming large surveys such as *Euclid*? In this section I focus on how these questions can potentially be pursued, leading to a better understanding of the evolution of disc galaxies.

7.2.1 Star formation histories of local barred galaxies using MaNGA

My results have shown that the colours of the discs of barred galaxies are redder than the discs of similar mass galaxies without bars. Furthermore, the inner components (bars and bulges) are redder than the corresponding discs, suggestive of older stellar populations. Nevertheless, this study used integrated colours of the discs, without colour gradients across them. In order to quantify the ages of the stellar populations, the star formation histories and investigate whether there are gradients across the individual components, one has to use spatially resolved spectroscopy. This is currently possible with integral field spectroscopy, and in particular with the SDSS-IV MaNGA survey, which will observe a representative sample of 10,000 nearby galaxies, the largest sample with resolved spectroscopic maps. I have already used data from the MaNGA survey in Chapter 5, when studying the kinematics of galaxies with offset discs and bars.

Out of the 40,000 possible MaNGA targets, I have fitted $\sim 1,300$ galaxies with strong bars. Thus, it is expected that ~ 300 barred galaxies that I fitted and studied

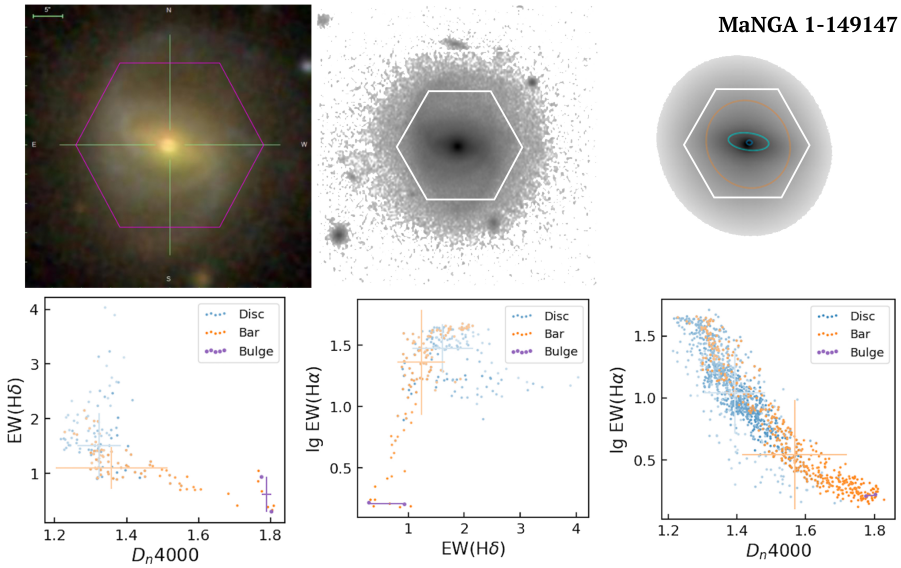

Figure 7.1: Illustration of how the decompositions can be used to study the star formation history indicators (Hα, Hδ, D4000Å break), extracted from the MaNGA maps, in the particular case of J112424.63+511405.7. The magenta, orange and blue points show the individual spaxels with S/N> 10 within the bulge, bar and disc components, respectively. The '+' signs of the same colours show the median values for each component.

in Chapter 3 will be observed by MaNGA by the end of the survey in 2020. My multi-component decompositions of these galaxies can be used as masks in the integral field spectroscopic maps, in order to extract the spaxels corresponding to the discs, bar and bulge components. It will then be possible to investigate the stellar population ages, metallicities and star formation histories of galaxy components using proxies such as Hα emission (probing current star formation), Hδ absorption (probing recent star formation) and D4000Å break (probing the quiescent population) in the largest integral field spectroscopic survey of nearby galaxies. An example of the star formation indicators extracted for the three different components of a barred galaxy observed by MaNGA, extracted using my decomposition masks, plotted against each other is shown in Figure 7.1. This particular example shows a galaxy with a quiescent stellar population and little or no star formation in the bulge, a young and star forming disc and a bar with intermediate stellar populations, with evidence for recent star formation. The stellar population ages and metallicities can be investigated using indicators such as Hβ and absorption lines Mgb, Fe5270Å and Fe5335Å measured by the MaNGA Data Analysis Pipeline, and overlaid on a single stellar population (SSP) prediction grid by, for example, Vazdekis et al. (2010). With a large sample provided by MaNGA, it will be possible to study the predicted enhancement of star formation in the bulges of barred galaxies and the decrease and the spatial distribution of star

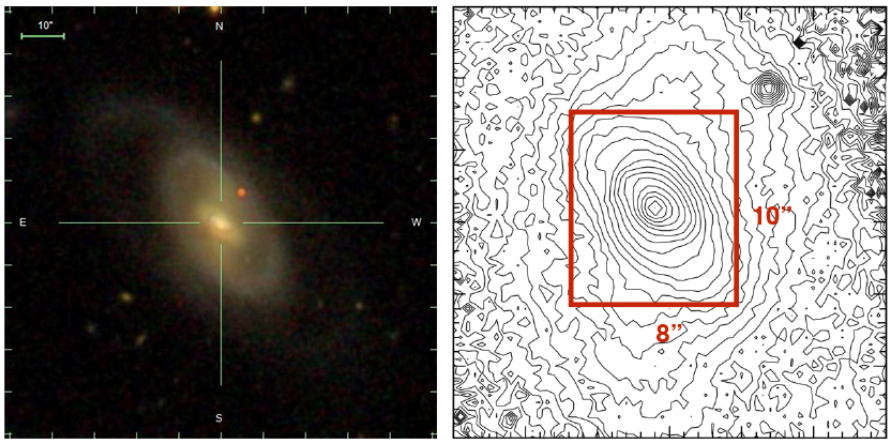

Figure 7.2: *Left*: *gri* colour composite SDSS image of PGC 045903, barred galaxy with the largest nuclear disc found. *Right*: 24″ × 24″ contour plot showing the inner isophotes of the nuclear disc with an extent of 10″ × 8″, corresponding to a radius of ∼ 3.6 kpc at the redshift of the galaxy, z=0.028.

formation in the discs and bars in a statistically significant way.

7.2.2 Investigating nuclear discs

With the decompositions of barred galaxies I have found that these galaxies host an overwhelming fraction (∼ 90%) of disc-like bulges, referred to as 'pseudobulges' by Kormendy & Kennicutt (2004) (also known as nuclear discs), believed to have been built from the gas driven inwards by the bar. When classifying the boxy/peanut bulges in Chapter 6, Erwin, Debattista and I serendipitously identified based on their discs isophotes a few barred galaxies showing unusually large nuclear discs. This included PGC 045903, a galaxy with the largest nuclear discs ever observed, with a diameter of ∼ 7 kpc (shown in Figure 7.2), which calls into question our understanding of the dynamical evolution of bars and the formation of these nuclear discs. Nuclear discs do not usually extend beyond the bar minor axis, having diameters of 0.5-4 kpc (Medling et al., 2014). PGC 045903 (epoch J2000, R.A.=13:12:56.70, Dec.=+47:27:23.90, z=0.028) is a barred spiral galaxy located at a distance of 125 Mpc. Based on my multi-component decompositions described in Chapter 3, the nuclear disc has a Sérsic index $n = 1.3$, an ellipticity $\epsilon = 0.38$ and magnitude of 17.1 in the r-band.

It is believed that these nuclear discs are the product of the integrated star formation in nuclear rings (Cole et al., 2014), which originate in the driving inwards of gas by the bar to settle onto x_2 orbits. These orbits are perpendicular to the major axis of the bar itself (i.e. along the minor axis of the bar, see Figure 1.6 in Chapter 1 for an

illustration), covering a large range of radii, extending past the minor axis of the bar. The gas driven inwards by the bar is usually confined within the minor axis of the bar and does not settle on the largest x_2 orbits. Star-forming nuclear rings have never been observed to extend past the minor axis of the bar itself. However, some galaxies have nuclear discs reaching to up to $15-20\%$ of their bar radius (e.g. Debattista et al. 2018), which is too large for them to be supplied by ongoing star formation. Since stars, unlike gas, are not efficiently trapped onto x_2 orbits, the formation of large nuclear discs in galaxies is a puzzle. One possibility is that the gas settles on such large radii after a strong interaction. Debattista et al. (2015) suggested that such a large nuclear disc is present in the Milky Way and is responsible for the high velocities observed in the bulge by the APOGEE survey. Curiously, the stars responsible for these large velocities are not young, suggesting if there is a nuclear disc in the Milky Way, then it is old.

The nuclear disc in PGC 045903 extends well past the minor axis of the bar, reaching a radius of ~ 3.6 kpc, i.e. $\sim 40\%$ of the bar radius. Unfortunately observations of this galaxy are only available from SDSS and DeCALS with inadequate spatial resolution to explore the substructure of the nuclear disc in greater detail. Therefore, this galaxy has been included in the *HST* Gems of the Galaxy Zoos program (SNAP proposal 15445, PI William Keel) and should be observed by *HST* during Cycle 25 or Cycle 26. Furthermore, to study the stellar populations and kinematics of the nuclear disc, we were awarded 4 hours of observing time with the Gemini GMOS IFU (GN-2018A-FT-208). These measurements will allow us to determine whether the stars in the nuclear disc are old or young, and metal-rich or metal-poor. A relatively metal-poor nuclear disc would favour an interaction driving gas to the center and forming the nuclear disc.

Since companion galaxies are not evident, if the nuclear disc is young, then some mechanism must be found for driving gas onto x_2 orbits with such large energies. Moreover, the kinematics will allow us to determine the ratio of rotation to random motion of the nuclear disc to help constrain the state of the gas when the stars were forming. A high rotation would indicate a gentle mechanism rather than a violent merger. In general, x_2 orbits do not support the bar, and, on contrary, simulations suggest that bars can be destroyed by the bar-induced massive central mass concentrations (Shen & Sellwood, 2004; Athanassoula et al., 2005). Studying the large nuclear disc in PGC 045903 it will be possible to establish the minimum mass required to destroy a bar and the maximum size of these objects. Thus, the combination of high resolution imaging with *HST* and IFU spectroscopy of the nuclear disc in PGC 045903 will help us to pinpoint the origin of large nuclear discs in galaxies.

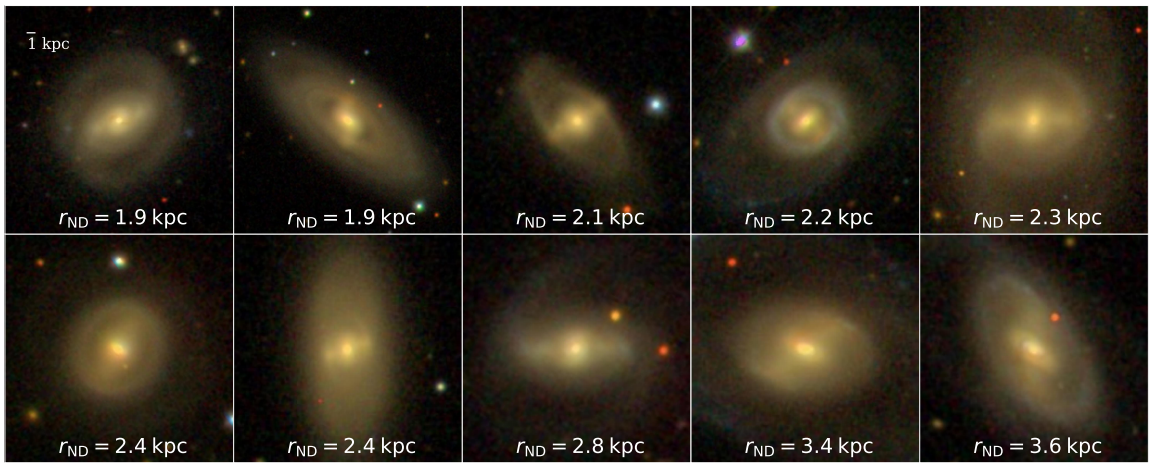

Figure 7.3: Examples of large nuclear discs identified at the centres of local barred galaxies, including PGC 045903 (2^{nd} row, last galaxy), with the measured radius of the nuclear disc in kpc. *gri* colour composite images from SDSS (the images are 30 × 30 kpc). A dedicated project would identify a large sample of such objects in the nearby Universe (SDSS) and higher redshifts (*HST*).

Nevertheless, it is unlikely that PGC 045903 is the only galaxy having a nuclear disc extending past the minor axis of the bar. There should be rather a class of such objects, which have not yet been identified. It is possible to identify a sample of such galaxies by inspecting galaxy isophotes, as has been demonstrated in our Galaxy Zoo Panoptes Project. In a preliminary analysis of SDSS galaxies with redshifts between $0.01 < z < 0.03$, flagged by Galaxy Zoo volunteers as having *obvious* and *dominant* bulges I identified ~ 40 galaxies with possible large nuclear discs, some examples being shown in Figure 7.3. PGC 045903 (2^{nd} row, last galaxy) is still the galaxy identified with the largest nuclear disc. Most of these large nuclear structures are hosted by red discs, with an inner ring surrounding the bar. In the future I plan to build a larger scale project to identify and build a sample of nuclear discs, considering SDSS galaxies within $z \lesssim 0.05$ and galaxies imaged by *HST* up to $z \sim 0.5$, with suitable resolution for these structures to be accurately identified. It would then be possible to study the statistical distribution of their photometric properties (disc sizes, colours etc.), as well as their spectroscopic properties (kinematics, stellar population ages, metallicity) by cross-matching with the MaNGA target sample.

7.2.3 Offset discs and bars in the local and higher redshift Universe

As shown in Chapter 4, Figure 4.5, image resolution plays an important role in identifying galaxies with offsets since it blurs the central part of the galaxy and causes

the bar to appear rounder. SDSS, having a typical resolution of $\sim 1.2''$, made it difficult to study these objects at redshifts $z > 0.06$, while their lower masses required the selection of galaxies with $z < 0.04$, in order to obtain a volume-limited sample. Furthermore, the SDSS spectroscopic survey is shallow ($m_r < 17.77$), making the identification of possible companions challenging. Two deeper surveys than SDSS, with better spatial resolution are the nearby Spitzer Survey of Stellar Structure in Galaxies (S^{4}G) and the higher redshift *HST* Legacy Surveys (COSMOS and CANDELS).

S^{4}G (Sheth et al., 2010) is an deep infrared survey in 3.6 and 4.5 μm of 2,352 nearby galaxies. Although the resolution of S^{4}G $\sim 2''$ (Salo et al., 2015) is worse than that of SDSS (FWHM typically $\sim 1.2''$), the sample contains galaxies up to a distance of $D \lesssim 40$ Mpc; this translates into physical resolutions $\lesssim 0.4$ kpc (~ 0.2 kpc at the median distance of the survey), thus the physical resolution is much better than that of SDSS. Another advantage of using S^{4}G is imaging in the infrared which is less affected by internal dust extinction and probes mostly the older stellar populations. Salo et al. (2015) decomposed the deprojected images of 2,277 galaxies in the S^{4}G sample using the same software as in Chapter 3 (GALFIT, Peng et al. 2010), into discs, bars and bulges (and nuclear point sources in some cases), as identified according to the visual classification of Buta et al. (2015). 855 of the S^{4}G galaxies were fitted including a bar component (213 with disc+bar+bulge, 184 nuclear point source+disc+bar and 458 with disc+bar). The decompositions of Salo et al. (2015) fixed all the components to have the same centre, since this ensures the fitting is well-behaved. This is not always physically motivated, as I have shown in Chapter 3, since a significant fraction of galaxies show signs of offsets between the different components. I have investigated the S^{4}G barred galaxies and visually identified a sample of 146 galaxies with *possible* offsets between the discs and bars (examples shown in Figure 7.4), and a further 43 galaxies with *possible* offsets between the discs and a second component (bulge or nuclear point source). The next step would be to rerun the best fit multi-component decompositions of the 189 S^{4}G galaxies allowing the component centres to vary freely in the fitting.

The *HST* COSMOS (Koekemoer et al., 2007) and CANDELS (Koekemoer et al., 2011) surveys are the largest surveys of resolved high redshift galaxies, and are ideal for studying the redshift evolution of galaxies with offset discs and bars. One advantage of the high redshift surveys is that the angular scale increases with redshift; 100 kpc corresponds to $\sim 12''$ at $z = 1$ compared to $\sim 100''$ at $z = 0.06$, making the visual identification of companion galaxies easier. Interactions are also more frequent at high redshifts (Patton et al., 2000, 2002; Conselice et al., 2003). If the fraction of

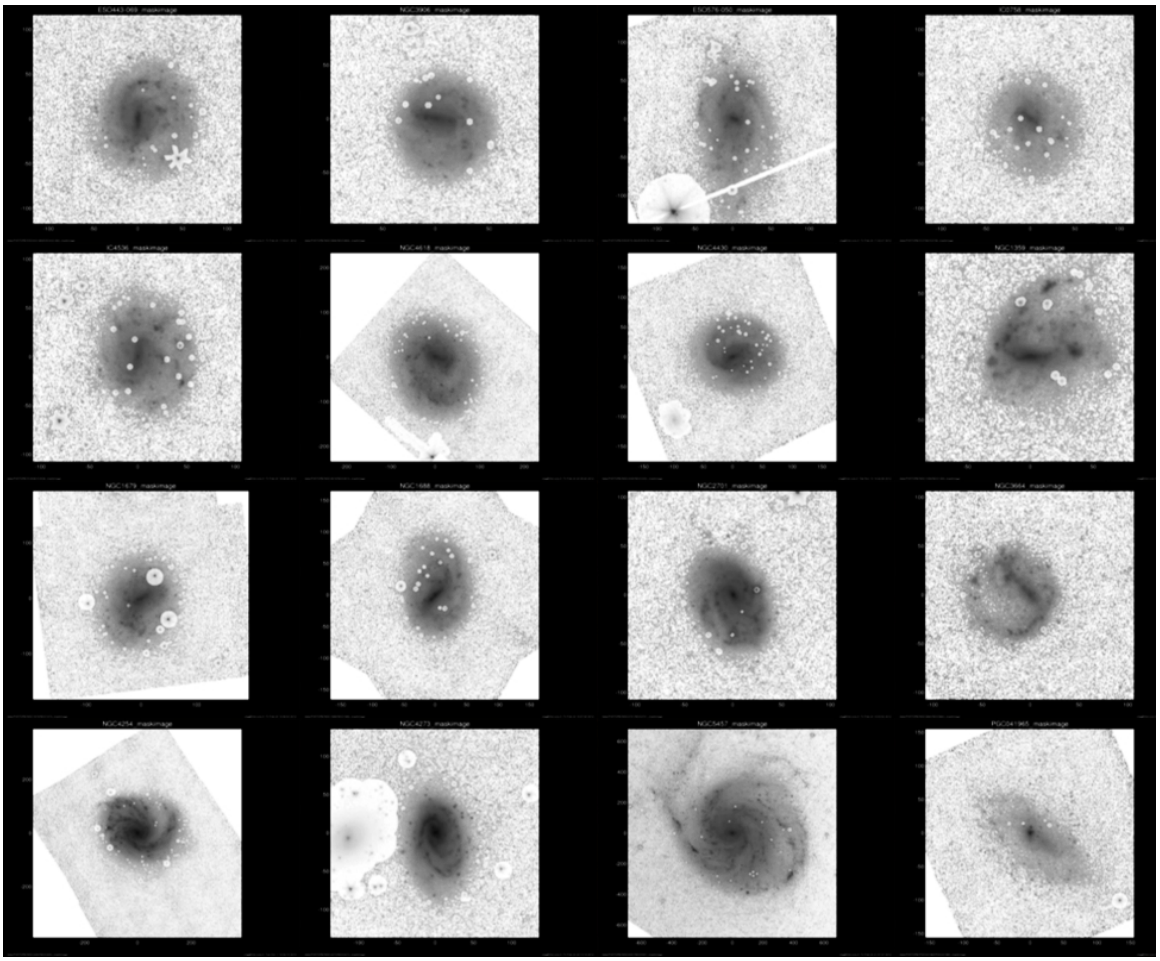

Figure 7.4: $3.6\mu m$ images of local ($D \lesssim 40$ Mpc) galaxies imaged by the S^{4}G survey showing offsets between the discs and bars (first three rows) and between the disc and the bulge/nucleus (last row). The mosaics of galaxy images and masks (correcting for foreground stars and other defects) are taken from Muñoz-Mateos et al. (2015).

galaxies with offsets discs and bars increases with redshift, this is a strong evidence for galaxy interactions being responsible for the offsets. The Galaxy Zoo: Hubble Bar Lengths project already asks the volunteers if the bar is offset from the galaxy centres.

7.2.4 Disc thickness as the origin of bar buckling

In Chapter 6 I explored the possible causes of bar buckling, finding that the rapid growth of bars is unlikely to be an explanation. One possibility left to explore is whether the the vertical random motions in the discs can suppress bar buckling. Raha et al. (1991) shows in some of the first simulations of galaxies undergoing the buckling instability that buckling occurs when the ratio of the vertical to radial random motion (σ_z/σ_r) decreases below a certain threshold, with buckling occurring earlier (and being more violent) in thin discs, compared to thick discs. More recently, Martinez-Valpuesta et al. (2006) showed that this threshold for buckling to occur is $\sigma_z/\sigma_r \sim 0.4$, which is then followed by an increase in the vertical random motion caused by buckling, driving the ratio to $\sigma_z/\sigma_r \sim 1$.

To test this observationally, one would need to measure the vertical and radial random motions in edge-on galaxies, which is currently difficult to achieve on large samples. However, σ_z and σ_r correlate with the vertical and radial scale lengths respectively (h_z and h_r) (van der Kruit, 1988), such that galaxies with higher random motions in the vertical direction are thicker. Therefore, measuring the thickness to the scale length ratio of discs (h_z/h_r) as a function of stellar mass for edge-on galaxies would help determine whether galaxy thickness can be a cause of buckling. If lower-mass barred galaxies are thicker compared to higher-mass unbuckled barred galaxies (without B/P bulges, as this increases the vertical scale height), this would be a good observational indication for a decrease in the vertical to radial random motion causing buckling.

There is some evidence that later-type galaxies with larger discs are thinner (Bershady et al., 2010), however there is no bar or B/P classification for the galaxies in their sample. Since the galaxies classified in Chapter 6 were all moderately inclined, it was not possible to measure the thickness of the galaxy discs. However, this would be possible with a sample of selected edge-on discs. If the thickness is indeed responsible for bar buckling, given the sharp increase observed in the fraction of boxy/peanut bulges at a mass of $M_* \approx 10^{10.4}\,M_\odot$, one would expect a transition in the thickness of discs around this mass. Lower mass galaxies, showing only a very small fraction of buckled bars should have slightly larger vertical random motions, while galaxies

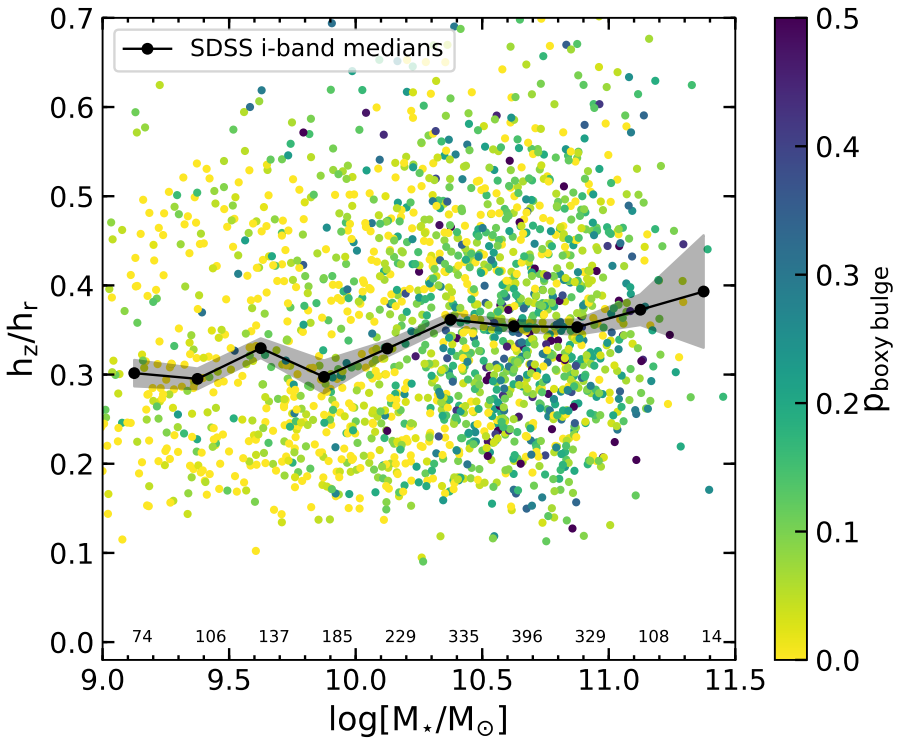

Figure 7.5: The ratio of the disc scale height to scale length, as measured by Bizyaev et al. (2014) using 1D profile fitting in i-band images, in a sample of $\sim 2,000$ edge-on discs selected from SDSS and Galaxy Zoo. The galaxies are coloured by the debiased vote fractions for the *boxy* answer for the *What is the shape of the bulge?* question asked to the volunteers after the edge-on question. The points show the median z_0/h in each mass bin, and the shaded area shows the standard error in each bin. The numbers illustrate the number of edge-on galaxies in each mass bin.

more massive than this threshold should again have larger vertical random motions because of the boxy/peanut structure itself.

With Galaxy Zoo, it is possible to identify edge-on galaxies, in both local (SDSS) and higher redshift galaxies (*HST* Legacy Surveys). The Galaxy Zoo project actually asks if a galaxy is seen edge-on, after the galaxy was classified as having a disc or features. Thus, it is even possible to investigate the redshift evolution of galaxy thickness. Once a sample of local and higher redshift edge-on discs is identified, it is possible to measure the thickness of the discs via galaxy decompositions with GALFITM. Peng et al. (2010) implemented in GALFIT the edge-on disc light profile given by van der Kruit & Searle (1981), as shown in Figure 19 of Peng et al. (2010) and discussed in their Section 7.2. As preliminary work, I used the catalogue of edge-on discs in SDSS from Bizyaev et al. (2014) and matched it to the Galaxy Zoo 2 catalogue. By requiring that at least 10 volunteers classified the galaxies as edge-on,

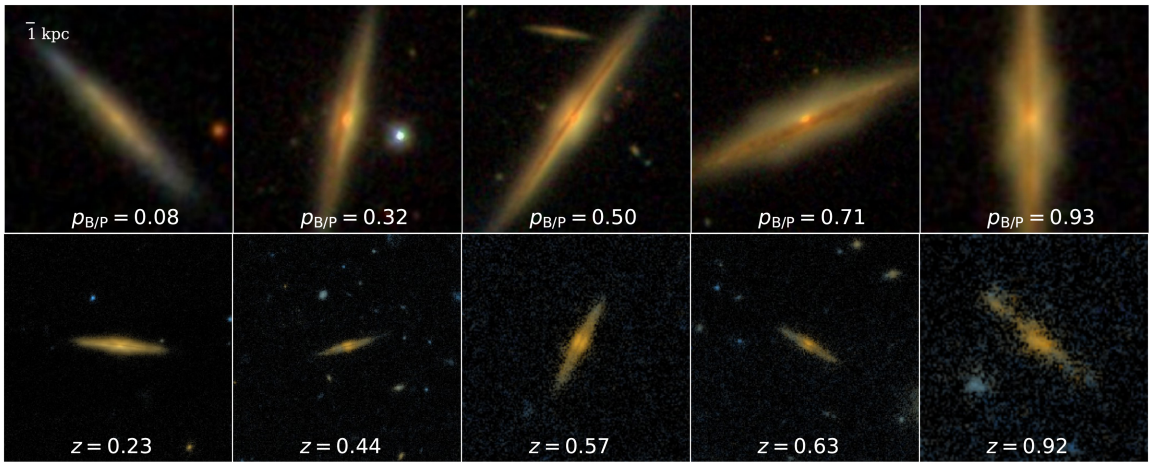

Figure 7.6: *First row:* Examples of the boxy/peanut bulge likelihood ($p_{\mathrm{B/P}}$) based on the Galaxy Zoo volunteers' classification of bulges of edge-on galaxies in SDSS images. With a suitable threshold on $p_{\mathrm{B/P}}$ it is possible to identify a sample of boxy/peanut bulges in the local Universe. *Second row:* Examples of galaxies with $p_{\mathrm{B/P}} > 0.3$ identified in *HST* COSMOS at various redshifts. The *HST* images have a different scale compared to the SDSS ones.

and a debiased vote fraction for features or disc $p_{\mathrm{features}} \geq 0.227$ (as recommended by Willett et al. 2013), I identified $\sim 2,000$ edge-on discs in SDSS, within a redshift of $z < 0.06$. Bizyaev et al. (2014) actually measured the ratio of the disc scale height to disc scale length by fitting 1D photometric profiles to surface brightness of the galaxies (the method is described in more detail in Bizyaev & Mitronova 2009). The central region of the galaxies (1/4 of the semi-major axis of the disc) was excluded in the analysis so that the measurements are not biased by large bulges extending above the plane of the disc. I plot the ratio of the disc scale height to scale length for the $2,000$ edge-on disc galaxies in Figure 7.5. The median disc scale height-to-length ratio increases with stellar mass, with perhaps a weak hint of a transition between a stellar mass of $M_* \approx 10^{10} - 10^{10.4}\ M_\odot$. Higher mass galaxies have larger thickness to length ratios, suggestive of higher random motions in the vertical direction, in agreement with simulations of bar buckling. However, there is no obvious thinning of the disc from low masses to $M_* \approx 10^{10}\ M_\odot$, implying a higher vertical random motion for low mass discs. Measuring the heights and radial scales with 1D profiles is probably inadequate as edge-on galaxies are highly affected by dust, and dust attenuation makes it difficult to extract accurate structural parameters. The presence of dust causes discs to appear thicker than they really are (Bizyaev et al., 2014). Thus, one needs to account for dust extinction in the measurements of the thickness of the discs.

In addition to measuring the thickness of discs it is possible to identify boxy/peanut bulges in edge-on galaxies, if the resolution is adequate and signal-to-noise is high.

As mentioned in Chapter 6, both the Galaxy Zoo 2 and Galaxy Zoo Hubble projects ask the question *'Does the galaxy have a bulge at its centre? If so, what shape?'* with the possible answers *Rounded*, *Boxy* or *No bulge*, after classifying a galaxy as being an edge-on disc. This question has not yet been explored in the Galaxy Zoo project. In general, the *Boxy* answer received only few classifications, unless the boxy/peanut features was obvious in the colour images, which results in small vote fractions for the boxy bulges ($p_{\rm boxy}$). Figure 7.6 shows examples of galaxies with various boxy/peanut likelihoods ($p_{\rm boxy}$) based on the Galaxy Zoo volunteers' in SDSS, and potential higher redshift edge-on galaxies with boxy/peanut structures identified in *HST* with ($p_{\rm boxy}$ >0.3). This figure suggests that boxy bulges can be identified in SDSS and *HST* images even with $p_{\rm boxy} < 0.5$. Therefore, I colour coded the galaxies in Figure 7.5 by the boxy bulge vote fractions. There is a clear increase in the boxy bulge likelihood above $10^{10.4}$ $M_{\odot}$, lower mass galaxies have mean $p_{\rm boxy} \sim 0.05$, and higher mass galaxies have mean $p_{\rm boxy} \sim 0.15$. This is in good agreement with the transition in the boxy/peanut fraction that I have found in moderately inclined galaxies in Section 6.5.3, at a similar stellar mass, suggesting that it will be possible to study boxy/peanut bulges in edge-on galaxies using Galaxy Zoo classifications, although the boxy bulge classification will need to be calibrated for a reliable study.

Studying the boxy/peanut features in edge-on galaxies will allow us to ultimately compare the fraction of galaxies hosting boxy/peanut bulges, with the caveat that it is not possible to establish if edge-on galaxies are barred simply based on imaging. Nonetheless, it is possible to assume that all boxy/peanut structures are linked to bars. Furthermore, it will be possible to compare the highest redshift galaxies with boxy/peanut bulges between the edge-on and moderately inclined studies. In Figure 7.6 (2^{nd} row), the highest redshift edge-on galaxy with a possible boxy/peanut structure (situated at $z \sim 0.9$) agrees well with the highest redshift galaxy with a boxy/peanut structure identified in a moderately inclined galaxy.

7.2.5 Properties of barred galaxies in the higher redshift Universe

In Chapter 3 I studied the properties and structural components of local barred galaxies using the decompositions that I developed. But how do these properties change with time? I plan to extend the work I have done at $z \sim 0$ to higher redshift galaxies, with existing data from the *HST* Legacy Surveys such as COSMOS and CANDELS. Detailed morphological classifications for these galaxies are already available from the GZ: Hubble and GZ: CANDELS projects. These surveys contain $\sim$ 600 ($\sim$ 500 in COSMOS Melvin et al. 2014, $\sim$ 100 in CANDELS Simmons et al. 2014) barred

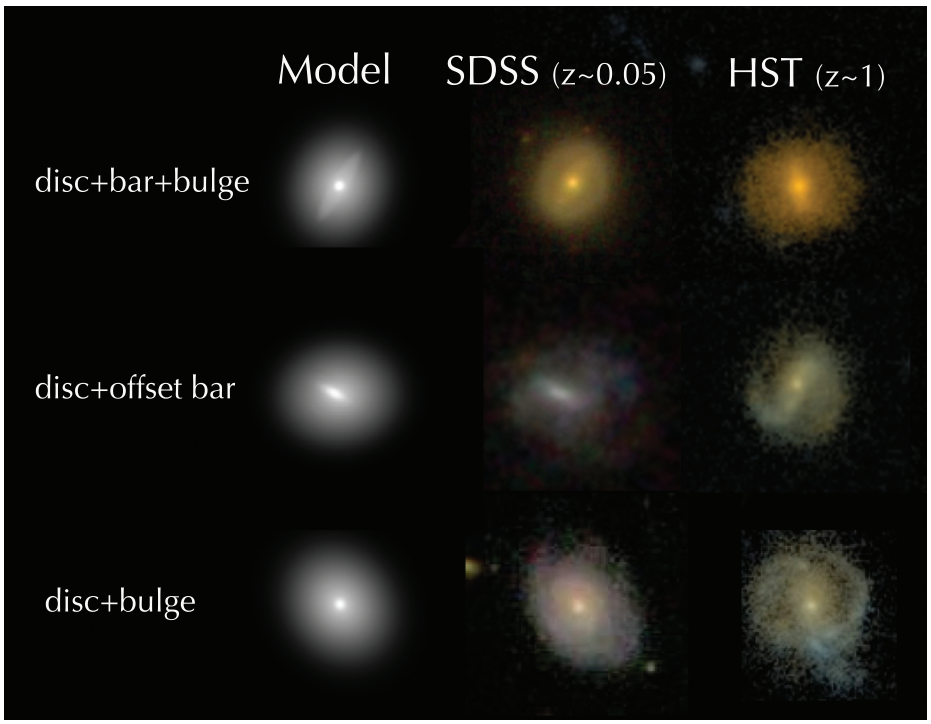

Figure 7.7: Examples of galaxies from the local Universe (SDSS) fitted with disc+bar+bulge, disc+offset bar and disc+bulge components, and similar resolution images from *HST* at $z \sim 1$.

galaxies between $0.2 < z < 2$, ideal to study the evolution of bars and associated structure in the Universe. This sample provides an ideal test for the evolution of the structural parameters, light ratios and rest-frame colours of galaxy components across cosmic time, when compared to the local barred galaxies presented in Chapter 3. Therefore, this study will be an important step for establishing the role of bars in the evolution of galaxies since $z \lesssim 2$. It will help establish how the properties of bars change over time and whether they are indeed responsible for the growth of bulges and the quenching of star formation in the galaxy discs.

The samples of barred galaxies studied in this thesis are currently the largest possible, both in the local Universe (SDSS) and the higher redshift Universe (*HST* Legacy Surveys). However, the future of galaxy morphology and evolution is very promising with the advent of even larger scale astronomical surveys such as the Large Synoptic Survey Telescope (LSST) and the ESA *Euclid* survey. The Galaxy Zoo classifications and my decompositions of SDSS and *HST* data will be an ideal basis for these future surveys.

For example, the upcoming large ESA mission, *Euclid*, probing a large area ($15,000$ deg^2) and including a 40 deg^2 area imaged to a great depth (Euclid Deep Fields), will provide millions of resolved galaxies for morphological studies through

exquisite imaging. With a 4 times better resolution and 3 NIR magnitudes deeper than is possible from the ground (Laureijs et al., 2011), *Euclid* will get the resolution of Sloan at $z \approx 1$ instead of $z \approx 0.05$, revealing the inner structures of galaxies up to $z \approx 1$. Considering the enormous number of galaxies imaged, it would take decades, even for the large number of volunteers participating in Galaxy Zoo to classify them. Although automated morphological classifications using machine learning algorithms have already been developed (e.g. Dieleman et al. 2015), these algorithms are reliable in classifying the galaxies into "smooth" (or elliptical) and "features" (or disc) galaxies when comparing to visual morphologies, while the classifications of the detailed galaxy morphology (the presence and prominence of bars, bulges, rings etc.) is less precise. Therefore, I would like to combine the detailed visual morphological classifications via online crowdsourcing, deep learning algorithms and multi-band galaxy profile fitting with GALFITM to detect and measure the properties of galaxy structures (discs, bars, bulges, rings, inner lenses, etc.) in *Euclid* data.

Some steps towards developing new algorithms for classifying morphology in large datasets, such as in the *Euclid* survey, have been achieved by the team of Marc Huertas-Company (Huertas-Company, 2016; Domínguez Sánchez et al., 2018). His work focuses on using different tools (like machine learning algorithms etc.) to estimate basic galaxy measurements and morphologies with Euclid. Using my expertise in galaxy fitting and detailed galaxy morphology I will be able to add a further step to the classification and measurement process by allowing humans to inspect the well-resolved galaxies and use GALFIT to measure further the detailed morphology of galaxies.

The recent work of Wright et al. (2017) has shown that combining human and machine classifications outperforms either individually. Galaxy Zoo has already developed the first steps in combining human and machine classifications with the Galaxy Zoo Express project (Beck et al., 2018). This project uses the SWAP algorithm (Space Warps Analysis Pipeline, Marshall et al. 2016), which updates the likelihood of a galaxy having a particular feature given the volunteer's previous performance in classifying galaxies with known morphologies. This reduces the number of classifications required to retire the images as well as providing a good training set for a machine learning algorithm. Beck et al. (2018) showed that with this algorithm it is possible to classify the entire Galaxy Zoo 2 dataset in 32 days with 93% accuracy, compared to the original timescale of ~ 1 year.

The majority of the sources detected by *Euclid* will either be unresolved, or contain no visible structure (i.e. elliptical galaxies). These galaxies can be efficiently classified as such using machine learning algorithms, by training the machine with

large training sets available via Galaxy Zoo (as already shown by Dieleman et al. 2015). This will significantly reduce the sample size to be classified from the *Euclid* survey to numbers currently possible with citizen science projects like Galaxy Zoo. The volunteers will then provide answers about the detailed morphology of these galaxies, which I can then fit using parametric functions to measure the physical properties of the inner structures. By implementing the combination of machine and human classifications, it will also be beneficial in finding and studying rare objects in the large volume Euclid will probe. The volunteers will be able to detect interesting objects like galaxies with offset discs and bars, offset nuclei, boxy/peanut bulges, at various redshifts, by selecting from a list of known objects and tagging the galaxy images, while also keeping open to "unknown unknowns" by allowing the volunteers to freely tag interesting objects. The technologies in large scale surveys are advancing fast and novel methods to accurately analyse galaxy morphologies need to be developed to keep up with the wealth of information that will be available in the future.

7.3 Concluding remarks

I conclude this thesis by interpreting my findings in the context of barred galaxy evolution. Observations show that bars started forming in galaxies ∼8-10 Gyrs ago (at $z \approx 1-2$), when mergers became less frequent. They form naturally out of disc instabilities, and simulations suggest that they can be triggered in interactions, however observations which might indicate that a bar has been tidally induced are still inconclusive. Initially, the light profile of bars is exponential, preserving the light profile of the discs. My results indicate that bars grow rapidly in size, as I do not observe a strong evolution in the bar size since $z = 1$, for fixed stellar mass (Section 6.5.4). Two Gyrs after bar formation (at $z \approx 0.75$), galaxies undergo a vertical dynamical instability, known as bar buckling, in which they break the vertical symmetry and thicken out of the plane of the disc (Section 6.5.5). After another ∼0.8 Gyrs, the bar orbits in the vertical direction stabilise, forming a boxy/peanut shape if viewed edge-on, and showing boxy isophotes and offset spur morphology when viewed moderately inclined (Section 6.5.1). Meanwhile, the light profile of bars changes, from exponential to a shallower, Gaussian, profile (Section 3.3.3).

Bars are believed to channel gas from the inner disc region to the centre of bar, where the gravitational potential is deepest. The gas accumulates on x_2 orbits perpendicular to the bar and collapses, triggering star formation, initially forming a ring.

The time integrated star formation leads to the formation of nuclear discs, or pseudobulges, that I so frequently found at the centre of barred galaxies (Section 3.4.3). It is unclear how rapid this process is, but the predominantly red colour of bulges that I observe (Section 3.2) suggests that they formed a few Gyr ago, probably before bar buckling, since all the buckled galaxies show evidence of bulges. Nevertheless, some studies suggest that the gas in the bulges can be replenished through continuous gas inflows that can trigger new star formation. The gas in the galaxy discs, on the other hand, is depleted, and star formation is suppressed compared to the discs of unbarred galaxies, as implied by their redder colours (Section 3.4.1). It is worth investigating further whether the colour of the entire disc is redder, or only to the inner region swept out by the bar.

Bars are generally believed to be robust and long-lived. Once formed, they are not easily destroyed. One suggested mechanism to destroy the bars is the growth of a massive central concentration. If the gas inflow is efficient and a significant fraction ($\sim$20%) of the gas is brought to x_2 orbits, where it cools and forms new stars, the growth of a bulge can weaken the bar and eventually destroy it (Debattista et al., 2006). This might be an explanation for the formation of inner lenses, found in this thesis to have structural properties similar to bars (Section 3.5): the stars and gas on x_2 orbits interact with those on x_1 orbits, causing the stars to slowly escape from the bar and the x_1 orbits to become rounder. The connection between bars and inner lenses requires further attention through both observations and simulations. Studying the large nuclear disc in PGC 045903 and other galaxies might give us a clue on how large these bulges can grow before they are able to destroy a bar.

In this thesis, I find that an important driver for changing the galaxy properties is stellar mass. The properties of barred galaxies change radically at a stellar mass $M_* \sim 10^{10.4} - 10^{10.5}\ M_\odot$. Lower mass galaxies can show bars and discs offset from each other, while there are almost no higher mass galaxies showing these offsets (Section 4.5.2), suggesting that the self-gravity and stellar velocity dispersion of galaxies are important for keeping the two components aligned. Galaxies with masses higher than this limit have bars that buckle to form the boxy/peanut bulges (Section 6.5.3). They also form large nuclear discs, sometimes with exceptional sizes (Section 7.3), and their bars have a flat light profile, in contrast with the lower mass galaxies which are predominantly bulgeless and have bars with exponential light profiles (Section 3.3.3). This mass at which galaxy properties change corresponds to the characteristic mass of $M_* \approx 3 \times 10^{10}\ M_\odot$ in the mass-size relation shown in Figure 1.5 (Section 1.1). Lower mass galaxies have young stellar populations, low surface mass densities and are disc dominated. Higher mass galaxies have older stellar populations, high surface

mass densities and high concentrations typical of bulges. Kauffmann et al. (2003b) attributed this sudden change in galaxy properties to feedback process (AGN and supernova feedback), that regulate the growth of galaxies. Thus, it would be worth exploring further the interplay between the dynamical effects due to bars and associated structures, star formation and feedback mechanisms to understand the physical origin of this characteristic mass at which the properties of barred galaxies change so significantly. Additionally, measurements of the velocity dispersion of barred and unbarred galaxies, and their individual components, are needed to investigate further the dynamical scaling relations presented in Section 1.1.

The research on the evolution of barred galaxies and the associated structures is far from being concluded, with many new exciting avenues still to be explored. Future space and ground based surveys, such as *Euclid* or LSST will provide unprecedented samples of galaxies, with both deeper imaging and better resolution, which will revolutionise the study of galaxy evolution. Understanding how barred galaxies evolve is important because they constitute a major fraction of the galaxy population, and it will ultimately lead to a better understanding of how our own galaxy, the Milky Way – a barred spiral – evolved.

Bibliography

Abadi M. G., Lambas D. G., Muriel H., 1998, ApJ, 507, 526

Abbott C. G., Valluri M., Shen J., Debattista V. P., 2017, MNRAS, 470, 1526

Abdurro'uf Akiyama M., 2017, MNRAS, 469, 2806

Abolfathi B., et al., 2018, ApJS, 235, 42

Abraham R. G., Merrifield M. R., Ellis R. S., Tanvir N. R., Brinchmann J., 1999, MNRAS, 308, 569

Abraham R. G., van den Bergh S., Nair P., 2003, ApJ, 588, 218

Abramowitz M., Stegun I. A., 1965, Handbook of mathematical functions with formulas, graphs, and mathematical tables

Aguerri J. A. L., 1999, A&A, 351, 43

Aguerri J. A. L., Balcells M., Peletier R. F., 2001, A&A, 367, 428

Aguerri J. A. L., Méndez-Abreu J., Corsini E. M., 2009, A&A, 495, 491

Ahn C. P., et al., 2014, ApJS, 211, 17

Algorry D. G., et al., 2017, MNRAS, 469, 1054

Alves D. R., 2004, ApJL, 601, L151

Appleton P. N., Struck Marcell C., 1996, FCP, 16, 111

Astropy Collaboration 2013, A&A, 558, A33

Athanassoula E., 1983, in Athanassoula E., ed., IAU Symposium Vol. 100, Internal Kinematics and Dynamics of Galaxies. pp 243–250

Athanassoula E., 1992, MNRAS, 259, 345

Athanassoula E., 1996, in Buta R., Crocker D. A., Elmegreen B. G., eds, Astronomical Society of the Pacific Conference Series Vol. 91, IAU Colloq. 157: Barred Galaxies. p. 309

Athanassoula E., 1999, in Sellwood J. A., Goodman J., eds, Astronomical Society of the Pacific Conference Series Vol. 160, Astrophysical Discs - an EC Summer School. p. 351 (arXiv:astro-ph/9812014)

Athanassoula E., 2000, in Alloin D., Olsen K., Galaz G., eds, Astronomical Society of the Pacific Conference Series Vol. 221, Stars, Gas and Dust in Galaxies: Exploring the Links. p. 243 (arXiv:astro-ph/0006403)

Athanassoula E., 2003, MNRAS, 341, 1179

Athanassoula E., Misiriotis A., 2002, MNRAS, 330, 35

Athanassoula E., Puerari I., Bosma A., 1997, MNRAS, 286, 284

Athanassoula E., Lambert J. C., Dehnen W., 2005, MNRAS, 363, 496

Athanassoula E., Machado R. E. G., Rodionov S. A., 2013, MNRAS, 429, 1949

Athanassoula E., Laurikainen E., Salo H., Bosma A., 2015, MNRAS, 454, 3843

Athanassoula E., Rodionov S. A., Peschken N., Lambert J. C., 2016, ApJ, 821, 90

Bacon R., et al., 2001, MNRAS, 326, 23

Bacon R., et al., 2010, in Ground-based and Airborne Instrumentation for Astronomy III. p. 773508, doi:10.1117/12.856027

Baldry I. K., Balogh M. L., Bower R. G., Glazebrook K., Nichol R. C., Bamford S. P., Budavari T., 2006, MNRAS, 373, 469

Baldwin J. E., Lynden-Bell D., Sancisi R., 1980, MNRAS, 193, 313

Bamford S. P., et al., 2009, MNRAS, 393, 1324

Bamford S. P., Häußler B., Rojas A., Borch A., 2011, in Evans I. N., Accomazzi A., Mink D. J., Rots A. H., eds, Astronomical Society of the Pacific Conference Series Vol. 442, Astronomical Data Analysis Software and Systems XX. p. 479

Barazza F. D., Jogee S., Marinova I., 2008, ApJ, 675, 1194

Barden M., Jahnke K., Häußler B., 2008, ApJS, 175, 105

Barden M., Häußler B., Peng C. Y., McIntosh D. H., Guo Y., 2012, MNRAS, 422, 449

Barnes E. I., Sellwood J. A., 2003, AJ, 125, 1164

Barrera-Ballesteros J. K., et al., 2014, A&A, 568, A70

Barton E. J., Geller M. J., Kenyon S. J., 2000, ApJ, 530, 660

Beck M. R., et al., 2018, MNRAS, 476, 5516

Begeman K. G., 1987, PhD thesis, Kapteyn Institute

Bekki K., 2009, MNRAS, 393, L60

Bekki K., Chiba M., 2005, MNRAS, 356, 680

Bekki K., Chiba M., 2007, MNRAS, 381, L16

Bekki K., Stanimirović S., 2009, MNRAS, 395, 342

Belfiore F., et al., 2018, MNRAS, 477, 3014

Bender R., Burstein D., Faber S. M., 1992, ApJ, 399, 462

Benedict G. F., Howell D. A., Jørgensen I., Kenney J. D. P., Smith B. J., 2002, AJ, 123, 1411

Berentzen I., Athanassoula E., Heller C. H., Fricke K. J., 2003, MNRAS, 341, 343

Berentzen I., Athanassoula E., Heller C. H., Fricke K. J., 2004, MNRAS, 347, 220

Berentzen I., Shlosman I., Martinez-Valpuesta I., Heller C. H., 2007, ApJ, 666, 189

Bershady M. A., Verheijen M. A. W., Westfall K. B., Andersen D. R., Swaters R. A., Martinsson T., 2010, ApJ, 716, 234

Bertin E., Arnouts S., 1996, A&AS, 117, 393

Besla G., Kallivayalil N., Hernquist L., van der Marel R. P., Cox T. J., Kereš D., 2010, ApJL, 721, L97

Besla G., Kallivayalil N., Hernquist L., van der Marel R. P., Cox T. J., Kereš D., 2012, MNRAS, 421, 2109

Bialas D., Lisker T., Olczak C., Spurzem R., Kotulla R., 2015, A&A, 576, A103

Binney J., 2005, MNRAS, 363, 937

Binney J., Petrou M., 1985, MNRAS, 214, 449

Binney J., Tremaine S., 1987, Galactic dynamics

Binney J., Tremaine S., 2008, Galactic Dynamics: Second Edition. Princeton University Press

Binney J., Gerhard O. E., Stark A. A., Bally J., Uchida K. I., 1991, MNRAS, 252, 210

Bizyaev D., Mitronova S., 2009, ApJ, 702, 1567

Bizyaev D. V., Kautsch S. J., Mosenkov A. V., Reshetnikov V. P., Sotnikova N. Y., Yablokova N. V., Hillyer R. W., 2014, ApJ, 787, 24

Blanton M. R., Roweis S., 2007, AJ, 133, 734

Blanton M. R., et al., 2001, AJ, 121, 2358

Blanton M. R., Eisenstein D., Hogg D. W., Schlegel D. J., Brinkmann J., 2005, ApJ, 629, 143

Blitz L., Spergel D. N., 1991, ApJ, 379, 631

Block D. L., Puerari I., Knapen J. H., Elmegreen B. G., Buta R., Stedman S., Elmegreen D. M., 2001, A&A, 375, 761

Blumenthal G. R., Pagels H., Primack J. R., 1982, Nature, 299, 37

Bosma A., 1981, AJ, 86, 1791

Bournaud F., Combes F., 2002, A&A, 392, 83

Bournaud F., Combes F., 2003, A&A, 401, 817

Bournaud F., Combes F., Semelin B., 2005a, MNRAS, 364, L18

Bournaud F., Combes F., Jog C. J., Puerari I., 2005b, A&A, 438, 507

Bramich D. M., Freudling W., 2012, MNRAS, 424, 1584

Brinchmann J., Charlot S., White S. D. M., Tremonti C., Kauffmann G., Heckman T., Brinkmann J., 2004, MNRAS, 351, 1151

Bruzual G., Charlot S., 2003, MNRAS, 344, 1000

Bundy K., et al., 2015, ApJ, 798, 7

Bureau M., Freeman K. C., 1999, AJ, 118, 126

Bureau M., Aronica G., Athanassoula E., Dettmar R.-J., Bosma A., Freeman K. C., 2006, MNRAS, 370, 753

Buta R. J., 2011, preprint, (arXiv:1102.0550)

Buta R. J., 2013, Galaxy Morphology. p. 155

Buta R. J., 2017, MNRAS, 471, 4027

Buta R., Crocker D. A., 1993, AJ, 105, 1344

Buta R. J., Byrd G. G., Freeman T., 2004, AJ, 127, 1982

Buta R. J., Corwin H. G., Odewahn S. C., 2007, The de Vaucouleurs Altlas of Galaxies. Cambridge University Press

Buta R. J., et al., 2015, ApJS, 217, 32

Cameron E., et al., 2010, MNRAS, 409, 346

Caon N., Capaccioli M., D'Onofrio M., 1993, MNRAS, 265, 1013

Capaccioli M., 1989, in Corwin Jr. H. G., Bottinelli L., eds, World of Galaxies (Le Monde des Galaxies). pp 208–227

Cappellari M., 2002, MNRAS, 333, 400

Cappellari M., 2013, ApJL, 778, L2

Cappellari M., 2016, ARA&A, 54, 597

Cappellari M., 2017, MNRAS, 466, 798

Cappellari M., Copin Y., 2003, MNRAS, 342, 345

Cappellari M., Emsellem E., 2004, PASP, 116, 138

Cappellari M., et al., 2011a, MNRAS, 413, 813

Cappellari M., et al., 2011b, MNRAS, 416, 1680

Cappellari M., et al., 2013, MNRAS, 432, 1709

Carignan C., Freeman K. C., 1988, ApJL, 332, L33

Carles C., Martel H., Ellison S. L., Kawata D., 2016, MNRAS, 463, 1074

Carollo C. M., 1999, ApJ, 523, 566

Casteels K. R. V., et al., 2013, MNRAS, 429, 1051

Cecil G., et al., 2016, MNRAS, 456, 1299

Cervantes Sodi B., 2017, ApJ, 835, 80

Ceverino D., Klypin A., 2007, MNRAS, 379, 1155

Chabrier G., 2003, PASP, 115, 763

Charlot S., Longhetti M., 2001, MNRAS, 323, 887

Cheung E., et al., 2013, ApJ, 779, 162

Cheung E., et al., 2015a, MNRAS, 447, 506

Cheung E., et al., 2015b, ApJ, 807, 36

Choi Y., et al., 2018, preprint, (arXiv:1805.00481)

Ciambur B. C., 2016, PASA, 33, e062

Ciotti L., 1991, A&A, 249, 99

Cisternas M., Sheth K., Salvato M., Knapen J. H., Civano F., Santini P., 2015, ApJ, 802, 137

Coelho P., Gadotti D. A., 2011, ApJL, 743, L13

Cole A. A., Tolstoy E., Gallagher III J. S., Smecker-Hane T. A., 2005, AJ, 129, 1465

Cole D. R., Debattista V. P., Erwin P., Earp S. W. F., Roškar R., 2014, MNRAS, 445, 3352

Combes F., Elmegreen B. G., 1993, A&A, 271, 391

Combes F., Sanders R. H., 1981, A&A, 96, 164

Combes F., Debbasch F., Friedli D., Pfenniger D., 1990, A&A, 233, 82

Conselice C. J., 2003, ApJS, 147, 1

Conselice C. J., Bershady M. A., Dickinson M., Papovich C., 2003, AJ, 126, 1183

Conselice C. J., Wilkinson A., Duncan K., Mortlock A., 2016, ApJ, 830, 83

Consolandi G., 2016, A&A, 595, A67

Consolandi G., Dotti M., Boselli A., Gavazzi G., Gargiulo F., 2017, A&A, 598, A114

Contopoulos G., Grosbol P., 1989, AAPR, 1, 261

Contopoulos G., Harsoula M., 2008, International Journal of Bifurcation and Chaos, 18, 2929

Contopoulos G., Papayannopoulos T., 1980, A&A, 92, 33

Courteau S., de Jong R. S., Broeils A. H., 1996, ApJL, 457, L73

Croom S. M., et al., 2012, MNRAS, 421, 872

Curtis H. D., 1918, Publications of Lick Observatory, 13, 9

Darg D. W., et al., 2010, MNRAS, 401, 1043

Dawson K. S., et al., 2013, AJ, 145, 10

Debattista V. P., Sellwood J. A., 1998, ApJL, 493, L5

Debattista V. P., Sellwood J. A., 2000, ApJ, 543, 704

Debattista V. P., Carollo C. M., Mayer L., Moore B., 2004, ApJL, 604, L93

Debattista V. P., Mayer L., Carollo C. M., Moore B., Wadsley J., Quinn T., 2006, ApJ, 645, 209

Debattista V. P., Ness M., Earp S. W. F., Cole D. R., 2015, ApJL, 812, L16

Debattista V. P., Ness M., Gonzalez O. A., Freeman K., Zoccali M., Minniti D., 2017, MNRAS, 469, 1587

Debattista V. P., Earp S. W. F., Ness M., Gonzalez O. A., 2018, MNRAS, 473, 5275

Desmond H., Ferreira P. G., Lavaux G., Jasche J., 2018, PhRvD, 98, 064015

Díaz-García S., Salo H., Laurikainen E., Herrera-Endoqui M., 2016, A&A, 587, A160

Dickinson H., et al., 2018, ApJ, 853, 194

Dieleman S., Willett K. W., Dambre J., 2015, MNRAS, 450, 1441

Djorgovski S., Davis M., 1987, ApJ, 313, 59

Domínguez Sánchez H., Huertas-Company M., Bernardi M., Tuccillo D., Fischer J. L., 2018, MNRAS, 476, 3661

Dressler A., Lynden-Bell D., Burstein D., Davies R. L., Faber S. M., Terlevich R., Wegner G., 1987, ApJ, 313, 42

Driver S. P., Popescu C. C., Tuffs R. J., Liske J., Graham A. W., Allen P. D., de Propris R., 2007, MNRAS, 379, 1022

Driver S. P., Popescu C. C., Tuffs R. J., Graham A. W., Liske J., Baldry I., 2008, ApJL, 678, L101

Driver S. P., et al., 2009, Astronomy and Geophysics, 50, 5.12

Dwek E., et al., 1995, ApJ, 445, 716

Elagali A., Wong O. I., Oh S.-H., Staveley-Smith L., Koribalski B. S., Bekki K., Zwaan M., 2018, MNRAS, 476, 5681

Ellison S. L., Patton D. R., Simard L., McConnachie A. W., 2008, AJ, 135, 1877

Ellison S. L., Nair P., Patton D. R., Scudder J. M., Mendel J. T., Simard L., 2011, MNRAS, 416, 2182

Elmegreen B. G., Elmegreen D. M., 1985, ApJ, 288, 438

Elmegreen B. G., Elmegreen D. M., Hirst A. C., 2004, ApJ, 612, 191

Elmegreen D. M., Elmegreen B. G., Ravindranath S., Coe D. A., 2007, ApJ, 658, 763

Emsellem E., Fathi K., Wozniak H., Ferruit P., Mundell C. G., Schinnerer E., 2006, MNRAS, 365, 367

Emsellem E., et al., 2007, MNRAS, 379, 401

Erwin P., 2004, A&A, 415, 941

Erwin P., 2015, ApJ, 799, 226

Erwin P., 2018, MNRAS, 474, 5372

Erwin P., Debattista V. P., 2013, MNRAS, 431, 3060

Erwin P., Debattista V. P., 2016, ApJL, 825, L30

Erwin P., Debattista V. P., 2017, MNRAS, 468, 2058

Erwin P., Sparke L. S., 2002, AJ, 124, 65

Erwin P., et al., 2015, MNRAS, 446, 4039

Eskridge P. B., et al., 2000, AJ, 119, 536

Eskridge P. B., et al., 2002, ApJS, 143, 73

Faber S. M., Jackson R. E., 1976, ApJ, 204, 668

Faber S. M., Dressler A., Davies R. L., Burstein D., Bell D. L., Terlevich R., Wegner G., 1987, in Faber S. M., ed., Nearly Normal Galaxies. From the Planck Time to the Present. pp 175–183

Fabricius M. H., Saglia R. P., Fisher D. B., Drory N., Bender R., Hopp U., 2012, ApJ, 754, 67

Falcón-Barroso J., et al., 2006, MNRAS, 369, 529

Falcón-Barroso J., Sánchez-Blázquez P., Vazdekis A., Ricciardelli E., Cardiel N., Cenarro A. J., Gorgas J., Peletier R. F., 2011, A&A, 532, A95

Fall S. M., Efstathiou G., 1980, MNRAS, 193, 189

Fanali R., Dotti M., Fiacconi D., Haardt F., 2015, MNRAS, 454, 3641

Fathi K., Beckman J. E., Piñol-Ferrer N., Hernandez O., Martínez-Valpuesta I., Carignan C., 2009, ApJ, 704, 1657

Feitzinger J. V., 1980, SSR, 27, 35

Fisher D. B., Drory N., 2008, AJ, 136, 773

Fisher D. B., Drory N., 2010, ApJ, 716, 942

Fisher D. B., Drory N., Fabricius M. H., 2009, ApJ, 697, 630

Fortin P., Athanassoula E., Lambert J.-C., 2011, A&A, 531, A120

Freeman K. C., 1970, ApJ, 160, 811

Frenk C. S., et al., 1999, ApJ, 525, 554

Freudenreich H. T., 1998, ApJ, 492, 495

Friedli D., Benz W., 1995, A&A, 301, 649

Fukugita M., Ichikawa T., Gunn J. E., Doi M., Shimasaku K., Schneider D. P., 1996, AJ, 111, 1748

Gadotti D. A., 2008, MNRAS, 384, 420

Gadotti D. A., 2009, MNRAS, 393, 1531

Gadotti D. A., 2011, MNRAS, 415, 3308

Gadotti D. A., Athanassoula E., Carrasco L., Bosma A., de Souza R. E., Recillas E., 2007, MNRAS, 381, 943

Gadotti D. A., Baes M., Falony S., 2010, MNRAS, 403, 2053

Gadotti D. A., Seidel M. K., Sánchez-Blázquez P., Falcón-Barroso J., Husemann B., Coelho P., Pérez I., 2015, A&A, 584, A90

Gaia Collaboration 2016, A&A, 595, A1

Gajda G., Łokas E. L., Athanassoula E., 2017, ApJ, 842, 56

Galloway M. A., et al., 2015, MNRAS, 448, 3442

Gao H., Ho L. C., Barth A. J., Li Z.-Y., 2018, ApJ, 862, 100

García-Lorenzo B., et al., 2015, A&A, 573, A59

Gavazzi G., et al., 2015, A&A, 580, A116

Gerin M., Combes F., Athanassoula E., 1990, A&A, 230, 37

Giuricin G., Mardirossian F., Mezzetti M., Monaco P., 1993, ApJ, 407, 22

Goulding A. D., et al., 2017, ApJ, 843, 135

Graham A. W., 2016, Galactic Bulges, 418, 263

Graham A. W., Worley C. C., 2008, MNRAS, 388, 1708

Graham M. T., et al., 2018, MNRAS,

Graves G. J., Faber S. M., Schiavon R. P., 2009, ApJ, 693, 486

Griffith R. L., et al., 2012, ApJS, 200, 9

Gunn J. E., Gott III J. R., 1972, ApJ, 176, 1

Gunn J. E., et al., 1998, AJ, 116, 3040

Hart R. E., Bamford S. P., Casteels K. R. V., Kruk S. J., Lintott C. J., Masters K. L., 2017, MNRAS, 468, 1850

Häussler B., et al., 2007, ApJS, 172, 615

Häußler B., et al., 2013, MNRAS, 430, 330

Hayashi E., et al., 2004, MNRAS, 355, 794

Hayashi E., Navarro J. F., Springel V., 2007, MNRAS, 377, 50

Haywood M., Lehnert M. D., Di Matteo P., Snaith O., Schultheis M., Katz D., Gómez A., 2016, A&A, 589, A66

Heckman T. M., 1980, A&A, 88, 365

Heller C. H., Shlosman I., Athanassoula E., 2007, ApJ, 671, 226

Hernquist L., 1990, ApJ, 356, 359

Hickox R. C., Mullaney J. R., Alexander D. M., Chen C.-T. J., Civano F. M., Goulding A. D., Hainline K. N., 2014, ApJ, 782, 9

Ho L. C., Filippenko A. V., Sargent W. L. W., 1997, ApJ, 487, 591

Hockney R. W., Hohl F., 1969, AJ, 74, 1102

Hohl F., 1971, ApJ, 168, 343

Hohl F., Feix M. R., 1967, ApJ, 147, 1164

Holmes L., et al., 2015, MNRAS, 451, 4397

Holtzman J. A., et al., 1999, AJ, 118, 2262

Hopkins P. F., Kereš D., Murray N., Quataert E., Hernquist L., 2012, MNRAS, 427, 968

Hoyle B., et al., 2011, MNRAS, 415, 3627

Hubble E. P., 1926, ApJ, 64

Hubble E., 1936, Science, 84, 509

Huertas-Company M., 2016, in Kaviraj S., ed., IAU Symposium Vol. 319, Galaxies at High Redshift and Their Evolution Over Cosmic Time. pp 118–125, doi:10.1017/S1743921315010911

Jacob J. C., et al., 2010b, preprint, (arXiv:1005.4454)

Jacob J. C., et al., 2010a, Montage: An Astronomical Image Mosaicking Toolkit (ascl:1010.036)

Jain B., VanderPlas J., 2011, JCAP, 10, 032

James P. A., Percival S. M., 2015, MNRAS, 450, 3503

James P. A., Percival S. M., 2016, MNRAS, 457, 917

James P. A., Percival S. M., 2018, MNRAS, 474, 3101

James P. A., Bretherton C. F., Knapen J. H., 2009, A&A, 501, 207

Jarosik N., et al., 2011, ApJS, 192, 14

Jiang L., et al., 2014, ApJS, 213, 12

Jing Y. P., Suto Y., 2002, ApJ, 574, 538

Jog C. J., 1997, ApJ, 488, 642

Jog C. J., 1999, ApJ, 522, 661

Jog C. J., 2000, ApJ, 542, 216

Jog C. J., 2002, A&A, 391, 471

Jogee S., Knapen J. H., Laine S., Shlosman I., Scoville N. Z., Englmaier P., 2002, ApJL, 570, L55

Jogee S., et al., 2004, ApJL, 615, L105

Jogee S., Scoville N., Kenney J. D. P., 2005, ApJ, 630, 837

Kallivayalil N., van der Marel R. P., Alcock C., Axelrod T., Cook K. H., Drake A. J., Geha M., 2006, ApJ, 638, 772

Kalnajs A. J., 1972, ApJ, 175, 63

Kalnajs A. J., 1977, ApJ, 212, 637

Kauffmann G., et al., 2003a, MNRAS, 341, 33

Kauffmann G., et al., 2003b, MNRAS, 341, 54

Kennedy R., et al., 2016, MNRAS, 460, 3458

Kerr F. J., 1957, AJ, 62, 93

Khoperskov S., Haywood M., Di Matteo P., Lehnert M. D., Combes F., 2018, A&A, 609, A60

Kim S., Staveley-Smith L., Dopita M. A., Freeman K. C., Sault R. J., Kesteven M. J., McConnell D., 1998, ApJ, 503, 674

Kim S., Dopita M. A., Staveley-Smith L., Bessell M. S., 1999, AJ, 118, 2797

Kim T., et al., 2015, ApJ, 799, 99

Kim E., Hwang H. S., Chung H., Lee G.-H., Park C., Cervantes Sodi B., Kim S. S., 2017, ApJ, 845, 93

Klypin A., Kravtsov A. V., Valenzuela O., Prada F., 1999, ApJ, 522, 82

Knapen J. H., 2005, A&A, 429, 141

Knapen J. H., Mazzuca L. M., Böker T., Shlosman I., Colina L., Combes F., Axon D. J., 2006, A&A, 448, 489

Koekemoer A. M., et al., 2007, ApJS, 172, 196

Koekemoer A. M., et al., 2011, ApJS, 197, 36

Kormendy J., 1977, ApJ, 218, 333

Kormendy J., 1979, ApJ, 227, 714

Kormendy J., 2013, Secular Evolution in Disk Galaxies. p. 1

Kormendy J., Bender R., 2012, ApJS, 198, 2

Kormendy J., Fisher D. B., 2008, in Funes J. G., Corsini E. M., eds, Astronomical Society of the Pacific Conference Series Vol. 396, Formation and Evolution of Galaxy Disks. p. 297 (arXiv:0810.2534)

Kormendy J., Kennicutt Jr. R. C., 2004, ARA&A, 42, 603

Kormendy J., Drory N., Bender R., Cornell M. E., 2010, ApJ, 723, 54

Krajnović D., Cappellari M., de Zeeuw P. T., Copin Y., 2006, MNRAS, 366, 787

Kraljic K., Bournaud F., Martig M., 2012, ApJ, 757, 60

Kruk S. J., et al., 2017, MNRAS, 469, 3363

Kruk S. J., et al., 2018, MNRAS, 473, 4731

Laigle C., et al., 2016, ApJS, 224, 24

Lake G., Norman C., 1983, ApJ, 270, 51

Laureijs R., et al., 2011, preprint, (arXiv:1110.3193)

Laurikainen E., Salo H., 2002, MNRAS, 337, 1118

Laurikainen E., Salo H., 2016, in Laurikainen E., Peletier R., Gadotti D., eds, Astrophysics and Space Science Library Vol. 418, Galactic Bulges. p. 77 (arXiv:1505.00590), doi:10.1007/978-3-319-19378-6_4

Laurikainen E., Salo H., 2017, A&A, 598, A10

Laurikainen E., Salo H., Buta R., Vasylyev S., 2004a, MNRAS, 355, 1251

Laurikainen E., Salo H., Buta R., Vasylyev S., 2004b, MNRAS, 355, 1251

Laurikainen E., Salo H., Buta R., 2005, MNRAS, 362, 1319

Laurikainen E., Salo H., Buta R., Knapen J. H., 2007, MNRAS, 381, 401

Laurikainen E., Salo H., Buta R., Knapen J. H., 2009, ApJL, 692, L34

Laurikainen E., Salo H., Buta R., Knapen J. H., 2011, MNRAS, 418, 1452

Laurikainen E., Salo H., Athanassoula E., Bosma A., Buta R., Janz J., 2013, MNRAS, 430, 3489

Laurikainen E., Salo H., Athanassoula E., Bosma A., Herrera-Endoqui M., 2014, MNRAS, 444, L80

Law D. R., et al., 2015, AJ, 150, 19

Law D. R., et al., 2016, AJ, 152, 83

Lee G.-H., Park C., Lee M. G., Choi Y.-Y., 2012, ApJ, 745, 125

Levine S. E., Sparke L. S., 1998, ApJL, 496, L13

Li C., Gadotti D. A., Mao S., Kauffmann G., 2009, MNRAS, 397, 726

Li Z.-Y., Ho L. C., Barth A. J., 2017, ApJ, 845, 87

Licquia T. C., Newman J. A., 2015, ApJ, 806, 96

Lin Y., Cervantes Sodi B., Li C., Wang L., Wang E., 2014, ApJ, 796, 98

Lin L., et al., 2017, ApJ, 851, 18

Lintott C. J., et al., 2008, MNRAS, 389, 1179

Lintott C., et al., 2011, MNRAS, 410, 166

Liszt H. S., Burton W. B., 1980, ApJ, 236, 779

Liu L., Gerke B. F., Wechsler R. H., Behroozi P. S., Busha M. T., 2011, ApJ, 733, 62

Łokas E. L., 2018, ApJ, 857, 6

Lotz J. M., Jonsson P., Cox T. J., Croton D., Primack J. R., Somerville R. S., Stewart K., 2011, ApJ, 742, 103

Lupton R., Gunn J. E., Ivezić Z., Knapp G. R., Kent S., 2001, in Harnden Jr. F. R., Primini F. A., Payne H. E., eds, Astronomical Society of the Pacific Conference Series Vol. 238, Astronomical Data Analysis Software and Systems X. p. 269 (arXiv:astro-ph/0101420)

Lütticke R., Dettmar R.-J., Pohlen M., 2000a, A&AS, 145, 405

Lütticke R., Dettmar R.-J., Pohlen M., 2000b, A&A, 362, 435

Lynden-Bell D., 1979, MNRAS, 187, 101

Lynden-Bell D., Kalnajs A. J., 1972, MNRAS, 157, 1

Madau P., Diemand J., Kuhlen M., 2008, ApJ, 679, 1260

Marchesini D., D'Onghia E., Chincarini G., Firmani C., Conconi P., Molinari E., Zacchei A., 2002, ApJ, 575, 801

Marinova I., et al., 2012, ApJ, 746, 136

Marshall P. J., et al., 2016, MNRAS, 455, 1171

Martel H., Kawata D., Ellison S. L., 2013, MNRAS, 431, 2560

Martig M., Bournaud F., Croton D. J., Dekel A., Teyssier R., 2012, ApJ, 756, 26

Martin P., 1995, AJ, 109, 2428

Martin P., Friedli D., 1997, A&A, 326, 449

Martin N. F., Collins M. L. M., Longeard N., Tollerud E., 2018, ApJL, 859, L5

Martinet L., Friedli D., 1997, A&A, 323, 363

Martinez-Valpuesta I., Shlosman I., 2004, ApJL, 613, L29

Martinez-Valpuesta I., Shlosman I., Heller C., 2006, ApJ, 637, 214

Martinez-Valpuesta I., Aguerri J. A. L., González-García A. C., Dalla Vecchia C., Stringer M., 2017, MNRAS, 464, 1502

Masters K. L., et al., 2010, MNRAS, 404, 792

Masters K. L., et al., 2011, MNRAS, 411, 2026

Masters K. L., et al., 2012, MNRAS, 424, 2180

McGaugh S. S., de Blok W. J. G., 1998, ApJ, 499, 41

McWilliam A., Zoccali M., 2010, ApJ, 724, 1491

Medling A. M., et al., 2014, ApJ, 784, 70

Melvin T., et al., 2014, MNRAS, 438, 2882

Méndez-Abreu J., Aguerri J. A. L., Corsini E. M., Simonneau E., 2008, A&A, 478, 353

Méndez-Abreu J., Sánchez-Janssen R., Aguerri J. A. L., Corsini E. M., Zarattini S., 2012, ApJL, 761, L6

Méndez-Abreu J., Debattista V. P., Corsini E. M., Aguerri J. A. L., 2014, A&A, 572, A25

Méndez-Abreu J., et al., 2017, A&A, 598, A32

Menéndez-Delmestre K., Sheth K., Schinnerer E., Jarrett T. H., Scoville N. Z., 2007, ApJ, 657, 790

Merritt D., Sellwood J. A., 1994, ApJ, 425, 551

Miller R. H., Prendergast K. H., 1968, ApJ, 151, 699

Moffat A. F. J., 1969, A&A, 3, 455

Moiseev A. V., Smirnova K. I., Smirnova A. A., Reshetnikov V. P., 2011, MNRAS, 418, 244

Monteagudo L., Gallart C., Monelli M., Bernard E. J., Stetson P. B., 2018, MNRAS, 473, L16

Moore B., Katz N., Lake G., Dressler A., Oemler A., 1996, Nature, 379, 613

Moore B., Ghigna S., Governato F., Lake G., Quinn T., Stadel J., Tozzi P., 1999, ApJL, 524, L19

Muñoz-Mateos J. C., et al., 2015, ApJS, 219, 3

Muldrew S. I., et al., 2012, MNRAS, 419, 2670

Naab T., Burkert A., 2003, ApJ, 597, 893

Nair P. B., Abraham R. G., 2010a, ApJS, 186, 427

Nair P. B., Abraham R. G., 2010b, ApJL, 714, L260

Navarro J. F., Eke V. R., Frenk C. S., 1996, MNRAS, 283, L72

Ness M., Lang D., 2016, AJ, 152, 14

Ness M., Debattista V. P., Bensby T., Feltzing S., Roškar R., Cole D. R., Johnson J. A., Freeman K., 2014, ApJL, 787, L19

Noguchi M., 1987, MNRAS, 228, 635

Noguchi M., 1988, A&A, 203, 259

Noordermeer E., Sparke L. S., Levine S. E., 2001, MNRAS, 328, 1064

Odewahn S. C., 1994, AJ, 107, 1320

Odewahn S. C., 1996, in Buta R., Crocker D. A., Elmegreen B. G., eds, Astronomical Society of the Pacific Conference Series Vol. 91, IAU Colloq. 157: Barred Galaxies. p. 30

Oh S., Oh K., Yi S. K., 2012, ApJS, 198, 4

Pardy S. A., D. Onghia E., Athanassoula E., Wilcots E. M., Sheth K., 2016, ApJ, 827, 149

Patterson F. S., 1940, Harvard College Observatory Bulletin, 914, 9

Patton D. R., Carlberg R. G., Marzke R. O., Pritchet C. J., da Costa L. N., Pellegrini P. S., 2000, ApJ, 536, 153

Patton D. R., et al., 2002, ApJ, 565, 208

Patton D. R., Torrey P., Ellison S. L., Mendel J. T., Scudder J. M., 2013, MNRAS, 433, L59

Patton D. R., Qamar F. D., Ellison S. L., Bluck A. F. L., Simard L., Mendel J. T., Moreno J., Torrey P., 2016, MNRAS, 461, 2589

Peebles P. J. E., 1982, ApJL, 263, L1

Peebles P. J. E., 1993, Principles of Physical Cosmology

Peletier R. F., et al., 2007, MNRAS, 379, 445

Pence W. D., Taylor K., Freeman K. C., de Vaucouleurs G., Atherton P., 1988, ApJ, 326, 564

Peng C. Y., Ho L. C., Impey C. D., Rix H.-W., 2002, AJ, 124, 266

Peng C. Y., Ho L. C., Impey C. D., Rix H.-W., 2010, AJ, 139, 2097

Peng Y., Maiolino R., Cochrane R., 2015, Nature, 521, 192

Pérez I., Sánchez-Blázquez P., 2011, A&A, 529, A64

Pérez I., et al., 2017, MNRAS, 470, L122

Perlmutter S., et al., 1999, ApJ, 517, 565

Peschken N., Łokas E. L., 2018, preprint, (arXiv:1804.06241)

Petrosian V., 1976, ApJL, 209, L1

Pfenniger D., Friedli D., 1991, A&A, 252, 75

Pfenniger D., Norman C., 1990, ApJ, 363, 391

Pierini D., Gordon K. D., Witt A. N., Madsen G. J., 2004, ApJ, 617, 1022

Planck Collaboration 2016, A&A, 594, A13

Portail M., Wegg C., Gerhard O., 2015, MNRAS, 450, L66

Quillen A. C., 2002, AJ, 124, 722

Quillen A. C., Minchev I., Sharma S., Qin Y.-J., Di Matteo P., 2014, MNRAS, 437, 1284

Raha N., Sellwood J. A., James R. A., Kahn F. D., 1991, Nature, 352, 411

Reese A. S., Williams T. B., Sellwood J. A., Barnes E. I., Powell B. A., 2007, AJ, 133, 2846

Regan M. W., Sheth K., Vogel S. N., 1999, ApJ, 526, 97

Reynaud D., Downes D., 1998, A&A, 337, 671

Rix H.-W., Zaritsky D., 1995, ApJ, 447, 82

Robichaud F., Williamson D., Martel H., Kawata D., Ellison S. L., 2017, MNRAS, 469, 3722

Robotham A. S. G., et al., 2012, MNRAS, 424, 1448

Robotham A. S. G., Taranu D. S., Tobar R., Moffett A., Driver S. P., 2017, MNRAS, 466, 1513

Saha K., Martinez-Valpuesta I., Gerhard O., 2012, MNRAS, 421, 333

Saha K., Pfenniger D., Taam R. E., 2013, ApJ, 764, 123

Sahni V., Starobinsky A., 2000, International Journal of Modern Physics D, 9, 373

Saintonge A., et al., 2011, MNRAS, 415, 32

Sakamoto K., Okumura S. K., Ishizuki S., Scoville N. Z., 1999, ApJ, 525, 691

Salim S., et al., 2007, ApJS, 173, 267

Salo H., et al., 2015, ApJS, 219, 4

Sánchez-Janssen R., Gadotti D. A., 2013, MNRAS, 432, L56

Sánchez S. F., et al., 2012, A&A, 538, A8

Sandage A., 1961, The Hubble Atlas of Galaxies

Sanders R. H., Tubbs A. D., 1980, ApJ, 235, 803

Scannapieco C., Athanassoula E., 2012, MNRAS, 425, L10

Scannapieco C., Gadotti D. A., Jonsson P., White S. D. M., 2010, MNRAS, 407, L41

Schawinski K., et al., 2014, MNRAS, 440, 889

Schaye J., et al., 2015, MNRAS, 446, 521

Schlegel D. J., Finkbeiner D. P., Davis M., 1998, ApJ, 500, 525

Schlegel D. J., et al., 2015, in American Astronomical Society Meeting Abstracts. p. 336.07

Schoenmakers R. H. M., Franx M., de Zeeuw P. T., 1997, MNRAS, 292, 349

Scoville N., et al., 2007, ApJS, 172, 1

Seigar M., Carollo C. M., Stiavelli M., de Zeeuw P. T., Dejonghe H., 2002, AJ, 123, 184

Sellwood J. A., 2013, Dynamics of Disks and Warps. p. 923, doi:10.1007/978-94-007-5612-0_18

Sellwood J. A., 2014, Reviews of Modern Physics, 86, 1

Sellwood J. A., Debattista V. P., 2009, MNRAS, 398, 1279

Sellwood J. A., Sánchez R. Z., 2010, MNRAS, 404, 1733

Sellwood J. A., Wilkinson A., 1993, Reports on Progress in Physics, 56, 173

Sersic J. L., 1968, Atlas de galaxias australes

Sharples R., et al., 2006, NAR, 50, 370

Shaw M., Axon D., Probst R., Gatley I., 1995, MNRAS, 274, 369

Shen J., Li Z.-Y., 2016, in Laurikainen E., Peletier R., Gadotti D., eds, Astrophysics and Space Science Library Vol. 418, Galactic Bulges. p. 233 (arXiv:1504.05136), doi:10.1007/978-3-319-19378-6_10

Shen J., Sellwood J. A., 2004, ApJ, 604, 614

Shen J., Rich R. M., Kormendy J., Howard C. D., De Propris R., Kunder A., 2010, ApJL, 720, L72

Sheth K., Vogel S. N., Regan M. W., Thornley M. D., Teuben P. J., 2005, ApJ, 632, 217

Sheth K., et al., 2008, ApJ, 675, 1141

Sheth K., et al., 2010, PASP, 122, 1397

Shlosman I., Begelman M. C., Frank J., 1990, Nature, 345, 679

Shlosman I., Peletier R. F., Knapen J. H., 2000, ApJL, 535, L83

Simard L., 1998, in Albrecht R., Hook R. N., Bushouse H. A., eds, Astronomical Society of the Pacific Conference Series Vol. 145, Astronomical Data Analysis Software and Systems VII. p. 108

Simard L., Mendel J. T., Patton D. R., Ellison S. L., McConnachie A. W., 2011, ApJS, 196, 11

Simkin S. M., Su H. J., Schwarz M. P., 1980, ApJ, 237, 404

Simmons B. D., et al., 2013, MNRAS, 429, 2199

Simmons B. D., et al., 2014, MNRAS, 445, 3466

Simmons B. D., et al., 2017, MNRAS, 464, 4420

Simon J. D., Geha M., 2007, ApJ, 670, 313

Skibba R. A., et al., 2012, MNRAS, 423, 1485

Skokos C., Patsis P. A., Athanassoula E., 2002, MNRAS, 333, 847

Smethurst R. J., Lintott C. J., Bamford S. P., Hart R. E., Kruk S. J., Masters K. L., Nichol R. C., Simmons B. D., 2017, MNRAS, 469, 3670

Smith J. A., et al., 2002, AJ, 123, 2121

Smithsonian Astrophysical Observatory 2000, SAOImage DS9: A utility for displaying astronomical images in the X11 window environment, Astrophysics Source Code Library (ascl:0003.002)

Sofue Y., Rubin V., 2001, ARA&A, 39, 137

Sparke L. S., Sellwood J. A., 1987, MNRAS, 225, 653

Spekkens K., Sellwood J. A., 2007, ApJ, 664, 204

Spindler A., et al., 2018, MNRAS, 476, 580

Spinoso D., Bonoli S., Dotti M., Mayer L., Madau P., Bellovary J., 2017, MNRAS, 465, 3729

Stanimirovic, S. and Staveley-Smith, L. and Jones, P. A. 2004, A New Look at the Kinematics of Neutral Hydrogen in the Small Magellanic Cloud (arXiv:astro-ph/0312223), doi:10.1086/381869

Stoughton C., et al., 2002, AJ, 123, 485

Strauss M. A., et al., 2002, AJ, 124, 1810

Strigari L. E., Bullock J. S., Kaplinghat M., Simon J. D., Geha M., Willman B., Walker M. G., 2008, Nature, 454, 1096

Swaters R. A., Schoenmakers R. H. M., Sancisi R., van Albada T. S., 1999, MNRAS, 304, 330

Swaters R. A., Sancisi R., van Albada T. S., van der Hulst J. M., 2009, A&A, 493, 871

Tacchella S., et al., 2015, Science, 348, 314

Taylor M. B., 2005, in Shopbell P., Britton M., Ebert R., eds, Astronomical Society of the Pacific Conference Series Vol. 347, Astronomical Data Analysis Software and Systems XIV. p. 29

Taylor E. N., et al., 2011, MNRAS, 418, 1587

Toomre A., 1964, ApJ, 139, 1217

Toomre A., 1966, in Woods Hole: Woods Hole Oceanographic Inst.

Toomre A., 1981, in Fall S. M., Lynden-Bell D., eds, Structure and Evolution of Normal Galaxies. pp 111–136

Trachternach C., de Blok W. J. G., Walter F., Brinks E., Kennicutt Jr. R. C., 2008, AJ, 136, 2720

Trujillo I., et al., 2018, preprint, (arXiv:1806.10141)

Tubbs A. D., 1982, ApJ, 255, 458

Tuffs R. J., Popescu C. C., Völk H. J., Kylafis N. D., Dopita M. A., 2004, A&A, 419, 821

Tully R. B., Fisher J. R., 1977, A&A, 54, 661

Unterborn C. T., Ryden B. S., 2008, ApJ, 687, 976

Valluri M., Shen J., Abbott C., Debattista V. P., 2016, ApJ, 818, 141

Vazdekis A., Sánchez-Blázquez P., Falcón-Barroso J., Cenarro A. J., Beasley M. A., Cardiel N., Gorgas J., Peletier R. F., 2010, MNRAS, 404, 1639

Vika M., Bamford S. P., Häußler B., Rojas A. L., Borch A., Nichol R. C., 2013, MNRAS, 435, 623

Vika M., Bamford S. P., Häußler B., Rojas A. L., 2014, MNRAS, 444, 3603

Villa-Vargas J., Shlosman I., Heller C., 2010, ApJ, 719, 1470

Vogelsberger M., et al., 2014, MNRAS, 444, 1518

Wada K., 2004, Coevolution of Black Holes and Galaxies, p. 186

Wake D. A., et al., 2017, AJ, 154, 86

Walcher C. J., et al., 2014, A&A, 569, A1

Wannier P., Wrixon G. T., 1972, ApJL, 173, L119

Wegg C., Gerhard O., 2013, MNRAS, 435, 1874

Wegg C., Gerhard O., Portail M., 2015, MNRAS, 450, 4050

Weinberg M. D., 1995, ApJL, 455, L31

Weinzirl T., Jogee S., Khochfar S., Burkert A., Kormendy J., 2009, ApJ, 696, 411

Wilcots E. M., Prescott M. K. M., 2004, AJ, 127, 1900

Willett K. W., et al., 2013, MNRAS, 435, 2835

Willett K. W., et al., 2017, MNRAS, 464, 4176

Wright D. E., et al., 2017, MNRAS, 472, 1315

Yasuda N., et al., 2001, AJ, 122, 1104

York D. G., et al., 2000, AJ, 120, 1579

Yoshino A., Yamauchi C., 2015, MNRAS, 446, 3749

Yozin C., Bekki K., 2014, MNRAS, 439, 1948

Zaritsky D., Rix H.-W., 1997, ApJ, 477, 118

Zaritsky D., et al., 2013, ApJ, 772, 135

Zasov A. V., Khoperskov A. V., 2002, Astronomy Reports, 46, 173

Zhao H., Evans N. W., 2000, ApJL, 545, L35

Zou Y., Shen J., Li Z.-Y., 2014, ApJ, 791, 11

Zwicky F., 1941, Hydrodynamics and the Structure of Stellar Systems. p. 137

de Blok W. J. G., McGaugh S. S., 1997, MNRAS, 290, 533

de Souza R. E., et al., 2004, ApJS, 153, 411

de Swardt B., et al., 2015, ApJ, 808, 90

de Vaucouleurs G., 1948, Annales d'Astrophysique, 11, 247

de Vaucouleurs G., 1955, AJ, 60, 126

de Vaucouleurs G., 1959, Handbuch der Physik, 53, 275

de Vaucouleurs G., 1963, ApJS, 8, 31

de Vaucouleurs G., Freeman K. C., 1972, Vistas in Astronomy, 14, 163

de Vaucouleurs G., de Vaucouleurs A., Corwin Jr. H. G., Buta R. J., Paturel G., Fouqué P., 1991, Third Reference Catalogue of Bright Galaxies. Volume I: Explanations and references. Volume II: Data for galaxies between 0^h and 12^h. Volume III: Data for galaxies between 12^h and 24^h.

van Dokkum P., et al., 2018, Nature, 555, 629

van Eymeren J., Jütte E., Jog C. J., Stein Y., Dettmar R.-J., 2011, A&A, 530, A29

van de Voort F., Davis T. A., Kereš D., Quataert E., Faucher-Giguère C.-A., Hopkins P. F., 2015, MNRAS, 451, 3269

van den Bergh S., 2002, AJ, 124, 782

van der Kruit P. C., 1988, A&A, 192, 117

van der Kruit P. C., Searle L., 1981, A&A, 95, 105

van der Marel R. P., 2001, AJ, 122, 1827

van der Marel R. P., Kallivayalil N., 2014, ApJ, 781, 121

van der Marel R. P., Alves D. R., Hardy E., Suntzeff N. B., 2002, AJ, 124, 2639